Master's thesis

NTNU
Norwegian University of Science and Technology
Faculty of Engineering
Department of Marine Technology

Magnus Onsrud

An Experimental Study on the Wave-Induced Vertical Response of an Articulated Multi-Module Floating Solar Island

Master's thesis in Marine Technology
Supervisor: Trygve Kristiansen
June 2019

NTNU
Norwegian University of
Science and Technology

Magnus Onsrud

An Experimental Study on the Wave-Induced Vertical Response of an Articulated Multi-Module Floating Solar Island

Master's thesis in Marine Technology
Supervisor: Trygve Kristiansen
June 2019

Norwegian University of Science and Technology
Faculty of Engineering
Department of Marine Technology

NTNU
Norwegian University of
Science and Technology

Preface

This Master's Thesis is the concluding part of my Master of Science degree in Hydrodynamics in Marine Technology/Naval Architecture at the Department of Marine Technology (IMT) at the Norwegian University of Science and Technology (NTNU) in Trondheim, Norway.

The Thesis investigates the wave-induced vertical hydrodynamic response of a hinged multi-module structure in different sea-conditions by experimental methods. The structure is a simplified component of a new concept for a floating solar island that consist of an array of these identical modules. They are articulated (hinged with two or more sections connected by a flexible joint) in order to have free relative rotation. The experimental study is limited to model tests of a single row of modules. The concept and design is developed by *Moss Maritime*. The goal is to utilize offshore solar power absorption by a structure that is built from industry-standard components with on-site construction/assembly and installation. Also having satisfactory sea-keeping abilities for the suggested operational areas. In such early phases of the concept design, *Moss Maritime* reached out to Professor Trygve Kristiansen at IMT, whom together proposed the hydrodynamic study as a research topic.

The reader should have prior knowledge of naval architecture, fluid mechanics, hydrodynamics and structure mechanics.

Trondheim, 7. juni 2019

Magnus Onsrud

Acknowledgment

I would like to express my sincere gratitude to my supervisor Professor Trygve Kristiansen. His availability, enthusiasm, knowledge and excellent supportive guidance has been crucial to the success and final outcome of this Thesis. I can't imagine having had a better mentor and advisor through the process. My humblest thanks also goes to my contact persons at *Moss Maritime*; Alexander Thøgersen, Arne Dolven and Finn-Christian Hanssen. Expressing the greatest interest, passion and motivation for the research topic, inspired me to always perform and finally delivering to them what I hope is a more than satisfactory product. Something they can further build upon to help the industry increase their contribution to green energy solutions in the future. Their invitation to concept and company briefings, and their visit during model tests led to great discussions and ideas for both the research and result. A special thanks also to Terje Røsten and Torgeir Wahl for their patience, helpful assistance and continuous support during the experiments. Trond Innset, my primary consultant for the design and the man behind the construction of the physical model, deserves my highest praise. Being an individual with great experience and knowledge that made the model tests possible.

M.O.

Abstract

Future energy demand is expected to increase substantially, and because of the impacts on our earth, new ways for supplying the market with cost-efficient, sustainable and green energy must be considered. Floating solar shows great promise; not compromising spatial availability by using vast open oceans exposed to sunlight, and with capability of carrying photovoltaic panels in offshore sea-conditions.

Floating solar shows great promise as a future energy supplement that does not compromise the already limited spatial availability on the earth. Vast open oceans that are exposed to sunlight could be beneficiary for floaters capable of carrying photovoltaic panels in offshore sea-conditions.

Today, nearly all floating solar is located within lakes and dams, unexposed to high environmental loads. The aim to move this concept offshore is consequently followed by significant technical challenges. This thesis examines the vertical hydrodynamic response of a new concept for a floating solar island by experimental methods. The concept is created by *Moss Maritime*, consisting of an array of hinged identical rigid floating modules. The hinges are restricted to only allow relative rotations, and the global structure is evenly moored at the edges. The idea is drawn from a desire for global hydrodynamic flexibility, following the incident waves. A simple layout of the standard modules, that are based on standardized components, achieves cost beneficent area effectiveness, robustness and long operational lifetime, with easy on-site fabrication of sub-elements, assembly and installation. This stage in the project cycle contains many levels of uncertainty. A preliminary concept study by experimental methods can therefore be a proper initial evaluation.

The simplified model, built in 1:20 scale, was tested with nine hinged identical modules in a single row in head waves. Achieving structural rigid stiffness, relative vertical motion flexibility and negligible mooring effects. Studying the suspected governing and critical vertical motions. Quantifying the hydrodynamic response amplitudes in heave and pitch, identifying the operational limit in terms of irregular sea-states, and uncovering maximum values of heeling, and occurrence of slamming. Instrumentation was limited to three bodies, hence measuring the first, middle and last module, using wave-probes, accelerometers and Oqus reflexive motion capture markers. Acquiring response amplitude operators, and the 1st, 2nd and 3rd harmonic accelerations. The model was tested in regular waves with full scale period varying from $2 - 13$s for wave-steepnesses corresponding to wave-heights ranging from $0.1 - 13$m. Several irregular wave tests followed, studying a range of peak periods between $4 - 12$s with significant wave heights from $1 - 4.5$m. Additional regular wave tests were done for a single, and two hinged modules to examine articulation effects, and for comparison with a derived multi-body theoretical model.

The experimental results for the regular waves revealed good handling, following the tested incident waves. However, the wave with 13s period and $1/20$ steepness experienced over-topping. Throughout, there were small changes in air-gap, but this property was quite sensitive to the steeper waves. High-frequency waves gave rapid and mechanical harmonic pitch rotations, suggesting large hinge loads and danger of fatigue. No apparent resonance were measured or observed, and the general highest response and accelerations were located at the first and last module. The results for heave indicated complete flexibility for wave periods greater than 5s, and 7s for pitch, where they both had the highest measured response around $2-2.5$s. Although never exceeding 10°rotational angles. A general observation was response propagation through the model, yielding a whipping motion. Adding to the expectancy of higher loads on the first and last module in the articulated row.

The developed theoretical model is grounded in earlier multi-body hydrodynamic response methods. The results by experimental comparison yielded improper evaluation, not giving the model any sufficient confidence for practical use at this stage. However, theoretical resonance and cancellation domains can to some extent be identified in both the regular and irregular wave-tests, but not completely consistent. An unfortunate missing interval of measured wave-series yielded inability to fully verify these domains.

The irregular wave-tests gave a large number of slamming and over-topping events when two or more quite steep successive waves excited the system. Giving high-frequency excitation in pitch, of which it could not recover in sufficiently high waves. The structure proved to be most sensitive to wave-steepness and pitch. Slamming had a tendency to propagate through the entire model, but the results still maintained largest responses and accelerations at the first and last module. The necessary operational criteria demands sufficiently long periods in terms significant wave height. The results mainly gave a suggested safe and unsafe domain in terms of these operational sea-state parameters.

The results from the multi-module solar island shows potential, but more work and research are needed for further development. At this stage, the structure could confidently handle sufficiently long-period sea-states.

Sammendrag

Energibehovet forventes å øke vesentlig i fremtiden, og på grunn av påvirkningen på jorda må nye muligheter vurderes for å levere kostnadseffektiv, bærekraftig og grønn energi. Flytende solkraft viser mye potensial; en løsning som ikke kompromitterer romlig tilgjengelighet på jorda ved å utnytte havet som er utsatt for sollys, og med evne til å bære fotovoltaiske paneler under disse sjøforholdene.

I dag ligger nesten alle flytende soløyer i innsjøer og dammer, ueksponert for store belastninger fra omgivelsene. Målet ved å flytte dette konseptet offshore følges av betydelige tekniske utfordringer. Denne oppgaven undersøker den vertikale hydrodynamiske responsen til et nytt konsept for en flytende soløy ved hjelp av eksperimentelle metoder. Konseptet eies av Moss Maritime, bestående av en rekke hengslede, identiske, stive flytende moduler. Hengslene tillater kun relative rotasjoner, og den globale strukturen er jevnt forankret i kantene. Ideen er hentet fra et ønske om global hydrodynamisk fleksibilitet hvor konstruksjonen følger de inkommende bølgene. Et enkelt oppsett av standardmodulene, som er basert på industri-standardiserte komponenter, oppnår kostnadseffektiv, områdeutnyttelse, robusthet og lang levetid, med enkel montering av underelementer og installasjon på stedet hvor øya skal operere. Denne fasen i prosjektsyklusen inneholder mange usikkerhetsnivåer. En foreløpig konseptstudie ved eksperimentelle metoder er en passende evaluering.

Den forenklede modellen, bygget i skala 1:20, ble testet med ni hengslede identiske moduler i en enkelt rad, eksponert for enrettet bølgetog. Modellen oppnår strukturell stivhet, relativ vertikal bevegelsesfrihet og ubetydelige fortøyningseffekter. Hensikten med studiet er å avdekke mistenkte styrende og kritiske vertikale bevegelser. Kvantifisere hydrodynamiske responsamplituder i hiv og stamp, identifisere operasjonsgrensen under uregelmessige sjøtilstander, og avdekke maksimalverdier for helninger og forekomster av sjøslag. Måle-instrumentene var begrenset til tre enheter, og dermed ble den første, midtre og siste modulen målt ved hjelp av bølge-prober, akselerometre og Oqus refleksive bevegelsesfangst markører. Hovedresultatene består av bevegelsesamplitude operatorer, og 1., 2. og 3. harmoniske akselerasjoner. Modellen ble testet i regulære bølger med full-skala periode varierende fra 2-13s for bølge-steilheter som tilsvarer bølgehøyder fra $0.1 - 13$m. Diss testene ble etterfulgt av flere irregulære bølgetester, bestående av topp-perioder mellom $4 - 12$s med signifikante bølgehøyder fra $1 - 4.5$m. Ytterligere regulære bølgeforsøk ble utført for en enkelt og to hengslede moduler for å undersøke koblingseffekter, og for sammenligning med en utledet teoretisk modell for en multi-kropp hydrodynamisk respons.

De eksperimentelle resultatene for regulære bølger bølgene viste god håndtering og evne til å følge de innkommende bølgene. Imidlertid ble modellen utsatt for over-topping for 13s bølgeperiode og $1/20$ steilhet. Gjennom forsøkene var det små endringer i luftgapet mellom vannoverflaten og dekket, men denne egenskapen var ganske følsom for de brattere bølgene. Høyfrekvente bølger gav raske og mekaniske harmoniske rotasjoner i stamp, noe som tyder på store belastninger i hengslene og fare for utmattelse. Ingen tilsynelatende resonans ble målt eller observert, og den generelle høyeste responsen og akselerasjonene

var ved den første og siste modulen i rekken. Resultatene for hiv indikerte komplett fleksibilitet for bølgeperioder større enn 5s, og 7s for stamp, hvor de begge hadde den høyeste målte responsen rundt $2 - 2.5$s. Allikevel oversteg aldri vinkelen i stamp 10 grader. En generell observasjon var responsutbredelse gjennom modellen, noe som konsekvent gav en bevegelsen til en pisk. Dette understreker også en forventning om større belastninger på den første og siste modulen.

Den utledede teoretiske modellen er basert på tidligere hydrodynamiske responsmetoder. Resultatene ved eksperimentell sammenligning gav lite trovertige resultater og indikerte en ugunstig praktisk bruk eller implementering på dette stadiet. Imidlertid kan teoretiske resonans- og kanselleringsdomener til en viss grad identifiseres i både de regulære og irregulære bølgetestene, men ikke alltid konsistent. Et uheldig manglende intervall av målte bølgeserier gav ikke mulighet til å fullt verifisere disse domenene.

Testene i irregulære bølger resulterte i et stort antall bølgeslag og over-topping, da to eller flere ganske bratte etterfølgende bølger eksiterte strukturen. Dette førte til høyfrekvent respons i stamp, som strukture ikke klarte å gjennomprette hvis kommende bølger var tilstrekkelig høye. Strukturen viste seg å være mest følsom for bølge-steilhet og stamp. Bølgeslag hadde en tendens til å forplante seg gjennom hele modellen, men resultatene opprettholdt de største responsene og akselerasjonene ved den første og siste modulen. De nødvendige driftskriteriene krever derfor tilstrekkelig lange perioder med hensyn til signifikant bølgehøyde. Resultatene gav i hovedsak et foreslått trygt og usikkert domene med hensyn til disse operasjonelle havtilstandsparametrene.

Resultatene fra multi-modul soløya viser potensial, men mer arbeid og forskning er nødvendig for videreutvikling. På dette stadiet kan strukturen trygt håndtere tilstrekkelig lavfrekvente sjøstater.

Nomenclature

Greek

ϕ	Velocity potential for the fluid
ϕ_0, ϕ_I	Incident wave velocity potential
ϕ_D	Velocity potential for diffraction waves
ϕ_R	Velocity potential for radiated waves
ζ	Free surface elevation
ζ_a	Wave amplitude
ω	Circular frequency
1ω	1st harmonic frequency
2ω	2nd harmonic frequency
3ω	4rd harmonic frequency
$\omega(t)$	Bell function
ω_p	Angular spectral peak frequency
$S(\omega)$	Spectral density
$H(\omega)$	Transfer function
$X((\omega, \beta))$	Excitation transfer function
η_i	Rigid body motion mode
$\dot{\eta}_i$	Rigid body velocity mode
$\ddot{\eta}_i$	Rigid body acceleration mode
ξ_j	Complex RAO; amplitude and phase of a modal response at ω
ν, k, K	Wave number in deep Water
ρ	Density of water
ρ_b	Structure/Body density
λ	Wave length / Scaling parameter
$\Re\{\}$	Real part of mathematical expression
$\Im\{\}$	Imaginary part of mathematical expression
A_γ	Normalizing factor in JONSWAP spectrum
γ	JONSWAP spectrum non-dimensional peak shape parameter
σ	Standard deviation / spectral width parameter
∇	Volume displacement, gradient
ϵ	Random phase angle
β	Wave-heading angle
$\delta(\omega_j)$	Response associated phase angle
$\vec{n}$, $\mathbf{n}$, n_k	Normal vector

Roman

H_s	Significant wave height
H	Wave height
T_p	Peak period
T	Wave period
T_n	Natural/Resonance period
F_N	Froude number
S_{xx}	Input spectral density
S_{yy}	Response spectral density
$\mathbf{S}_j(\mathbf{x})$	Vector shape function
A_{kj}	Added mass coefficient
B_{kj}	Damping coefficient
$B_{visc,j}$	Viscous damping coefficient
C_{kj}	Restoring coefficient
M_{kj}	Component of the generalized mass matrix
F_j	Exciting force
M_j	Exciting moment
C_D	Drag coefficient
C_M	Mass coefficient
i	Imaginary number ($\sqrt{i} = -1$)
S_B	Wetted body surface
g	Gravitational acceleration
I	Area of inertia
I_{kj}	Product of inertia
k_s	Mooring line stiffness
$\overline{GM}_L$	Longitudinal metacentric height
$\overline{GM}_T$	Transverse metacentric height

Abbreviations

PV	Photo voltaic
GDP	Gross domestic product
ALS	Accidental damage limit state
2D	Two-dimensional
3D	Three-dimensional
RAO	Response amplitude operator
WF	Wave frequency
LF	Low frequency
HF	High frequency
FK	Froude-Krilof force/pressure
EOM	Equation of motion
DOF	Degrees of freedom
WEC	Wave energy converter
FFT	Fast Fourier transform
CoG	Centre of gravity
VCG	Vertical centre of gravity

Innhold

Kapittel 1

Introduction

The world is rapidly experiencing an increase in energy demand. Since the industrial revolution, the supply of energy has always been in correlation to the development of new technology. Today, this challenge is even more comprehensive and complicated due to the its impact on the earth. Climate change, spatial availability, an ever-growing population and materialistic culture requires more innovation and focus on the environment when developing new technology to meet the demand of sustainable energy.

This challenge demands us to examine areas of interest that will create new and sustainable sources of energy. Possibilities that have been globally comprehensive and in focus for the last decades, using the solar, tidal, wave, atomic and wind energy supply. Each with its own possibilities, limitations and requirements. In particular, the solar energy contributor as a major source, shows great promise. However, the extraction requires vast areas and advance material technology for constructing panels able to absorb the radiation, whilst keeping high efficiency.

New concepts for creating solar parks offshore are rising in numbers each year. This study is a preliminary initial examination of such a concept, with a focus on the operational ability that such a park requires in much more harsh conditions than any conventional existing parks; offshore.

1.1 Solar Energy

Solar energy is classified as clean and affordable in the global market classification, and shows great potential as a major energy supplier in the present state of the industry. In a global perspective, the projected population growth from 2016 to 2050 shows an increase of $+0.8$ [%/year], which in comparison has a projected energy consumption rate of $+1.4$ [%/year] (Kristiansen and Borvik, 2018). The latter based on findings by economic growth per capita and energy intensity decrease (Energy/GDP). Examining this state of the global energy situation, wind and solar power shows the most promise within sustainable energy overall. When looking at the energy consumption rate, the average daily insulation of solar power in Southern Spain was measured at 200 [W/m^2] in 2017 (Kristiansen and Borvik, 2018). Which means that the demand can be covered by Photo Voltaic (PV) panel farms at a size of 500x500 [km^2], supplying 10 [TW] at 20% efficiency. This size is equivalent to 0.07% of the world ocean.

A recent presentation of studies conducted by *Multiconsult* regarding the state of the industry within floating solar power showed that the annual installation capacity has almost doubled in the market from 2015 to 2017. Based on known projects, the forecast for 2018 is an increase of +444% (Gazdowicz, 2018). The market shows and increased trend in development, supply and quality of PV panels. Hence, solar power shows great promise for the development within utilizing PV farms, especially offshore where there is sufficient supply of solar radiation.

1.2 Floating Solar Islands

Floating solar islands within the field of renewable energy is considered a promising utilization of the power source. Installing PV farms offshore in the form of floating solar islands are a way to implement the energy provision without compromising the already limited spatial availability on the earth. Moving this energy source offshore naturally comes with new challenges. The floating solar parks that exists today are placed within lakes and water dams, where there is little to no exposure to a a sea environment creating significant loads on the structure. Exposing a structure to waves and currents have significant influence on the feasibility of the design. Interest areas for the installation of these types of structures are Asia, South America and Africa.

1.2.1 Challenges

The offshore floating solar parks are exposed to an environment that challenges the designs and operational criteria, both in terms of extracting the solar energy, and survive and operate long-term in the sea environment. Furthermore being accessible for maintenance and repair. When exposed to the offshore sea environment, the structure itself still needs to have a sufficiently low deflection in order to avoid breakage and damage to the PV panels, provide enough buoyancy and flexibility. Desired hydroelastic of hydrodynamic flexible behaviour, i.e. the structure's ability to move with the larger waves and sustain the shorter higher frequency ones will be governing. Moreover, avoiding critical events like slamming and over-topping. Maintenance, salt water-corrosion and pollution limiting the efficiency of the panels must be taken into account as well. In addition having proper installation and sea-keeping methods like mooring. These methods must also be evaluated in terms of the waves, variation in water levels, currents and other exciting loads. After all, the lifetime should exceed 25 years for it to be profitable to implement.

After discussing all these criteria, it is important to remind ourselves of the need for cost-efficiency while keeping the operational ability. The concept and design itself becomes irrelevant if it does not stand out as reliable and profitable. However, the PV performance is expected to be higher when solar parks are moved offshore, because of the possibility of natural cooling of the electric system. Furthermore, availability of modules and inverters are expected to increase due to a booming PV industry. The development of better panels that are more robust, keeping operational efficiency when heated and exposed to sea spray will contribute to the effort of increasing the use of solar energy.

1.3 Multi-Module Floating Island Concept

Moss Maritime has developed a concept for a floating solar park that can attain sufficient hydrodynamic flexibility and structural strength, still handling relatively rough sea states, while being a cost-efficient, easily built, assembled, installed, maintained and implemented concept. Initial operational criteria is to handle a significant wave height H_s of 4-5 [m] and a Tyfoon category 4. The latter meaning that we tolerate damage that can be repaired, but not loosing the structure all together (Thøgersen, 2018). In short, the floating island consists of several stiff floating barge-like modules which are connected by joints that restrains translations, but allows rotations. Hence being an array of articulated modules. The overall structure is moored evenly along the sides and at the corners to obtain sufficient sea-keeping. The modules themselves are square frame platforms that can carry PV panels and buoyant by four floaters. The concept is developed with the cost-efficiency in mind, being assembled by relatively cheap standardized components. The overall park will then consists of an array of these modules, whereas the number itself, chosen dimensions, geometry and structural properties must be evaluated. Although, being a new concept, experimental studies and to best effort supported by numerical or analytical models are needed to evaluate its feasibility. Standing as the first important part in the project cycle.

1.4 Objective & Scope

This Master's Thesis investigates the wave-induced vertical heave and pitch response of a row of articulated modules. Testing a single module, two modules and nine modules connected by horizontally stiff hinges allowing pitch rotation. The single and two modules tests in regular waves only, and the nine modules tests in both regular and irregular waves. The assessment is focused on the global flexibility of the multi-module structure, where it should by its design follow the incident waves. Revealing governing physical behaviour, handling and feasibility in terms of desired operational criteria. Uncovering the main challenges that such a structure will face in different wave-conditions. It is an experimental study, where accelerometers and motion capture will be utilized to measure the wave-structure interaction. Vertical response amplitude operators (RAO) is the prime result to be investigated, but also examining the acceleration harmonics. Naturally, observations of the model tests will also be of great importance. The work is a continuation of a preliminary study performed from August to December 2018. The main objectives of this Master's Thesis can be summarized as:

1. Designing and building a physical model of nine identical hinged rigid modules, giving the possibility to test one single, two and nine modules acting as the floating island component.

2. Perform an experimental study on the single module, two hinged modules and nine

hinged modules model in regular waves, whilst measuring important vertical wave-structure interactions.

3. Develop a theoretical model for the multi-body hydrodynamic interaction by potential theory for one and two bodies, and compare it to the experimental results.
4. Perform an experimental study on the nine hinged modules in irregular waves, in order to evaluate the concepts' operational criteria. If time, perform the same study on one single and two modules model.
5. Investigate the potential for water-impact events (slamming and over-topping) in the regular and irregular sea-states.
6. Investigate the effect of articulation by observation and measurements of the three different model tests, and in addition discuss possible occurring phenomena by literary references and the theoretical model.
7. Determine a suggested operational limit for the preliminary concept based on vertical translation and rotations, resonance and present water-impacts.
8. Suggest and/or uncover important effects that may need further evaluation and/or investigation to proceed with the development and improvement of the current design.

1.5 Master Thesis Outline

Chapter 2 describes the concept design and geometry of the floating solar island proposed by *Moss Maritime*.

Chapter 3 describes the main theory and equations regarding regular waves, irregular waves, response-theory, Morison's equation and linear viscous damping, articulated multi-body response-theory and experimental methods.

Chapter 4 outlines the experiments; defining the three different models with one, two and nine articulated modules, the test set-up and methods to acquire the relevant data under which wave-series. In addition some notes on specific post-processing with corresponding examples and error sources.

Chapter 5 presents and discusses the results from the experiment with regular waves for each model test. For the case with nine articulated modules, discussions related to observed and suspected phenomena occurring for the hydrodynamic-response are included. The measured and calculated response amplitude operators are compared to the derived theoretical model, which is formulated in detail in *Appendix B*.

Chapter 6 presents and discusses the results from the irregular wave tests for the nine modules model.

Chapter 7 summarizes the main results from *Chapter 5* and *Chapter 6*, draws conclusions from the study, and gives suggestions for further work and research topics.

Kapittel 2

Concept Geometry

This chapter gives a brief summary of the new concept. Thus, in short, it consists of many hinged rigid floating square modules that are fitted with PV panels. The structure is to be evenly moored at the edges, i.e. at each corner and along the edges. The concept is drawn from a desire for applicable installation worldwide, with a simple layout of standard modules that are based on standardized components. Achieving area effectiveness, robustness and long operational lifetime, with easy on-site fabrication of sub-elements where pending site locations can receive these and transport them to the assembly site. Consequently a combination of local and world wide fabrication. The information given in this section, alongside all figures and drawing are given as a courtesy of *Moss Maritime* (Thøgersen, 2018).

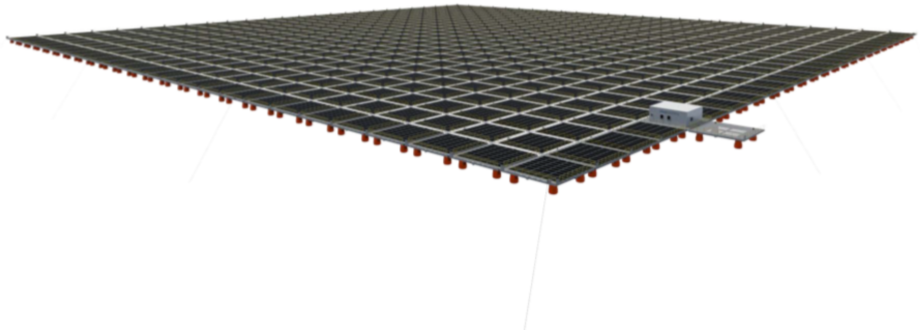

Figur 2.1: Concept of the complete multi-module floating solar park

2.1 Module Description

The single module are relatively small rigid structures that are kept buoyant with sufficient free-board by four floaters. The module itself is mainly a frame of standardized beam elements and stiffeners that will support the PV panels and outfitting. Hinges located on each side of the frame acts as the connections between the modules. *Figure 2.2* shows an artistic illustration of the single module.

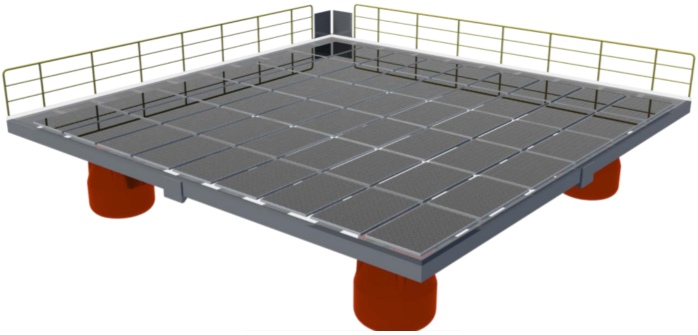

Figur 2.2: Concept illustration of a single module

The technical drawing with geometric properties and dimensions can be found in *Appendix A*, *Figure A.1*. These properties, which are initial choices and rough estimations of the design, will stand as the basis for the experimental study.

2.1.1 Floaters, Frame & Hinges

The floaters, frame and hinges are shown in the following figures. The important factor is to note that the hinges are constructed to only restrain the movements of the structure in translations, i.e. horizontal motions and allowing relative rotations, and thus the desire for global hydrodynamic flexibility. This desire is illustrated in *Figure 2.5*.

Figur 2.3: Concept illustration of the module frame and floaters

A more detailed figure of the floater and a concept drawing of the hinge are shown in *Figure 2.4*.

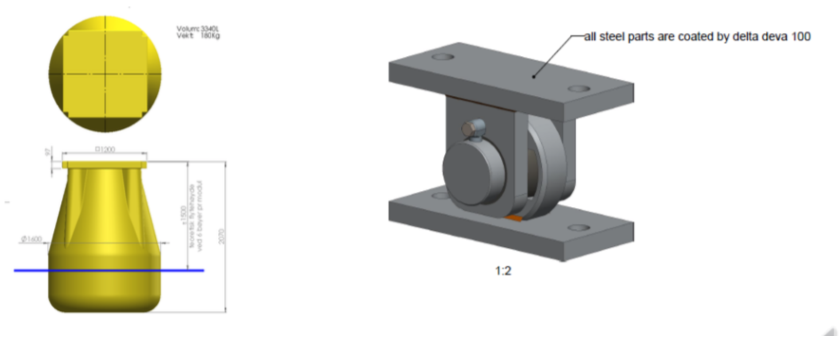

Figur 2.4: Illustrations of the floater and hinge component used on the floating modules. Both standardized components supplied by contractors for *Moss Maritime*. The dimensions shown in the figure to the left are outdated, where its proper are shown in *Appendix A*.

Figur 2.5: Side-view illustrations of the desired global hydrodynamic flexibility of the structure.

2.1.2 Concept Uncertainties & Challenges

The concept, being at a stage of initial work in the project cycle, contains many levels of uncertainty. As a business case, the concept geometry is an initial and rough estimation. Hence, the standing geometry is not preliminary tested or verified. On the same grounds, important details like distance between the hinged modules are not established, which can lead to collisions of the individual model frames at both low rotations in yaw, and moderate rotations in pitch and roll. However, the combination of more modules in all directions in the horizontal plane is assumed to provide sufficient stiffness to avoid such events. Furthermore, if the dimensions, free-board, and draft are also rough estimates that are not necessarily avoiding water impact, exit or entry problems in rougher sea states are possible. The preliminary initial study will naturally be a study of these factors.

These arguments exposes challenges and uncertainties, but also the integration of power lines and the solar energy construction circuits, the choice of suitable PV panels and how these systems can survive and operate are a huge challenge. However, based on the early stage and the scope of this Master's Thesis, these factors are not a included.

Kapittel 3

Theory

This chapter represents the general theories and assumptions that are used in the study of the floating solar island. All theory has been derived by others, and is utilized and applied for the different aspects of the experimental study. However, formulation of a theoretical model for the wave-induced vertical response of a single and two articulated modules are derived on the author's own premise. Overall representing the theoretical grounding for evaluating and determining whether the concept satisfy the conditions imposed to operational criteria, and to some extent verify experimental and theoretical results.

In summary, the section reviews engineering tools in hydrodynamic classification to quickly determine governing wave-induced loads, the nature of sea states made of regular and irregular waves and its properties. Furthermore, the response in regular waves by linear potential theory under steady state conditions, with no forward speed and stable buoyancy in calm water for the structure. Whereas reviewing topics for solving the wave-structure interaction problem. Moreover, inclusion of the hydrodynamics for hinged multi-bodies and a brief review of the derived theoretical response amplitude operators for one and two modules.

3.1 Sea Environment

The basic assumption is the aspects of free-surface fluid flow problems based on potential theory, where the sea-water is incompressible and invicid with irrational flow. Thus describing the fluid vectors by the velocity potential ϕ. It has no physical meaning itself, but is utilized for convenience within mathematical analysis (Faltinsen, 1993). By application of the Laplace and Bernoulli equation, and introducing kinematic and dynamic free-surface conditions, in addition to boundary conditions that are applicable for a given system, the complete mathematical problem of determining the velocity potential is described. By this utilization and introducing the wave elevation ζ, all the tools are established for a proper formulation of linear wave theory (Airy Theory).

3.1.1 Hydrodynamic classification & Engineering Tools

Both viscous effects and potential flow effects may be important in determining the wave-induced motions and loads on marine structures (Faltinsen, 1993). The wave radiation and diffraction around the structure is included in the latter effect. An estimated classification of dominant forces by the size of the structure versus the incident waves is illustrated in figure 3.1. This is based on results for horizontal wave forces on a vertical bottom-fixed cylinder, Morison's equation with a mass coefficient of 2 and a drag coefficient of 1, and linear McCamy Fuchs theory (MacCamy and Fuchs, 1945) in the diffraction regime. The result yields a rough estimation and can justify assumptions for the hydrodynamic problem.

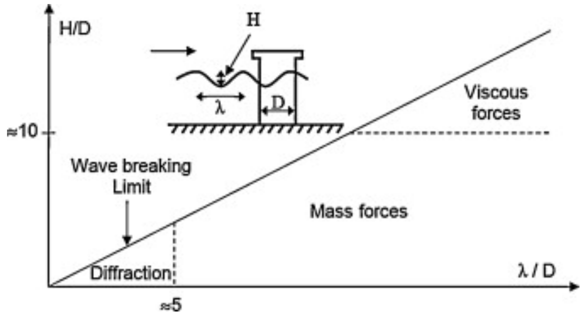

Figur 3.1: Relative importance of mass, viscous drag and diffraction forces on marine structures (Faltinsen, 1993)

Assuming D is the typical dimension of the structure and λ the incoming wave length, a quantitative study shows that the ratio of large"or smallstructures relative to the sea state, λ/D, yields the dominating loads.

3.1.2 Regular Waves

From a hydrodynamical point of view, it is sufficient to analyze a structure in incident sinusoidal waves of small steepness. Moreover, it is possible to obtain results in irregular seas by linear superposition of these regular steady state conditions. In the regular wave theory, the solution oscillates with the same frequency as the incident wave frequency. Consequently avoiding time dependency (Newman, 1977).

The linear wave theory for propagating waves is based on assuming a free-surface of infinite extent and a horizontal sea bottom (Faltinsen, 1993). Regular waves propagating in the, e.g., x-direction for both finite and infinite water depths have relation properties and are derived from the velocity potential, velocity and acceleration components, dynamic pressure, and the wave elevation profile (Newman, 1977)

$$\zeta = \zeta_a \sin(\omega t - kx) \tag{3.1}$$

Figure 3.2 illustrates the shape and main parameters of the regular wave profile. Regular waves means oscillations in time with period T and in space with wavelength (Pettersen et al., 2014). The energy density of the wave is constant in the transverse direction of the profile.

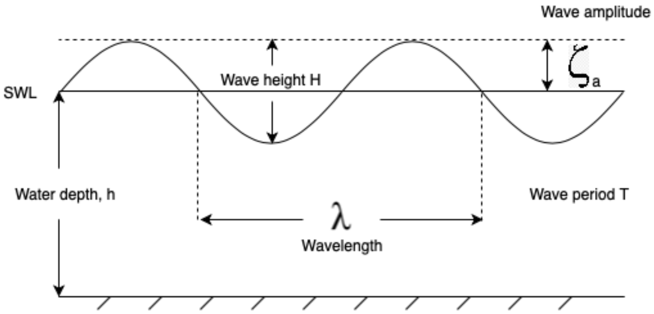

Figur 3.2: Illustration of the regular sinusoidal wave profile with its main parameters. Wave period T, wave height H, wave length λ, wave amplitude $\zeta_a = H/2$, and the steepness of the wave H/λ.

The linear theory is a first order approximation in satisfying the free surface condition, but it can be improved by introducing a Stokes' expansion". This introduces higher order terms, which consistently keeps the free-surface condition. It can be shown that the second-order velocity potential is zero, resulting in the second-order wave elevation (Faltinsen, 1993)

$$\zeta_2 = -\frac{1}{2}\zeta_a^2 k \cos[2(\omega t - kx)] \tag{3.2}$$

which can be combined with *(3.1)*

$$\zeta = \zeta_a \sin(\omega t - kx) - \frac{1}{2}\zeta_a^2 k \cos[2(\omega t - kx)] \tag{3.3}$$

The second-order solution sharpens the wave crests and makes the troughs more shallow (Faltinsen, 1993). This provides a 1st and 2nd order Airy wave theory. Furthermore, an important result is the combined kinematic and dynamic condition, yielding combined free surface condition

$$\frac{\partial^2 \phi}{\partial^2} + g\frac{\partial \phi}{\partial z} = 0 \qquad \text{evaluated on} \qquad z = 0 \tag{3.4}$$

where, the velocity potential in deep water is

$$\phi = \frac{g\zeta_a}{\omega} e^{kz} \cos(\omega t - kx) \tag{3.5}$$

and with dispersion relation and dynamic pressure, respectively

$$\omega^2 = kg \tag{3.6}$$

$$P_D = \rho g \zeta_a e^{kz} \sin(\omega t - kx) \tag{3.7}$$

3.1.3 Irregular Waves

By the irregular description of the sea environment, we get a more general and real description of the sea state, but in a statistical point of view. Resulting in more realistic responses, including non-linear phenomena, as high and low frequency responses and the occurrence wave entry and impacts. Hence, a more realistic study of the structures survivability in more extreme and real sea states (Steen, 2014). Linear theory is used to simulate irregular sea and to obtain statistical estimates. We can write the wave elevation of a long-crested irregular sea propagating in the positive x-direction as the sum of the wave components, i.e. by superposition of different regular waves.

$$\zeta = \sum_{j=1}^{N} A_j \sin(\omega_j t - k_j x + \epsilon_j) \tag{3.8}$$

where A_j, ω_j, k_j and ϵ_j are the wave amplitude, circular frequency, wave number and random phase angle, respectively, of wave component j. Note that the random phase angles are uniformly distributed between $[0, 2\pi]$ and constant in time (Faltinsen, 1993).

For deep water, the frequency and wave number are related by the dispersion relation for the gravity driven waves. The amplitude can be expressed in terms of the wave spectrum $S(\omega)$ in frequency domain, i.e.

$$\frac{1}{2}A_j^2 = S(\omega_j)\Delta\omega \tag{3.9}$$

where $\Delta\omega$ is a constant difference between successive frequencies. The relationship between a time domain and the frequency domain representation of the wave profile by the spectrum is illustrated in *Figure 3.3*. By assuming that the sea is a stationary process, i.e. studying a limited time period, this spectrum can be estimated from eave measurements (Kinsman, 1965).

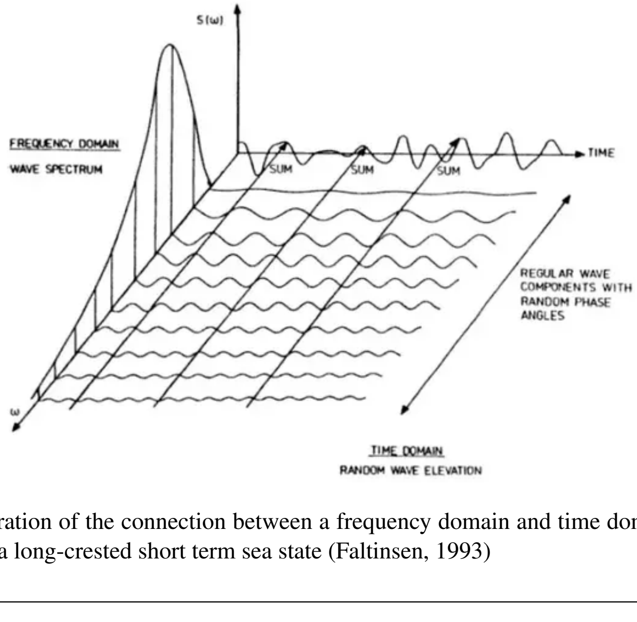

Figur 3.3: Illustration of the connection between a frequency domain and time domain representation of waves in a long-crested short term sea state (Faltinsen, 1993)

There are different wave spectra one can use with their own statistical characteristics, each recommended from the type of sea state that is reviewed. Some important properties regarding the irregular sea state is the significant wave height H_s, defined as the mean of the one third highest waves, the mean period and zero up-crossing period. The JONSWAP spectrum is commonly used, so notes on this spectrum is presented in *Appendix* **??**.

3.2 Linear Wave-Induced Motions & Loads on Floaters

This section will provide an overview of the linear theory for studying wave-induced motions of and loads on the floating structure. These can to a large extent can be described by linear theory. On the other hand, describing horizontal motions of moored structures is highly dependent on non-linear effects. For incident regular waves with amplitude ζ_a with relatively small wave steepness, i.e. far from breaking, linear theory corresponds to wave-induced response amplitudes that are linearly proportional to ζ_a.

3.2.1 Response in Irregular Waves

The analysis of the response to each wave component in *(3.8)* can be done separately in linear theory. The sum of the different components yields the overall response. In the steady state, the response can be written as

$$\sum_{j=1}^{N} A_j |H(\omega_j)| sin(\omega_j t + \delta(\omega_j) + \epsilon_j) \tag{3.10}$$

where $|H(\omega_j)|$ is the transfer function, or response amplitude per unit Wave Amplitude. $\delta(\omega_j)$ is the phase angle associated with the response. From this transfer function and the wave spectrum of the sea state, all statistical properties of both the environment and response are contained and accessible.

RAO for Irregular Waves

In irregular waves, the transfer function is the equivalent to the Response Amplitude Operator (RAO) (Steen, 2014). By spectrum analysis, from an input wave spectrum S_{xx}, one can measure the response spectrum S_{yy}. The transfer function is thus determined by

$$|H(\omega)|^2 = \frac{S_{yy}}{S_{xx}} \tag{3.11}$$

This expression is grounded in stochastic analysis, where both the incident waves and the yielding response are stochastic variables (Moan et al., 2010).

3.2.2 Response in Regular Waves

As mentioned, from linear superpositioning of the regular wave components, we can obtain results in irregular seas. Consequently by analysis in regular waves of small wave steepness will provide a sufficient way to obtain the motion and load response. The hydrodynamic problem is handled as two sub-problems; the wave excitation loads, and the hydrodynamic loads identified as added mass, damping and restoring terms (Faltinsen, 1993). The former are forces and moments occurring from incident waves on the body when it is fixed, and the loads are composed of Froude-Kriloff and diffraction forces and moments. The latter are forces and moments occurring from the oscillating structure with the same frequency as the incident waves. The rigid body motion modes η are usually defined in a Cartesian coordinate system, where there are translatory displacements and angular displacements of the rotational motions.

Hydrodynamic coefficients

The added mass and damping loads are steady-state hydrodynamic forces and moments due to forced harmonic rigid body motions (Faltinsen, 1993). The restoring force follows the hydrostatic and mass considerations for a freely floating body. These loads occurring from the oscillating structure is implemented in the equation of motion as coefficients, respectively A_{ij}, B_{ij} and C_{ij}, with the studied load component i from the translatory or rotational motion j. The added mass and damping coefficients is usually significantly influenced by the body geometry. The added mass can physically be described as dynamic pressures occurring in the disturbed fluid, and the damping by radiated energy. The restoring force can be understood as a stiffness of the system due to forces and moments occurring due to change in water displacement, i.e. submerged volume.

Linearized Wave Excitation Loads

For a restrained structure in incident waves, the wave is exciting forces and moments which can be divided into two effects. One is the unsteady pressure induced by the undisturbed waves, which yields the Froude-Kriloff force. The other is a force resulting from the structures presence and impermeability, called diffraction force.

The dynamic pressure force is determined from linear potential theory, where this force component can be explicitly expressed by the velocity potential of the incident wave. The diffraction force can be determined similarly to the forced body oscillation sub-problem. Hence solving the boundary value problem for the velocity potential. The forces are obtained by numerical techniques for a general body shape, where the forces are integrated over the wet surface of the body.

The Equation of Motion

For a steady-state sinusoidal motion by using linear and angular momentum, the equation of rigid body motions can be written as

$$\sum_{k=1}^{6}[(M_{jk}+A_{jk})\ddot{\eta_k}+B_{jk}\dot{\eta_k}+C_{jk}\eta_k]=F_je^{-i\omega t} \qquad (j=1,2,...,6) \tag{3.12}$$

where M_{jk} are the components of the generalized mass matrix of the structure, and F_j the complex amplitudes of the exciting forces and moments. Naturally given by the real part.

The equation of motion depends on the studied mode of the rigid body. The coordinate system is often body fixed or Earth-fixed, and for these rigid body modes we have

$$\vec{s} = \eta_1\vec{i} + \eta_2\vec{j} + \eta_3\vec{k} + \vec{\omega} \times \vec{r} \tag{3.13}$$

where

$$\vec{\omega} = \eta_4\vec{i} + \eta_5\vec{j} + \eta_6\vec{k} \qquad \text{and} \qquad \vec{r} = x\vec{i} + y\vec{j} + z\vec{k}$$

for the motion $\vec{s}$ of the structure.

Discussion of Natural Frequencies

When assessing the amplitudes of the response, the wave excitation and damping levels, and the natural periods are important parameters. If the floating structure is excited by an oscillation period close to or in the vicinity of its natural period, large motions will follow. Meanwhile, if the level of damping in the system is high or the excitation low, it can be difficult to distinguish the response at resonance periods.

$$T_{n,i} = 2\pi\sqrt{\frac{M_{ii} + A_{ii}}{C_{ii}}} \tag{3.14}$$

One can predict which modes that will yield critical resonance oscillations by the system characteristics.

3.2.3 Wave-Body Interaction

This section will present an overview of solving the wave-body interaction problem based on the previously discussed linear wave-induced motions and loads. Resulting in both theoretical and experimental regular waves RAO. The expressions and explanations are based on the works of Odd Magnus Faltinsen (Faltinsen, 1993) and Marilena Greco (Greco, 2018). Due to the floating solar island geometry and the given sea state, it is assumed deep water and long waves in an Earth-fixed coordinate system.

The Excitation Problem

For linear potential theory, the wave frequency loads occurring from excitation force F and moment M can be written as the pressures p on the wet surface of the body S_B with the normal vector $\vec{n}$ directed into the body as

$$\vec{F} = \int_{S_B} p\vec{n}dS \qquad \vec{M} = \int_{S_B} p\vec{r} \times \vec{n}dS \tag{3.15}$$

The linear loads occur from the dynamic and static pressure, where we study the dynamic pressure using the free-surface condition in order to apply the expression to the wave elevation later. Which yields the force for a component k

$$p = -\rho\frac{\partial\phi}{\partial t} - \rho gz, \qquad F_k = -\rho\frac{\partial\phi}{\partial t}n_k dS \qquad (k = 1, 2, ..., 6) \tag{3.16}$$

Which have the properties n_k for $k = 1, 2, 3$ for forces and $(\vec{r} \times \vec{n})$ for $k = 4, 5, 6$ for moments.

When dealing with the radiation and diffraction in wave-structure interaction, the incident waves' velocity potential is needed.

$$\Re\{\phi_0(x,y,z)e^{i\omega t}\} \tag{3.17}$$

where assuming linearity and steady state, we can perform the analysis in the frequency domain. The fluid velocity potential is governed by satisfying the Laplace equation, such that

$$\nabla^2\phi = 0, \qquad |\nabla\phi| \to 0 \qquad \text{as} \qquad z \to 0$$

Furthermore, the superposition principle is valid, so components of loads and motions can be taken as a sum for obtaining the global response. However, the diffraction problem must be solved prior to the calculation of the excitation sub-problem from the incident waves. Here, the body is fixed and interacting with the incident waves, and the velocity potential can be written as the sum of the incident and the diffraction.

$$\phi(x,y,z,t) = \phi_0(x,y,z,t) + \phi_D(x,y,z,t) \tag{3.18}$$

which can describe the Froude-Kriloff and diffraction loads in the excitation problem. Moreover, this excitation can be described as a transfer function in terms of frequency and heading $X_k(\omega,\beta)$ by applying the impermeability condition $\frac{\partial\phi_D}{\partial n} = -\frac{\partial\phi_0}{\partial n}$, as

$$F_{\text{exc,k}} = -\int_{S_B}\rho\frac{\partial\phi_0}{\partial t}n_k dS - \int_{S_B}\rho\frac{\partial\phi_D}{\partial t}n_k dS = \zeta_a\Re\{e^{i\omega t}X_k(\omega,\beta)\} \qquad (k=1,2,...,6) \tag{3.19}$$

The transfer function makes it possible to estimate excitation loads for any wave amplitude in linear theory.

$$|X_k(\omega,\beta)| = \left|\frac{F_{\text{exc,k}}}{\zeta_a}\right| \tag{3.20}$$

The Radiation Problem

The body is now forced to oscillate with no incident waves. The motion for the mode j can be written as

$$n_j = \Re\{\eta_{ja}e^{i\omega t}\} \tag{3.21}$$

From this forced oscillation the radiation velocity potential follows

$$\phi_R(x,y,z,t) = \Re\Big\{\sum_{j=1}^{6}\dot{\eta}_j\phi_j\Big\} \tag{3.22}$$

where $\dot{\eta}_j$ is the velocity in mode j and ϕ_j the potential per unit velocity.

The body boundary condition states that the fluid on the body needs to move with the body over the wetted surface, i.e. $\frac{\partial\phi_j}{\partial n_j}$, and in addition, the radiation condition for the outgoing waves must physically be present and the fluid disturbance must die out as we move downwards in the deep water, i.e. $z \to \infty$.

The moving body tends to generate radiated waves and is subjected to loads identified as added mass, damping and restoring terms, as previously described. The added mass and damping are connected to the dynamic pressure yielding a radiation force

$$F_{\text{rad,k}}(t) = -\int_{S_B} \rho \frac{\partial \phi_R}{\partial t} n_k dS \qquad (k = 1, 2, ..., 6) \tag{3.23}$$

where it can be showed that

$$F_{\text{rad,k}}(t) = \sum_{j=1}^{6} [-A_{kj}\ddot{\eta}_j - B_{jk}\dot{\eta}_j] \tag{3.24}$$

which again defines the added mass and damping coefficient in terms of frequency, respectively as

$$A_{kj}(\omega) = \Re\Big\{\rho \int_{S_B} \phi_j n_k dS\Big\} \quad \text{and} \quad B_{kj}(\omega) = -\omega\Im\Big\{\rho \int_{S_B} \phi_j n_k dS\Big\} \tag{3.25}$$

Assuming mean buoyancy by body weight $\rho g V = mg$, where V is displaced volume and m the mass of the body. The restoring loads are connected to hydrostatic pressure and are caused by the changes in buoyancy due to rigid motions. This force can be written for the mode k in terms of the restoring coefficient as

$$F_{\text{hydrostat.},k} = -\sum_{j=1}^{6} C_{kj}\eta_j \tag{3.26}$$

The Haskind Relation

The Haskind relation presents a link between the radiation and diffraction acting as load estimates. This makes us able to calculate the previously discussed diffraction load in the excitation problem if we solve the radiation problem first. This can be used to, for example, control diffraction calculations by computer programs. The excitation force from *(3.19)* can now be expressed for the forces ($k = 1, 2, 3$) as

$$F_{\text{exc},k}(t) = -\int_{S_B} \rho \frac{\partial \phi_0}{\partial t} n_k dS + \sum_{j=1}^{3} a_{0j} A_{kj} \tag{3.27}$$

where a_{0j} is the acceleration of the body (Newman, 1977).

3.2.4 Linear Body Motions in Regular Waves

Now, the linear body motions are evaluated by Newtons 2nd law

$$\sum_{j=1}^{6} M_{kj}\ddot{\eta}_j = F_k \qquad (k = 1, 2, ..., 6) \tag{3.28}$$

where, using *(3.21)* in steady state with no forward speed and stable buoyancy in calm water, we get in partial matrix form for the system

$$\sum_{j=1}^{6} \Big[-\omega^2(\mathbf{M}_{kj} + \mathbf{A}_{kj}(\omega)) + i\omega\mathbf{B}_{kj}(\omega) + \mathbf{C}_{kj} \Big] \boldsymbol{\eta_j} = \zeta_a \mathbf{X}_k(\omega, \beta) \tag{3.29}$$

where $\mathbf{M}_{kj}$ is the mass matrix, including body mass, moments of inertia, products of inertia and coordinates for the centre of mass.

Theoretical RAO for Regular Waves

When the excitation and radiation problems are solved, and the mass matrix is known, *(3.29)* can be solved as the Response Amplitude Operator

$$RAO = |\mathbf{H}(\omega, \beta)| \tag{3.30}$$

providing the transfer function of the body motion amplitude, i.e.

$$\mathbf{H}(\omega, \beta) = \frac{\eta_a}{\zeta_a} = \Big[-\omega^2(\mathbf{M} + \mathbf{A}(\omega)) + i\omega\mathbf{B}(\omega) + \mathbf{C} \Big]^{-1} \mathbf{X}(\omega, \beta) \tag{3.31}$$

The time evolution can be taken as the real part of $\zeta_a \mathbf{H} e^{i\omega t}$. Note that this only can be solved analytically for simple geometries. In a general case, only an estimation is possible, either by use of strip theory or numerical tools.

Experimental RAO for Regular Waves

Based on the discussed regular wave theory, we can naturally use regular wave tests to acquire the RAO's of motions and loads. In an experimental setting, it is important to have generated waves that are as close to sinusoidal as possible and at the same time stable and stationary. Furthermore, satisfying these requirements for a long enough period of time in order to obtain steady-state structural response. Conducting an experiment in a tank, a problem that may occur is tank wall reflection, which will introduce non-stationary effects.

As before, we can define the Response Amplitude Operator as the ratio between the fundamental component of the measured response and the incident wave (Steen, 2014).

$$RAO = \left| \frac{\eta_{a,j}}{\zeta_a} \right| \tag{3.32}$$

3.3 Morison's Equation

In order to calculate wave loads on circular cylindrical structural members of fixed offshore structures when viscous forces matter, the Morison's equation (Morison et al., 1950) is often used. This method can hence be applied for cylindrical and slender components of offshore structures in the first hydrodynamic sub-problem to include viscous forces. The horizontal force dF on a strip of length dz of a vertical rigid cylinder can be written as

$$dF = \rho \frac{\pi D^2}{4} dz C_m a_1 + \frac{\rho}{2} C_D D dz |u| u \tag{3.33}$$

where the positive direction is in the wave propagation direction, cylinder diameter D, the horizontal undisturbed fluid velocity and acceleration u and a_1, and the mass and drag coefficient C_M and C_D. The coefficients needs to be empirically determined. Morison forces are calculated on the cylinder's wet area then summed over all integration points.

If the cylinder is in motion, the velocity is replaced by the relative-velocity projected on the same plane, so we can write the horizontal hydrodynamic force on the cylinder as

$$dF = \frac{\rho}{2} C_D D dz |u - \dot{\eta}_1|(u - \dot{\eta}_1) + \rho C_M \frac{\pi D^2}{4} dz a_1 - \rho(C_M - 1)\frac{\pi D^2}{4} dz \ddot{\eta}_1 \tag{3.34}$$

For both equations, they have inertia and drag components, as can be recognized by the coefficient products. Note that the inertia term does not depend on the relative acceleration term, and that the values of the coefficients are not necessarily the same as in *(3.33)* and *(3.34)*. By a frequency domain solution, the term $|u - \dot{\eta}_1|(u - \dot{\eta}_1)$ must be linearized. This linearization will depend on the wave model: regular and irregular waves must provide the same energy dissipation by the linearized and non-linearized drag force. For simplification, most of proposed linearized forms assume a fixed cylinder in a unidirectional flow (Housseine et al., 2015).

3.3.1 Linear Viscous Damping

In the equation of motion, only potential damping by wave generation association is included. However, this terms can instead be representative as a viscous damping coefficient. This property is in general a non-linear term. For slender and small structures, a common assumption is little to no wave generation when the body is oscillating in steady state. Here, viscous damping is of great importance. Using *(3.34)*, the drag term for a cylinder in motion with relative velocity is the main source of viscous damping.

For a relative velocity, not necessarily in phase, we have that

$$\dot{\eta}_r = u - \dot{\eta} = A\cos(\omega t + \phi) \tag{3.35}$$

where

$$u = u_a \sin(\omega t) \qquad \eta = \eta_1 \cos(\omega t) + \eta_2 \sin(\omega t)$$

so that

$$A = \sqrt{(u - \omega\eta_2)^2 + (\omega\eta_1)^2} \tag{3.36}$$

Neglecting the phase angle, the non-linear drag term on a small strip on the structure can be expressed as

$$dF_{drag,NL} = \frac{\rho}{2} C_D D A^2 |\cos(\omega t)|\cos(\omega t) \tag{3.37}$$

Now assuming the linear drag force on the form with coefficient K_L

$$dF_{drag,L} = \frac{\rho}{2} C_D D K_L A \cos(\omega t) \tag{3.38}$$

where K_L is expressed, and be found by equal work done over one period, as

$$K_L = \int_0^T (dF_{drag,L} - dF_{drag,NL})\dot{\eta}_r dt = 0 \qquad K_L = \frac{\int_0^T |\cos(\omega t)|\cos(\omega t)^2 dt}{\int_0^T \cos(\omega t)^2 dt} = \frac{8A}{3\pi}$$

As a result, the linearized drag term, related to the incident flow field velocity u and the structural motion velocity $\dot{\eta}$

$$dF_{drag,L} = \frac{4\rho C_D DA}{3\pi}(u - \dot{\eta}) \tag{3.39}$$

Thus yielding the viscous damping coefficient, in terms of the

$$B_{visc} = \frac{4\rho C_D DA}{3\pi} \tag{3.40}$$

3.4 Articulated Multi-Body Hydrodynamic Response

Expanding the theoretical approach discussed in linear wave-induced motions and loads to include more than one body that is connected by hinges requires another theoretical formulation and notation. These articulated bodies' exposure to wave effects is vital for the global system response of the floating solar island concept.

Defining a Cartesian coordinate system (x, y, z) with $z = 0$ at the mean free surface, positive upwards, assuming infinite water depth and linear potential flow with waves propagating in the positive x-direciton. The fluid velocity is defined as the gradient of the velocity potential, with the wave number and linearized free-surface condition

$$\phi(x, y, z)e^{i\omega t}$$

$$K = \frac{\omega^2}{g} \qquad K\phi - \frac{\partial \phi}{\partial z} = 0 \quad \text{on} \quad z = 0$$

When introducing more than one body, we define the body index $k = 1, 2, ..., N$ where N being the total number of bodies. Each body has a submerged area S_k and a submerged area S for the entire structure. As previously argued, the velocity potentials in the wave-body interaction problem can be decomposed as

$$\phi = \phi_D + \phi_R = \phi_I + \phi_S + \phi_R \tag{3.41}$$

where $\phi_D = \phi_I + \phi_S$ is the velocity potential solution to the diffraction problem, consisting of the incident wave and the scattering from the presence and impermeability of the body. The latter with a boundary condition $\frac{\partial \phi_D}{\partial n} = 0$ on S. While the radiation ϕ_R by the body motions.

The hydrodynamic pressure and moments by excitation and added mass and damping terms for a 6 degrees of freedom (DOF) single body will yield the same expressions as in *(3.19)* and *(3.25)*.

$$X_i = -i\omega\rho \int\int_S \phi_D n_i dS \qquad A_{ij} - \frac{i}{\omega}B_{ij} = \rho \int\int_S \phi_j n_i dS$$

The extended notation for $N > 1$ bodies, the excitation force $X_i^{(k)}$ acting on body k from a surface S_k, is the contribution to the global integral above, from the surface S_k. The radiation potentials due to body k are defined similarly in the form $\phi_j^{(k)}$

From this formulation, the added mass and damping coefficients will require double subscripts for a multi-body system, where one needs to distinguish the effects of each body's motions on the others. Hence a logical formulation for separated bodies. From the works of J. N. Newman (Newman, 2001), it is suggested to use a logical notation for separate bodies viewed as elements of a single global body with submerged surface S for a case of articulated bodies. A more compact notation that follows the original indices (i, j), but extended to include all relevant separate effects of the body. For example, a two-body system, each with 6 DOF would have modes $j = 1, 2, ..., 12$. The modes then represent the appropriate modes and are also a useful extension when applying generalized coordinates.

This formulation as generalized coordinates will properly represent different rigid body modes of multiple bodies. Combining hinge deflection modes and bending modes in a single set of generalized mode shapes suitable for hydroelastic analysis. The formulation requires specification of the different modes. Appropriate modes for representing up to four hinged bodies are shown in *Figure 3.4*.

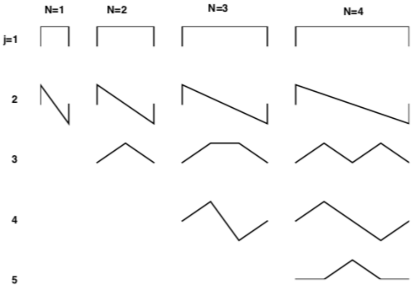

Figur 3.4: Generalized modes used to represent the motions of N identical bodies connected by $N - 1$ simple hinges. These mode shapes are defined to be either symmetric or antisymmetric about $x = 0$. The first two modes correspond to global heave and pitch without hinge deflections. The remaining modes represent the hinge deflections with zero displacement at the ends (Newman, 2001).

If a set of generalized modes $j = 1, 2, ..., J$, defined with corresponding set of generalized normal velocity components n_j, no changes to extend the definitions of the hydrodynamic terms are required. Hence, unchanged fundamental properties, both for symmetric properties of the hydrodynamic coefficients and the use of the Haskind relation.

3.4.1 Body Motions of Hinged Bodies

The following continues to expand upon the discussion regarding the hinged rigid bodies by generalized modes with a specific view on the vertical body motions, i.e. heave and pitch. Still assuming N rigid bodies and similar mathematical formulation as reviewed above, we define the transverse hinges locations at

$$x = x_n \qquad (n = 1, 2, ..., N - 1)$$

where each body length L is defined by the distance between two adjacent hinges, i.e.

$$L = x_{n+1} - x_n$$

As before, each body of the N bodies have 6 DOFs and in addition $N - 1$ generalized modes"corresponding to the deflection of the hinges. Following this formulation for the vertical motions of each body associated with the modes in heave, pitch and hinge deflection, we can utilize the generalized modes to determine the equation of motion for an array describing the system (Newman, 1997).

By the work, of J.N. Newman, for simplicity we assume that the hinges are located in the plane $z = 0$. The total number of DOF can each be described by an appropriate function $f_j(x)$, which describes the elevation due to the motion with unit amplitude in each separate mode. In the temporal domain, the respective mode is multiplied by the corresponding amplitude $a_j(t)$, which, by superpositioning all modes, can be written as

$$f(x,t) = \sum_{j=1}^{N+1} a_j(t) f_j(x) \tag{3.42}$$

or in frequency domain as

$$f(x,t) = \Re\Big\{e^{i\omega t} \sum_{j=1}^{N+1} \xi_j f_j(x)\Big\} \tag{3.43}$$

where ξ_j is the complex response amplitude operator representing the amplitude and phase of each modal response at the frequency ω.

As described earlier, choosing a compact notation indexing (j) for the vertical heave and pitch, but now including the hinges, the heave and pitch mode for the first rigid body, respectively has $(j = 1, 2)$ and the first hinge deflection $(j = 3, 4)$ and so on.

Generalizing the Hinge Modes

When defining the generalized modes, it is convenient to normalize the x-coordinate relative to the length of each body. This is done by defining the modes as functions of $u = \frac{x}{L}$, so that the hinge axes are at

$$u = u_n = \frac{x_n}{L} \qquad \text{(N even: } u = 0, \pm 1, \pm 2, ...) \qquad \text{(N odd: } u = 0, \pm\frac{1}{2}, \pm\frac{3}{2}, ...)$$

In all cases, heave and pitch modes are defined by the vertical displacement

$$f_1 = 1 \qquad f_2 = -uL$$

With first considering $N = 2$ modules with one hinge at $u = 0$, the hinge can be symmetric about $u = 0$, which is referred to as the tent function $t(u)$ due to the modal form.

$$t(u) = 1 - |u| \qquad 0 < |u| < 1 \qquad\qquad t(u) = 0, \quad |u| > 1$$

With generalized modes to represent hinge deflections of an array of N bodies, the set of modes can be defined if they are either symmetric about $u = 0$, ($j$odd) or anti-symmetric ($j$even). By combining this with the tent function, it can be showed that

$$f_j(u) = t(u-u_n)+t(u-u_{n-1}) \qquad \Big(j = 3, 5, 7, ..., 2\Big[\frac{N-1}{2}\Big]+1\Big) \quad \Big(n = 1, 2, 3, ..., \Big[\frac{N-1}{2}\Big]+1\Big)$$

$$f_{N+1}(u) = t(u - u_{N/2}) \qquad (N \quad \text{even}) \qquad \text{as} \quad \frac{N}{2} \quad \text{generalized symmetric modes}$$

$$f_j(u) = t(u-u_n)-t(u-u_{N-1}) \qquad \Big(j = 4, 6, 8, ..., 2\Big[\frac{N+1}{2}\Big]+1\Big) \quad \Big(n = 1, 2, 3, ..., \Big[\frac{N-1}{2}\Big]+1\Big) \tag{3.44}$$

These results are illustrated in *Figure 3.4*.

Expressing the Hydrodynamic Solution

By the previously stated fluid properties, the radiation potential due to the body motions can be expressed by the complex amplitude of each mode.

$$\phi_R = \sum_{j=1}^{J} \xi_j \phi_j \tag{3.45}$$

In each mode the velocity potential ϕ_j is the corresponding unit-amplitude radiation potential. Both the radiation and diffraction potentials have the same boundaries, but the former can be expressed by the normal component of the displacement on the body surface associated with mode j. Hence

$$\frac{\partial \phi_j}{\partial n} = i\omega n_j \qquad \frac{\partial \phi_D}{\partial n} = 0 \qquad \text{where} \quad n_j = f_j n_z \tag{3.46}$$

where the z-component normal vector on the body surface is defined from the fluid into the body now.

Thereby, again the added mass and damping coefficients

$$\omega^2 a_{ij} - i\omega b_{ij} = -i\omega\rho \int\int_S \phi_j n_i dS \tag{3.47}$$

and the general wave excitation force

$$X_i = -i\omega\rho \int\int_S \phi_D n_i dS \tag{3.48}$$

where the indices (i, j) takes on the values within the ranges of the rigid body modes $(1, 2)$ and the extended ones $(3, 4, ...)$

Still considering vertical displacements, we furthermore define the hydrostatic restoring matrix as

$$c_{ij} = \rho g \int\int_S f_i n_j dS = \rho g \int\int_S f_i f_j n_z dS \tag{3.49}$$

The Array Equation of Motion

By the current assumptions of rigid bodies and the results from *(3.47)*, *(3.48)* and *(3.49)*, the equation of motion (EOM) is derived by the inclusion of the inertial force coefficient matrix M_{ij}.

$$M_{ij} = \int m(x) f_i(x) f_j(x) dx \tag{3.50}$$

where the integration is over the entire array, and $m(x)$ the longitudinal density of mass.

In general, we can for the array of hinged bodies, where there is no external constraints, apply the same procedure as described in *Chapter 3.2.3*. Resulting in a similar EOM, but expressed by the complex amplitude of each mode. Hence

$$\sum_{j=1}^{N+1} \xi_j[-\omega^2(M_{ij} + a_{ij}) + i\omega b_{ij} + c_{ij}] = X_i \qquad (i = 1, 2, 3..., N+1) \tag{3.51}$$

The summation is over all modes, including heave, pitch and the hinge deflections. After solving the linear system of equations for the $N + 1$ unknown mode amplitudes ξ_j, the motion of the array can be evaluated by modal superposition. Yielding the following results.

$$\begin{aligned} f(x_n,t) &= \Re\Big\{(\xi_1 - \xi_2 x_n + \xi_j + \xi_{j+1})e^{i\omega t}\Big\} \quad \text{for} \quad \Big(n = 1, 2, ..., \Big[\frac{N-1}{2}\Big]\Big) \quad \Big(j = 2n+1\Big) \\ f(x_n,t) &= \Re\Big\{(\xi_1 - \xi_2 x_n + \xi_j)e^{i\omega t}\Big\} \quad \text{for} \quad \Big(n = \frac{N}{2}\Big) \quad \Big(j = 2n+1\Big) \\ f(x_n,t) &= \Re\Big\{(\xi_1 - \xi_2 x_n + \xi_j - \xi_{j+1})e^{i\omega t}\Big\} \quad \text{for} \quad \Big(n = \Big[\frac{N-1}{2}\Big], ..., N-1\Big) \quad \Big(j = 2N - 2_{n+1}\Big) \end{aligned} \tag{3.52}$$

where the two first equations represent the vertical motions due to heave and pitch, and the last represents the superpositioning of the symmetric and anti-symmetric hinge modes. A similar approach is used typically for Wave Energy Converters (WEC) (Rogne, 2014).

3.5 Theoretical RAO for the Wave-Induced Vertical Response on a Single & Two-Articulated Modules

Here, a brief presentation of the developed theoretical model RAO, calculated for the wave-induced vertical response of the floating solar island component is shown. The computed results are done for the single module and two articulated modules, defined as $N = 1$ and $N = 2$ number of bodies. The computational outputs are RAOs in heave and pitch, using linear potential theory, various assumptions, simplifications of the hydrodynamic solution and modal analysis. An in-depth definition, formulation and derivation and their sample-frequency plots are shown in *Appendix B*.

The model is grounded in the method described in *Chapter 3.4* above, but derived from scratch. The mathematical formulation, procedure and system definitions are also influenced by the works of T. Mathai, whom studied the use of generalized modes in hydrodynamic analysis of multiple bodies. (Mathai, 2000).

The theoretical RAOs for heave and pitch are shown below, with $N = 1$ and $N = 2$ bodies respectively. The derivation uses i, j indices for mode definitions and body index, but the explicit expressions are shown with conventional indices by choice, as they will be directly compared to experimental results. The computations and plots are done in *Matlab*. Unfortunately, being based on modal analysis, the $N = 2$ pitch RAO expression is not superimposed, but only explicitly written for the global pitch mode. The reason being that an explicit expression for the relative pitch mode is not directly derived, but included and calculated in *Matlab*.

The theoretical $N = 1$ heave and pitch RAO are respectively written as

$$\left|\frac{\eta_{3a}^{(N=1)}}{\zeta_a}\right| = \left|\frac{[4A\rho g - \omega^2 A_{33} - \omega B_{visc,3} e^{i\pi/2}] \cos\left(\frac{kl}{2}\right) e^{-kd}}{-\omega^2(m + A_{33}) + C_{33} + i\omega B_{visc,3}}\right| \tag{3.53}$$

$$\left|\frac{\eta_{5a}^{(N=1)}}{k\zeta_a}\right| = \left|\frac{-[4A\rho g - \omega^2 A_{33} - \omega B_{vsic,3}]\left(\frac{lD}{2}\right) \cos\left(\frac{kl}{2}\right) e^{-kd} e^{i\pi/2}}{-k[\omega^2(I_5 + A_{55}) + C_{55} + i\omega B_{visc,5}]}\right| \tag{3.54}$$

and similarly for $N = 2$ as

$$\left|\frac{\eta_{3a}^{(N=2)}}{\zeta_a}\right| = \left|\frac{[4A\rho g - \omega^2 A_{33} + \omega B_{visc,3} e^{i\pi/2}][\cos(kl_f) + \cos(k(l + l_f))] e^{-kd}}{-\omega^2(m + A_{33}) + C_{33} + i\omega B_{visc,3}}\right| \tag{3.55}$$

$$\left|\frac{\eta_{5a}^{(N=2)}}{k\zeta_a}\right| = \left|\frac{-[4A\rho g - \omega^2 A_{33} - \omega B_{vsic,3} e^{i\pi/2}](2l_f D + lD)[\cos(kl_f) + \cos(k(l + l_f))] e^{-kd}}{-k[\omega^2(I_5 + A_{55}) + C_{55} + i\omega B_{visc,5}]}\right| \tag{3.56}$$

which are plotted and examined for different wave-frequencies. Revealing theoretical resonance, cancellation and linear viscous damping effects. The latter being a drag coefficient dependent property as described in *Chapter 3.3.1*.

3.6 Experimental Methods

Model tests are an important aspect of hydrodynamic studies. Its aims are to evaluate the design data to verify performance, verify and calibrate theoretical and numerical methods, and obtain understanding of physical problems.

Based on the works of Sverre Steen in Experimental Hydrodynamics at the Norwegian University of Science and Technology (Steen, 2014), this section will give a brief overview of some theoretical and practical aspects for the experimental study of the multi-module floating solar island.

3.6.1 Modelling Laws

When it is intended to represent the full-scale system with a physical model in smaller scale, we need to be able to determine the proper properties by scaling laws. These scaling laws are results from achieving similarity in forces between model and full scale. Consequently, we have three conditions that must be fulfilled: geometric, kinematic and dynamic similarity.

Geometric similarity means that the geometry of the structures in model and full scale have the same shape and constant length scales between them. Kinematic similarity demands equal ratios between velocities. The dynamic similarity is achieved by having the same ratio for the force contributions that are present in the problem; inertia, viscous, gravitational, pressure, elastic and surface forces.

Regarding the dynamic similarity, there are two major scaling methods for hydrodynamic modelling; Froude and Reynolds scaling. These can not simultaneously be satisfied. A choice is made in terms of the nature of the problem. Using Froude scaling means that the importance of similarity in gravity and inertia forces will be dominating, versus using Reynolds that correctly scales viscous forces.

Due to the nature of the multi-module island system in a real sea state, gravity waves that excite the system responses will be vital. Thus Froude scaling must be satisfied for proper modelling and study of the design concept. This is also the most common in conventional model testing. The required ratio between inertia and gravity forces gives the relation

$$\frac{F_i}{F_g} \propto \frac{U^2}{gL} \tag{3.57}$$

where the Froude number equivalently will yield for model and full scale

$$\frac{U_M}{\sqrt{gL_M}} = \frac{U_F}{\sqrt{gL_F}} = F_N \tag{3.58}$$

The other physical parameters can be derived from dimensional analysis. Including structural mass, force, moment, acceleration, time and pressure.

3.6.2 Offshore Testing

These tests cover a wide range of model tests. From determining hydrodynamic coefficients from decay tests, to complex platform structures including mooring exposed to waves, wind and currents. The main objectives for these tests are; to determine hydrodynamic damping, added mass, RAOs and other quantities used as input to numerical simulations and verify concepts. Ensuring that one has properly understood and accounted for physical phenomena and established operational limits.

Regarding the test requirements, one must consider problems with wall reflection effects in the testing tank. The observed motion responses are usually split into different frequency regimes. This depends on the dynamic properties of the structure and excitation source. Wave frequency (WF) motions mainly consist of linear wave forces. Then low frequency (LW) motions taking place at resonant frequency well below the wave frequency range where the excitations are mainly non-linear wave forces (wave-drift). Lastly the high frequency (HF) motions that take place at resonant frequencies well above the wave frequency, which again are mainly non-linear wave forces, including impact loads.

For offshore testing procedures, short and long crested irregular waves are most frequently used. The procedure itself is dependent on the complexity of the test, but in short, we can summarize the main steps as environment calibration, static calibration for verification and calibration of system properties, and decay tests for verifying natural periods, damping and dynamic performance. One must keep the operational criteria in mind to cover different loading conditions in the test. Measurements will naturally depend on its purpose, but typically we have mooring line tensions, module relative motions, accelerations at specific points, impact loads and over-topping, and video recording.

Kapittel 4

Model Tests

The purpose of the experimental model tests in different sea states is to test the offshore floating solar island concept in order examine its hydrodynamic properties. The model tests were conducted in February 2019 in the large towing tank at the department of Marine Technology, Tyholt, Trondheim.

The overall experimental study was done in three parts; firstly, testing a single module with full instrumentation. Secondly, repeating the same test procedure with 2 hinged modules with full instrumentation. Thirdly, the final and most comprehensive test with 9 modules. The latter restricting the implementation of instrumentation, which resulted in full instrumentation on the 1st, 5th, and 9th module only. These three parts will from now on be defined as, respectively, case 1, case 2 and case 3.

Waves generated by the wave-maker acts as the governing environmental loads on the structure. The model was moored, naturally yielding some effects and influences on the overall model. Wave elevation, changes in air-gap at the ends of the global structure, vertical acceleration, and heave and pitch response were measured.

This chapter presents a thorough description of the models, the experimental setup and instrumentation. Moreover, describing the test conditions and post-processing of data.

4.1 Modelling & Scaling Laws

As discussed in *Chapter 3.6*, the data from the model tests are transmissible to the full scale structure by utilizing appropriate scaling laws. For this study, 1:20 Froude-scaling was applied in order to ensure similarity between inertia and gravity forces. The reason being governing environmental loads by gravity driven waves. The scaling parameters are shown in *Table 4.1* below.

Tabell 4.1: Froude-Scaled parameters where $\lambda = L_F/L_M$, and ρ_F and ρ_M, are respectively the fluid density for the full scale and model scale structure.

Physical Parameter	Unit	Multiplication Factor
Length	[m]	λ
Structural mass	[kg]	$\lambda^3\rho_F/\rho_M$
Force	[N]	$\lambda^3\rho_F/\rho_M$
Moment	[Nm]	$\lambda^4\rho_F/\rho_M$
Acceleration	[m/s^2]	$a_F = a_M$
Time	[s]	$\sqrt{\lambda}$
Pressure	[Pa]	$\lambda\rho_F/\rho_M$

4.2 The Models & Case Definitions

The tested models, i.e. case 1, 2 and 3, are built by identical single-modules. A simplification of the module structure described in *Chapter 2*. *Figure 4.1* shows the case 1 model, fully instrumented in the tank. The experimental study of the different cases were done to examine the properties of the single module, the dynamic influence of articulation in the simplest case, i.e. 2 hinged modules, and 9 modules to identify the hydrodynamics of a large component of the solar island concept.

Being restricted to vertical response in various sea-states, the model tests had, to some extent, a necessity of being generic and doable with the equipment and time available. Phenomena related to mooring, and structural loads on the hinges and panels were therefore excluded. The floaters were modelled as vertical cylinders, keeping an approximately identical buoyancy without including complicated water-rise-up effects that would occur in the original concept. The top frame, consisting of several stiffeners and beams are to complex details to model with 1:20 scaling. Consequently, this component was modelled with a uniform plate component. In general, the weight of the structure was a challenge, where the model required a very light-weight design and corresponding light materials in order to keep the structural and hydrostatic properties. This resulted in the top frame having gaps and openings. However, still maintaining satisfactory stiffness and rigidity. The models where hinged in one direction, creating a single row, hence representing a component of the solar island.

4.2.1 Single Module

The symmetric single module model is shown in *Figure 4.1*. The PV panels are not directly included, but they are represented as a part of the preliminary weight of the structure. A technical drawing of the single model is shown in *Appendix A* in *Figure A.2*.

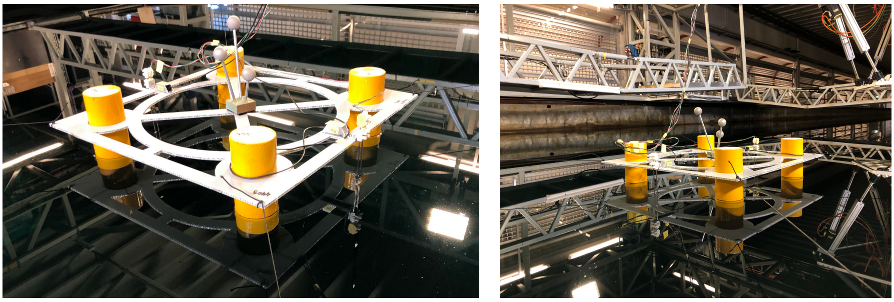

Figur 4.1: Case 1: Single module model, launched with instrumentation and mooring lines.

The floaters are made of divynicell foam material, which provides excellent material properties and light weight. These were sprayed with light yellow paint to increase the smoothness of the surface and limit absorption of water. The plate is made of a sufficiently light honeycomb material. As intentionally modelled, the honeycomb plate yields a very large bending stiffness, allowing the assumption to exclude structural displacement effects when exposed to wave-loads. Each floater is secured to the plate by two aluminum filling wires. The floaters are piercing the plate to move the vertical centre of gravity to correct full-scale property. This factor and the symmetric property of the structure also yields very similar moments of inertia. The mooring lines were secured at approximately $45°$ at the corners and slightly upwards to the tank at walls. The elasticity of these cords were 10 [N/m] to ensure limited influence. Especially as these cords would not yield any resonance below a period of 30 seconds, well away from the environmental load range. The main parameters and dimensions are shown in *Table 4.2*, including the hinges applied in case 2 and 3. The hinges adds a distance of 10% of the module length between the articulated modules.

Tabell 4.2: Model and full-scale main dimensions and properties of the single model, with instrumentation and ballast.

Description	Parameter	Model scale	Full scale
Plate length	L	600.0 [mm]	12.0 [m]
Floater diameter	D	80.0 [mm]	1.6 [m]
Floater height	h	131.5 [mm]	2.63 [m]
Module draught	d	56.5 [mm]	1.13 [m]
Module mass	M	1.136 [kg]	9088 [kg]
Vertical centre of gravity	VCG	0.122 [mm]	2.44 [m]
Mooring line spring stiffness	k_s	10 [N/m]	4000 [N/m]
Distance between hinged modules	l	60.0 [mm]	1.2 [m]
Distance from bottom to hinge	z_h	139.0 [mm]	2.78 [m]

4.2.2 Two Articulated Modules

The two identical modules are articulated by hinges. These were created to isolate a single degree of rotation allowing relative pitch and heave motion without any significant friction. To implement the desired design in an efficient manner, the use of two hinges at each edge was utilized. The hinges themselves are made of small L-beams fixed on the neighbouring modules, connected by a loosescrew with insignificant weight. This is shown in *Figure 4.3*, also showing the use of dummy"weights to balance the wave probes at the fore and aft end of the articulated structure. *Figure 4.2* shows the case 2 model with full instrumentation in the tank.

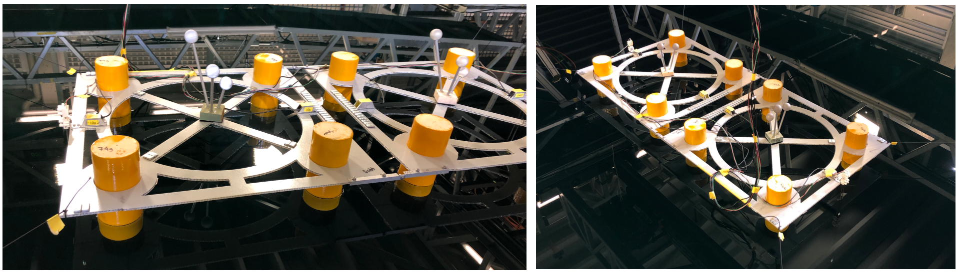

Figur 4.2: Case 2: two articulated modules, launched with instrumentation and mooring lines.

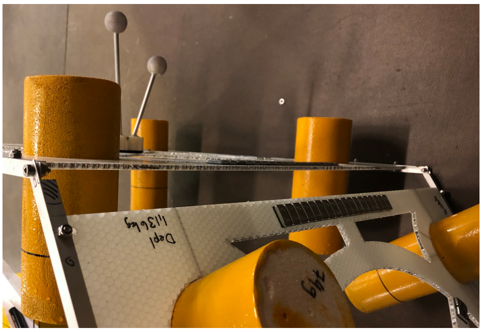

Figur 4.3: Case 2: two articulated modules showing hinge detail.

4.2.3 Nine Articulated Modules

The main experimental study of the floating solar island concept is with utilization of nine in-line articulated identical modules as shown in *Figure 4.4*. The case 3 set-up follows the same procedure as case 2 described above. The main difference being the instrumentation, where the structure's mooring lines and fixed wave probes measuring air-gap is located at the fore and aft of the structure. The accelerometers and motion capture reflectors were only measured at the first, middle and last module.

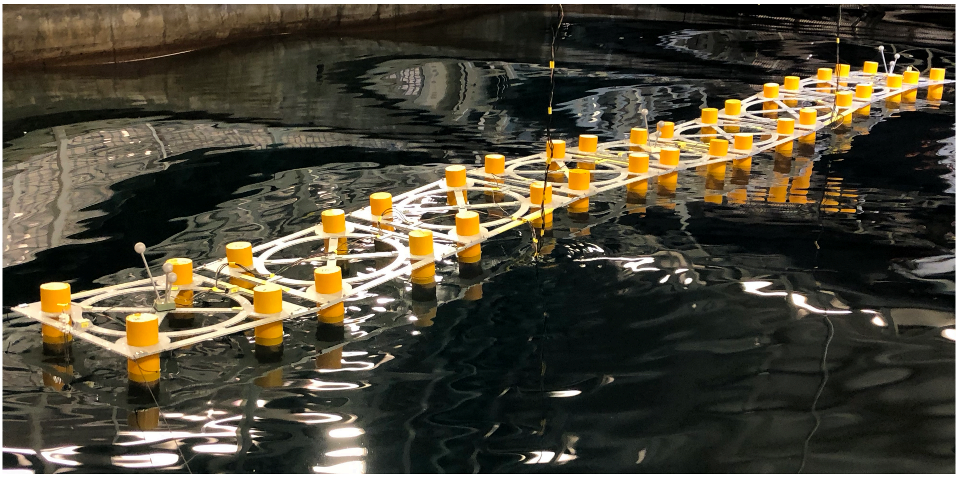

Figur 4.4: Case 3: nine articulated modules, launched with instruments and mooring lines in incident regular waves.

An overview of the in-line hinged model and a detailed lay-out of the first module is shown in *Figure 4.5* below.

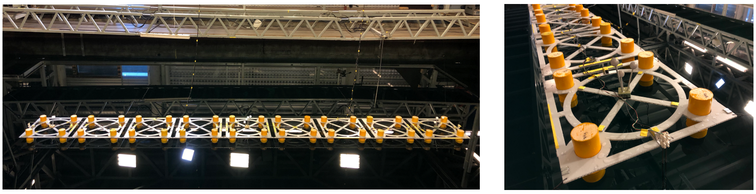

Figur 4.5: Case 3: nine articulated modules (left), and details for the first module (right), launched with instrumentation and mooring lines.

4.3 Experimental Setup

The experimental setup was identical for the three different cases, with the exception being instrumentation of the respective models. *Figure 4.6* illustrates the setup for the case 3 model tests. The first module in the figure also represents the case 1 model tests, and then expanding with an additional module in the negative x-direction for case 2. The wave probes are kept in the same positions, except the fixed probes.

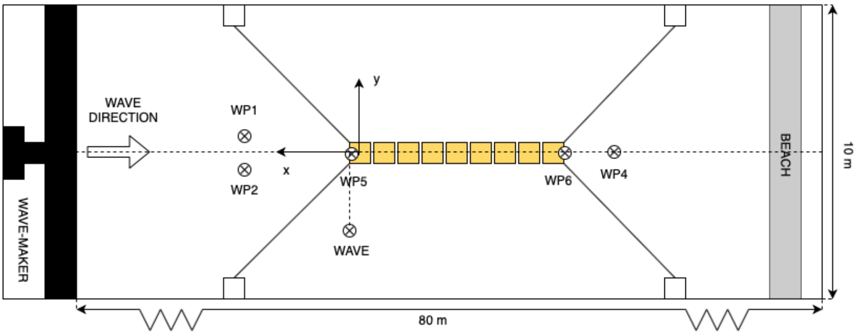

Figur 4.6: Top view illustration of the experimental set-up for the case 3 model test. Identical set-up for tests with 1 and 2 modules, with the tank global coordinate system (as shown) in the centre of the first module.

The fixed global coordinate system for the tank is shown in the figure above, with the global origin positioned in the centre of the first module. The waves are propagating in negative x-direction, with the z-direction down towards the seabed. This coordinate system is important with regards to all instrumentation with their respective calibration and direction definitions. The beach provides a damping at the end to increase energy dissipation of the waves and make the surface calm between wave-series. The illustration incorrectly scales the size of the tank, as the distances from the wave-maker, the beach and the tank walls to the model are quite large. By observations and measurements, this resulted in negligible tank wall and reflected wave effects.

An illustration of the motion capture instruments and the accelerometers for a single module, two articulated modules, and nine articulated modules are shown in *Figure 4.7*.

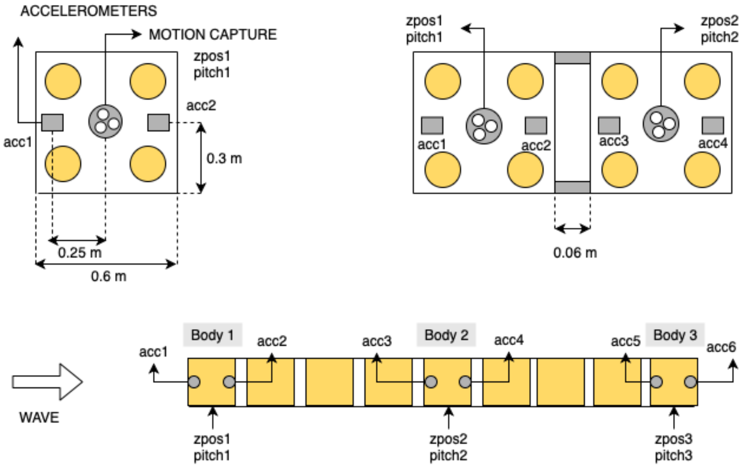

Figur 4.7: Top view illustration of the accelerometers and motion capture instruments with their channel names for one module (top left), two modules (top right), and nine modules (bottom). Model-fixed wave probes are not included.

4.3.1 Instrumentation

The wave height, vertical accelerations, six degrees of freedom (DOF) motions, and air-gap on the front and back end of the structure were measured. Each instrument was calibrated, and the sampling frequencies were 50 [Hz] for the motion capture, and 200 [Hz] for the rest. Here, a brief overview of the instrumentation is given using the channel names.

Wave Probes

Six wave-probes were present, all defined with positive direction upwards. *wp1* and *wp2* where positioned at the same x-position, registering the incident waves first, *wave* positioned in-line with the front end of the model, measuring the incident wave entering the structure, and *wp4* positioned in the middle of the tank behind the model. The latter measuring the wave leaving the structure and can register unwanted reflected waves from the beach. This wave-probe also provides a steady-state indication for case 3 regular wave tests, where the entire model would be in proper wave-body interaction. Furthermore, *wp5* and *wp6* were attached to the front and back end of the respective model, measuring the relative wave elevation in terms of the plate, i.e. change in air-gap.

Accelerometers

Accelerometers were placed as shown in *Figure 4.7*, positioned in-line with adjacent floaters on the respective bodies. Measuring the vertical accelerations at these points, calibrated and defined with positive acceleration upwards. Giving the possibility to study accelerations and combined accelerometer positions for heave and pitch response calculations by initial integration.

Motion Capture

The tank motion capture system, limited to three seperate bodies, could measure a 6 DOF motion in the (x,y,z) direction (3D), in addition to the residuals related to the position of the instruments. This is done by four sets of cameras located in each corner of the tank in proximity of the model, and a tree"with three fitted reflexive markers. This tree"can be seen in *Figure 4.1* positioned in the horizontal centre.

The relative positions of the markers yields the capability of measuring roll, pitch and yaw in addition to the translational movements by the single markers. Inaccuracy of the system mainly originated in water reflections, which could confuse the cameras when identifying the correct markers. However, the accuracy was fixed to a body containing three markers with acceptance of a few millimeters deviation. Meaning that water reflection was insufficient to disrupt the measurement. The greater concern is the long model moving out of frame.

The motion capture was calibrated in terms of the local body's centre of gravity (CoG), but the measurements used the global coordinate system. Hence, horizontal movements, like surge, was measured with respect to the centre of the first model (at $x = 0$). Rotational movement followed the calibration in terms of local CoG, meaning measured degrees are relative to each body's CoG. So translations required manual offset removal during post-processing, but rotations did not. Since the system follows the coordinate system shown in *Figure 4.6*, so positive heave motion is downwards in the tank, surge is positive when moving against the waves (to the left) and pitch rotation is positive when the right/back end of a model is moving down and the left/front end is moving up (as positive rotation follows the tank y-axis).

Camera

Many test runs were recorded with a camera placed as close to the model as possible, with the intention of revisiting tests. Mainly, all the regular waves with a wave-steepness of $H/\lambda = 1/40$ and $H/\lambda = 1/20$ were recorded. Where H is the wave height and λ the wave length. Partial recordings were done for irregular sea-states for the same purpose.

4.4 Wave-series Characteristics

The experimental study is in both regular and irregular waves with different conditions in order to acquire a wide variety of measurements to determine the hydrodynamic behaviour of the structure. To establish a proper response, the variety in regular waves was set by a range of wave periods T, with different wave heights H determined by a defined wave steepness H/λ. Quantifying the dynamic response of the structure in both low- and high-frequency range. Irregular sea-states defined by an input spectrum yields a more realistic response measurement. Observing events such as slamming or over-topping. Both critical to the solar island concept, due to the structural integrity of the PV panels and the supporting components. During tests for case 1 and case 2, observations and results ended in revisiting the wave-series characteristics. Therefore, the case 3 study has a different range in regular wave characteristics.

4.4.1 Regular Waves

The wave period $T = 2\pi/\omega$ and the wave steepness H/λ, varied for each wave-series. Each wave was run for a sufficient amount of time in order to achieve steady-state, and stopped before any beach-reflected waves could disturb the measurements. The water was given enough time to become still between each run.

The case 1 and case 2 model tests were exposed to the wave-series shown in *Table* **??** in full scale.

After the completion of the first two cases, which had less available time, preliminary results showed that a higher period range should be implemented in the final study with 9 modules. The wave-series characteristics was hence expanded for case 3, as suspected hydrodynamic phenomena would occur for higher-frequency waves still related to the operational criteria for the floating solar island. The upper limitation of the tank was $T = 13s$ for the 1:20 scaling. The case 3 regular wave-series characteristics is shown in full-scale in *Table 4.4*. The same tables for the wave series in model-scale can be found in *Appendix D*.

Tabell 4.3: Test conditions for regular waves in full scale for case 1 and case 2 model tests.

T [s]	λ [m]	H/ $\lambda = 1/60$ H [m]	H/$\lambda = 1/40$ H [m]	H/$\lambda = 1/30$ H [m]	H/$\lambda = 1/20$ H[m]
6.0	56.2072	0.9368	1.4052	1.8736	2.8104
7.0	76.5042	1.2751	1.9126	2.5501	3.8252
8.0	99.9238	1.6654	2.4981	3.3308	4.9962
8.5	112.8046	1.8801	2.8201	3.7602	5.6402
9.0	126.4661	2.1078	3.1617	4.2155	6.3233
9.5	140.9082	2.3485	3.5227	4.6969	7.0454
10.0	156.1310	2.6022	3.9033	5.2044	7.8065
10.5	172.1344	2.8689	4.3034	5.7378	8.6067
11.0	188.9185	3.1486	4.7230	6.2973	9.4459
11.5	206.4832	3.4414	5.1621	6.8828	10.3242
12.0	224.8286	3.7471	5.6207	7.4943	11.2414

Tabell 4.4: Test conditions for regular waves in full scale for case 3 model tests.

T [s]	λ [m]	H/ $\lambda = 1/60$ H [m]	H/$\lambda = 1/40$ H [m]	H/$\lambda = 1/30$ H [m]	H/$\lambda = 1/20$ H[m]
2.0	6.2452	0.1041	0.1561	0.2082	0.3123
2.5	9.7582	0.1626	0.2440	0.3253	0.4879
3.0	14.0518	0.2342	0.3513	0.4684	0.7026
3.5	19.1260	0.3188	0.4782	0.6375	0.9563
4.0	24.9810	0.4163	0.6245	0.8327	1.2490
4.5	31.6165	0.5269	0.7904	1.0539	1.5808
5.0	39.0327	0.6505	0.9758	1.3011	1.9516
5.5	47.2296	0.7872	1.1807	1.5743	2.3615
6.0	56.2072	0.9368	1.4052	1.8736	2.8104
6.5	65.9653	1.0994	1.6491	2.1988	3.2983
7.0	76.5042	1.2751	1.9126	2.5501	3.8252
7.5	87.8237	1.4637	2.1956	2.9275	4.3912
8.0	99.9238	1.6654	2.4981	3.3308	4.9962
8.5	112.8046	1.8801	2.8201	3.7602	5.6402
9.0	126.4661	2.1078	3.1617	4.2155	6.3233
9.5	140.9082	2.3485	3.5227	4.6969	7.0454
10.0	156.1310	2.6022	3.9033	5.2044	7.8065
10.5	172.1344	2.8689	4.3034	5.7378	8.6067
11.0	188.9185	3.1486	4.7230	6.2973	9.4459
11.5	206.4832	3.4414	5.1621	6.8828	10.3242
12.0	224.8286	3.7471	5.6207	7.4943	11.2414
12.5	243.9547	4.0659	6.0989	8.1318	12.1977
13.0	263.8614	4.3977	6.5965	8.7954	13.1931

4.4.2 Irregular waves

For case 1, two irregular wave tests were conducted. However, they were done using a pink noise spectrum with a significant wave height $H_s = 4m$, with frequency ranges $(\omega_1, \omega_2) = (\frac{1}{8}, \frac{1}{12})$ and $(\omega_1, \omega_2) = (\frac{1}{6}, \frac{1}{12})$. The observed input was closer to a storm, yielding very large amounts of water-impact events. These disrupted the instruments and gave invalid measurements and are therefore not included. This spectrum type contains waves with over-all large energy and height within a relatively short frequency interval. Consequently creating very steep waves that consistently broke. The choice for environmental input was therefore changed for case 2 and case 3. The irregular sea-state was simulated by a JONSWAP spectrum, which is described in *Appendix C*. Because of limited time, only one irregular sea-state was tested for case 2, and unfortunately its measurements were corrupted by unknown reasons. So these are not included either.

By consulting Moss Maritime (Hanssen, 2019), the test setup for case 3 was reevaluated to be focused around the steepness curve to evaluate the structure's operational limits (DNVGL, 2007). Properly investigating suitable operational sites in terms of significant wave height H_s and peak period T_p, close to and further away from the wave breaking limit. A simplified steepness curve, restricted to $H_s = 4m$ was delivered by *Moss Maritime* for this purpose. This curve and the indicated points showing the irregular wave-fields that were tested are shown in *Figure 4.8* and correspondingly in *Table 4.5*. The same table can be found in model-scale in *Appendix D*.

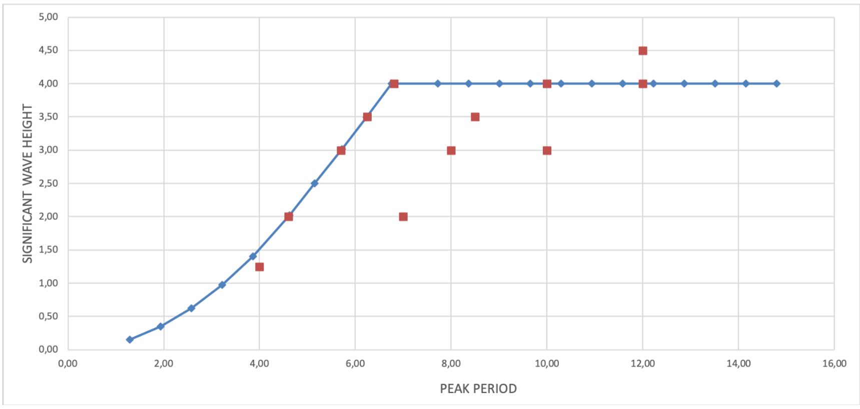

Figur 4.8: Simplified steepness curve, restricted to a significant wave height of $H_s \leq 4$[m], with the red points indicating the irregular sea states which were tested.

Tabell 4.5: Test conditions for irregular waves in full scale for model tests with 9 articulated modules, using JONSWAP spectrum with steepness parameter $\gamma = 3.3$.

T_p [s]	4.0	4.6	5.7	6.8	7.0	8.0	8.5	10.0	12.0
H_s [m]	1.25	2.0	3.0	4.0	2.0	3.0	3.5	3.0 3.5 4.0	4.0 4.5

4.5 Post-Processing

Case 1 and 2 had both a total of 46 regular waves tests. Moreover, 92 regular wave tests and 12 irregular wave tests produced usable data for case 3. *Matlab* was used for post-processing the, including reading channel data, data "cutting", filtering and extracting the interesting statistical properties and handling visualization. Spectral analysis by Fourier Transform was done with *Matlab* fast Fourier transform (FFT). This section briefly covers the essential steps, showing examples of collected data to illustrate methods and evaluations that is prior to any final results. Discussing uncertainties, errors, preliminary impacts and alteration of data.

Further on in the Thesis, examples and results of data are presented by channel names. These are illustrated in *Figure 4.6* and *4.7*. Where the wave-probes are named as *wp1*, *wp2*, *wave*, *wp4*, *wp5* and *wp6*. The motion capture heave response are listed as *zpos1*, *zpos2* and *zpos3* for the respective instrumented bodies, with pitch in the same manner as *pitch1* and so on. Lastly, the accelerations are named *acc1* and *acc2* for the first body, continuing as *acc3*, *acc4*, *acc5* and *acc6* for the second/middle and last module.

This section only uses examples from regular wave tests, but an almost identical process was done for the irregular wave data. The main difference being that no steady state occurs, and there is larger emphasis on spectral analysis application.

4.5.1 Measurement Outputs

All instruments creates time-series, and zero-measurements were taken prior to all test runs. However, offsets could still occur. In addition, the motion capture system did not take zero-measurement in terms of the global coordinate system. These offsets are therefore removed by subtracting the average along the time series before incident waves excited the system. Examples of different outputs are shown following the offset removal in *Figure 4.9*.

Due to the nature of the tank, the tests needed manual initiation and termination. Meaning that the measurements starts as the wave-maker begins to operate and is stopped instantaneously. The post-processing benefits from a decaying measurement, especially for data filtering. Therefore, all the measurements were subjected to a Gaussian bell function of the form

$$f(t) = g(t)\omega(t) \qquad \text{where} \quad \omega(t) = \begin{cases} 1 & \text{for} \quad t = [t_0, t_1] \\ {}^{-\frac{1}{4}t^2} & \text{for} \quad t = (t_1, t_{\text{end}}] \end{cases}$$

where the output measurement is the function $g(t)$ and the bell function $\omega(t)$, which creates a fake decay. This is effect is shown in *Figure 4.10*.

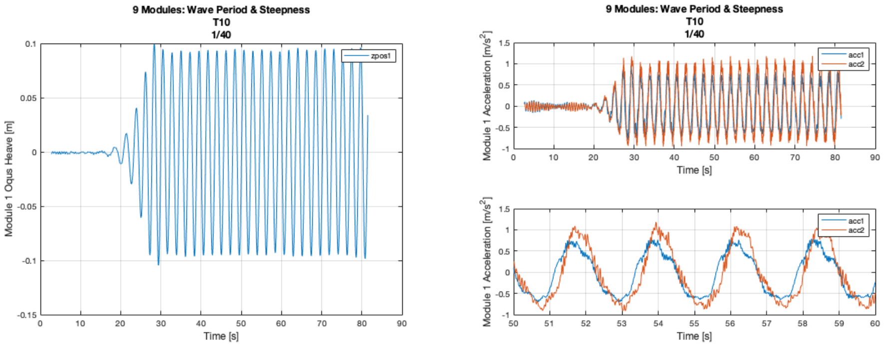

Figur 4.9: Measurement output examples for case 3, showing unprocessed time-series for the motion capture heave response on body 1 (*zpos1*) (left), and the acceleration of body 1 (*acc1* and *acc2*) (right).

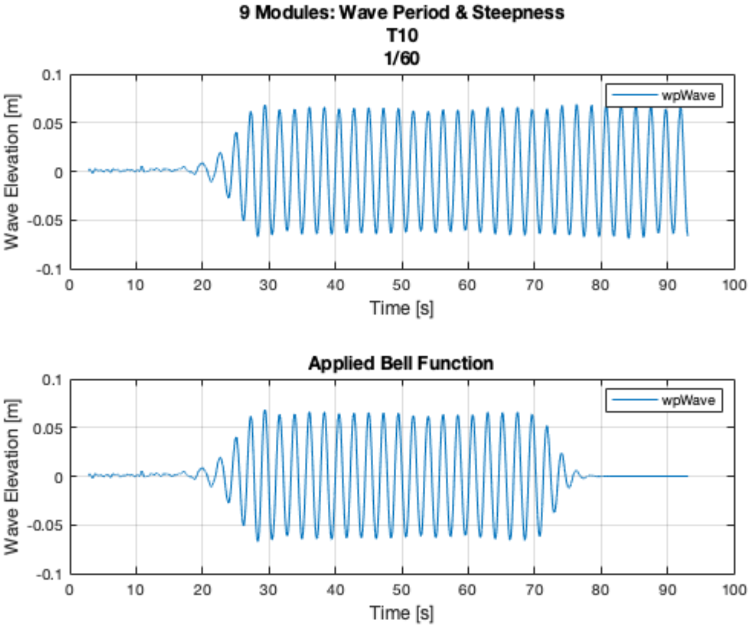

Figur 4.10: Unprocessed output measurement of the wave-probe *wave* (top), and the same measurement with applied bell decay function (bottom).

The definitions of the intervals for the bell function $\omega(t)$ are selected to keep the original measurement until a sufficient number of periods of the incident waves are left, still maintaining sufficient steady-state interval for the regular wave tests.

4.5.2 Data Filtering & Spectral Analysis

The data filtering is done with the *Matlab* band-pass function. It enables isolation of 1st, 2nd and 3rd order effects that occur in the wave-body interaction. A method that also removes high-frequency noise. This performance varies by the generated wave input, and computed results must be evaluated by this in mind when unstable waves were generated for a few time-series.

A spectral analysis by FFT is done to compute the frequency harmonics of the system. The method that follows is to define the band-pass frequency using a 4% interval of the respective order. The 1st order peak frequency should correspond to the incident wave frequency input, which has a band-pass filter process shown in *Figure 4.11*.

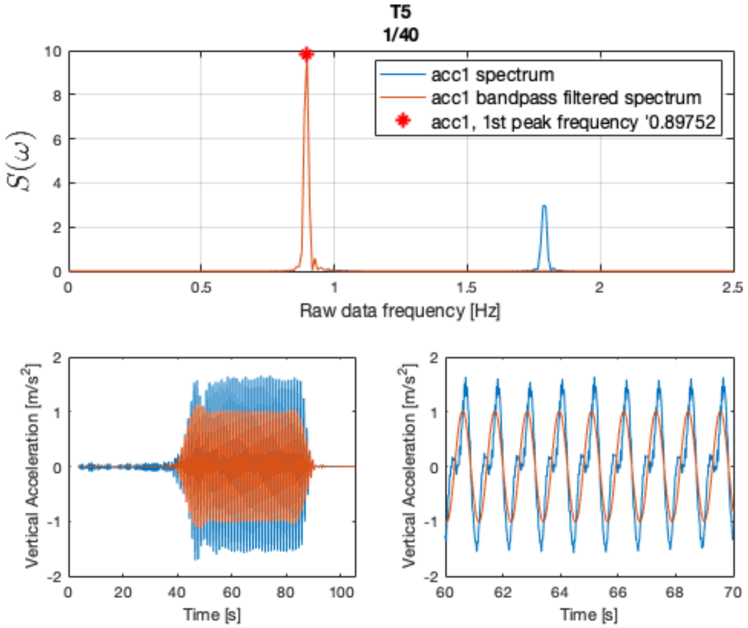

Figur 4.11: Example of a 1st order band-pass filtering process for *acc1* in regular waves with $T = 5$ [s] and $H/\lambda = 1/40$. Both unfiltered and filtered Computed spectrum is shown at the top. The corresponding time domain measurements are shown at the bottom.

4.5.3 Steady State

For each regular wave test, after the previously discussed processing, time intervals were defined to isolate steady-state measurements. Yielding the ability to compute experimental hydrodynamic structural response to the different wave-conditions. For case 1 and 2, this steady state evaluation was done based on incident wave measurements from *wave*. For case 3, the same procedure was done by using *wp4*, situated behind the module to be certain of that the whole structure was in steady-state wave-body interaction. This is shown in *Figure 4.12*.

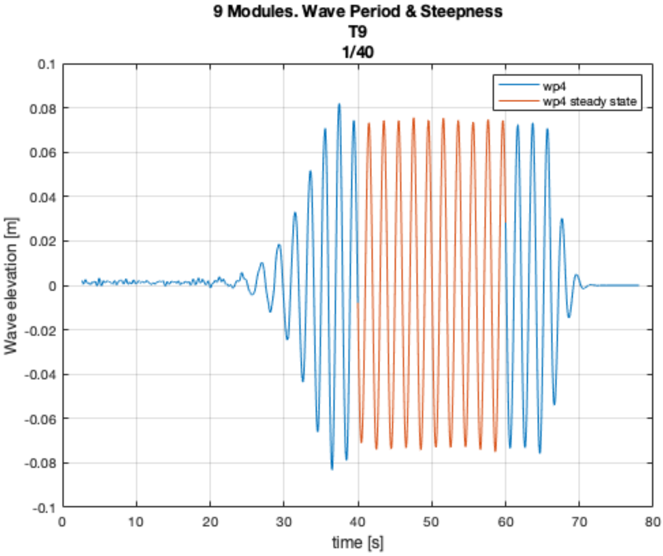

Figur 4.12: Time series of the wave measurements at *wp4* from case 3 in $T = 9$ and $H/\lambda = 1/40$, illustrating unprocessed data (blue) and the steady state interval (red).

The steady state data is collected for all relevant measurements for the respective chosen order of any filtered data. These measurements are used for computing statistical properties and other quantities of the respective run. consequently yielding response amplitude operators and acceleration harmonics.

4.6 Error Sources

Some sources of error are present during the experimental study. For the physical model, It is difficult to guarantee complete symmetry, correct weight distribution and geometry. This will affect the structural properties of the model and hence yield modelling errors in terms of the full-scale structure described in *Chapter 2*. More properties that might deviate are the structural stiffness, inertia and centre of gravity. These were difficult to model correctly due to weight restrictions, as the module structure in itself is quite light. However, no significant indications of modelling errors came to light during model construction, design and tests. However, the results are naturally directly correlated with the model, so using the results to evaluate the full-scale structure must be taken with caution.

Furthermore, the study was designed to avoid the effect of mooring lines as much as possible to achieve near isolation of vertical response. Small variations in the pretension of 10 [N/m] and the lines presence will also influence the wave-body interaction. Due to the elasticity of of the lines, one can argue that the influence is limited, but this stiffness was not measured or validated.

The water temperature in the tank can influence the generated waves and the instruments. The instruments are also prone to drift slightly over time, possibly producing slightly different measurements during a test. The wave-maker in general also have small deviations from the theoretical wave inputs. More deviation was observed for the shortest and longest waves in terms of regularity and heights, and the waves had a tendency to have a sharper crest than intended. The post-processed RAOs are also represented in frequency/period domain, whom may therefore include small errors as the generated waves can dissipate slightly.

Some of the case 2 and case 3 tests were run with offline channels for the model-fixed wave probes. These will therefore not be included in the results section. Moreover, the instruments in the case 3 model tests were greatly separated. So two electrical cord bundles exited the model. For case 1 and 2, a single cord bundle hung over the side of the model. In all cases, these could slightly influence the measured model response. However, no critical influence was observed. Lastly, the motion capture system in case 3 had greater challenge keeping all the bodies within camera frame. This resulted in higher residuals for some measurements and even very short periods of time where the measurements were lost. This occurrence can be seen in the data as flat-linesfor heave and pitch, i.e. *zpos* and *pitch* data plots in time domain.

Regarding case 3, some of the generated high-frequency waves were unstable. This is because of the limitations of the wave-maker and the nature of the long tank where waves could dissipate or become deformed. These measurements are shown in *Appendix H* and further discussed in *Chapter 5*.

Kapittel 5

Results & Discussion - Regular Waves

This chapter presents the experimental results for the model tests in regular waves. Not all resulting plots are included, as specific choices for one or several measurements are taken to highlight relevant findings or stand as exemplary results for the respective output. Firstly, a wave height evaluation is presented, where the measured and theoretical regular wave inputs are examined to review the environmental loads that are exciting the model. Secondly, a presentation of the findings for vertical response, shown as RAOs and harmonics. The data is mainly presented as non-dimensional quantities, plotted against the non-dimensional wave-number kl. Where $l = 8.4$m is the full-scale length between adjacent floaters. The period/frequency dependent wave-number uses theoretical values for simplicity, which proved satisfactory for evaluation. Furthermore, a comparison between the experimental results for each case and the theoretical model for one and two articulated modules are reviewed and discussed. Regarding case 3, by observation and literature references, some additional discussion concerning non-measured effects are present. Including articulation effects, wave-diffraction, near-trapping of waves, and hinge loads.

5.1 Wave Height

Measured wave heights at *wp2* compared to the theoretical inputs are presented in *Figure 5.1* for every steepness. Following kl corresponding to the case 3 wave-series, the figure gives an impression of the accuracy of the generated waves in terms of the characteristic input. In general, the input and output waves are in good relation, giving a satisfactory representation of the desired environment.

There is a considerable distance between the wave-maker and *wp2*. Consequently, the waves are expected to deviate due to slight dissipation. The residual distance between the theoretical and measured wave heights are shown in *Figure 5.2*. Revealing a near general trend for higher deviation when the waves are steeper.

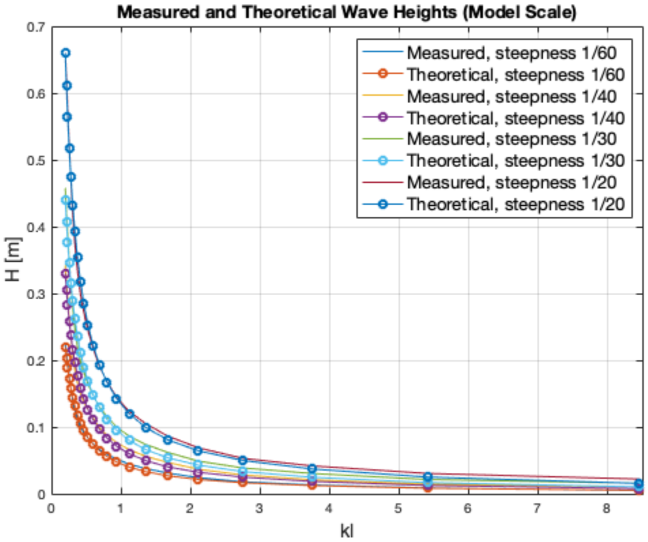

Figur 5.1: Measured and theoretical regular wave heights for regular waves measured by *wp2*, in model scale, plotted against the non-dimensional wave-number kl.

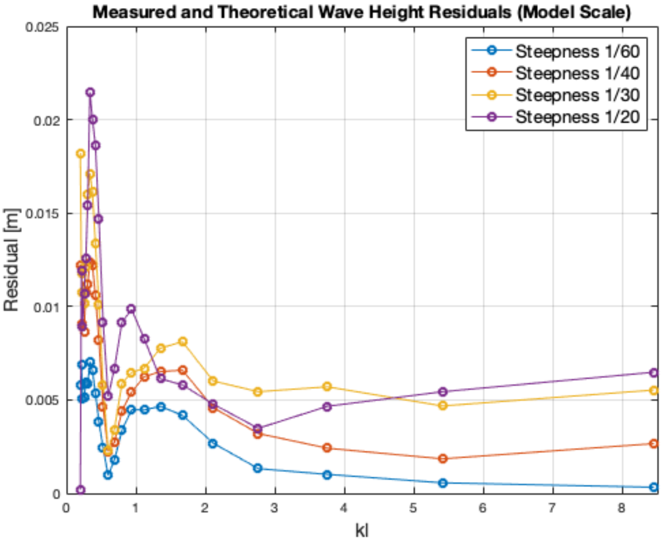

Figur 5.2: Residual plot for the measured regular wave heights at *wp2* and the theoretical regular wave heights, plotted against the non-dimensional wave-number kl.

The general wave height evaluation result shows that the generated waves were slightly larger than the input characteristics. However, the largest deviation, which occurs for the steeper waves with peak residuals in the lower wave-frequency domain, is less than 10% of the input wave heights. A satisfactory generated output. It's worth to note that the most theoretically accurate with stable residuals are generated waves with a $kl \geq 2$, which corresponds to a full-scale period of $T \geq 5$s. For the longer-periods, the residuals have more relative variation, where the smallest seems to occur for wave periods in the domain $[6, \quad 8]$ [s]. From observations, the suspected reason for the occurring residual peaks for the longer waves are deformations of the propagating wave.

Figure 5.3 below shows the measured wave heights at all wave-probes for $H/\lambda = 1/60, 1/40$. The result suggests good agreement, making it sufficient to assume negligible effects that would disrupt the waves propagating through the model.

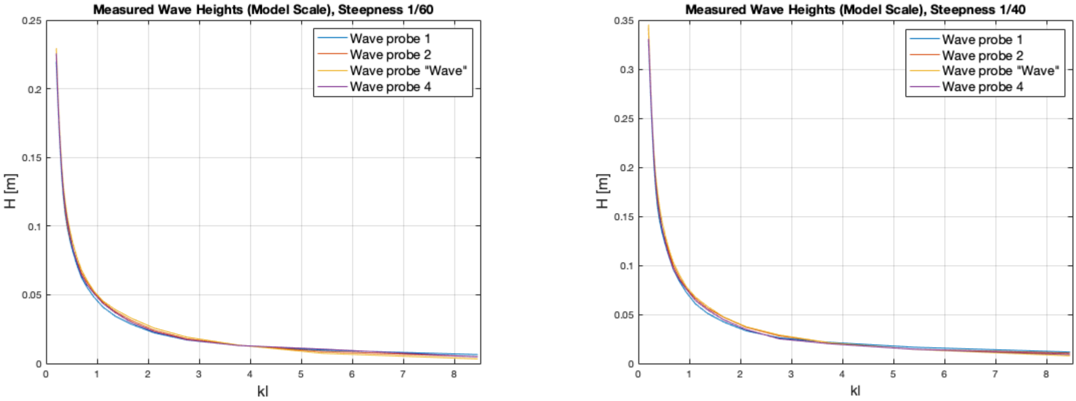

Figur 5.3: Measured regular wave heights at all wave-probes for a wave steepness $H/\lambda = 1/60$ (left) and $H/\lambda = 1/40$(right), plotted against the non-dimensional wave-number kl.

Similar figures for every steepness can be found in *Appendix E*. Note that the figure showing the measured wave heights for the steepness $H/\lambda = 1/20$ at *wp1* goes towards some unrealistically high value. The reason for this is that the incident wave compromised the instrument, as *wp1* was positioned, calibrated and zero-measured closer to the mean free-surface. Submergence of these instruments gave nonphysical spikes in the measurements.

5.2 Example of Position Response by Acceleration Measurements

Using case 3 measurements as an example, this section briefly presents how the vertical responses are obtained by integration of the accelerated bodies. Consequently giving an additional vertical hydrodynamic response output.

Figure 5.4 shows the 1st order filtered time-series for the accelerometer *acc1*, located at the foremost end of the model, and its corresponding velocity and position. This integration is done by the numerical trapezoid method in the regular wave tests, rather than integrating in the frequency domain. Although the latter method is applied in the irregular wave tests.

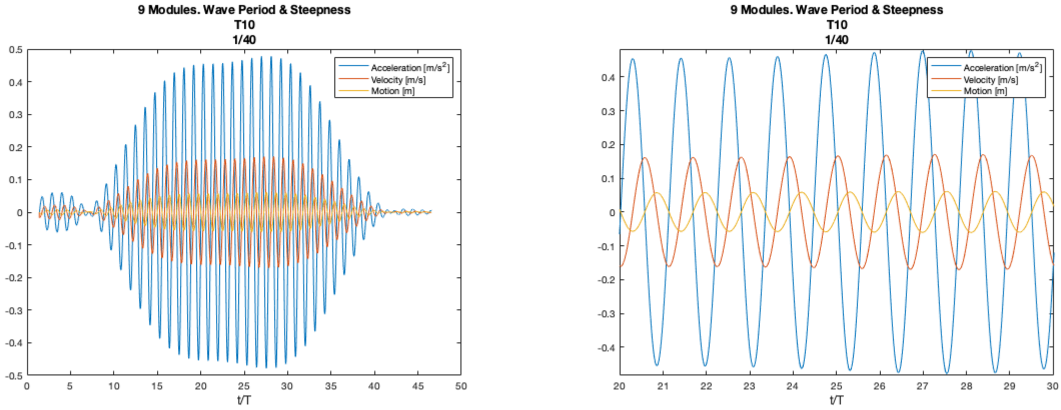

Figur 5.4: Example of a 1st order filtered acceleration measurement at *acc1*, and its corresponding calculated velocity and accelerometer position in dimensionless time t/T, where T is the wave period for the respective measurement.

A 1st order filtered acceleration is shown for $H/\lambda = 1/40, 1/20$ with the same wave period in *Figure 5.5*. The acceleration is made dimensionless by the gravitational constant g. The result shows an increase in magnitude for steeper waves. Next, *Figure 5.6* shows the corresponding calculated position of the accelerometer, made dimensionless by the incident wave amplitude ζ_a. The results highlights the fact that the accelerometer has a vertical heave response that nearly exactly follows the incident wave, even though it is exposed to a higher acceleration for the steepest wave.

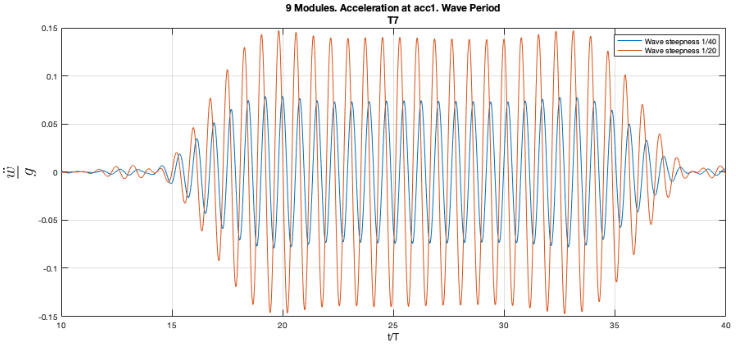

Figur 5.5: 1st order filtered acceleration *acc1* for wave steepness $H/\lambda = 1/40, 1/20$ made non-dimensional by the gravitational constant g, plotted in dimensionless time t/T. Where T is the wave period for the respective measurement.

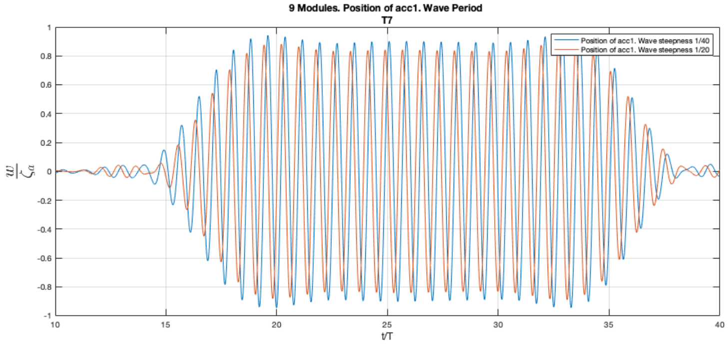

Figur 5.6: Calculated position of the 1st order filtered accelerometer *acc1* for wave steepness $H/\lambda 1/40, 1/20$, made non-dimensional by the incident wave amplitude ζ_a, plotted in dimensionless time t/T. Where T is the wave period for the respective measurement.

5.2.1 Accelerometer Positions to Heave & Pitch Response

The accelerometer positions yields a mathematically calculated vertical response at the instrument's position for a specific order. The continuing example still shows the 1st order band-pass filtered and numerically integrated accelerations, however, this procedure naturally contains possible numerical errors. This effect is carried on when combining accelerometer positions to calculate the respective body's heave and pitch response. The accelerometer positions ω on the first body, i.e. the corresponding positions of *acc1* and *acc2*, are shown in *Figure 5.7* below.

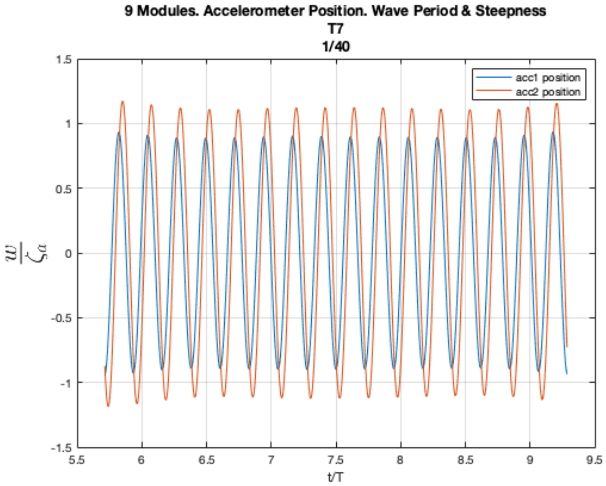

Figur 5.7: Calculated position of the 1st order filtered accelerometers *acc1* and *acc2*, plotted in dimensionless time t/T and position by the incident wave amplitude ζ_a

Next, the calculated heave and pitch response from these positions are shown in *Figure 5.8*.

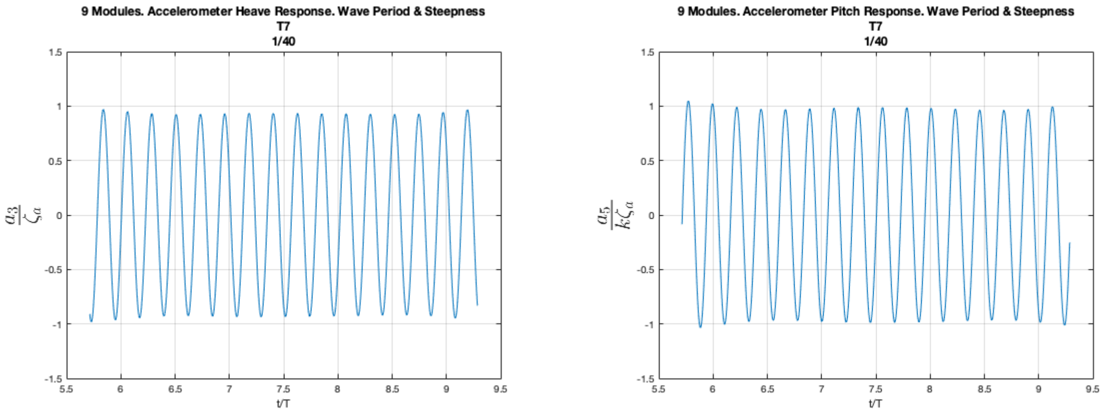

Figur 5.8: Calculated heave response (left) and pitch response (right) for the first body, from the 1st order filtered accelerometers *acc1* and *acc2*. Plotted in dimensionless time t/T and in position by the incident wave amplitude ζ_a and wave-number k.

The heave response is acquired by using the average of the two accelerometers throughout the time-series. This method is justified by symmetry of the instrumentation and the structure. The pitch response is found by using trigonometry, as the output is in degrees, just like for the motion capture output. The magnitudes of the two positions at a specific time combined with the distance between the accelerometers, yields a mathematical expression to obtain the angle. Keeping the same positive rotation as the motion capture. Hence, the method of getting the corresponding body heave a_3 and pitch a_5 response from the accelerometers for a single instrumented body is found by the following expressions.

$$a_3^{t_n} = \frac{\text{pos}1^{t_n} + \text{pos}2^{t_n}}{2} \qquad a_5^{t_n} = \arcsin\Big(\frac{\text{pos}1^{t_n} - \text{pos}2^{t_n}}{2l_a}\Big)$$

where t_n is the current time-step, and l_a the distance from the accelerometer to the horizontal centre of gravity. The output is in meters and degrees. The expression consequently gives a translatory and rotational reference at the horizontal CoG at the top plate of the model. This is inconsistent with the motion capture system which, especially with rotational response, has a different reference frame. However, the vertical CoG reference frame, which is 2.44 meters from the bottom in full scale, is only approximately 0.5 meters away from this frame. This magnitude is not sufficient to compromise the calculated RAOs, but must be kept in mind.

5.3 Case 1: Single Module

5.3.1 Vertical Response Amplitude Operators

The wave-induced vertical response of the models were measured by motion capture markers and by accelerometers. For the single module model, this instrumentation captured a complete measurement of the structure response. Results based on the first order motion capture (Oqus) and accelerometer positions in terms of the incident wave measured at *wave* are presented here. This wave-probe is just for the calculations in both case 1 and 2.

Heave RAO

The motion captured response and combined positions of the accelerometer positions in heave, $\eta_3^{(1\omega)}$ and $a_3^{(1\omega)}$ respectively, resulted in a 1st order RAO shown for every wave-steepness in *Figure 5.9*.

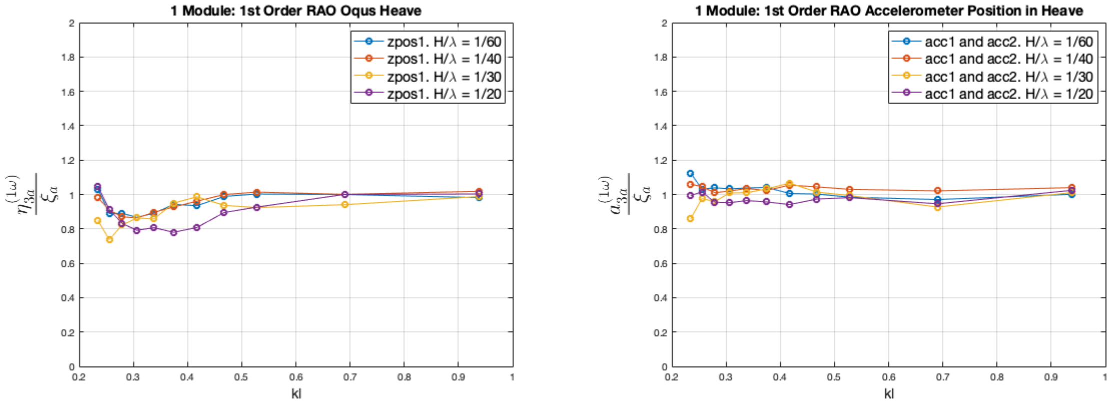

Figur 5.9: Single module model 1st order heave RAO, for the case 1 regular wave series, showing the motion capture 1st order RAO (left) and the combined accelerometer positions 1st order RAO (right). Both made non-dimensional by the incident wave amplitude ζ_a, plotted against the dimensionless wave-number kl.

In general, there is good agreement between the calculated RAOs. For both instruments and every wave steepness, the module seems to follow the incident wave for $kl > 0.7$, which corresponds to a full-scale wave-period $T < 7$s. For lower kl, the module has a lower vertical response than the incident wave, which also become more distinct for $H/\lambda = 1/20$, consequently experiencing loss in air-gap. However, this loss is not large enough to create water impact effects on the top frame. This observation is also smaller when examining the 1st order combined accelerometer positions, where it suggests a better hydrodynamic ability to follow the longer waves. This suggests that the measured acceleration of these waves are smaller than the motion capture. For $H/\lambda = 1/30$, both plots show a deviation from the general trend at $T = 11.5$s, and $T = 12$s. An odd observation when comparing to the waves generated at $H/\lambda = 1/20$. Moreover, this deviation is quite small, and does not compromise the general results, which is good hydrodynamic flexibility.

Pitch RAO

Figure 5.10 shows the motion capture and combined positions of the accelerometer positions in pitch, $\eta_5^{(1\omega)}$ and $a_5^{(1\omega)}$ respectively. The measurements were transformed to radians prior to calculation.

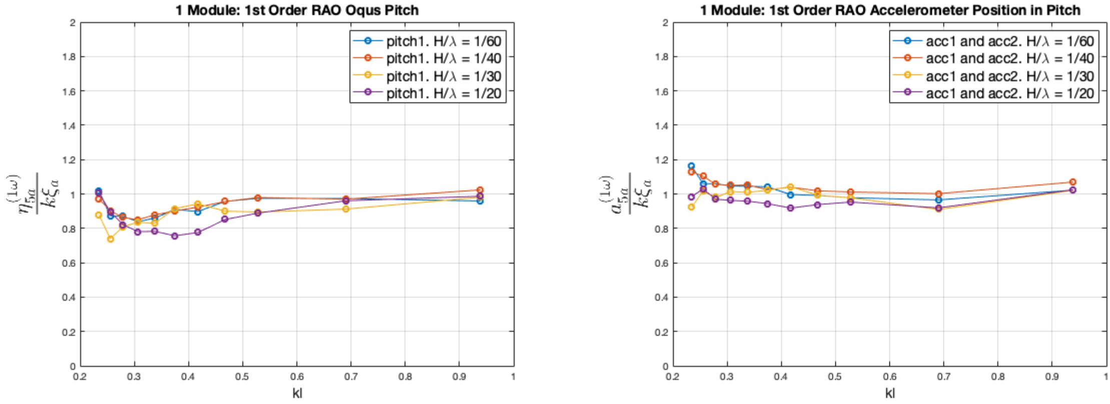

Figur 5.10: Single module model 1st order pitch RAO, for the case 1 regular wave series. The motion capture 1st order RAO (left) and the combined accelerometer positions 1st order RAO (right). Both made non-dimensional by the incident wave amplitude and wave-number $k\zeta_a$, plotted against the dimensionless wave-number kl.

When acquiring the 1st order RAO in pitch by the two different instruments, the result is similar to the RAO in heave described above. Within the same intervals of different wave-periods, there is a good ability to follow the incident waves. In contrast to the heave response, a slightly larger spread occurs here. However this is not significant when evaluating the wave-structure interaction, but it indicates the structures tendency to be more influenced by the wave-steepness when it comes to rotational response. In addition, the indicated increase at the lowest kl numbers could suggest that even larger waves with a period $T > 12$s could be approaching a wave-series containing some level of resonance. Although this is beyond the intended operational criteria for the concept. The same conclusions for heave and pitch in case 1 can be drawn, as no indications of resonance and good ability to follow the incident waves are present for these kl wave-series. Moreover, it seems that the accelerometers have a tendency to predict higher response in both DOF.

5.3.2 Investigation of Harmonics

In order to compare the magnitudes of the harmonic accelerations, the mean values of the steady-state amplitudes for each wave-series are presented here. The 1st, 2nd and 3rd order accelerations $\ddot{\omega}^{(1\omega)}$, $\ddot{\omega}^{(2\omega)}$, $\ddot{\omega}^{(3\omega)}$ are made non-dimension by g, and are plotted against the non-dimensional wave-number kl. These measurements naturally occurs at the positions of the accelerometers. The 1st order harmonic acceleration will represent the linear wave-excitation forces, while the other two revealing the magnitudes of higher order acceleration effects. The most important being viscous effects, which is the 3rd order harmonic component (Kristiansen, 2019). This excitation is labeled as a Morrison effect.

1st Harmonic Acceleration

Figure 5.11 shows the 1st harmonic accelerations for every wave-steepness.

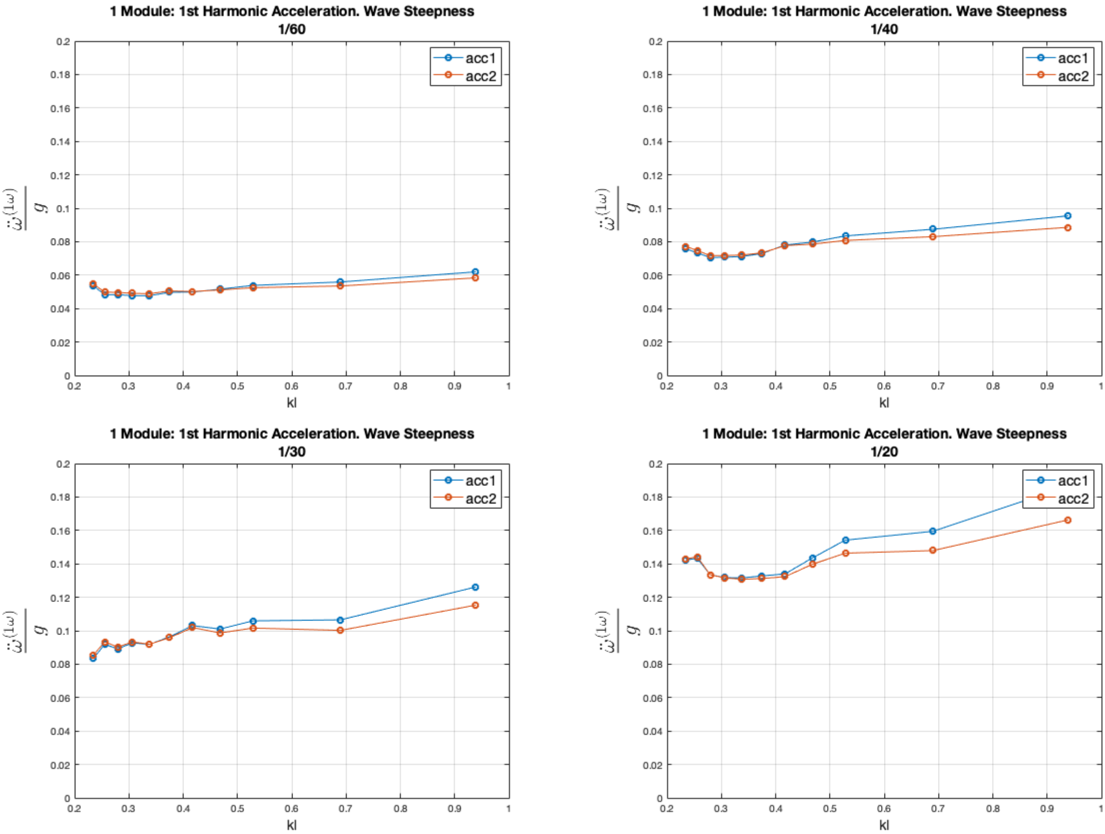

Figur 5.11: Measured 1st harmonic accelerations, $\ddot{\omega}^{(1\omega)}$, at the different accelerometers for each wave-series for every H/λ. Made non-dimensional by the gravity g and plotted against the non-dimensional wave-number kl.

This acceleration generally increases with increasing wave-steepness, and the foremost *acc1* has the greatest magnitude when the two measurements deviate at shorter wave periods, indicating energy dissipation through the module during excitation. With increasing wave-number, both harmonic accelerations increases, where this increase becomes greater when the wave is steeper. Both ends have mooring, but a greater force seems to be experienced in the front. Hence, the wave-entry excites the structure with a higher amount of energy. This effect is expected to change or become more significant with two or more articulated modules.

2nd Harmonic Acceleration

Figure 5.12 shows the 2nd harmonic acceleration, $\ddot{\omega}^{(2\omega)}$, at the the positions of *acc1* and *acc2*. As expected, this harmonic acceleration is much lower that the 1st harmonic. Naturally as the linear wave-excitation is the dominant source of structural loads. The general trend occurs here as well, being and increase in magnitude with increased wave-steepness. The plotted lines are slightly more inconsistent for each steepness, but the 2nd order effect is assumed to contain larger numerical errors through band-pass filter and small measured values. Which could be an influence on the resulting plots. However, in contrast to 1st harmonic, the deviation between the two accelerometers is now shifted, except when $H/\lambda = 1/20$. Where the fore-most accelerometer *acc1* has lower values for $kl > 0.4$.

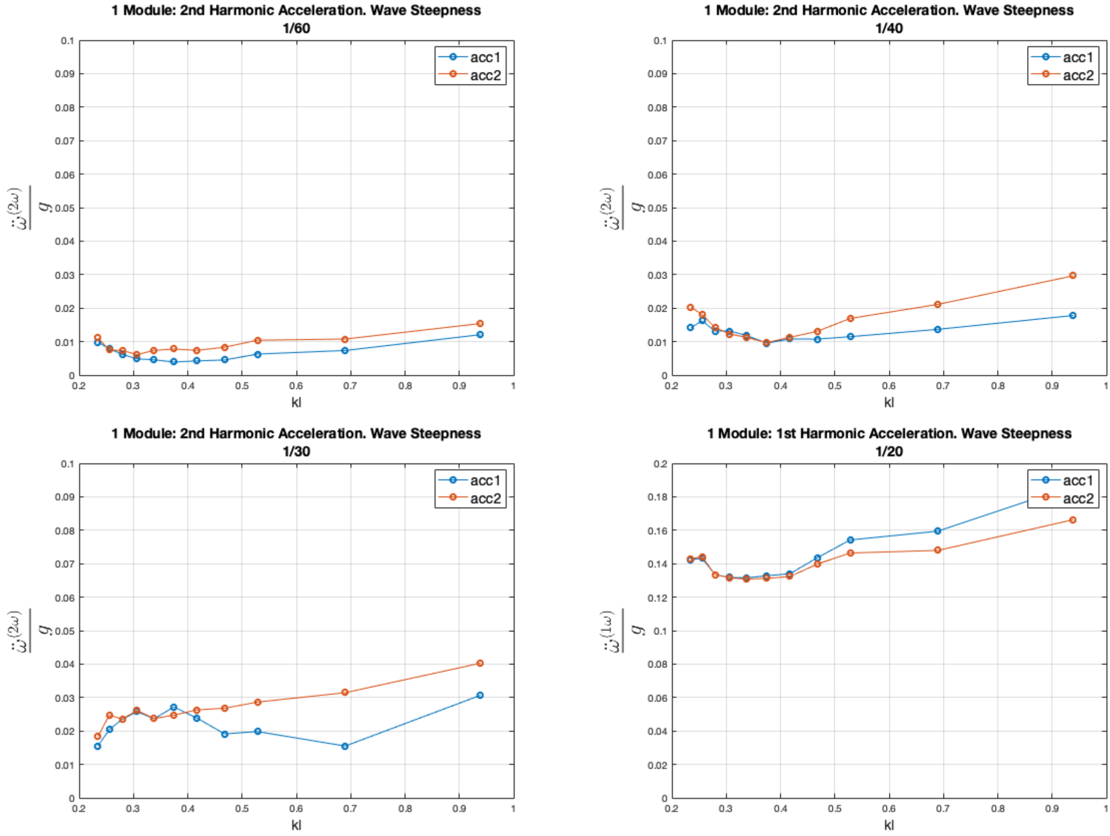
1 Module: 2nd Harmonic Acceleration. Wave Steepness 1/60

1 Module: 2nd Harmonic Acceleration. Wave Steepness 1/40

1 Module: 2nd Harmonic Acceleration. Wave Steepness 1/30

1 Module: 1st Harmonic Acceleration. Wave Steepness 1/20

Figur 5.12: Measured 2nd harmonic accelerations, $\ddot{\omega}^{(2\omega)}$, at the different accelerometers for each wave-series for every H/λ. Made non-dimensional by the gravity g and plotted against the non-dimensional wave-number kl.

This result suggests that, in general, 2nd order effects become larger with increasing steepness and shorter wave-periods, which seems reasonable. When the two accelerometers deviates in magnitude, the largest acceleration is located at the back-end of the module, i.e. at the wave-exit. In addition, this result is changed for $H/\lambda = 1/20$, as mentioned above. For this steepness, the magnitude of the acceleration is much larger than the relative increase in wave-steepness that is measured for both 1st and 2nd harmonics.

3rd Harmonic Acceleration

The measured 3rd harmonic acceleration, $\ddot{\omega}^{(3\omega)}$, is shown in *Figure 5.13*. For $H/\lambda = 1/60$ and $H/\lambda = 1/40$, the magnitude seems to be nearly identical. The general magnitude of this harmonic acceleration is also in the vicinity of the 2nd harmonic acceleration. A deviation between the two accelerometers develops for $H/\lambda = 1/30$, with a general higher magnitude at the fore-most accelerometer for $kl < 0.7$, before it shifts.

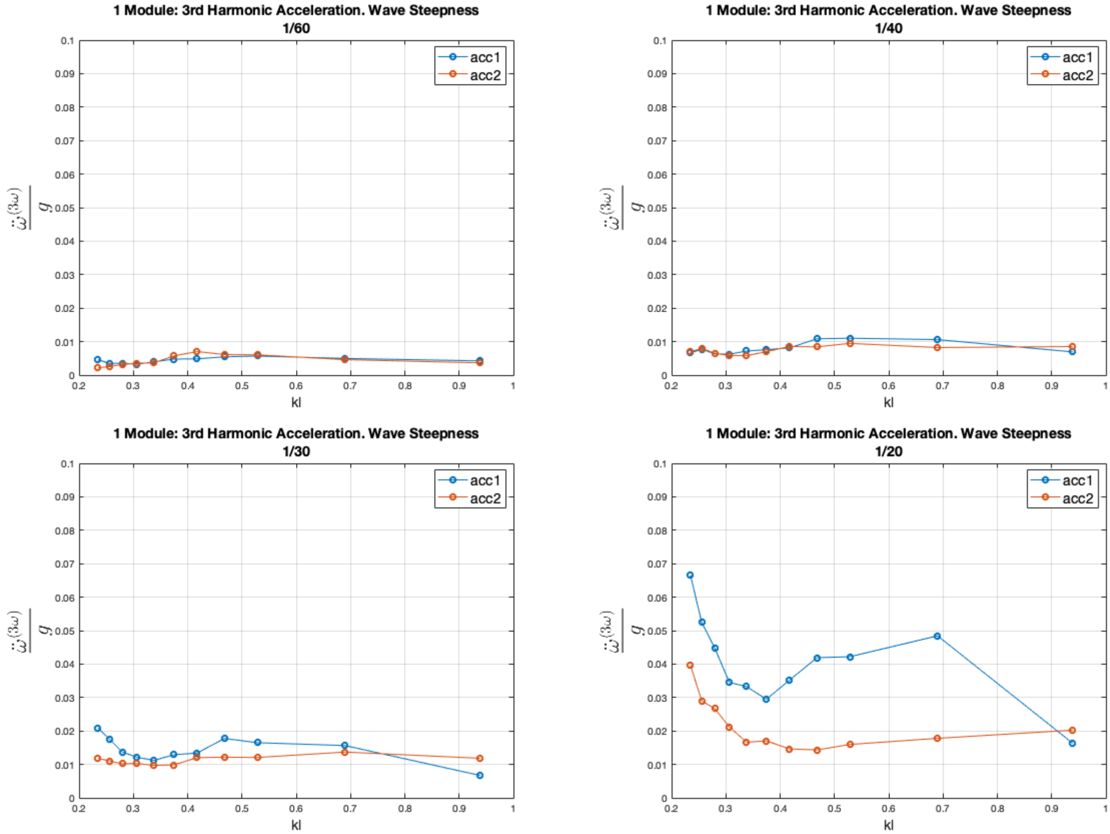

Figur 5.13: Measured 3rd harmonic accelerations, $\ddot{\omega}^{(3\omega)}$, at the different accelerometers for each wave-series for every H/λ. Made non-dimensional by the gravity g and plotted against the non-dimensional wave-number kl.

For $H/\lambda = 1/20$, the magnitude suddenly and rapidly increases overall, expect for the back-end at $kl > 0.4$, where it becomes more consistent with the other steepnesses. *acc1* has a quite large increase, which would physically suggest a rapid increase in viscous excitation. When correlating this increase with the heave and pitch RAO showed in *Figure 5.9* and *Figure 5.10*, where $H/\lambda = 1/20$ has a significant drop and could indicate more submergence of the floaters, one can argue that viscous effects will become quite much larger than for the other steepnesses with the same referral. Where this loss in air-gap will be most vital at the wave-entry, as this point will carry and transfer motion to the stiff structure. Consequently possibly result in less air-gap loss at the wave-exit point.

5.4 Case 2: Two Articulated Modules

5.4.1 Vertical Response Amplitude Operators

The wave-induced vertical response of the case 2 model was measured by motion capture markers and by accelerometers. Similarly as case 1, but with twice the number of instruments. RAOs based on the first order motion capture (Oqus) and combined accelerometer positions are presented here.

Heave RAO

The motion captured response and combined positions of the accelerometer positions in heave, $\eta_3^{(1\omega)}$ and $a_3^{(1\omega)}$, has resulting RAOs as shown in *Figure 5.14*. In general, there is some agreement between the two, but again, the accelerometer positions gives an overall higher measurement. Especially for $kl < 0.7$, although the largest difference occurs at $kl < 0.4$ for $H/\lambda = 1/20$. However, the general trend shows that the model has a moderately good ability to follow the incident wave for these kl as with case 1. The plots reveal an indication of a generally lower response operator for the second module, but this is not consistent for every wave-steepness.

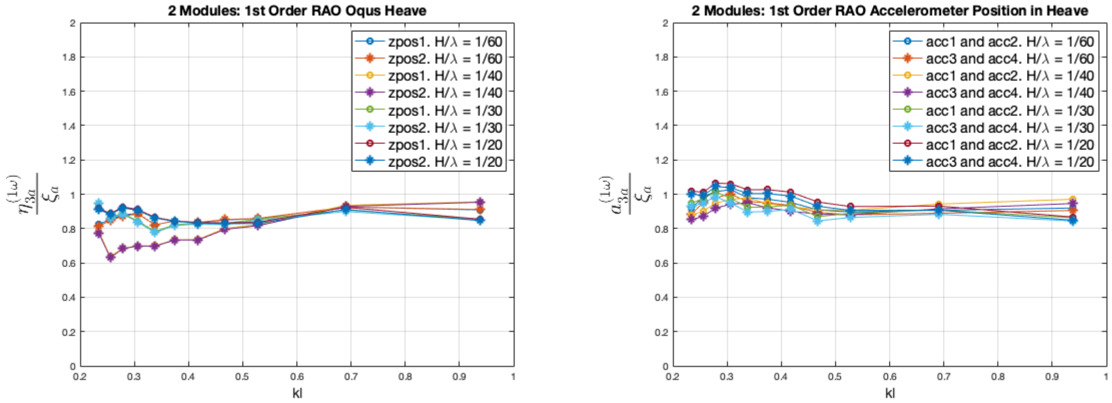

Figur 5.14: Two modules model, 1st order heave RAO, for the case 2 regular wave series. The motion capture 1st order RAO (left), and the combined accelerometer positions 1st order RAO (right). Both made non-dimensional by the incident wave amplitude ζ_a, plotted against the dimensionless wave-number kl.

Pitch RAO

The motion captured response and combined accelerometer positions in pitch, $\eta_5^{(1\omega)}$ and $a_5^{(1\omega)}$ respectively, had a 1st order RAO result as shown in *Figure 5.15*. Again, general agreement for the two differently acquired RAOs, where the overall deviation occurs as in heave for at the same kl, and moderately good ability to follow the incident wave. More consistently, however, a stronger indication of larger pitch responses occur at the second body. This difference in magnitude is a factor of approximately 0.15 for $H/\lambda = 1/30$. The difference is still present for the less steep waves, but the factor is decreased to approximately 0.1.

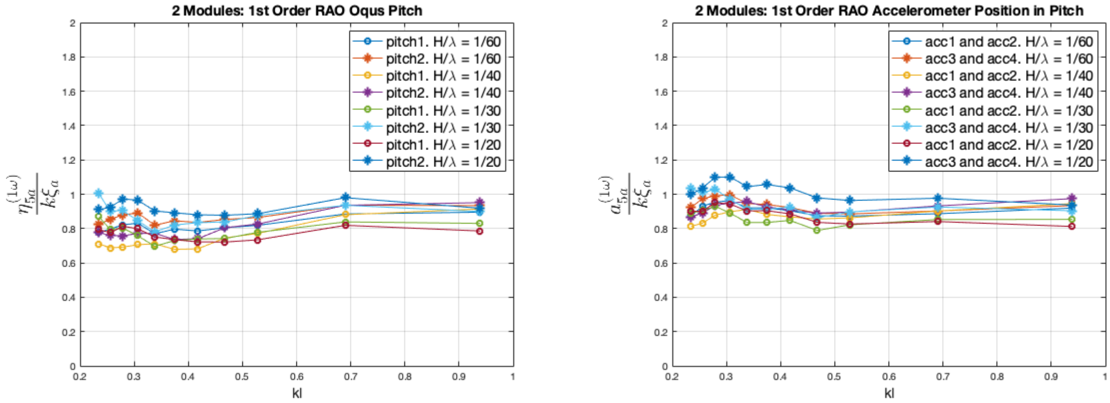

Figur 5.15: Two modules model, 1st order pitch RAO, for the case 2 regular wave series. The motion capture 1st order RAO (left), and the combined accelerometer positions 1st order RAO (right). Both made non-dimensional by the incident wave amplitude and wavenumber $k\zeta_a$, plotted against the dimensionless wave-number kl.

5.4.2 Investigation of Harmonics

Just as in case 1, in order to compare the magnitudes of the harmonic accelerations, the mean values of the steady-state amplitudes for each wave-series are presented here.

1st Harmonic Acceleration

Figure 5.16 below shows the 1st harmonic accelerations for every wave-steepness at all accelerometers. As in case 1, This acceleration generally increases with increasing wave-steepness. The accelerometer positioned at the front and back of the model, *acc1* and *acc4*, has the greatest magnitude when the measurements deviate from each other at $kl > 0.5$. A similar observation to case 1. Throughout the wave-series, with increasing wave-number, all harmonic accelerations increase, where this increase becomes greater when the wave is steeper.

Largest accelerations are observed at the ends. When evaluating this difference between the models global ends, it is expected that an articulated structure of several models will have a "whippingeffect as the energy propagates through the length. A result supporting the fact that there could be a possibility of a general where larger accelerations occur at the global ends. This effect was expected to become more significant from case 1.

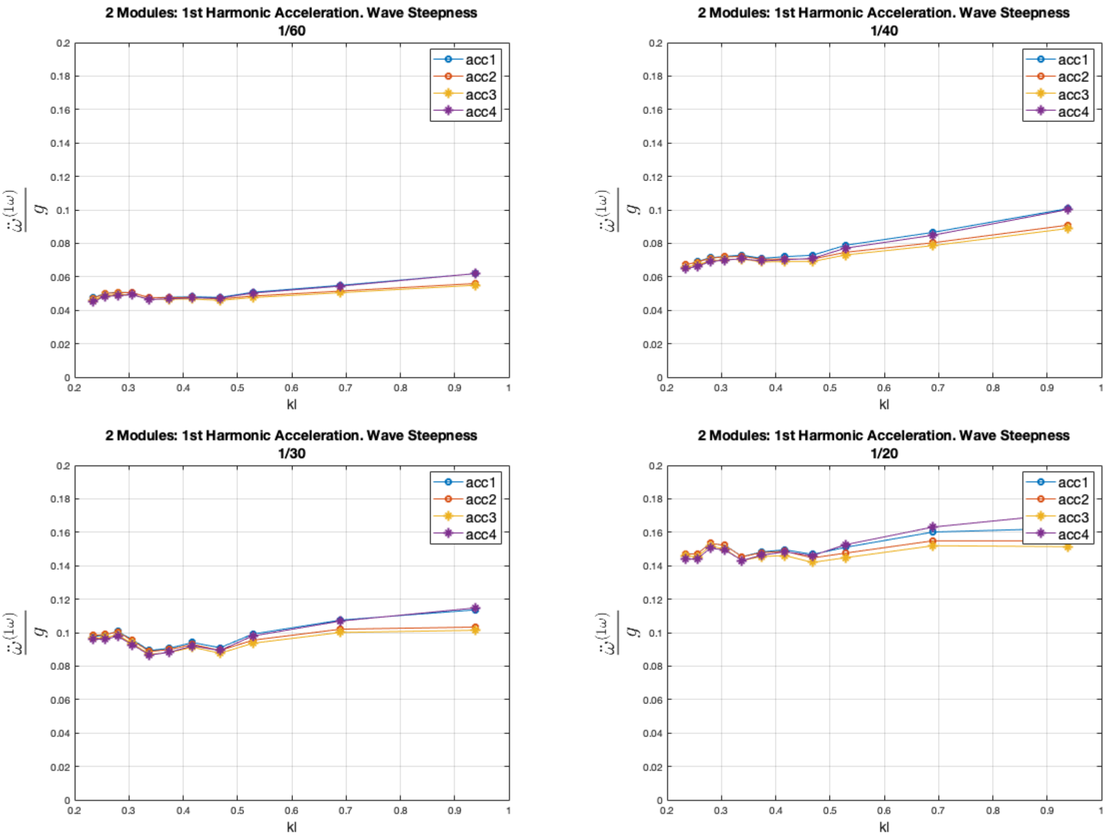

Figur 5.16: Measured 1st harmonic accelerations, $\ddot{\omega}^{(1\omega)}$, at the different accelerometers for each wave-series for every H/λ. Made non-dimensional by the gravity g and plotted against the non-dimensional wave-number kl.

2nd Harmonic Acceleration

Figure 5.17 shows the 2nd harmonic accelerations, $\ddot{\omega}^{(2\omega)}$, at *acc1*, *acc2*, *acc3* and *acc4*. As expected, and as in case 1, this harmonic acceleration is much lower that the 1st harmonic acceleration shown in *Figure 5.16*. The general trend occurs here as well, being and increase in magnitude with increased steepness, but a generally larger deviation between the accelerometers is present.

Again, the first and last accelerometer have the larger magnitudes for all wave-series, and the result for $H/\lambda = 1/20$ is quite different. Here, the deviation between the instruments are relatively small, but the overall magnitude has been given a significant relative increase. The plot for $H/\lambda = 1/30$ has a much higher acceleration at the final accelerometer *acc4*. For all plots, the largest acceleration occurs at this point, and generally showing the least acceleration at the second accelerometer, i.e. the back of the first module.

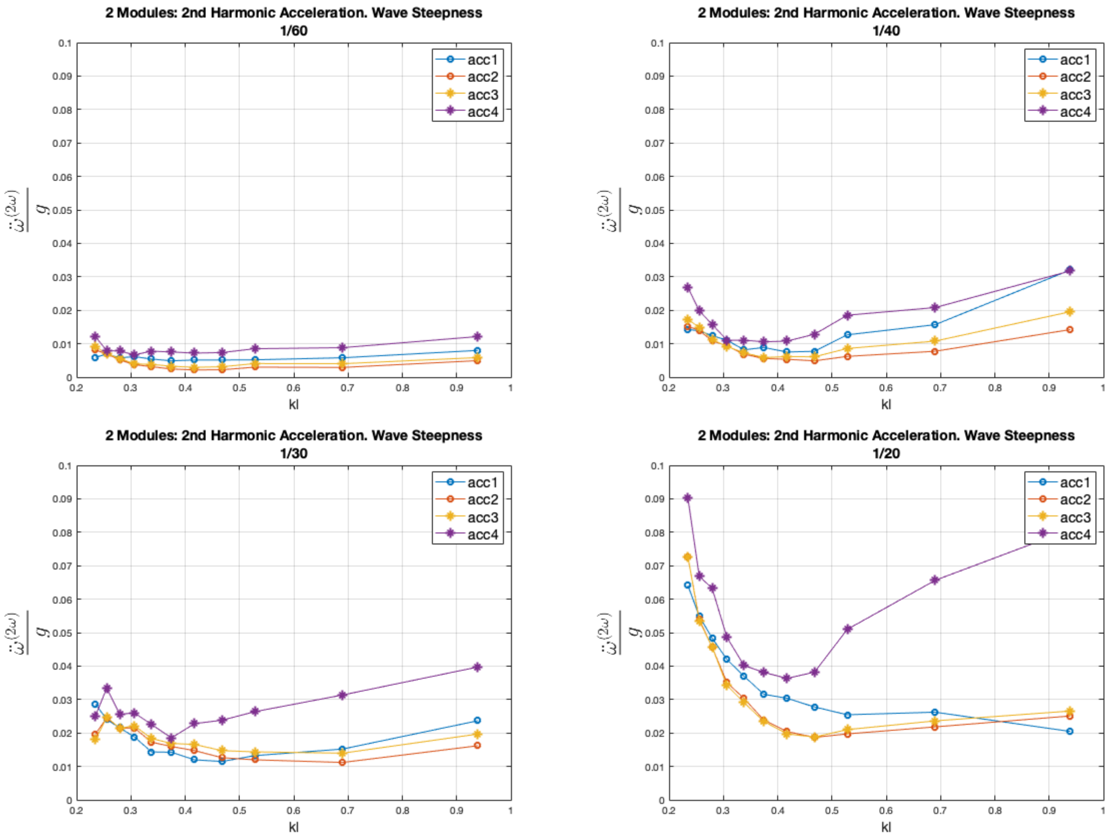

Figur 5.17: Measured 2nd harmonic accelerations, $\ddot{\omega}^{(2\omega)}$, at the different accelerometers for each wave-series for every H/λ. Made non-dimensional by the gravity g and plotted against the non-dimensional wave-number kl.

3rd Harmonic Acceleration

Figure 5.18 shows the 3rd harmonic acceleration, $\ddot{\omega}^{(3\omega)}$, at *acc1*, *acc2*, *acc3* and *acc4* accelerometers. Again, similarities to case 1 occurs, but the deviation and general increase in acceleration magnitude is higher for the two steepest wave-series.

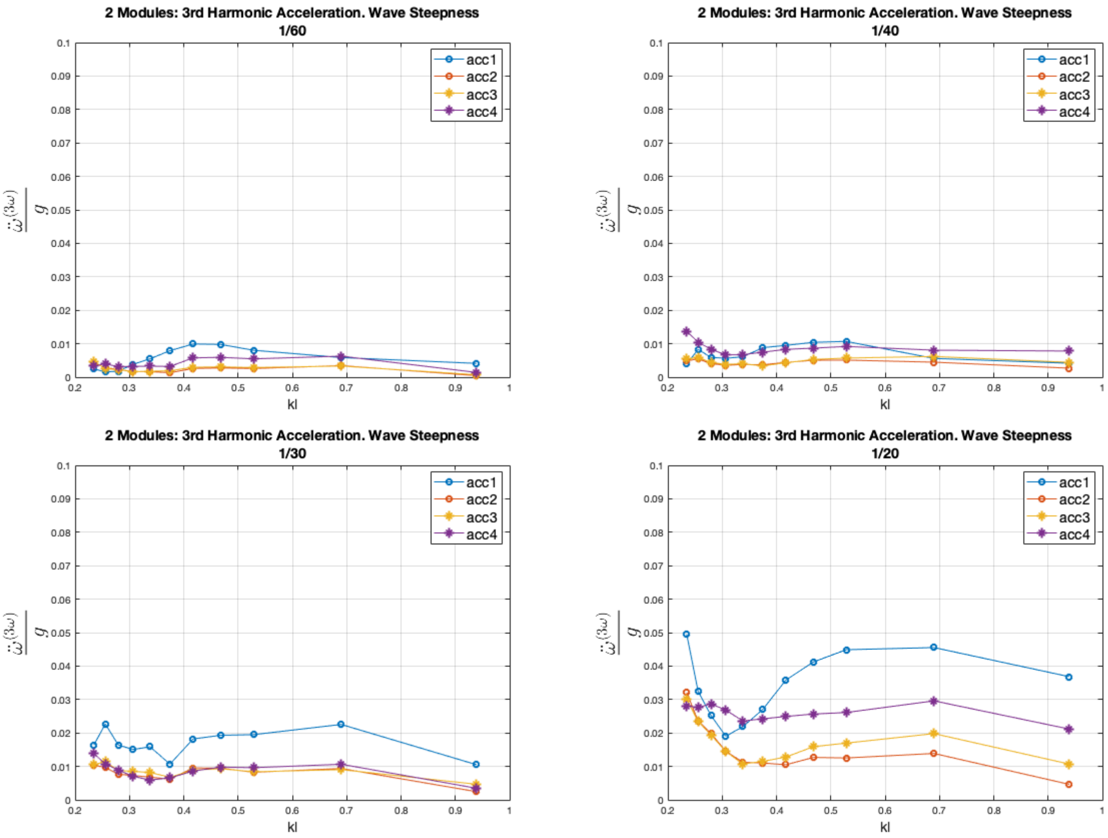

Figur 5.18: Measured 3rd harmonic accelerations, $\ddot{\omega}^{(3\omega)}$, at the different accelerometers for each wave-series for every H/λ. Made non-dimensional by the gravity g and plotted against the non-dimensional wave-number kl.

5.5 Case 3: Nine Articulated Modules

Now, it is worth to repeat that the case 3 wave-series are an expansion of the previous ones, containing a larger wave period range. However, the wave-maker experienced problems generating the high-frequency waves. Some measurements revealed presence of unstable waves, and these are listed in *Table 5.1*. An example of the event is shown in *Figure 5.19*. The time-series for the wave-probe and its corresponding spectrum for all these HF generated waves, whereas some are unstable, are shown in *Appendix H*.

Wave Period T [s]	Wave Steepness H/λ
2.0	1/30, 1/20
2.5	1/30, 1/20
3.0	1/20

Tabell 5.1: Unstable generated waves for the case 3 wave-series. Full-scale values.

Therefore, care must be taken with the wave-series for $T = [2, 2.5, 3]$ [s], corresponding to the three highest kl numbers. This naturally influences the measurements, but also filtering and calculations of statistical properties. Especially accelerations, due to higher sampling rate and sensitivity. However, the results are kept in the RAOs and harmonic accelerations to give some indication of the dynamic response.

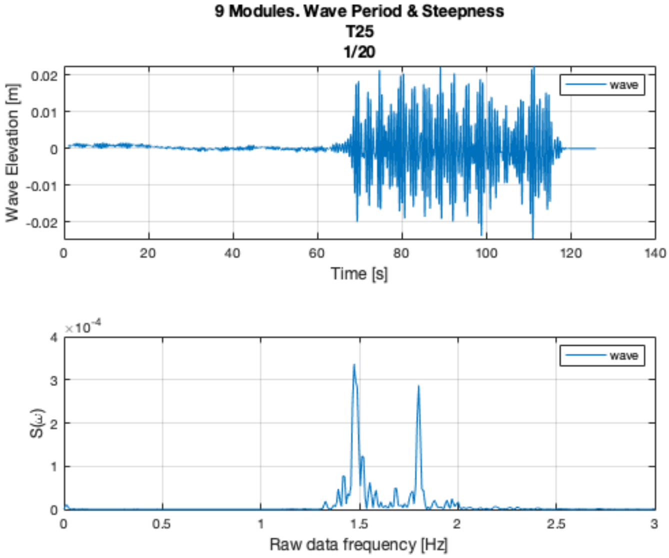

Figur 5.19: Example of unstable regular wave-field measurement of the generated incident waves with wave period $T = 2.5$s and steepness $H/\lambda = 1/20$.

5.5.1 Vertical Response Amplitude Operators

The wave-induced vertical response of the model for case 3 had instrumentation, as mentioned, on the first, middle, and last module of the articulated row. Results based on the first order motion capture (Oqus) and accelerometer positions are presented here.

Heave RAO

The heave RAO obtained from the motion capture measurements is shown in *Figure 5.20*. As before, the result is obtained by using the mean amplitude of the steady-state measurements, whereas wave-probe *wp4* is used to ensure reached steady-state for all modules.

The same RAO is obtained, as before, by plotting the combined positions of the accelerometers at each of the three measured bodies. This RAO is presented in *Figure 5.21*.

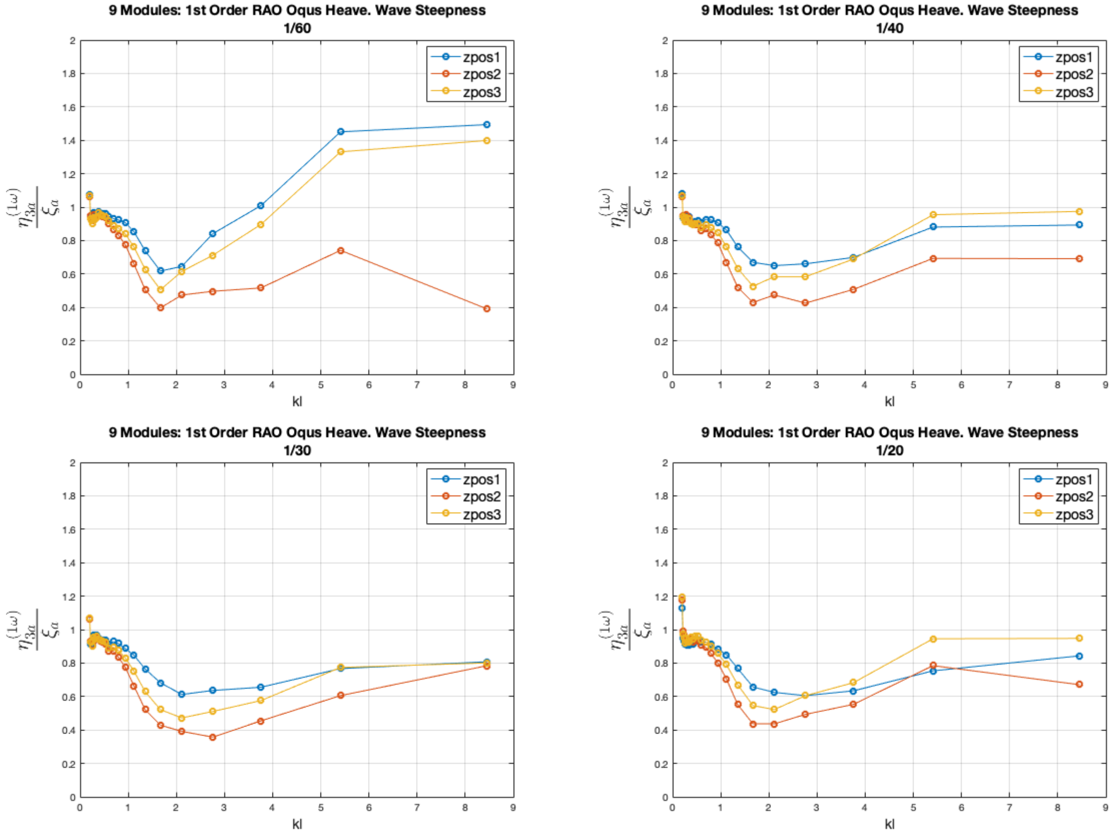

Figur 5.20: Nine modules model, 1st order motion capture heave RAO, for the case 3 regular wave series. Made non-dimensional by the incident wave amplitude ζ_a, plotted against the dimensionless wave-number kl.

The results suggests that the heave response has an acceptable ability to follow the incident wave for $kl < 0.5$, just like in the previous cases. However, at the lowest kl numbers, which corresponds to a wave period of $T = 13$s and $T = 12.5$s, there is a peak that is present for every wave steepness. However, the value itself is not particularly significant for the structures' hydrodynamic handling. Furthermore, for $0.5 < kl < 5$, corresponding to a wave-period interval of about $T = [3, 12]$ the RAO has a through that contains it lowest values. Where the lowest value, as by general trend, is for the middle module.

At the highest kl numbers, which corresponds to a wave period of $T = 2$s, it was somewhat expected that a higher heave response would be present. This characteristic yields a wave-length that is approximately half the length of a single module. When this happens, due to the periodic excitation, the incident wave will wave-crests at approximately each floater of each module. This will intuitively yield higher response. However, only $H/\lambda = 1/60$ suggests this event for the first and last module.

With an increasing wave-steepness, the general trend in terms of RAO development and magnitude stays almost the same. The largest deviation exists for $H/\lambda = 1/60$ as argued above.

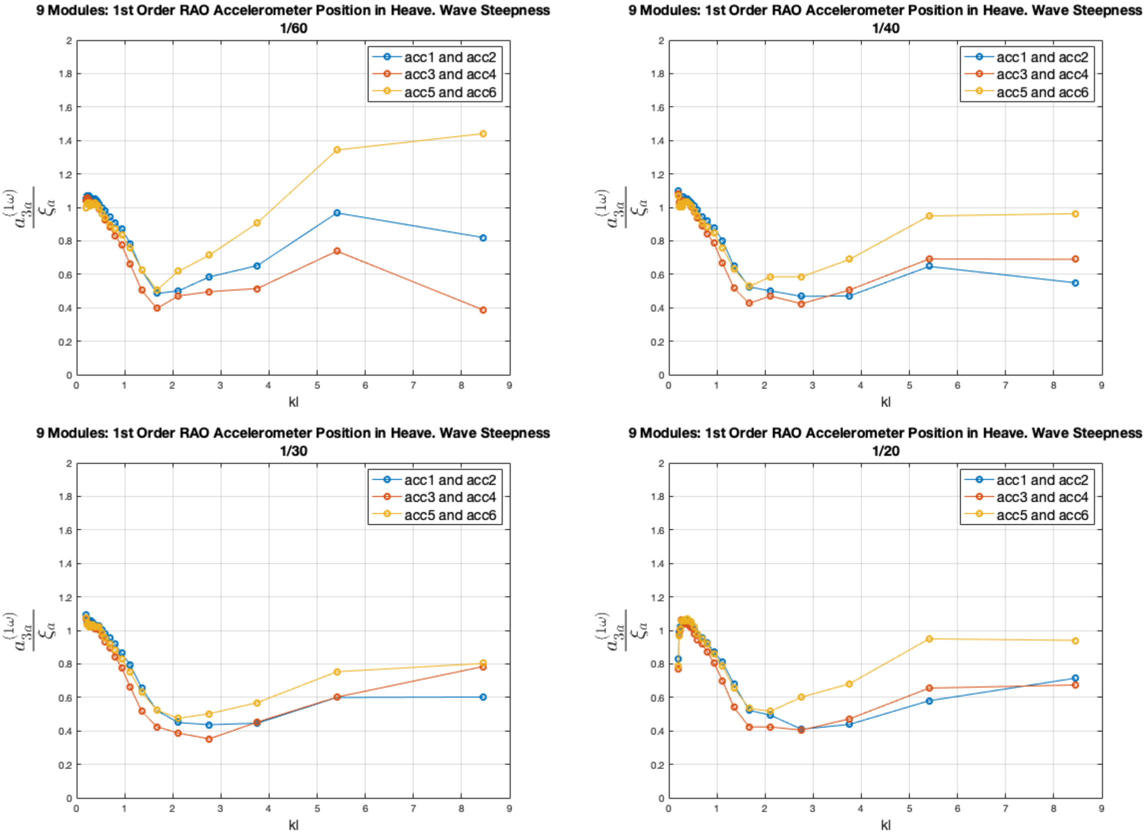

Figur 5.21: Nine modules model, 1st order combined accelerometer positions for heave RAO, for the case 3 regular wave series. Made non-dimensional by the incident wave amplitude ζ_a, plotted against the dimensionless wave-number kl.

The RAO aqcuired by motion capture and by accelerometer positions are in good agreement. The smaller peaks at the lowest kl numbers are not present in the latter result. However for $H/\lambda = 1/20$ at the lowest kl corresponding to $T = 13$s, there is a sudden drop for. By observation of this test run, the first and last module experienced over-topping. Furthermore, the general same trend and magnitude exists for all $kl < 5$, but for higher wave-numbers there is a shift between which of the bodies that have the highest response and some change in magnitude.

In review, the heave regular RAOs and observations of the tests, indicates no disadvantage for the hydrodynamic response of the structure for the case 3 wave-series, but for $H/\lambda = 1/20$ at $T = 13$s over-topping occurred. Standing as the only critical event for the regular wave-tests.

Pitch RAO

Figure 5.22 shows the resulting RAO for motion-capture measured pitch response. The same result is again produced by combining the accelerometer positions, shown in *Figure 5.23*.

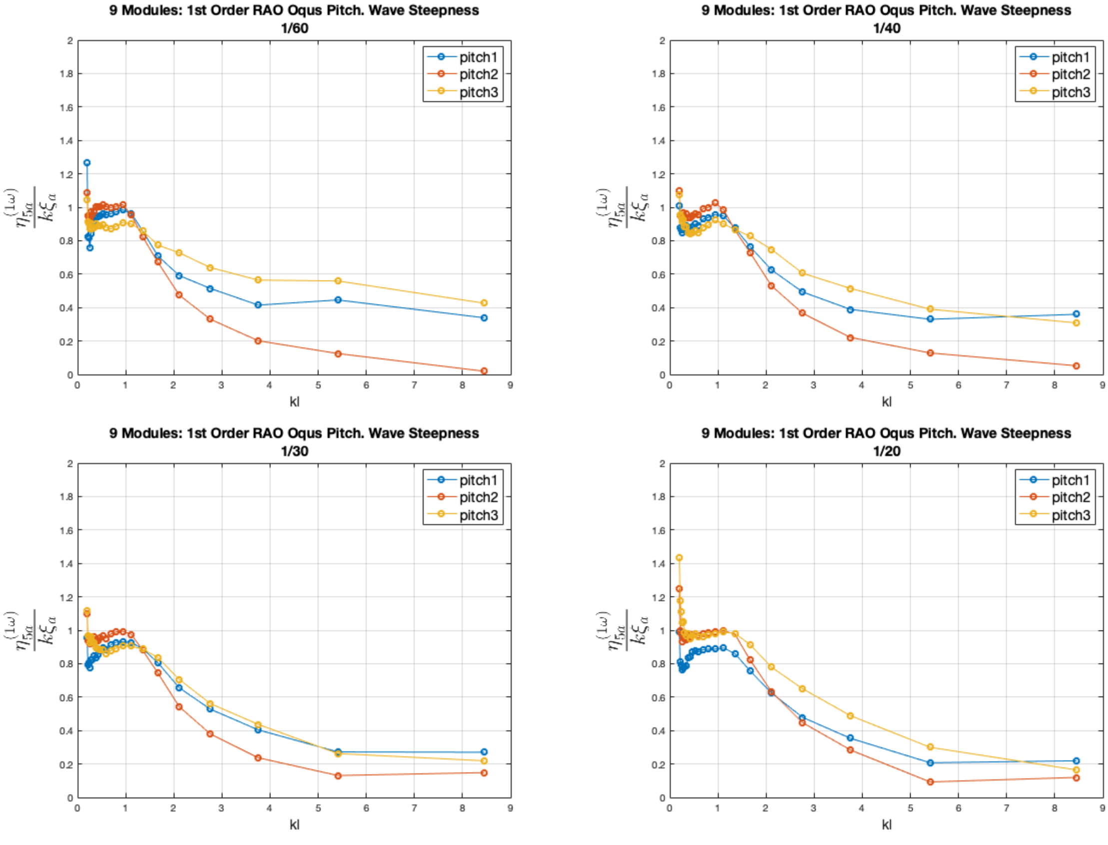

Figur 5.22: Nine modules model, 1st order motion capture pitch RAO, for the case 3 regular wave series. Made non-dimensional by the incident wave amplitude and wave-number $k\zeta_a$, plotted against the dimensionless wave-number kl.

The previously mentioned over-topping of the first module at the lowest kl number can be seen for both RAOs, but the motion capture measurements does not seem to capture this extent. Here, a noticeable difference between the two methods exists, where the motion capture predicts a lower response at the first module. The accelerations on the other hand indicate increase in response for both the first and last module, which is more likely. However, the accelerations predicts this large responses for all H/λ. Although, a quite consistent trend of higher response at the first and last module is present, as it was in heave.

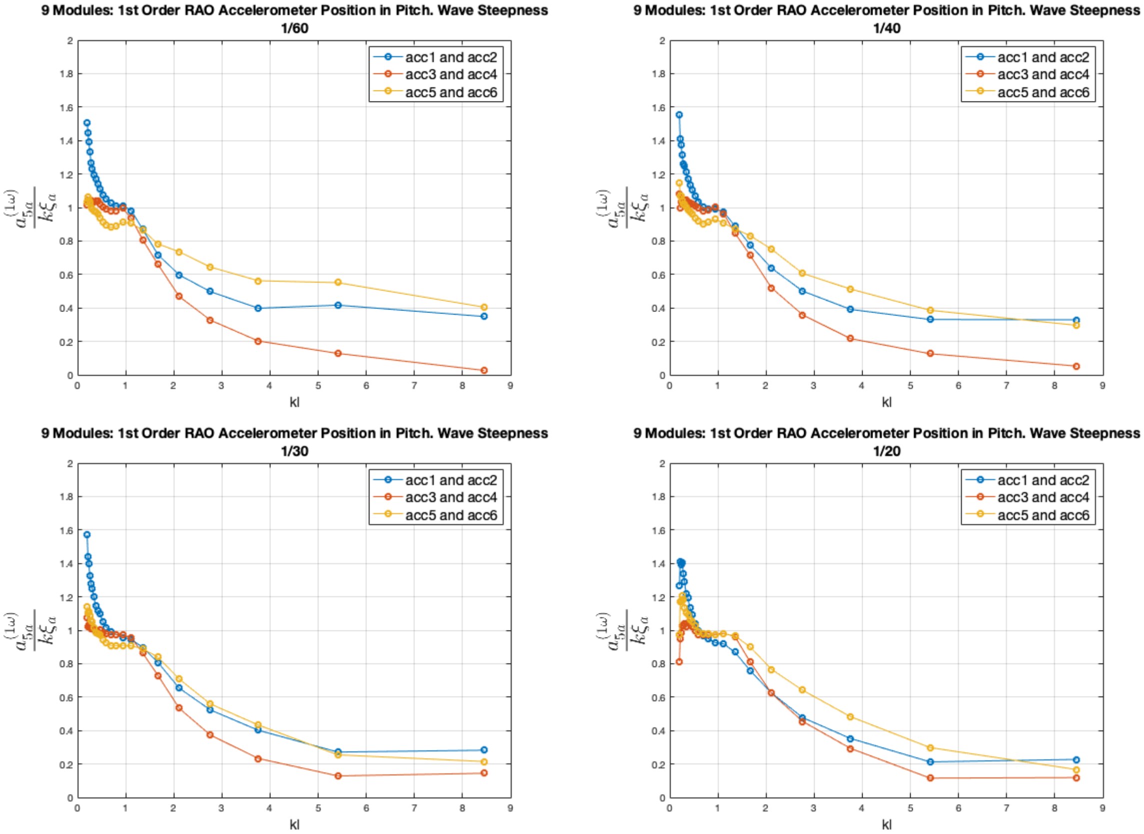

Figur 5.23: Nine modules model, 1st order combined accelerometer positions for pitch RAO, for the case 3 regular wave series. Made non-dimensional by the incident wave amplitude and wave-number $k\zeta_a$, plotted against the dimensionless wave-number kl.

5.5.2 Investigation of Harmonics

As in the previous cases, in order to compare the magnitudes of the harmonic accelerations, the mean values of the steady-state amplitudes for each wave-series are presented here.

1st Harmonic Acceleration

The 1st harmonic acceleration is shown in *Figure 5.24*. The result indicates that significant changes and development of the harmonic acceleration occurs when $kl < 1$ and becomes $kl > 1$. In the former case, there is less spread over the different accelerometers in terms of magnitude. However, the first body, i.e. *acc1* and *acc2*, both have the largest and lowest magnitude in acceleration. The highest acceleration occurs at the back end of the first module, and the lowest at the front end of the same module.

When $kl > 1$, the general result is that the highest acceleration occurs at the very end of the model, i.e. at *acc6* positioned at the back end of the last module. This accelerometer is then in magnitude followed by *acc1*. This could indicate a "whippingeffect, as discussed in case 2 above. Furthermore, the lowest acceleration occurs at the front end of the last module. The steady decrease throughout the model shows that the front of the model, which has the next to largest acceleration, is followed by its next accelerometer and so on. Suggesting a steady decrease in acceleration from front to end, except at the final one.

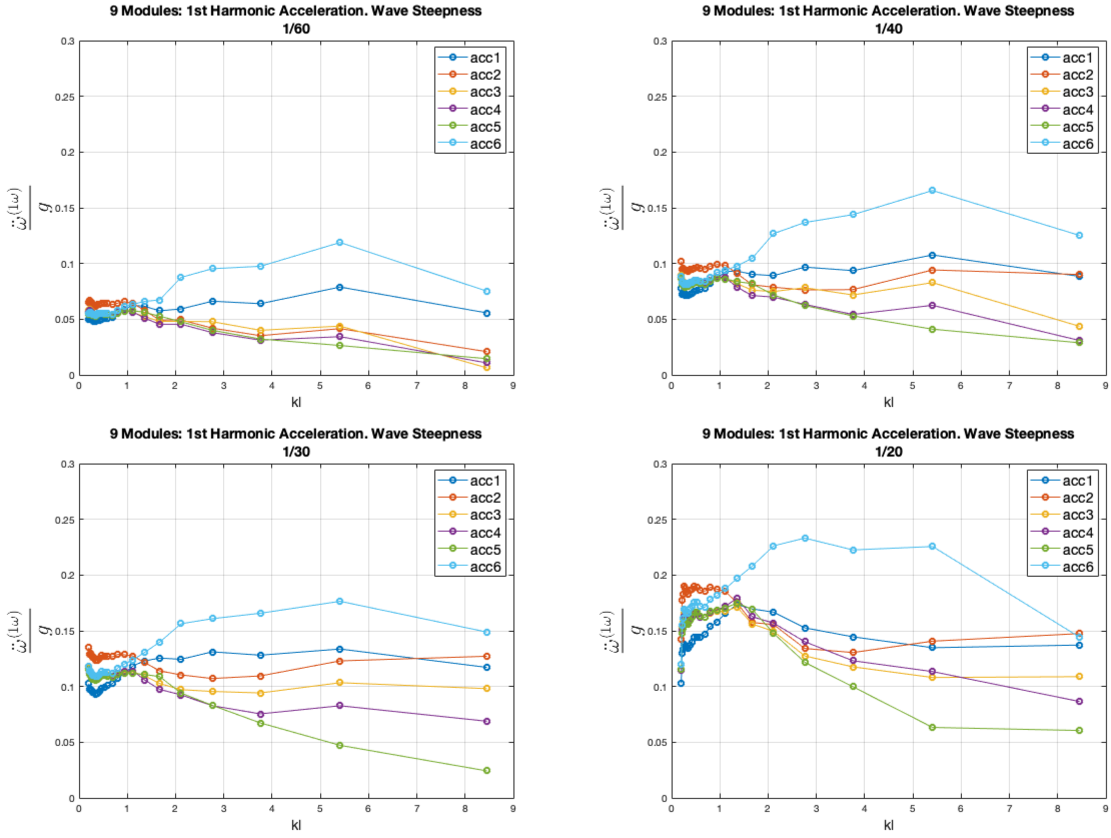

Figur 5.24: Measured 1st harmonic accelerations, $\ddot{\omega}^{(1\omega)}$, at the different accelerometers for each wave-series for every H/λ. Made non-dimensional by the gravity g and plotted against the non-dimensional wave-number kl.

2nd Harmonic Acceleration

The 2nd harmonic accelerations are presented in *Figure 5.25*. As before and as expected, the magnitudes are much smaller. The interesting observation is the measurements at

$kl < 3$ for every wave steepness, except $H/\lambda = 1/20$, where a general increase for all accelerations are present. The highest acceleration occurs at *acc1*, while the middle body, i.e. *acc3* and *acc4* has the lowest.

When $kl > 3$, the deviations becomes smaller. The sorted order of magnitude shifts here for $H/\lambda = 1/30$, and the overall result for $H/\lambda = 1/20$ is somewhat different from the others. These sharp wave crests seems to slightly boost the acceleration.

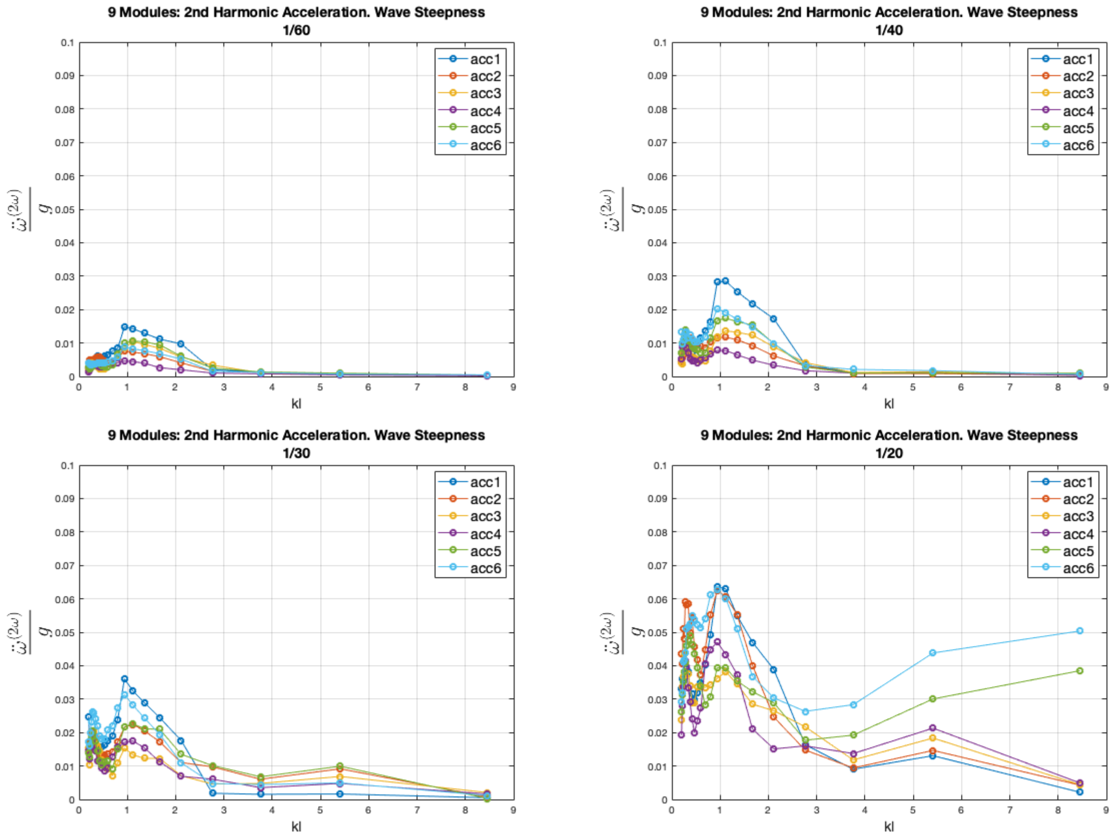

Figur 5.25: Measured 2nd harmonic acceleration, $\ddot{\omega}^{(2\omega)}$, at the different accelerometers for each wave-series for every H/λ. Made non-dimensional by the gravity g and plotted against the non-dimensional wave-number kl.

3rd Harmonic Acceleration

Figure 5.26 shows the measured 3rd harmonic accelerations. As in the previous cases, this harmonic has a magnitude in the same vicinity as the 2nd harmonic. It does not vary much throughout the wave series, but indications of an increase interval exists for $kl < 5$. In addition, for $H/\lambda = 1/20$, there is a significant increase in acceleration for the front and end of the entire model, and for the lowest kl numbers there is an increase for all accelerometers.

One can argue that the general higher accelerations for the lower kl numbers is due to higher viscous effects by larger waves. Studying the plots reveals slight variations at the different floaters as well, where the disturbed flow-field that excites the structure varies.

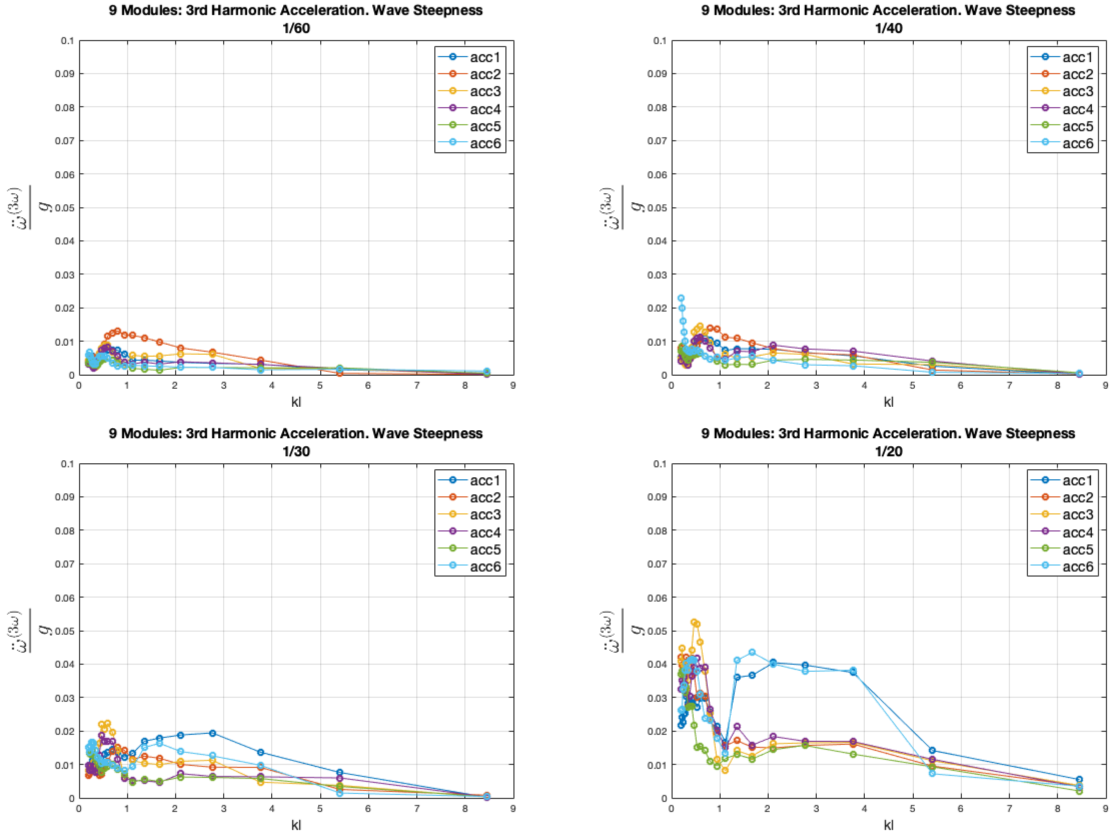

Figur 5.26: Measured 3rd harmonic acceleration, $\ddot{\omega}^{(3\omega)}$, at the different accelerometers for each wave-series for every H/λ. Made non-dimensional by the gravity g and plotted against the non-dimensional wave-number kl.

5.6 A Discussion of Articulation & Multi-body Effects

This section is a brief review and discussion of the observed and measured parameters that indicates how the effect of articulation influences the module hydrodynamic response. Being overall results for the different cases and examining the first modules eventual change. By literature references, also discussing articulation effects in terms of the array of cylindrical floaters and possible increase or decrease in hinge loads by the wave-series characteristics.

The literature reference is mainly the works of Evans and Porter, whom studied near-trapping of waves by circular arrays of vertical cylinders (Evans and Porter, 1997), and

Maniar and Newman studying wave-diffraction by a long array of cylinders using potential theory on bottom fixed and surface piercing cylinders (Maniar and Newman, 1997). Presenting these with the intention of including possible effects that were not properly measured or studied during the experimental study on the floating solar island component.

5.6.1 Effects by Model Tests Results

When comparing the computed RAOs and plotted harmonics for the three different cases described above, there is little significant indications of articulation effects with increased number of modules for the case 1 and 2 kl wave-series. In this domain, suggesting no problems in vertical structural response or integrity when adding modules.

When studying the heave and pitch RAOs for the different cases, from case 1 to case 2 the response has a lower minimum and generally lower magnitude, especially for the lower kl. When increasing to nine hinged modules, there is more variation in RAO between the three measured bodies as kl approaches 1, but no significant increase or decrease in magnitude. However this is not the case when having two modules. The overall lowest heave and pitch response occurs in case 2. For the 1st harmonic, there is no particular difference in the acceleration of the first module when going from case 1 to case 2. For $kl = [0.2, \quad 0.3]$, case 1 has an initial decrease which case 2 doesn't have. When increasing to 9 modules, the acceleration at the aft of the first module becomes larger, and the overall measurements for each kl is stable along the same magnitude. Suggesting the loss of slight cancellation in the accelerated body. For the 2nd and 3rd harmonic, going from one to two hinged modules seems to give a slightly higher acceleration in the front and slightly lower at the aft of the first module.e

In review, there is no significant effects for the thre cases from the vertical measurements. The results does not evolve or change in a manner to indicate important effects. So, any occurring diffraction, excitation or radiation phenomena is most likely to be in the horizontal plane. By observation of the regular and irregular model tests, the cylindrical floaters are exposed to wave-diffraction and viscous forces.

5.6.2 Wave Diffraction & Near-trapping of Waves

The concept geometry of the module, having a spacing l between the floaters with a diameter D, hence consisting of an array of cylinders, could experience resonance and excitation from near-trapping of waves for some specific wave-numbers.

J.N. Newman and H.D. Maniar studied an array of bottom-mounted circular cylinders by linear theory, and found a connection between the existence of trapped waves in a channel and loads acting on the elements (Maniar and Newman, 1997). Examining bottom-mounted cylinders is a significant difference, but this phenomenon, related to trapped waves, could also be discussed in terms of the floating solar island concept. Maniar and Newman argue that when the number of cylinders become large, which it will for the solar park, near-resonant modes occur between adjacent cylinders at critical wave-numbers, which causes unusually large loads on each element. These loads are shown in *Figure 5.27*.

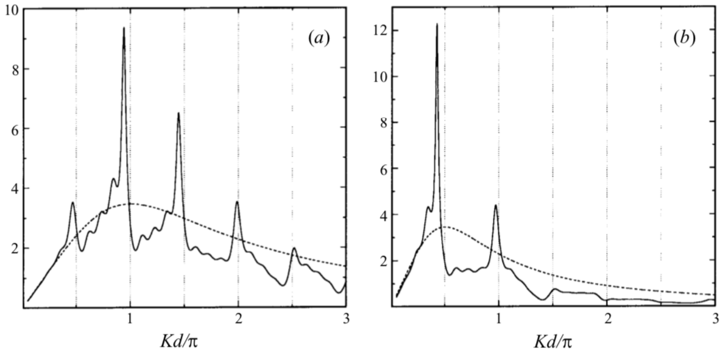

Figur 5.27: Magnitude of the load on the middle cylinder of an array N = 9 (solid line) and comparison with the load on a single isolated cylinder (dashed line). The propagation of the incident waves is in the direction parallel to the array ($\beta = 0$). (a) $a/d = 1/4$ and (b) $a/d = 1/2$, where a is the cylinder radius and $2d$ the spacing between adjacent cylinder axes. The magnitudes shown are normalized on the basis of unit wave amplitude, density, gravity, cylinder radius and depth (Maniar and Newman, 1997).

As the module concept geometry of the floating solar island has a floater radius to adjacent floater spacing ratio of $(D/2)/(l/2) = 1/5$, it is fairly close to the plot for $N = 9$ cylinder array in the left figure above. Indicating large loads from Dirichlet and Neumann trapped modes occurring for different non-dimensional wave-numbers in the plot, where $d = l/2$ in our case. The highest peak for the model corresponds to a $kl \approx 5.0$. This domain can be identified in the computed RAOs, where more wave-series should have been tested in this vicinity. Altering the floater geometry could reveal opportunities for structural alteration of the island component to better handle desired operational criteria in terms of this phenomena. However, viscous damping and nonlinear effects would most likely reduce the large-amplitude motions of the free-surface and thus associated peak loads.

A similar result is found by D.V. Evans and R. Porter (Evans and Porter, 1997), where they compute the resultant force on four cylinders in a circular array against the wave-number for different a/d ratios. A good correspondence to the geometry of the single floater. Also exposing the current concept geometry of the floater dimensions and adjacent distance to a high possibility of resonant forces. Again suggesting the idea to re-visit the concept design for desired operational criteria during further development. These forces will induce moments on the top frame, which is of concern because of the PV panels that needs to be sheltered from significant environmental loads.

5.6.3 Hinge loads

No measurements or quantity studies were performed in order to assess the loads on the hinges connecting the multi-body system. However, by observation there are one indication to the occurrence of higher loads for high-frequency waves; "mechanicalpitch motion. For wave-series characteristics that excite the system by incident waves with a wavelength corresponding to the approximate length of a single or two modules consequently gave a seemingly "mechanical"and harmonic pitch oscillations. Which also gave a higher frequent hinge deflection. Over-time, one can discuss the magnitude of fatigue this will impose on the critical component. An example of this is shown in *Figure 5.28*.

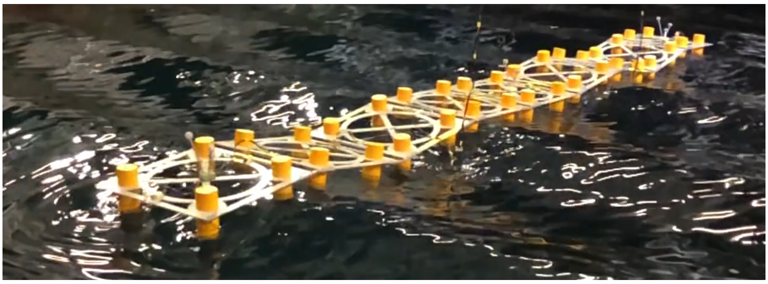

Figur 5.28: Image of the case 3 model test in regular waves with a wave period $T = 4.5$s and wave steepness $H/\lambda = 1/20$. Corresponding to a wave-length of $\lambda \approx 25$m.

On a related note, a computational analysis for the effects of waves on very large hinged vessels consisting of several modules, connected by simple hinges is done by C. Lee and J. Newman (Lee and Newman, 2000). Here they consider an array consisting of five rectangular barge modules in head waves. Their geometry is significantly larger bodies than the modules studied here. However, some notes worth considering for further evaluation of the critical hinge loads for the floating solar island can be grounded in this study. A key result in the article is that "One of the most important issues in the design of hinged structures is the shear force which acts on the hinges. Peak shear forces occur with maximum values on the forward hinges. Decreasing the stiffness of the modules tends to reduce the shear forces, as expected". Which can be argued to be quite generalized for all hinged structures in hydrodynamic interaction.

5.7 Theoretical Model Comparison

In this section, the experimental RAOs are compared to the theoretical model RAOs for $N = 1$ and $N = 2$ number of modules. Whom are expressed in *Chapter 3.5*, and derived in *Appendix B*. The latter also showing and discussing general results, and calculated resonance and cancellation periods. This comparison is suitable for case 1 and case 2, by number of present bodies and suggestively dominant linear wave-excitation loads. However, the theoretical model is also evaluated to some extent by case 3 comparison.

Figure 5.29 shows the case 1 heave and pitch RAO, computed from motion capture measurements for for every wave-steepness, compared to the $N = 1$ theoretical RAO. *Figure 5.30* shows the same comparison for case 2 and the $N = 2$ theoretical model. Both in the case 1 and 2 wave-series characteristics non-dimensional kl domain.

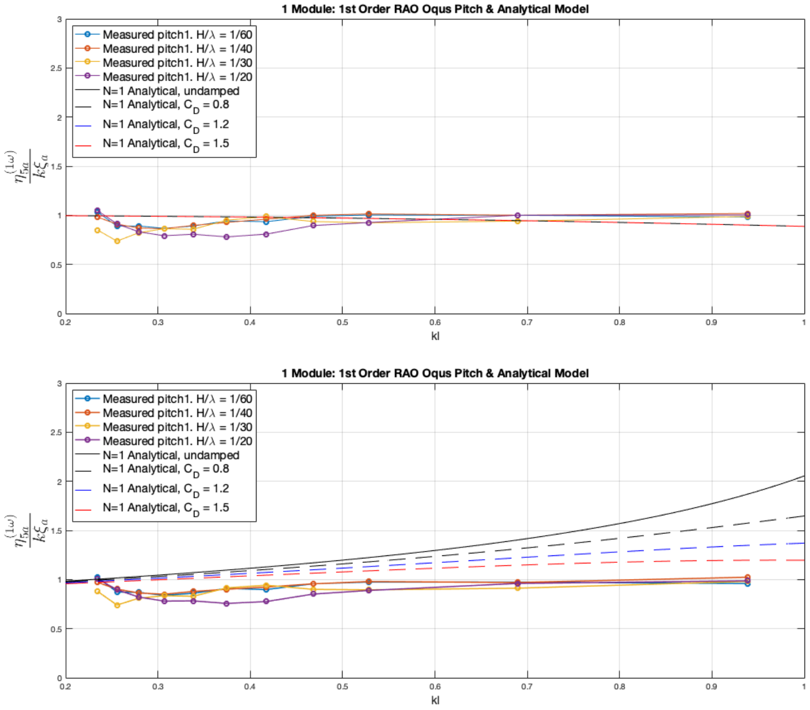

Figur 5.29: 1 module, 1st order vertical RAO in heave (top) and pitch (bottom) from motion capture measurements in $H/\lambda = 1/60, 1/40, 1/30, 1/20$, compared to the theoretical heave and pitch RAO with $N = 1$ bodies. Including undamped and viscous damped with drag coefficients $C_D = 0.8, 1.2, 1.5$. Made non-dimensional by the wave amplitude ζ_a and wave-number k plotted against the non-dimensional wave-number kl.

For case 1, there is some level of correspondence between the model test and theoretical model in heave. However, the theoretical approach does not capture the sightly lesser response for the lowest kl numbers, and, independent of the different drag coefficients, it has a general decrease as kl increases. The theoretical pitch RAO overestimates the response for larger kl, which is due to close vicinity of the estimated resonance period, corresponding to $kl = 1.25$, i.e. $T = 5.2$s. The viscous damping term has significant influence and is closer to the experimental results for the largest C_D.

In case 2, the deviation between the measured and theoretical heave RAO becomes higher for the higher kl numbers. The latter again not capturing the lesser response for the lowest kl numbers. The pitch RAO comparison shows a closer trend, but the theoretical model seems to be unlikely over-damped. Again, this response is more influenced by the drag coefficients.

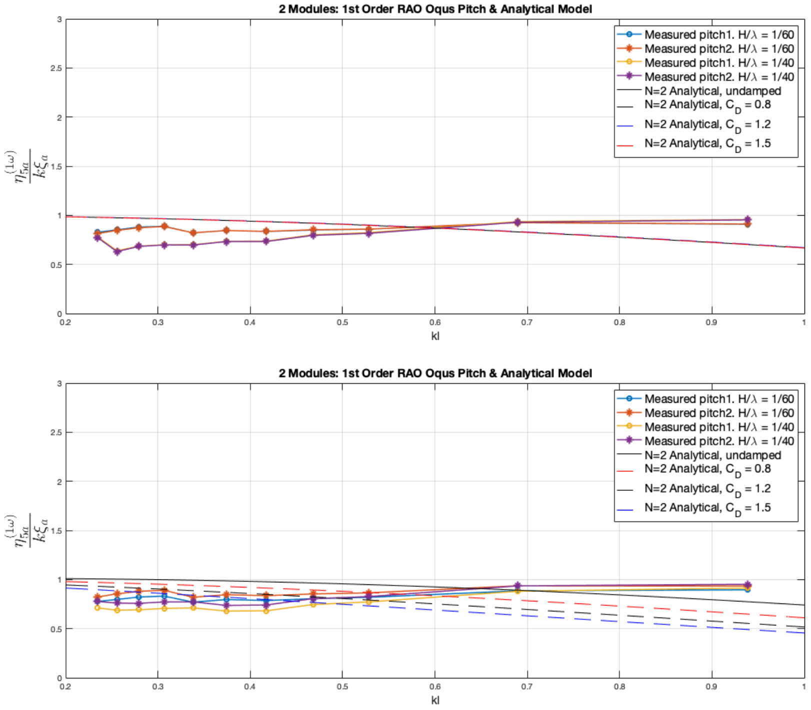

Figur 5.30: 2 modules, 1st order vertical RAO in heave (top) and pitch (bottom) from motion capture measurements in $H/\lambda = 1/60, 1/40, 1/30, 1/20$, compared to the theoretical heave and pitch RAO with $N = 2$ bodies. Including undamped and viscous damped with drag coefficients $C_D = 0.8, 1.2, 1.5$. Made non-dimensional by the wave amplitude ζ_a and wave-number k plotted against the non-dimensional wave-number kl.

Examining the correspondence does not give any support to the theoretical model. An unfortunate choice in model tests wave-series characteristics only shows kl domains missing interesting wave-structure interaction phenomena. With the theoretical pitch resonance in close vicinity for $N = 1$, but no indication of this amplification is present in the measured response.

The comparison between the case 3 RAO in $H/\lambda = 1/40$, computed from motion capture measurements, and both the $N = 1$ and $N = 2$ theoretical RAOs for corresponding kl numbers are shown in *Figure 5.31*. The same plot for every H/λ can be found in *Appendix I.2*. As previously discussed, the effect of articulation and adding modules at low kl numbers were quite insignificant, suggesting possible proper evaluation between case 3 and the theoretical RAO. However, as seen below, the theoretical model states that interesting hydrodynamics happen for $kl > 1$. A domain were no data is acquired to properly evaluate articulation effects from the model tests.

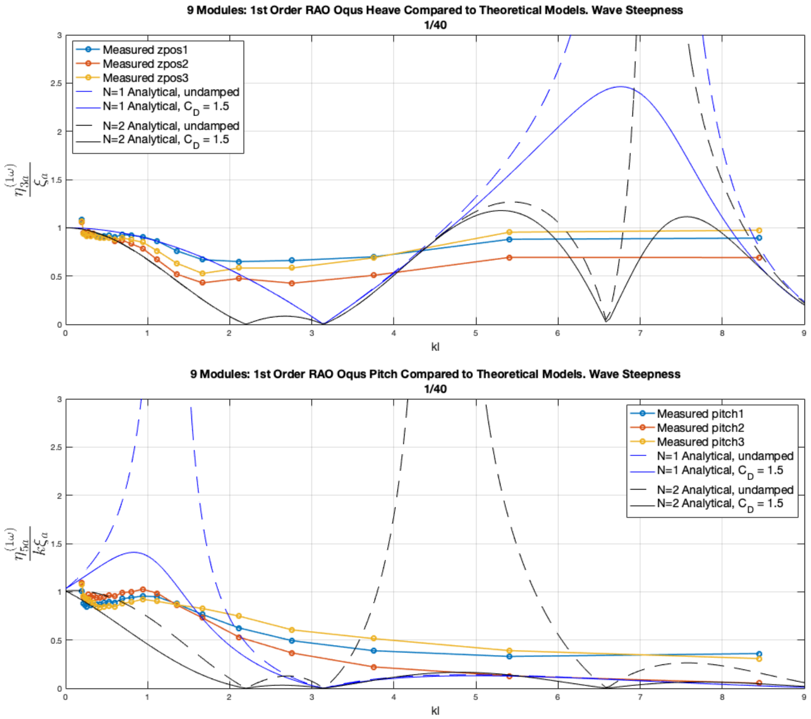
9 Modules: 1st Order RAO Oqus Heave Compared to Theoretical Models. Wave Steepness 1/40

9 Modules: 1st Order RAO Oqus Pitch Compared to Theoretical Models. Wave Steepness 1/40

Figur 5.31: 9 Modules, 1st order vertical RAO in heave (top) and pitch (bottom) from motion capture measurements in $H/\lambda = 1/40$, compared to the theoretical heave and pitch RAO with $N = 1$ and $N = 2$ bodies. Both shown as undamped and viscous damped with drag coefficient $C_D = 1.5$. Made non-dimensional by the wave amplitude ζ_a and wave-number k plotted against the non-dimensional wave-number kl.

Examining *Figure 5.31*, there is an existing trend between the theoretical and experimental results. On the other hand, the theoretical cancellation and resonance are not captured by the measurements. There are slight increase and decrease in response amplitude within these theoretical domains, but not to the extent that validation can be argued. Unfortunately for heave, the theoretical resonance is within an interval $5.5 < kl < 8$, were no regular wave-series were tested. Corresponding to the period interval $2 < T < 2.5$. The theoretical pitch resonance is close to terminated by the viscous terms, which naturally are physical properties present in the experiment, but there is a much lower measured response for the theoretical increase at the low kl numbers. The slope of the measured decrease for increasing kl are also less, and never becoming quite as small for all bodies.

In review, the case 1 and 2 comparison shows some correspondence for heave, but less so for pitch. For the case 3 comparison between the measured and theoretical RAOs, there is some correspondence in trend, but lack of tested wave-series gave inability to completely examine heave resonance. However, the result shows promise for further development of the theoretical model, as the many simplifications can be altered. The final model should at this point not be confidently used to evaluate the floating solar island concept.

Kapittel 6

Results & Discussion - Irregular Waves

This chapter summarizes and discusses the main results for the irregular wave tests. Not every relevant figure is shown, but some are placed to highlight key findings findings. Here, the only focus is on the case 3 model standing as the main study of the floating solar island concept. As discussed in *Chapter 3.6*, the main purpose of the irregular wave tests is to investigate the occurrence and level of critical water-impact events.

First, a discussion of the input and corresponding generated wave spectrum is done. Evaluating the accuracy if the wave-maker and revealing deviations in the spectral/sea-state parameters; significant wave height H_s and peak period T_p. Secondly showing the corresponding motion spectrum for the instrumentation. Thirdly, the calculated vertical response amplitude operators, lastly followed by a discussion of slamming. All plots resulting plots related to the irregular wave tests can be found in *Appendix K* and *Appendix J.1*.

6.1 Input Spectrum

The wave heights of the generated irregular waves were measured by the wave probes throughout the tank. The input spectrum thus refers to the power spectral density of the irregular waves over a time span.

6.1.1 Wave Spectrum

In *Figure 6.1* the power spectral densities for two of the irregular wave-series are shown. Both of the plots contain the measured sea-state, yielding a power spectral density, for every wave-probe, with its corresponding JONSWAP spectrum. The figure to the left is for a irregular sea-state with a significant wave height $H_s = 3$m and peak period $T_p = 5.7$s, and $H_s = 4$m and peak period $T_p = 10$s to the right. The latter being a much less steep sea-state. The legends shows the calculated spectral parameters that is measured on each respective wave-probe. The spectrum parameters are found by using spectral moments (Myrhaug and Lian, 2009) with *Matlab*.

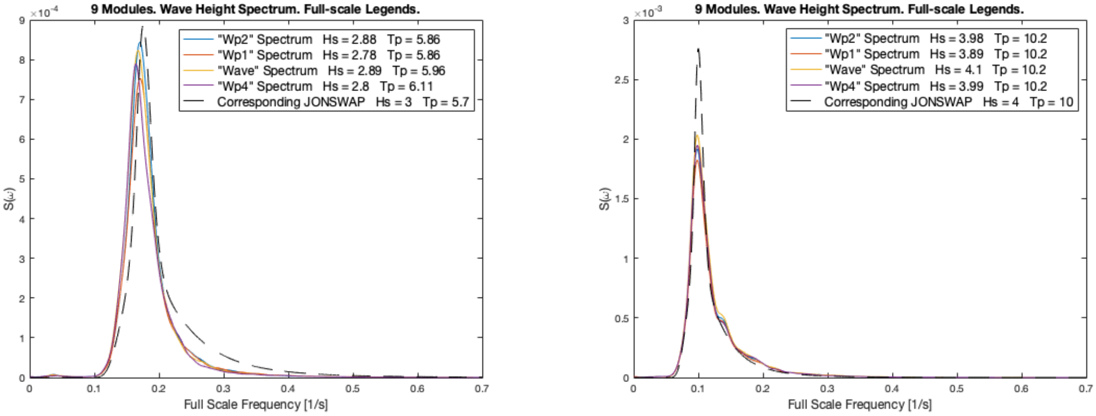

Figur 6.1: Figure to the left shows the experimental power spectral density at every wave-probe for the generated irregular waves with its corresponding input JONSWAP spectrum for $H_s = 3$m and $T_p = 5.7$s. The figure to the left shows the same power spectral density for $H_s = 4$m and $T_p = 10$s.

There is a noticeable difference between the measured generated wave power spectral density than the theoretical JONSWAP spectrum input. When referring to the change in significant wave height, peak period and the steepness curve, the general trend is that the sea states further away from the wave-breaking limit and with higher H_s has larger deviation. This indicates that larger waves are harder to sustain in the tank. Moreover, for some of these longer and higher waves with lower spectral areas and peaks, have a more clear residual, which are shown in *Figure 6.2* for all irregular wave-series at *wp2* and *wave*.

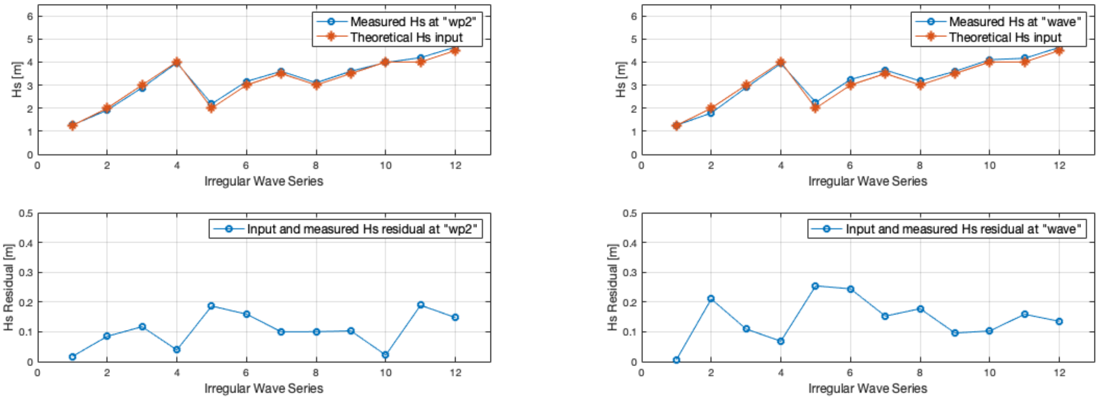

Figur 6.2: Theoretical and measured significant wave height H_s deviation, showing the input and measured H_s at wave-probe *wp2* (left) and at *wave* (right). Each respective upper figures shows the wave-characteristics for each wave-series, while the lower figures shows the corresponding measured and theoretical residual.

Furthermore, closer to the steepness curve with lower peak periods, a slight phase shift between the theoretical JONSWAP input and the measured wave spectral density is present. This is most likely due to more unstable and breaking waves.

In addition, there is also difference in the spectral density between the different wave-probes that are present in the tank. This phenomenon is mainly difference in the peak magnitudes, i.e. difference in energy and hence significant wave-height. This difference is not very significant, but its presence suggests some variations in the waves throughout the tank, that can influence the response amplitude operators by a choice of which wave-probe that should be used as a reference in the calculation.

6.2 Response Spectrum

The spectral analysis of the response by motion capture and accelerometer measurements are presented with its respective wave-spectrum for the specific irregular wave test. The reason for this is to better correlate the response spectrum grounded in the excitation by irregular waves that also are represented as a power spectral density.

6.2.1 Heave Motion Spectrum

Figure 6.3 shows the spectral densities for the heave response for the three bodies' respective motion capture instruments, i.e. *zpos1*, *zpos2* and *zpos3*. In addition, the spectral density of the generated irregular sea state is included in the same plot, which is an irregular wave field with $T_p = 4\text{s}$ and $H_s = 1.25\text{m}$. Representing a very high frequent and steep irregular wave-field, and the motion spectrum clearly reveals a more unstable heave response. The plural peaks could indicate resonance, and the differences in the three modules shows that the overall highest heave motion lies at the module in front. Then followed by the module located at the end of the model, and lastly by the module in the middle. Furthermore, the shift of this order of magnitude also varies mostly where the last module experiences the highest response, followed by the first. This conclusion could also be correlated to the general trend discovered in the regular waves RAOs.

The figure to the left shows the entire frequency interval. However, the general practise in irregular wave spectral analysis is to cut the measurements at appropriate ends of the wave spectrum that excites the system. The reason being that excitation peaks at very low wave energy domains are not physical (Kristiansen, 2019). The figure to the right shows the result after this cut, which will stand as the spectral analysis interval that will govern the response amplitude operators.

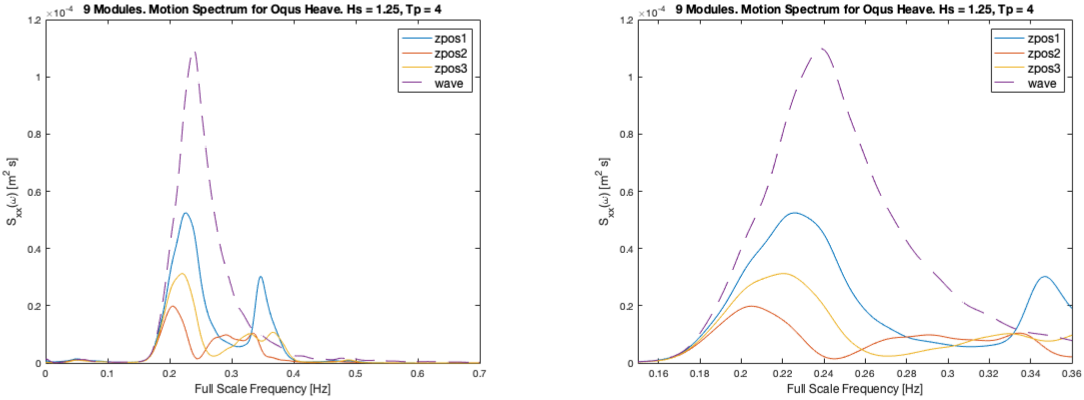

Figur 6.3: Motion Spectrum for the motion capture heave measurements, shown in model scale spectral density and plotted against the full-scale frequency, for an irregular wave field with significant wave height $H_s = 1.25$m and peak period $T_p = 4$s. The figure to the left contains the full frequency interval, while the figure to the right is cut accordingly to general practise of irregular wave spectral density analysis.

The figure to the left in *Figure 6.3* has a slight increase in spectral density at approximately 0.05 [Hz]. This is also an occurring phenomenon in the motion spectrum for the irregular wave-series. A possible explanation could be the presence of *seiching*, which can be described as sloshing in the towing tank. *Figure 6.4* shows the motion spectrum in Heave for the motion capture measurements. This result is a better representation of the general results from all the other wave-series.

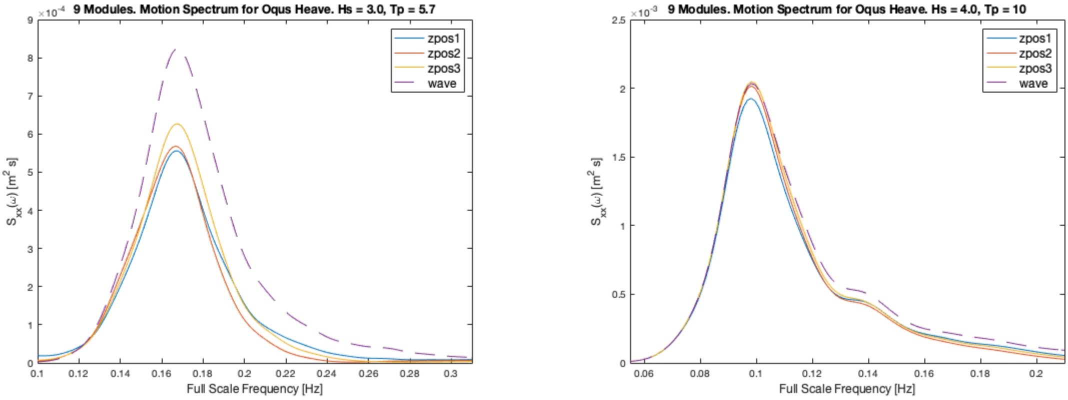

Figur 6.4: Motion Spectrum for the motion capture heave measurements, shown in model scale spectral density and plotted against the full-scale frequency. The shown irregular wave field is with significant wave height $H_s = 3$m and peak period $T_p = 5.7$s (left), and $H_s = 4$m and peak period $T_p = 10$s (right).

The general trend in the results when examining the motion spectrum is that the deviation in spectral density between the different modules becomes smaller when the wavefields are less steep, i.e. with longer peak-period in terms of appropriate significant wave height. Suggesting a steepness sensitive model.

The heave motion response spectrum is also acquired by combining the positions of the accelerometers at each module, as in the regular wave analysis. The positions are obtained by integration in the spectral domain, and the same plot as in *Figure 6.4* is reproduced by this method in *Figure 6.5*.

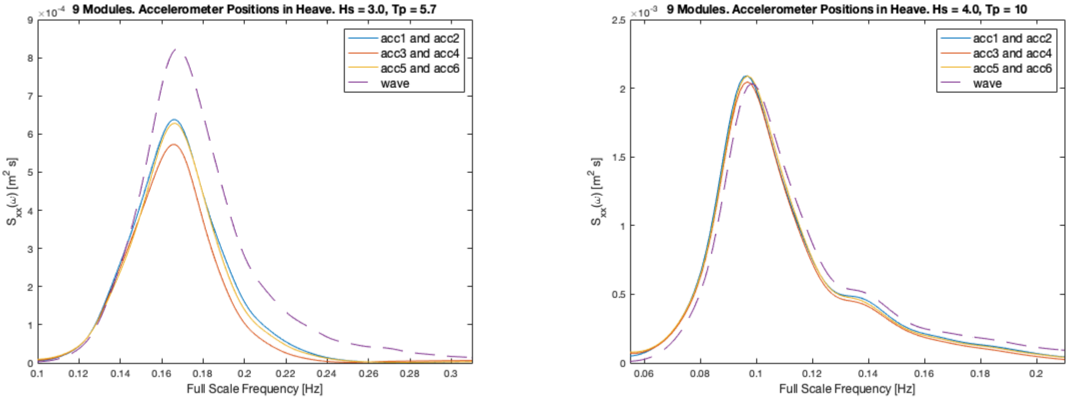

Figur 6.5: Motion Spectrum for the combined accelerometer positions for each body, shown in model scale spectral density and plotted against the full-scale frequency. The shown irregular wave field is with significant wave height $H_s = 3$m and peak period $T_p = 5.7$s (left), and $H_s = 4$m and peak period $T_p = 10$s (right).

The general heave response of the model seems to be quite good. Generally Near identical to the generated wave spectrum for the more low-frequency irregular waves. Results like shown in *Figure 6.3* is more inconsistent than the overall general results for every sea-state. An anomaly is also occurring for $H_s = 4$m and $T_p = 6.8$s, which can be found in *Appendix I*. Here *zpos1* deviates greatly and peaks around a frequency of 0 [Hz]. Results like originates in having too large residuals in the motion capture cameras, where the oqus reflectors goes out of frame. Consequently giving huge spikes or flatten the temporal measurements.

6.2.2 Pitch Motion Spectrum

Figure 6.6 shows the motion capture spectral densities for the pitch response at the three instrumented modules. Two examples are shown, where one is the pitch spectral density for the irregular sea-state with $H_s = 3$m and $T_p = 5.7$s, and with $H_s = 4$m and $T_p = 10$s, i.e. the same examples as for the heave motion spectrum. Note that the wave spectrum density is present for the purpose of illustration, but is thus not directly compatible due to the difference in units.

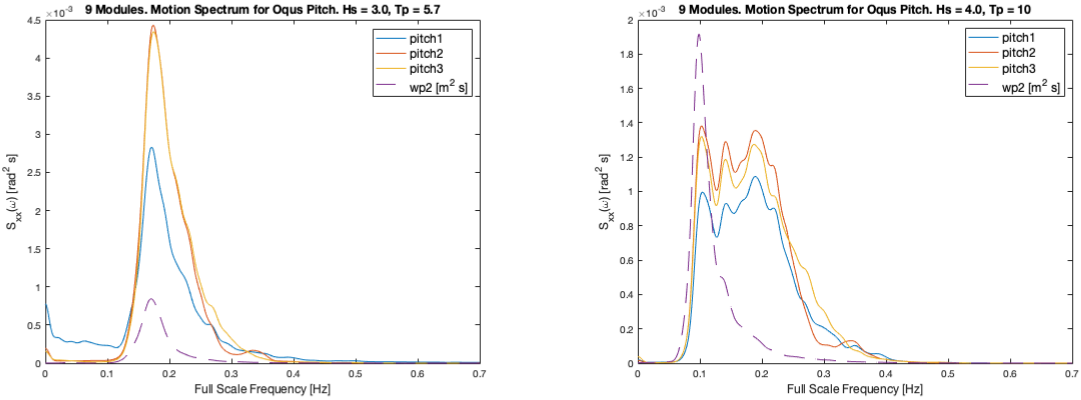

Figur 6.6: Uncut motion Spectrum for the motion capture pitch measurements, shown in model scale spectral density and plotted against the full-scale frequency. The shown irregular wave field is with significant wave height $H_s = 3$m and peak period $T_p = 5.7$s (left), and $H_s = 4$m and peak period $T_p = 10$s (right). The figure includes the corresponding generated irregular-wave field as illustration. Note that differences in the plot units are present.

The results are presented without cutting an appropriate frequency interval to show the full trend in the general results for different irregular wave-series. The examples strongly implies a higher and wider response in terms of the occurring wave-frequencies in the irregular wave-field, in comparison to the heave response. For the less steep wave-field in the figure on the right, where relatively lower wave spectral densities for the higher frequencies, have the capability of greatly exciting pitch motion on the structure. Suggesting that wave-fields containing high-frequency waves will yield higher structure response. Which will naturally have a great influence on the structural hinge loads.

6.2.3 Vertical Response Amplitude Operator

Irregular Heave RAO

The measured RAO by the motion capture markers and combined accelerometer positions on the three of the nine modules are shown in *Figure 6.7* and *Figure 6.8*, respectively, for two irregular wave-series. The plots to the left are for an irregular wave-field with $H_s = 3$s and $T_p = 5.7$s, and $H_s = 4$s and $T_p = 10$s to the right. Keeping to the same states as those presented above.

The results are acquired by the discussed spectral analysis and applying the experimental RAO discussed in *Chapter 3.6*. The wave-spectrum and its corresponding motion spectrum that is measured by the instruments are cut, yielding own intervals of the dimensionless wave-number kl that are applicable for the respective sea-state input.

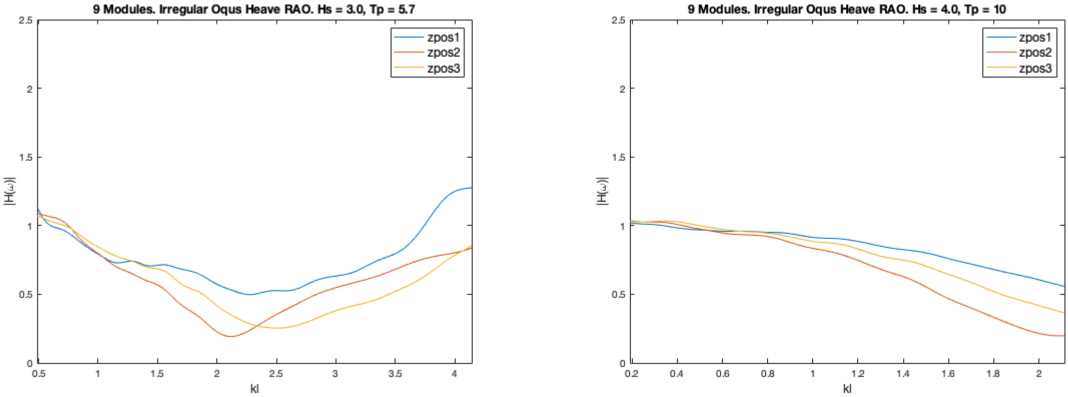

Figur 6.7: Heave RAO for motion capture measurements for each instrumented module, in irregular waves with $H_s = 3$m and $T_p = 5.7$s (left), and with $H_s = 4$m and $T_p = 10$s (right). Represented as the transfer function $|H(\omega)|$ plotted against the dimensionless wave-number kl.

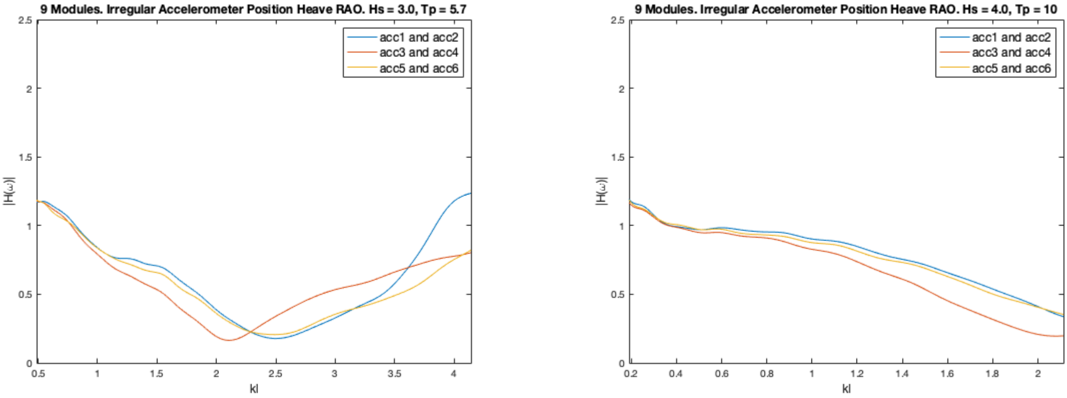

Figur 6.8: Heave RAO for combined accelerometer positions for each instrumented module, in irregular waves with $H_s = 3$m and $T_p = 5.7$s (left), and with $H_s = 4$m and $T_p = 10$s (right). Represented as the transfer function $|H(\omega)|$ plotted against the dimensionless wave-number kl.

There are some differences in magnitude and detailed behaviour of the different measured modules between the two methods/measurements of acquiring the heave RAO. However, the overall trend along the wave-number kl and occurring maximum values are sufficiently similar. Hence acting as some slight indication of appropriately acquiring the experimental stochastic transfer function and the capability of the different instruments.

When comparing the irregular heave RAO for these two irregular wave-series to the case 3 regular heave RAO shown in *Figure 5.20* for the same kl numbers, good correlation regarding the trend is present. This being the decrease and increase for approximately $0.5 < kl < 4$ for the left figures above, and for $|H(\omega)| \approx 1$ for the lowest kl numbers for the right figures. However, the irregular heave RAO has a lower magnitude overall. These examples also contain the result that the largest response amplitude operator mostly lies at the first module, i.e. *zpos1*, and equally *acc1 and acc2*. Further supporting the expectancy of largest excitation at either the first or last module in the global model.

Another observation of the irregular RAOs in heave, is that the decrease in the vicinity of $kl \approx 2$ and $kl \approx \pi$ is correlated to the theoretical decrease and cancellation domain in the theoretical model as discussed in *Appendix B*.

Irregular Pitch RAO

Figure 6.9 below shows the pitch RAO acquired by motion capture measurements in irregular waves with $H_s = 3$m and $T_p = 5.7$s to the left, and with $H_s = 4$m and $T_p = 10$s to the right.

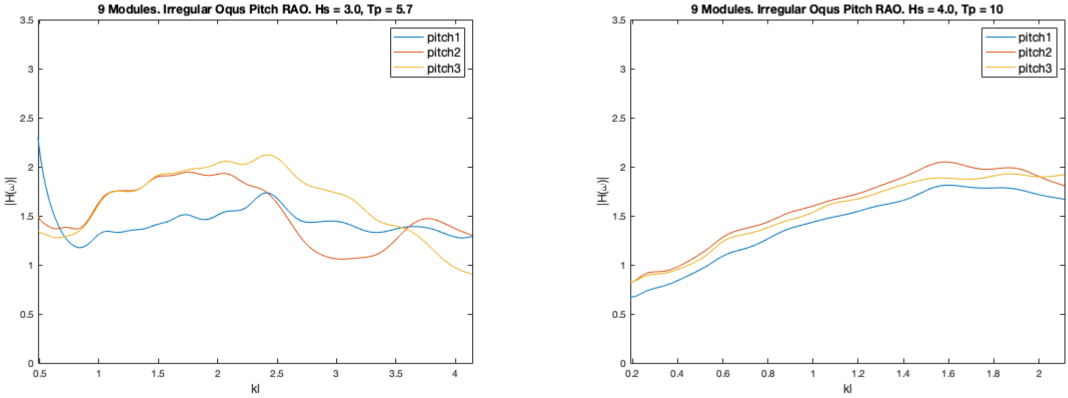

Figur 6.9: Pitch RAO for motion capture measurements for each instrumented module, in irregular waves with $H_s = 3$m and $T_p = 5.7$s (left), and with $H_s = 4$m and $T_p = 10$s (right). Represented as the transfer function $|H(\omega)|$ plotted against the dimensionless wave-number kl.

The result for irregular pitch RAO for these kl numbers are in some correlation to the case 3 regular pitch RAO shown in *Figure 5.22*. Mostly in terms of trends in increase and decrease, and by having the first module at the lowest response. However the magnitude of the RAOs are almost twice as high in the irregular sea-state. Meaning that the irregular pitch response is probably much more crucial and governing to the hydrodynamic response. The same high magnitude is shown for the other irregular wave-series, whose RAOs are shown in *Appendix K*.

Again referring to the theoretical RAO, the calculated pitch resonance for $N = 1$ bodies is in the vicinity of $kl \approx 1.25$ and $kl \approx 5$ for $N = 2$. When looking at the irregular RAOs, these non-dimensional wave-number domains also contains an increase in response. Studying the irregular RAOs for all measurements, the kl domains for theoretical cancellation and resonance shows correlating decrease and increase in the response amplitude. Thus suggesting similar trend in measured and calculated results, as declared for the regular wave comparison results.

6.3 Slamming & Over-topping

The model test irregular wave-series shown in *Table 4.3* were chosen to examine the occurrence of critical events along the simplified steepness curve shown earlier in *Figure 4.8*. With aim to identify domains for significant wave height and peak period combinations that did not yield any or little water-impact on the top frame of the modules. The nature of these irregular wave-fields consequently generated steep and rapidly breaking waves for many of the full-scale 3-hour simulated sea-state tests.

Figure 6.10 shows the simplified steepness curve, composed by *Moss Maritime* with its structure operational criteria in mind. It contains the points of the H_s and T_p combinations that were tested, all with $\gamma = 3.3$ regarding the necessary JONSWAP spectrum input parameters. In addition, the irregular-wave fields are marked with the approximate number of observed slamming during the simulation. The solid line is an eye-fitted curve, marking suggested safe and unsafe domains for the operational design.

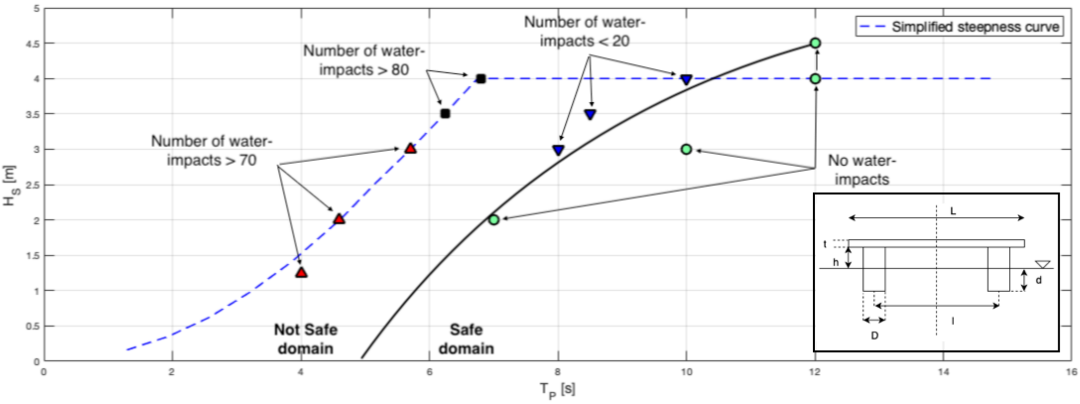

Figur 6.10: Simplified steepness curve showing the irregular wave-series that were tested (points), which are marked with the approximate number of observed slamming during simulation of a 3-hour sea-state. The solid curve is eye-fitted and represents suggested H_s and T_p combinations within safe and unsafe domain, in terms of zero observed water-impacts. The figure also includes single module model geometry, with values for the properties as in *Table 4.2*.

By observation and video review, the main result is that the structure seems to be quite sensitive to wave steepness in general. The regular wave tests showed good and satisfactory results in general, with over-topping observed for $T = 13$s with $H/\lambda = 1/20$ only. But when the model was exposed to two or more successive steep waves, the model generally experienced slamming and over-topping. High pitch motion for these steep high frequency waves, followed by a large wave was a typical event that were recurrent along the steepness line. The heave response seemed unable to assist the rotation enough if the incident wave height was of some amplitude. When slamming occurred, it usually propagated through the entire structure as local components move relatively equal in response to the critical wave. However, the observations of water-impacts that were located on local parts of the model, indicates more events in general at the first and last module. In addition, breaking waves on structure entry or within the structure, almost always led to slamming if the wave was sufficiently high.

Tests with less steep H_s and T_p combinations, clearly showed that the longer the periods, the better hydrodynamic flexibility. As well as in the regular wave tests, the structure handles very high waves if provided with a steepness far away from wave-breaking. However, as the eye-fitted curve shows, this input parameter relation between wave period and height is most likely not linear. The higher waves acquired even longer periods.

The general hydrodynamic response suggests largest motions at the first and last module. A re-occurring "whip"movement was present, suggesting larger loads and necessary strengthening. Mooring studies are clearly necessary for proper hydrodynamic flexibility, the very foundation of the concept design.

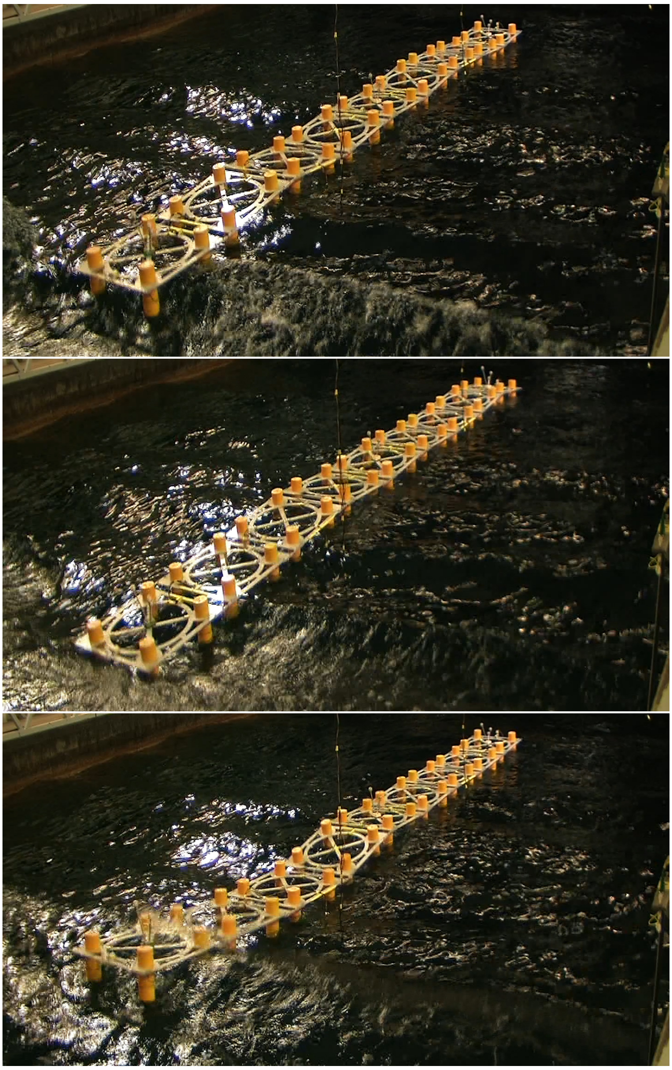

Figur 6.11: Model seen from the front at an angle in irregular waves with $H_s = 4$m and $T_p = 6.8$s. The three figures are consecutive captured frames of the video, following a single wave from the top figure to the bottom figure.

Figure 6.11 shows three extracted photos of a short time period in consecutive order for a steep incident wave, taken in $H_s = 4$m and $T_p = 6.8$s. An irregular wave test with high-frequent water-impacts. The image at the top illustrates a near-breaking wave entering the model, where the front module is almost out-of-water. When the wave passes further down, the drop on the first module has a sufficient pitch rotation and heave translation so that the consecutive wave results in slamming on the front. This is seen in the middle image. In the third image, one can see the water-impact propagating to the next module due to the following movement caused by articulation.

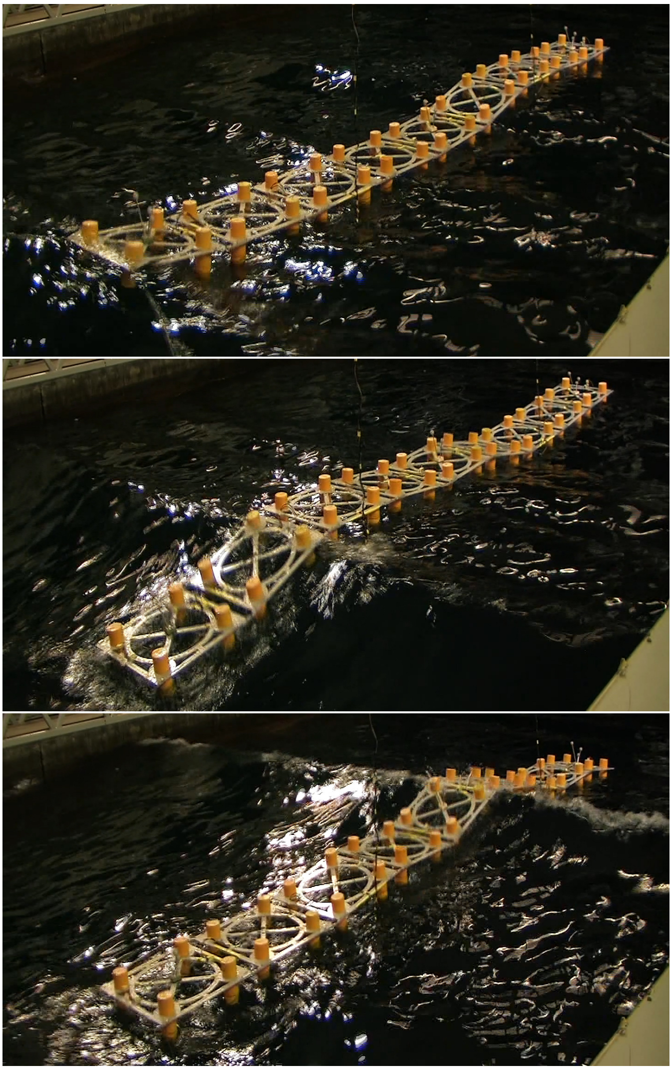

Figur 6.12: Model seen from the front at an angle in irregular waves with $H_s = 4$m and $T_p = 10$s. The three figures are consecutive captured frames of the video, following a single wave from the top figure to the bottom figure.

Another example of such a process is shown in *Figure 6.12*, presented in the same manner. This example is for $H_s = 4$m and $T_p = 10$s, which is a sea-state that had a lesser number of critical events. The ones that occurred were usually due to a breaking wave or a near-breaking entry wave. The image at the top shows a slight over-topping on the first module for a near-breaking wave. Then, as seen in the middle image, the large pitch response is transferred to the second module which experiences water-impact on its rear end. So begins typical slamming propagation through the model.

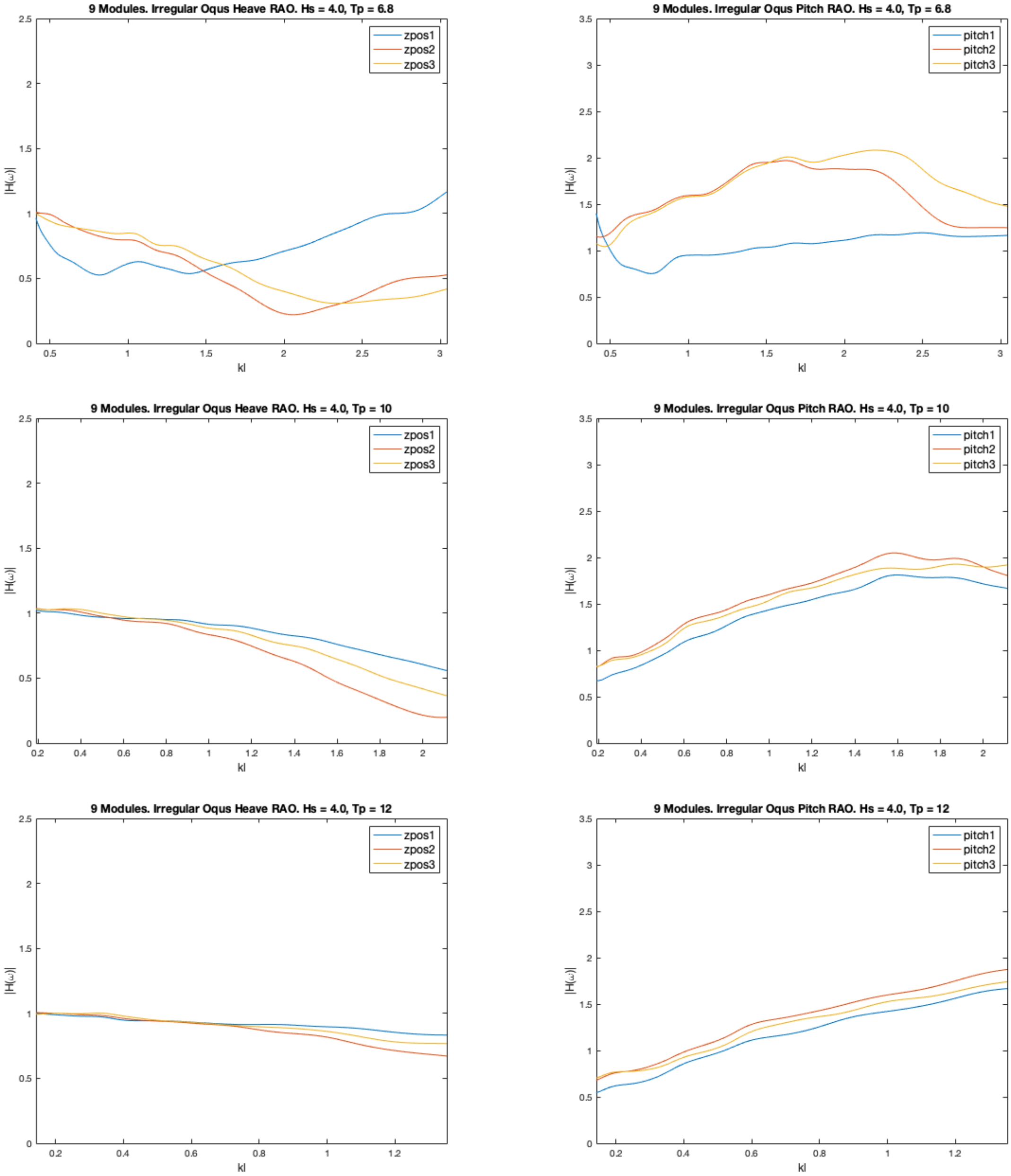

Figur 6.13: Motion capture RAO in heave in the left column, and motion capture RAO in pitch in the right column, calculated in the irregular waves $H_s = 4$m and $T_p = 6.8$s at the top row, $T_p = 10$s at the middle row, and $T_p = 12$s at the bottom row.

The two examples shown in *Figure 6.11* and *Figure 6.11*, and including a no observed slamming irregular wave test at $H_s = 4$m and $T_p = 12$s, has the heave and pitch RAO presented in *Figure 6.13*. Where the figures to the right are the motion capture heave RAO, and motion capture pitch RAO to the left. The rows are the different sea-states.

Kapittel 7

Conclusion & Further Work

This chapter contains a summary of the most important results found and discussed in *Chapter 5* and *Chapter 6* from the experimental study. Emphasizing the case 3 model test. Reviewing the overall structure performance and design in terms of its operational purpose. Moreover, drawing conclusions that mainly evaluates the operational limits in terms of the study results. Lastly, a proposal for further research when further developing the concept design.

7.1 Summary of Results

The high-frequency regular wave-tests with periods $T = 2.0, 2.5, 3.0$s had unstable generated waves for $H/\lambda = 1/30, 1/20$ due to the limitations of the wave-maker and the large domain of the tank. Nonetheless, the corresponding results are included, but care must be taken during evaluation of these high kl numbers.

From observations of the case 3 model tests in regular waves, the only critical event was slight over-topping of the first module for $T = 13$s and $H/\lambda = 1/20$. The structure seemed to be globally flexible in terms of the incident regular waves, meaning great ability to follow the incident wave-fields. Meanwhile, a relatively large loss and gain in air-gap on the floaters where present, but no out-of water situations. Indications of possible large effects of wave-diffraction and viscous excitation and damping were present. Moreover, for the higher frequency waves, especially with wave-lengths corresponding to module dimensions, a "mechanicalrapid and steep pitch rotation response lead to suspicion of larger hinge loads and danger of fatigue. From the measurements, it is clear that the largest vertical accelerations occur at the first and last module in the articulated structure. The definitive largest harmonic amplitude was located at the last module's aft, and was approximately 20% higher than the front. Moreover, it was 50% higher than a rough mean value estimation of the other accelerometers. This order naturally follows in the vertical response, but the differences in magnitude are not generally so vast. By the calculated heave RAOs, the structure follows the waves when $T > 5$s in heave, and $T > 7$s in pitch. The largest calculated amplification factor was found to be approximately 1.4, occurring on the first and last module for wave periods with $2-2.5$s. This domain gave the highest amplification for both DOF. In heave, for every steepness, a slight cancellation occurs with its lowest amplification factor of 0.4 at the middle module for $T=4$s. However at this wave-field, the possible loss of air-gap seems to be compensated by the pitch response. In general, the RAO acquired by use of motion capture versus combined accelerometers yielded some deviations, but an overall satisfactory trend and magnitude. In pitch, the difference in response magnitude is less across the bodies than in heave, but the middle module still has the lowest. The amplification operator decreases for lower periods. However, for the highest periods when $T > 6s$, the middle module is slightly higher for almost all H/λ. Here, the two different acquired RAOs are quite different, where the accelerometer positions indicates the first module to have quite much higher pitch response. By observation, a "whip motionpropagating through the structure revealed an increased excitation and response on the last module. The pitch angles never exceeded $10°$on the measured bodies.

The irregular wave tests, conducted with 3-hour simulations using JONSWAP spectral inputs, revealed a more steepness sensitive wave-structure interaction. By observation, a quite large amount of slammings occurred on the ends or through the entire structure for many of the H_s and T_p combinations. This event was almost guaranteed if the incident wave was breaking within the proximity of the structure, or if two or more consecutive steep waves were followed by a sufficiently high wave. Which is something that also could occur in sea-states further away from the breaking wave limit. A Typical process was that high-frequency excitation yielded corresponding steep pitch rotations, vulnerable to following larger waves. Thus, critical sea-states consisting of steep and high-frequent fields should be avoided. As before, the largest response and acceleration was located on the first and last module. By the irregular excitation, a generally higher loss and gain in air-gap was present than the regular wave tests. As shown in *Figure 6.10*, the suggested safe domain requires sufficiently long peak periods for increasing significant wave heights to ensure very low occurrence of water-impacts. Avoiding critical events that compromise the integrity of the structure and its operational objective.

From both the irregular and regular wave tests, by observations and RAOs, the structure should operate at lower-frequency waves with periods larger than 7s. Then naturally having appropriate significant wave heights to avoid steep wave excitation. The preliminary suggested operational criteria with $H_s = 4-5$m and $T_p = 10$s should be changed. The periodic requirement is sufficient, but to ensure uncompromising structural integrity for the PV panels, the corresponding significant wave height should not be less than 5m. $H_s = 4$m should have T_p12s. So, referring to *Figure 6.10* for recommended operational limits when considering fitting operational areas. To keep these results, it is necessary to maintain the mooring elasticity of the structure.

The developed theoretical model is grounded in earlier multi-body hydrodynamic response methods. The results by experimental comparison yielded improper evaluation, not giving the model any sufficient confidence for practical use at this stage. However, theoretical resonance and cancellation domains can to some extent be identified in both the regular and irregular wave-tests, but not completely consistent. An unfortunate missing interval of measured wave-series yielded inability to fully verify these domains.

Evaluating the regular wave test results for the three different cases shows little indication of significant articulation effects on the vertical excitation when increasing the number of modules for $T > 6$s. It is unfortunate that case 1 and case 2 were not measured with the same wave period range, as the most noticeable measurements are for higher frequency waves. Hence, to some extent, we can suggest that the floating solar island concept may be very efficient within the suggested safe domain. However, this does not override the results described above, which leaves room for possible improvements regarding module geometry. Wave-diffraction and viscous effects were present by observation of the model tests, where the current geometry will have near-trapped waves and structure modes that may have increased excitation.

7.2 Conclusion

The wave-induced vertical response of an articulated multi-module structure of identical floaters in different wave conditions have been investigated. The concept was simplified, but stand as an appropriate component for preliminary results leading to further development. The overall results shows potential, but more work and research are needed for further development. At this stage, the structure could confidently handle sufficiently long-period sea-states. By measurements, observations and some suggestive theoretical results, an operational appropriate sea-state has wave-period greater than 7s, and for irregular wave test, a corresponding sufficiently less steep significant wave height. This statement naturally grounded in the tested wave-field period ranges; $2 - 13$s. Properties necessary for large offshore floating structures, capable of withstanding large wave motions while preferably acting as globally flexible, are present.

The main concerns originates from the irregular wave-fields, where successive steep high-frequency waves revealed a pitch sensitive structure. Large pitch excitation yielded water-impact vulnerability, where the wave heights needn't be sufficiently large. Similar waves with lower wave heights would also consequently induce consistent mechanical pitch rotations, suggesting larger hinge loads and danger of fatigue. However, staying within the longer period domain still states the uses of rigid hinged modules to be a good premise for flexibility and safe fitting for PV panels. Articulation effects for these longer periods were insignificant, so the concept could easily be fitted with specific arrays for operational sites. However, the greatest response amplification was located at the first and last module of the articulated structure, whom also experienced a propagating whip motion. Suspecting these modules, acting as the floating solar island's outer perimeters, to be exposed to higher loads. Hence, considering to strengthen these components and future emphasis on mooring analysis.

Not all decisive variables for the structure's hydrodynamic performance are investigated. However, the experimental study shows potential for a premise with good hydrodynamic flexibility when the waves are sufficiently long. A concept worthy of further development and evaluation, that can possibly be a meaningful contribution to green energy.

7.3 Recommendations for Further Work

There are a large number of different aspects of the multi-module floating solar island concept that needs to be investigated in order to properly develop the current design. The conducted study is only a simplified model of a single row of floater modules. By the required time and effort to use experimental methods, it would be beneficiary to further develop the theoretical model. Expanding it to properly implement the rigid hinged multi-body modal analysis for a larger number of modes and modules. In addition building a numerical model within linear and second-order potential theory, such as WADAM/WAMIT (DNVGL, 2018) to better acquire proper hydrodynamic solution.

Regarding the experimental study, it was unfortunate that the first two cases did not include the same wide variety of regular waves-fields. Especially for the lower periods which contains interesting phenomena by both measurements, observations and theory. This is also the case for irregular wave tests, where further further evaluation of articulation effects is a vital part of the concept. A factor that to the greatest effort should influence the choice of module array size for different operational sites.

The simplified model was by observation exposed to wave-diffraction and viscous effects. These influences could create structural moments on the top frame holding the sensitive PV panels. In addition, the simplified floaters does not reflect the original components suggested by *Moss Maritime*. The curvature of the originals will most likely yield water-rise up effects. The module's floater geometry and the geometry of the module itself, is a decisive variable that greatly governs the hydrodynamic response and the steepness-sensitive nature, which could be altered for higher or lower frequency sea-sates. The simplification by using horizontal and elastic mooring lines also requires further attention. Naturally influencing the stiffness of the system, but important to maintain the uncovered hydrodynamic flexibility, without loosing structural integrity. Lastly, the hinges are critical components that needs to be further assessed. The reason being expected large excitation loads and fatigue that could compromise the concept premise.

Bibliografi

Cengel, Y. A., Cimbala, J. M., 2010. Fluid Mechanics: Fundamentals and Applications. Second Edition in SI Units. McGraw-Hill.

DNVGL, 2007. Recommended Practice DNV-RP-C205, Environmental conditions and environmental loads. `https://rules.dnvgl.com/docs/pdf/DNV/codes/docs/2008-10/RP-C205.pdf`.

DNVGL, 10 2018. Strength assessment of offshore structures - sesam software. `https://texfaq.org/FAQ-citeURL`.

Evans, D., Porter, R., 1997. Near-trapping of waves by circular arrays of vertical cylinders. School of Mathematics, University of Bristol, Bristol BS8 1TW, UK P11: S0141-1187(97)00015-1.

Faltinsen, O., 1993. Sea Loads on Ships and Offshore Structures. Cambridge University Press.

Gazdowicz, S., 12 2018. State of the industry: Floating solar. Presentation. Section Solar, Storage and Smart Grids - Oslo.

Greco, M., 2018. TMR 4215: Sea Loads Lecture Notes. Department of Marine Technology, NTNU.

Hanssen, F., Feb. 2019. private communication.

Housseine, C., Monroy, C., Hauteclocque, G., 6 2015. Stochastic linearization of the morison equation applied to an offshore wind turbine. Proceedings of the ASME 2015 34th International Conference on Ocean, Offshore and Arctic Engineering OMAE2015.

Kinsman, B., 1965. Wind Waves. Englewood Cliffs, N.J.: Prentice-Hall Inc.

Kristiansen, T., Apr. 2019. private communication.

Kristiansen, T., Borvik, P., 6 2018. Investigation of an air-cushion supported solar island. honoring sympsosium of prof. bernard molin. Presentation OMAE2018-78533, Madrid, Spain.

Lee, C., Newman, J., 2000. An assessment of hydroelasticity for very large hinged vessels. Department of Ocean Engineering, Massachusetts Institute of Technology Cambridge, MA 02139, U.S.A. Journal of Fluids and Structures (2000) 14, 957-970.

MacCamy, R., Fuchs, R., 1945. Wave forces on piles: A diffraction theory. Department of the Army, Corps of Engineers, Beach Erosion Board Office of the Chief of Engineers Technical Memorandum no. 69, 7499–7506.

Maniar, H., Newman, J., 1997. Wave diffraction by a long array of cylinders. Department of Ocean Engineering, Massachusetts Institute of Technology Cambridge, MA 02139, U.S.A. Journal of Fluid Mechanics (1997) vol. 339, pp. 309-330.

Mathai, T., 2000. Use of generalized modes in hydrodynamic analysis of multiple bodies. Proceedings of the Tenth (2000) International Offshore and Polar Engineering Conference The Glosten Associates, Inc. Seattle, WA, USA.

Moan, T., Haver, S., Spidsøe, N., 2010. Stochastic Theory of Sealoads. Department of Marine Technology, NTNU.

Morison, J., O'brien, M., Johnson, J., Schaaf, S., 1950. The Force Exerted by Surface Waves on Piles. Berkeley, University of California.

Myrhaug, D., Lian, W., 2009. Marine Dynamics Lecture Notes. Department of Marine Technology, NTNU.

Newman, J., 1977. Marine Hydrodynamics. Cambridge: The MIT press.

Newman, J., 1997. Wave Effects on Hinged Bodies. Part I - Body Motions. `https://www.wamit.com/Publications/Hinged1.pdf`.

Newman, J. N., 2001. Wave effects on multiple bodies. Massachusetts Institute of Technology Cambridge, USA MA 02139.

Pettersen, B., Myrhaug, D., Faltinsen, O., 2014. Marine Hydrodynamics. Kompendieforlaget, Akademika Forlag.

Rogne, Ø. Y., 2014. Numerical and experimental investigation of a hinged 5-body wave energy converter. Ph.D. thesis, Norwegian University of Science and Technology.

Steen, S., 2014. Experimental Methods in Marine Hydrodynamics. Department of Marine Technology, NTNU.

Thøgersen, A. M., Oct. 2018. private communication.

Yeung, R. W., 1980. Added mass and damping of a vertical cylinder in finite-depth waters. Department of Ocean Engineering, Massachusetts Institute of Technology, Cambridge, MA A 02139, USA.

Appendix A

Concept & Model Drawings

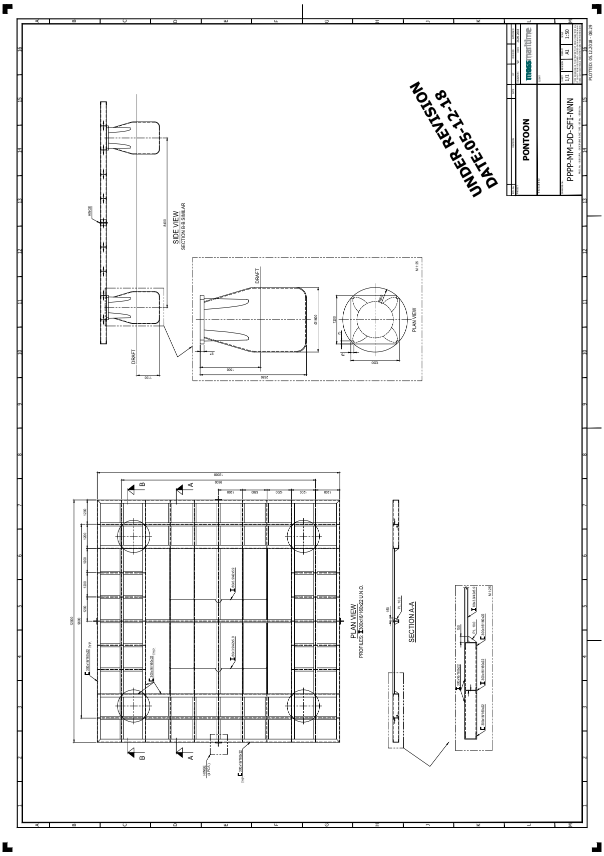

Figur A.1: Technical drawing of the single module component provided by *Moss Maritime*

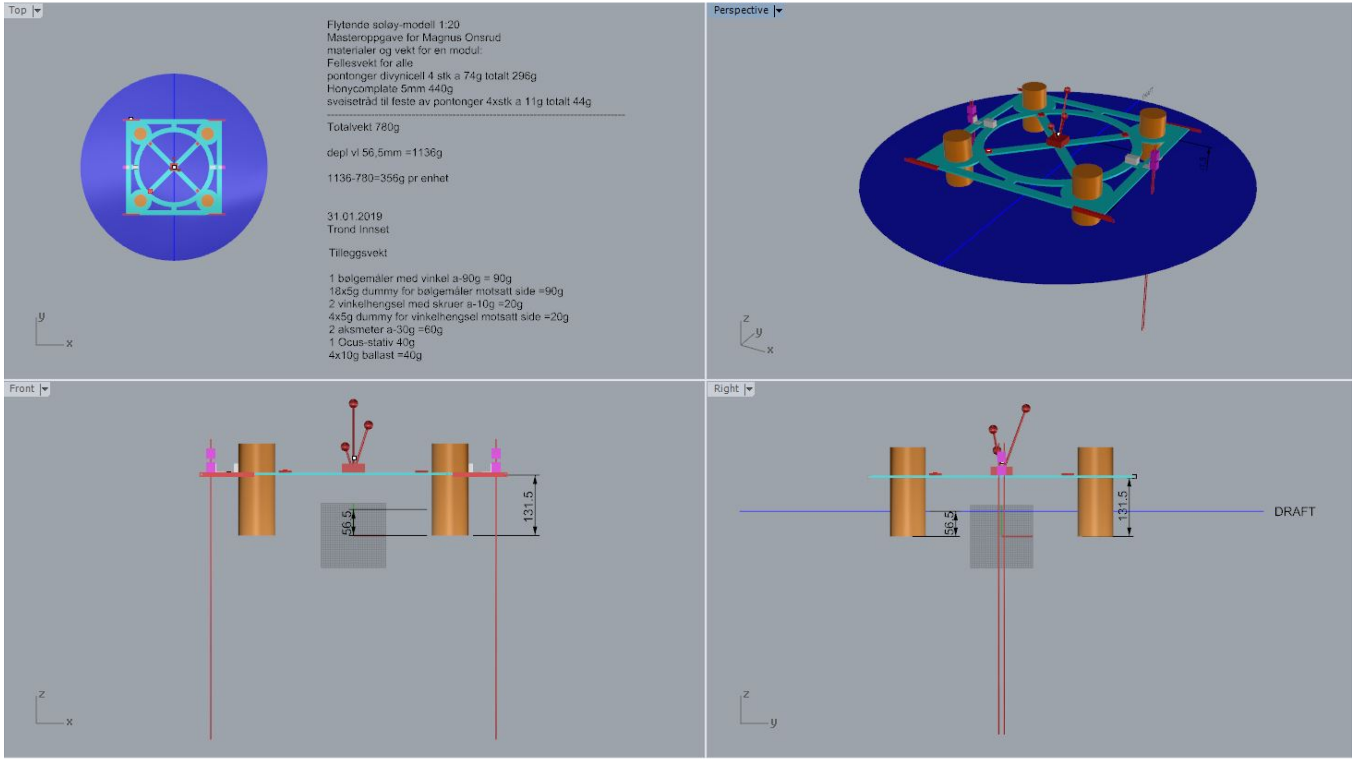

Flytende soløy-modell 1:20
Masteroppgave for Magnus Onsrud
materialer og vekt for en modul:
Fellesvekt for alle
pontonger divynicell 4 stk a 74g totalt 296g
Honycomplate 5mm 440g
sveisetråd til feste av pontonger 4xstk a 11g totalt 44g

Totalvekt 780g

depl vl 56,5mm =1136g

1136-780=356g pr enhet

31.01.2019
Trond Innset

Tilleggsvekt

1 bølgemåler med vinkel a-90g = 90g
18x5g dummy for bølgemåler motsatt side =90g
2 vinkelhengsel med skruer a-10g =20g
4x5g dummy for vinkelhengsel motsatt side =20g
2 aksmeter a-30g =60g
1 Ocus-stativ 40g
4x10g ballast =40g

Figur A.2: CAD drawing of the experimental single module model. Instrumentation shown as for the single module, two modules tests, and for the first and last module in the nine modules test.

Appendix B

Theoretical Model of the Vertical Response

The theoretical model for the hinged multi-module structure is based on assuming linear potential theory and using modal analysis to compute the hydrodynamic response for vertical heave and pitch motion. The formulation is grounded in the method presented in *Chapter 3.4.1*, but here it is limited to $N = 1$ and $N = 2$ articulated modules. Moreover, the model has potential for relatively simple extension to include more bodies and modes. The formulation for the more specific application of the vertical response for a small number of bodies, also draws from the work of T. Mathai, whom used a similar model in hydrodynamic analysis of multiple bodies (Mathai, 2000).

B.1 Model Formulation

Assuming valid linear potential theory and the incident regular waves being the only source of structure excitation. Defining the number of bodies N and a corresponding earth-fixed coordinate system that is located at the mean free surface and global structure horizontal CoG. Which, by symmetry, is the same vertical position independently of number of bodies. The horizontal position is either in the middle module for $Nodd$ or the middle hinge for $Neven$ number of bodies. This is illustrated in *Figure B.1*.

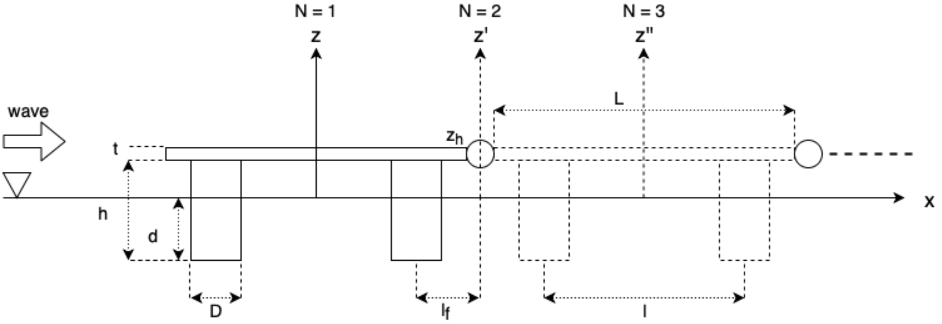

Figur B.1: Figure of the geometric model with respective definitions for dimensions, showing coordinate system for using N number of bodies and direction of wave-propagation. $N = 1$ body is a single module (full line) with (x, z) reference. $N = 2$ are two hinged modules (full and dotted line) with (x, z') reference, and the hinge is located at $(0, z_h)$.

The total number of degrees of freedom $j = (1, 2, ..., N + 1)$ is restricted to vertical modes. This consequently yields one translatory motion; heave, and one rotationary motion; pitch. Each mode is presented by a vector shape function $\mathbf{S}_j(\mathbf{x})$ with Cartesian components (U_j, V_j, W_j) for a 6 DOF system. Meaning that, in our case, it only has the component (W_j). Hence following a modal shapes as shown in *Figure 3.4*.

$\mathbf{S}_j(\mathbf{x})$ gives the excursion of a point x on the body, when the body is displaced by 1 unit amplitude in mode j. Thus, we can express the rigid body modes for heave and pitch respectively as

$$j = 1 \qquad \text{Rigid heave mode}$$

$$j = 2 \qquad \text{Rigid pitch mode}$$

where the shape function is a unit vector in corresponding direction, and for $j = 2$, we have the vector shape function

$$\mathbf{S}_j(\mathbf{x}) = \mathbf{S}_{j-1} \times \mathbf{x} \qquad \text{for} \qquad j = 2$$

using cross multiplication. Yielding the rigid mode shape functions for heave and pitch expressed in *Table B.1* to the left.

By the defined rigid body modes $j = 1, 2$, the complex amplitude of the structure motions in unit-amplitude ξ_j is determined by Newtons 2nd law, corresponding to a similar array equation of motion as in *(3.51)*. Now taking the sum of the two predefined rigid body modes, yielding for a single body

$$\sum_{j=1}^{2} \xi_j[-\omega^2(M_{ij} + a_{ij}) + i\omega b_{ij} + c_{ij}] = X_i \qquad (i = 1, 2) \tag{B.1}$$

Assuming frequency independent coefficients. Where X_i is the complex amplitude of the wave excitation in the mode i. c_{ij} includes the hydrostatic and gravitational restoring force. The time factor $e^{i\omega t}$ is factored out, but it is possible to obtain temporal variation by multiplication

$$\Re\left\{\xi_j e^{i\omega t}\right\} \tag{B.2}$$

The elements of the mass matrix

$$M_{ij} = \int_V \rho_b(\mathbf{x})\mathbf{S}_i(\mathbf{x}) \bullet \mathbf{S}_j(\mathbf{x})dV \tag{B.3}$$

where ρ_b is the density of the structure, $\mathbf{S}_i$ and $\mathbf{S}_j$ is the shape function for the i'th and j'th mode respectively, and V the volume of the structure. Furthermore, in the final computations, we assume equal density for the structure components. Here, symmetry is utilized on the multi-body structure.

The hydrostatic restoring coefficient, in the earth-fixed coordinate system defined above, can similarly be expressed as

$$c_{ij} = \rho g \int_S (\mathbf{S}_i(\mathbf{x}) \bullet \mathbf{k})(\mathbf{S}_j(\mathbf{x}) \bullet \mathbf{n})dS \tag{B.4}$$

where $\mathbf{k}$ and $\mathbf{n}$ are the unit vectors in z-direction and the unit vector into the body, respectively. This formulation also generally contains a divergence term, but for the chosen modes this term vanishes (Mathai, 2000).

By extension to multiple bodies, *(B.1)* is extended with $2N$ DOF. Now applying generalized modes consistent with constraints that allow relative pitch rotation between $N = 2$ hinged modules. Utilizing symmetry about $(x, z) = (0, 0)$ in the predefined coordinate system, the hinge location is at $(x, z) = (0, z_h)$, where z_h denotes the distance from the mean free-surface to the vertical position of the hinge. So, choosing modes by utilizing symmetry results in 2 rigid modes of the ensemble, and 2 generalized modes for opposite oscillation. These mode definitions are shown in *Table B.1*, where the table to the left shows the ensemble rigid modes, corresponding to global heave and pitch, and generalized modes for opposite oscillation of the respective modules to the right.

j	W_j
1	1
2	$-x$

j	Body 1, W_j	Body 2, W_j
3	1	-1
4	$-x$	x

Tabell B.1: Table showing the shape functions for $N = 2$ bodies, where the 2 rigid body modes of the ensemble is expressed in the left table, and the 2 generalized modes for opposite oscillation is expressed in the right table.

If the model was to be extended to a large row of modules $N > 2$, one could assume hydrodynamic coupling limited to adjacent modules to simplify the calculations.

B.2 Equation of Motion for full Array

By the defined shape functions by rigid modes of the $N = 2$ bodies ensemble and the generalized symmetric modes, the array EOM shown in *(B.1)* can be extended.

$$\sum_{j=1}^{N+1} \xi_j[-\omega^2(M_{ij} + a_{ij}) + i\omega b_{ij} + c_{ij}] = X_i \qquad (i = 1, 2, 3) \qquad (j = 1, 2, 3) \tag{B.5}$$

The procedure for determining the complex unit amplitude of the different modes prior to super-positioning, is to determine the exciting forces and hydrodynamic coefficients for the full array, i.e. for every mode. Furthermore, it is necessary to apply linear transformations to convert the hydrodynamic parameters from generalized modes to conventional modes. These are the same as shown in the work done by T. Mathai (Mathai, 2000), but only concerning heave and pitch DOF in the computed analysis presented here.

B.2.1 Hydrodynamic Solution

The model and calculations will initially be based on the following assumptions.

- The structure is exposed to incident regular regular waves with amplitude ζ_a and frequency ω in deep water.
- No current exposure.
- Steady-state conditions.
- The structure have zero forward speed.
- The structure is freely floating and the mean buoyancy is balanced by the body weight.
- The mass distribution of the structure neglects the inertia from the top frame component.
- Linear potential flow theory is valid.
- Strip theory and long-wave approximation are valid.
- Frequency independent added mass and damping coefficients, neglecting wave radiation damping.
- No mooring present, structure simplified as a single top plate and identical cylindrical floaters.

By the established model of the global structure and the application and formulation of the generalized modes, we can solve the hydrodynamic problem of excitation and radiation. Naturally using linearity, decomposition and superposition.

For the radiation problem, governed by the radiation potential in *Equation 3.45*, the added mass and damping coefficients can be written as

$$\omega^2 a_{ij} - i\omega b_{ij} = -i\omega\rho \int_S \phi_j(\mathbf{S}_j(\mathbf{x}) \bullet \mathbf{n}) dS \tag{B.6}$$

and again the general wave excitation force

$$X_i = -i\omega\rho \int\int_S \phi_D(\mathbf{S}_j(\mathbf{x}) \bullet \mathbf{n}) dS \tag{B.7}$$

These equations are solved separately by the modal excitation and radiation problem as described in *Chapter 3.2.3*, consequently yielding an array of equations that can be substituted in *(B.5)*.

B.2.2 Simplification of the Hydrodynamic Solution

When this similar method and formulation is used for studying the hydrodynamic multi-body wave-structure interaction, the works done by Newman and Mathai use numerical and software tools in order to determine the modal added mass and damping coefficients. This is not the case in this Thesis. Hence very rough estimations of both the excitation and mentioned coefficients are applied.

The approximate expressions for the added mass in heave that corresponds to floater geometry from tabular values for freely floating cylinders are used (Pettersen et al., 2014). The modal coefficient is onward found by applying the shape function, which means that the vertical heave coefficient is used when computing the pitch and coupled added mass. A same approach is done for the viscous damping coefficient, following the expression in *(3.40)* for each modal forced motion. This component is highly dependent on the drag coefficient, which here is implemented with different values in the final plot to indicate its influence. No real study has been done in order to select an appropriate drag component, but experimental observation suggested important viscous forces occurring on the floaters.

The modal excitation is found by the vertical Froude-Kriloff pressure force exciting the floaters in each mode. As for the coefficients, only vertical excitation and corresponding integration is implemented in the final calculation. The diffraction component uses the Haskind relation, discussed in *Chapter 3.2.3*, that again utilizes the corresponding modal added mass coefficient and vertical acceleration of the body. Which were discussed in

The modal velocity potentials are explicitly used as in *(B.7)* and *(3.5)*.

B.2.3 Wave-Structure Interaction

The incident wave velocity potentials for linear waves propagating in positive x-direction with dispersion relation

$$\phi_0 = \frac{g\zeta_a}{\omega}\mathrm{exp}(kz + ikx - i\omega t) \tag{B.8}$$

yields the wave elevation from the dynamic free-surface condition

$$g\zeta + \frac{\partial \phi}{\partial t} = 0 \qquad \text{on} \qquad z = 0 \tag{B.9}$$

$$\zeta = i\zeta_a \mathrm{exp}(ikx - \omega t) \tag{B.10}$$

which, for the current model and assumptions, we can write as

$$\phi_0 = \frac{g\zeta_a}{\omega} e^{kz} \cos(\omega t - kx) \tag{B.11}$$

The resulting dynamic pressure, x- and z-component acceleration are respectively, with wave number k

$$p_0 = \rho g \zeta_a e^{kz} \sin(\omega t - kx) \tag{B.12}$$

$$a_{0j} = \omega^2 \zeta_a e^{kz} \cos(\omega t - kx) \qquad \text{and} \qquad a_{0j} = -\omega^2 \zeta_a e^{kz} \sin(\omega t - kx) \tag{B.13}$$

Vertical Excitation

The excitation forces in heave is due to the Froude-Kriloff and diffraction loads occurring all the floaters. Due to symmetry, this will yield a left and right contribution evaluated at different positions in x-direction in terms of number of bodies N with respective floaters.

The excitation force can therefore be expressed as

$$F_{FK,j} = -\frac{4N}{2}\int_{S_B} p_{0,left}(\mathbf{S}_j(\mathbf{x}) \bullet \mathbf{n})dS\Big|_{x<1} - \frac{4N}{2}\int_{S_B} p_{0,right}(\mathbf{S}_j(\mathbf{x}) \bullet \mathbf{n})dS\Big|_{x>1} \tag{B.14}$$

as there are $4N$ floaters on the system, with equal hydrodynamic distribution for $x < 0$ and $x > 0$, with the diffraction force similarily

$$F_{D,j} = \frac{N}{2}a_{0j}A_{ij}\Big|_{x<0} + \frac{N}{2}a_{0j}A_{ij}\Big|_{x>0} \tag{B.15}$$

where $j = 1, 3$ will yield the global heave mode with $N = 1$ and $N = 2$ respectively, where the evolution of the mathematical expression will be the floater contributions and terms associated with phase difference between the left and right contributions in beam sea. Similarly, for pitch, the shape functions will give excitation moments by modal function and consequently an additional factor representing the left and right momentum "arm"acting on the cross-sectional area of the floaters. The evaluated distances for hydrodynamic pressure integration and diffraction will be symmetric and can be equally implemented for $N = 2$ bodies.

Inserting the expressions for the pressure and acceleration, evaluating the z-component at $z = -d$, with the normal vector pointing into the fluid, and the integration over the contributed wetted surface yields for $N = 1$ and $j = 1$

$$F^{(N=1)}_{FK,1} = 4A\rho g\zeta_a e^{-kd}\cos\left(\frac{kl}{2}\right)\sin(\omega t) \qquad F^{(N=1)}_{D,1} = -A_{11}\omega^2\zeta_a e^{-kd}\cos\left(\frac{kl}{2}\right)\sin(\omega t) \tag{B.16}$$

By including viscous damping, the response amplitude operators will be more realistic as the resonance peaks and cancellation domains are expected to be corrected. Utilizing the linearized drag force over a strip from *Equation 3.39* and the viscous damping coefficient it holds, shown in *(3.40)*, we can extend the excitation (and radiation) terms. However, it requires using appropriate drag coefficients for each mode. These are expected to have values within the range of 0.5 and 2 (Cengel and Cimbala, 2010), and in reality for the linearized term it needs to be found by iteration. This is neglected, where calculations are performed with different magnitudes of the drag coefficient.

Thus by inclusion of damping, we have the total excitation force for $N = 1$ in heave and pitch mode $j = 1, 2$ expressed as

$$F^{(N=1)}_{exc,j=1} = [4A\rho g - \omega^2 A_{11} - \omega B_{visc,1}e^{i\pi/2}]\cos\left(\frac{kl}{2}\right)e^{-kd}\zeta_a\sin(\omega t) \tag{B.17}$$

In the same manner, using $j = 2$, the $N = 1$ pitch mode excitation can be written as

$$F^{(N=1)}_{exc,j=2} = -[4A\rho g - \omega^2 A_{11} - \omega B_{vsic,1}e^{i\pi/2}]\left(\frac{lD}{2}\right)\cos\left(\frac{kl}{2}\right)e^{-kd}\zeta_a\sin(\omega t) \tag{B.18}$$

where the added mass and viscous damping coefficients from the Haskind relation and viscous excitation component remains the same as in heave $j = 1$, as the vertical excitation that induces the pitch $j = 2$ moment, originates from the same properties.

Following the same procedure with extension to $N = 2$ bodies, we get the $j = 3$ global heave, and $j = 4$ global pitch to be expressed as.

$$F^{(N=2)}_{exc,j=3} = [4A\rho g - \omega^2 A_{21} + \omega B_{visc,1} e^{i\pi/2}][\cos(kl_f) + \cos(k(l + l_f))]e^{-kd} \tag{B.19}$$

$$F^{(N=2)}_{exc,j=4} = -[4A\rho g - \omega^2 A_{21} - \omega B_{vsic,1} e^{i\pi/2}](2l_f D + lD)[\cos(kl_f) + \cos(k(l + l_f))]e^{-kd} \tag{B.20}$$

where A_{21} is a number of floaters factor increase of A_{11} as the coefficients are assumed to be identical for each floater.

The superposition of pitch excitation, adding $j = 4$ to *(B.20)* is not included, as it is not derived by hand, but only calculated in *Matlab*.

Radiation

The modal hydrostatic force from *B.4* will in global heave modes follow *3.26* and give the restoring coefficients

$$C_{11} = 4A\rho g \tag{B.21}$$

where, as in excitation, C_{21} will be a factor increase by number of floater contributions when extending to $N = 2$ bodies.

This again will have an added mass coefficient A_{21} following A_{11}. Considering *Equation 3.25*, the added mass coefficient in heave by the four contributions of the floaters will be equivalent to half the contribution of the added mass in heave for an elliptical disk for each floater (Pettersen et al., 2014). From a standardized table in (Pettersen et al., 2014), page 3.66, we can approximate the single floater added mass coefficient as

$$A_{11} = \frac{1}{2}\Big[0.637 \frac{\pi}{6} \rho (\frac{D}{2})^3\Big] \tag{B.22}$$

For rotations, the restoring term occurs from the change in displacement on the floaters when it rotates in pitch. These changes consequently creates a destabilizing and stabilizing moment, which we can express in general as

$$M_{stab} = -\rho g \int_{A_w} x^2 dS \eta_j$$

$$M_{destab} = \rho g V \Big[\int_m z dm/m - \int_V dV/V\Big]\eta_j$$

for $j = 2, 4$. The sum of these moments defines the restoring moment and hence the coefficient

$$F_{hydrostat,j} = -\rho g V \Big[\int_{A_w} x^2 dS/V + z_B - z_{CoG}\Big]\eta_j = -C_{ij}\eta_j \qquad (j = 1, 4)$$

where the terms in the parenthesis is the distance between the centre of gravity and the meta centre. Thus, using $N = 1$ as an example, we get

$$C_{12} = \rho g \nabla \overline{GM}_L \tag{B.23}$$

The modal added mass coefficients for the rotational DOF is found by the radiation force from forced pitch motions of the structure. The heave added mass coefficients are known, so by applying the shape functions as in modal excitation with a varying contribution of floaters from different number of bodies, we get explicitly for $N = 1$

$$A_{12} = A_{11} \int_{\pm\frac{l}{2}-\frac{D}{2}}^{\pm\frac{l}{2}+\frac{D}{2}} x^2 dx = A_{11}\Big(\frac{l^2D + 3D^3}{2}\Big) \tag{B.24}$$

in terms of the total system added mass coefficient in global heave modes $(j = 1, 3)$ in general and when implementing $N = 2$ number of bodies

$$A_{24} = A_{21} \int_{\text{floaters}} x^2 dx \tag{B.25}$$

B.3 Theoretical RAO

For the purpose of direct RAO comparison with experimental results, the indices are shifted back to conventional ones, where modal number 3 and 5 represents heave and pitch respectively. Unfortunately, as previously mentioned, the superposition of pitch mode for $N = 2$ is not explicitly derived, but calculated in *Matlab*. Hence, the explicit expression for $N = 2$ pitch RAO is only shown for the global pitch mode, i.e. $j = 4$. Combining the excitation and radiation shown above, the $N = 1$ and $N = 2$ module(s), after respective evaluation, wet surface integration, the following two equations are obtained.

$$\Big|\frac{\eta_{3a}^{(N=1)}}{\zeta_a}\Big| = \Big|\frac{[4A\rho g - \omega^2 A_{33} - \omega B_{visc,3} e^{i\pi/2}]\cos\left(\frac{kl}{2}\right)e^{-kd}}{-\omega^2(m + A_{33}) + C_{33} + i\omega B_{visc,3}}\Big| \tag{B.26}$$

$$\Big|\frac{\eta_{5a}^{(N=1)}}{k\zeta_a}\Big| = \Big|\frac{-[4A\rho g - \omega^2 A_{33} - \omega B_{vsic,3}]\left(\frac{lD}{2}\right)\cos\left(\frac{kl}{2}\right)e^{-kd}e^{i\pi/2}}{-k[\omega^2(I_5 + A_{55}) + C_{55} + i\omega B_{visc,5}]}\Big| \tag{B.27}$$

where *(B.26)* and *(B.27)* is the heave and pitch RAO for $N = 1$ bodies, and

$$\Big|\frac{\eta_{3a}^{(N=2)}}{\zeta_a}\Big| = \Big|\frac{[4A\rho g - \omega^2 A_{33} + \omega B_{visc,3} e^{i\pi/2}][\cos(kl_f) + \cos(k(l + l_f))]e^{-kd}}{-\omega^2(m + A_{33}) + C_{33} + i\omega B_{visc,3}}\Big| \tag{B.28}$$

$$\Big|\frac{\eta_{5a}^{(N=2)}}{k\zeta_a}\Big| = \Big|\frac{-[4A\rho g - \omega^2 A_{33} - \omega B_{vsic,3} e^{i\pi/2}](2l_f D + lD)[\cos(kl_f) + \cos(k(l + l_f))]e^{-kd}}{-k[\omega^2(I_5 + A_{55}) + C_{55} + i\omega B_{visc,5}]}\Big| \tag{B.29}$$

(B.28) and *(B.29)* is the heave and pitch RAO for $N = 2$ bodies. Using conventional indices. The latter also including inertia from the mass matrix. The resulting RAO can then be plotted against a sample of frequencies to reveal the structural response in terms of a frequency domain analysis.

B.3.1 Results & Discussion

The *Matlab* plotted RAOs of the single and two hinged modules are shown below, using different values for the drag coefficient C_D that governs the viscous damping and excitation terms. *Figure B.2* shows the plotted RAO for $N = 1$ number of modules, and *Figure B.3* for $N = 2$ number of bodies. All plotted with respect to the non-dimensional wave-number kl corresponding to the case 3 wave-series characteristics.

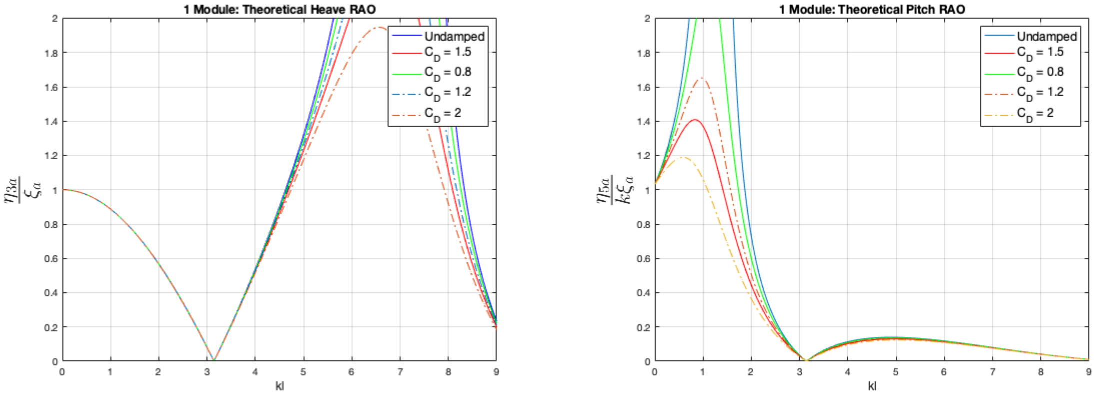

Figur B.2: Theoretical model heave (left) and pitch (right) RAO with $N = 1$ number of bodies using conventional indices, including undamped and viscous damped with drag coefficients $C_D = 0.8, 1.2, 1.5, 2.0$, plotted against the non-dimensional wave-number kl.

The results for $N = 1$ states and shows the resonance and cancellation that occurs for $kl \approx 7$ and $kl = \pi$, respectively. Corresponding to a resonance period $T_{n,3}^{(N=1)} = 2.2$s and hence a wavelength of $\lambda \approx 7.5$m, which seems reasonable as two wave-crests at this characteristic would be located in the vicinity of adjacent floaters simultaneously. The heave cancellation wave-number is also in agreement with wave-crest and trough at adjacent cylinders. Resonant pitch is located at $kl = 1.25$ which corresponds to a resonance period $T_{n,5}^{(N=2)} = 5.2$s. The increase relative pitch amplitude along kl is quite steep, suggesting an ability to follow the incident waves with sufficiently long periods $T > 7$ only.

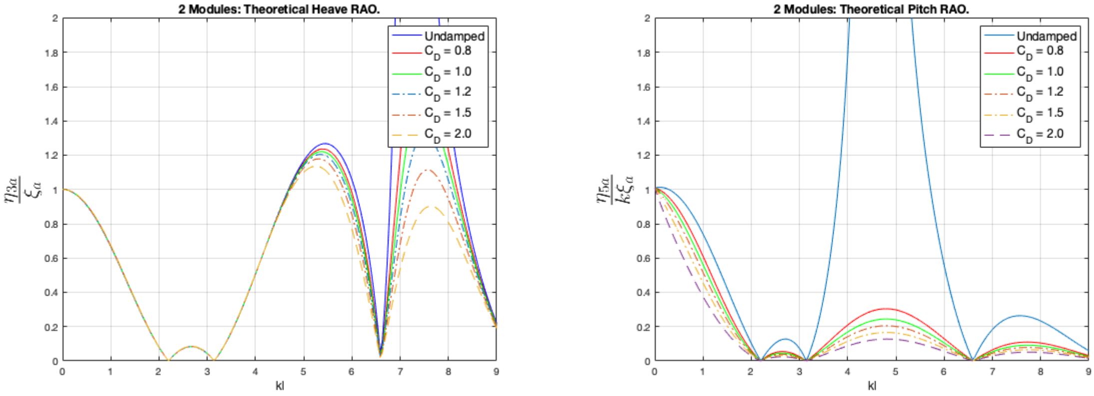

Figur B.3: Theoretical model heave (left) and pitch (right) RAO with $N = 2$ number of bodies using conventional indices, including undamped and viscous damped with drag coefficients $C_D = 0.8, 1.2, 1.5, 2.0$, plotted against the non-dimensional wave-number kl.

Comparing the two models, there is a shift in resonant domains. Extending the indicated T constraint for good ability to follow the wave to include lower periods, and more cancellations are present. The most plausible reason for this is the change in the earth-fixed reference system as shown in *Figure B.1*. Evaluating the wave-lengths for the additional cancellation periods, shown at $kl \approx 2.2$ and $kl \approx 6.67$, reveals that the former is very close to the case where wave-crest and trough are at adjacent floaters on each module. The latter suggests short waves that have wave-crests on the left module and wave-trough's on the right module, which is also a period close to heave resonance for $N = 1$. Seemingly reasonable. The influence by various viscous drag coefficients are more significant in heave than for pitch. For the lowest kl, pitch seems to be unrealistically over-damped.

The heave resonance occurs at $kl = 7.5$, i.e. the heave resonant period is $T_{n,3}^{(N=2)} \approx 2.12$s, which is fairly close to $T_{n,3}^{(N=1)}$ and the HF cancellation waves. In pitch, the shift in resonance from $N = 1$ is larger, as $kl = 4.8$ so that $T_{n,5}^{(N=2)} = 2.65$s. Suggesting that adding another module gives little change in heave resonance period, but lowered the resonance period in pitch.

The theoretical model is unfortunately not properly tested, as the wave-series characteristics for the case 1 and case 2 model tests are only a small interval of kl. this comparison and an additional evaluation of the theoretical model in terms of the case 3 model test is discussed in *Chapter 5.7*.

Without mooring, major uncertainties are present, being mainly the hydrodynamic coefficients and isolation of vertical excitation components. As a result, the theoretical model needs work. The first proposition for further development is to apply numerical software to determine appropriate coefficients or use reference values for the cylindrical floaters suggested by Ronald W. Yeung (Yeung, 1980). Moreover, correct model implementation of hinge restrictions and relative module response are also questioned. A similar study is conducted by Newman (Lee and Newman, 2000), with an array of 5 barges, but there is little correlation between the two results.

Appendix C

JONSWAP Irregular Wave Spectrum

During experimental model testing, the energy spectrum of the input waves must be accurate in order to produce realistic wave frequency responses (Steen, 2014). To check if this generated input is comparable to realistic sea conditions, the spectral density of the input wave field can be compared to the JONSWAP spectrum. This gives a theoretical description of the irregular sea state and can be applied for fully developed, fetch limited wind seas. This is intended to be utilized in the coming experimental study.

The JONSWAP spectrum $S_j(\omega)$ is given by

$$S_j(\omega) = \frac{5}{16} A_\gamma H_s^2 \omega_p^4 \mathrm{exp}\Big[-\frac{5}{4}\Big(\frac{\omega}{\omega_p}\Big)^{-4}\Big]\gamma e^{-0.5(\frac{\omega-\omega_p}{\sigma\omega_p})^2} \tag{C.1}$$

where T_p is the peak period and γ the non-dimensional peak shape parameter. This parameter can, if no values of it are given, have the following applied values

$$\begin{aligned}
\gamma_p &= 5 && \text{for} \quad \frac{T_p}{\sqrt{H_s}} \leq 3.6 \\
\gamma_p &= e^{5.75-1.15\frac{T_p}{\sqrt{H_s}}} && \text{for} \quad 3.6 \leq \frac{T_p}{\sqrt{H_s}} < 5 \\
\gamma_p &= 1.0 && \text{for} \quad 5 \leq \frac{T_p}{\sqrt{H_s}}
\end{aligned} \tag{C.2}$$

and the spectra width parameter σ can be found as (Myrhaug and Lian, 2009)

$$\sigma = \begin{cases} \sigma_a & \text{for} \quad \omega \leq \omega_p \\ \sigma_b & \text{for} \quad \omega > \omega_p \end{cases} \tag{C.3}$$

Typical values for the spectral width parameter are $\sigma_a = 0.07$ and $\sigma_b = 0.09$, and a normalization factor A_γ is given by

$$A_\gamma = 1 - 0.0287 \ln(\gamma) \tag{C.4}$$

Appendix D

Wave-Series in Model Scale

Tabell D.1: Test conditions for regular waves in model scale.

T [s]	λ [m]	H/ $\lambda = 1/60$ H [m]	H/$\lambda = 1/40$ H [m]	H/$\lambda = 1/30$ H [m]	H/$\lambda = 1/20$ H[m]
0.4472	0.3123	0.0052	0.0078	0.0104	0.0156
0.5590	0.4879	0.0081	0.0122	0.0163	0.0244
0.6708	0.7026	0.0117	0.0176	0.0234	0.0351
0.7826	0.9563	0.0159	0.0239	0.0319	0.0478
0.8944	1.2490	0.0208	0.0312	0.0416	0.0625
1.0062	1.5808	0.0263	0.0395	0.0527	0.0790
1.1180	1.9516	0.0325	0.0488	0.0651	0.0976
1.2298	2.3615	0.0394	0.0590	0.0787	0.1181
1.3416	2.8104	0.0468	0.0703	0.0937	0.1405
1.4534	3.2983	0.0550	0.0825	0.1099	0.1649
1.5652	3.8252	0.0638	0.0956	0.1275	0.1913
1.6771	4.3912	0.0732	0.1098	0.1464	0.2196
1.7889	4.9962	0.0833	0.1249	0.1665	0.2498
1.9007	5.6402	0.0940	0.1410	0.1880	0.2820
2.0125	6.3233	0.1054	0.1581	0.2108	0.3162
2.1243	7.0454	0.1174	0.1761	0.2348	0.3523
2.2361	7.8065	0.1301	0.1952	0.2602	0.3903
2.3479	8.6067	0.1434	0.2152	0.2869	0.4303
2.4597	9.4459	0.1574	0.2361	0.3149	0.4723
2.5715	10.3242	0.1721	0.2581	0.3441	0.5162
2.6833	11.2414	0.1874	0.2810	0.3747	0.5621
2.7951	12.1977	0.2033	0.3049	0.4066	0.6099
2.9069	13.1931	0.2199	0.3298	0.4398	0.6597

Tabell D.2: Test conditions for irregular waves in model scale.

T_p [s]	0.8944	1.0286	1.2746	1.5205	1.5652	1.7889	1.9007	2.2361	2.6833
H_s [m]	0.0625	0.1000	0.1500	0.2000	0.1000	0.1500	0.1750	0.1500 0.1750 0.2000	0.2000 0.2250

Appendix E

Wave Height Plots - Regular Waves

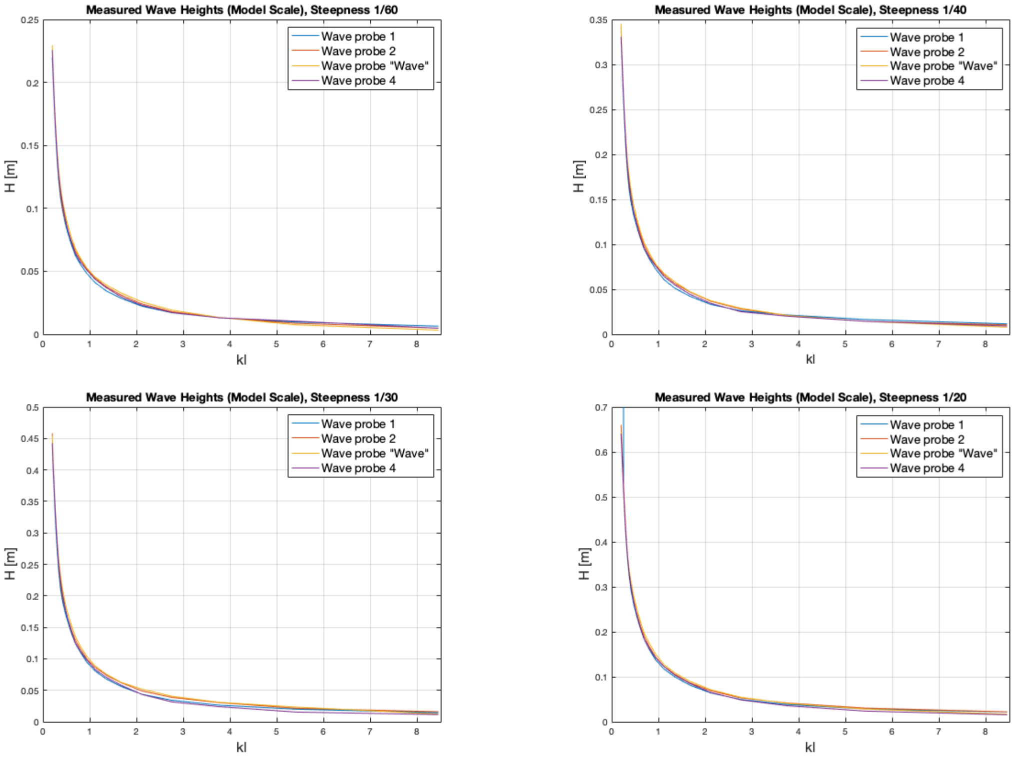

Figur E.1: Measured regular wave heights at all wave probes for wave steepness $H/\lambda = 1/60$ (top left), $H/\lambda = 1/40$ (top right), $H/\lambda = 1/30$ (bottom left) and $H/\lambda = 1/20$ (bottom right)

Appendix F

Example Measurements - Regular Waves

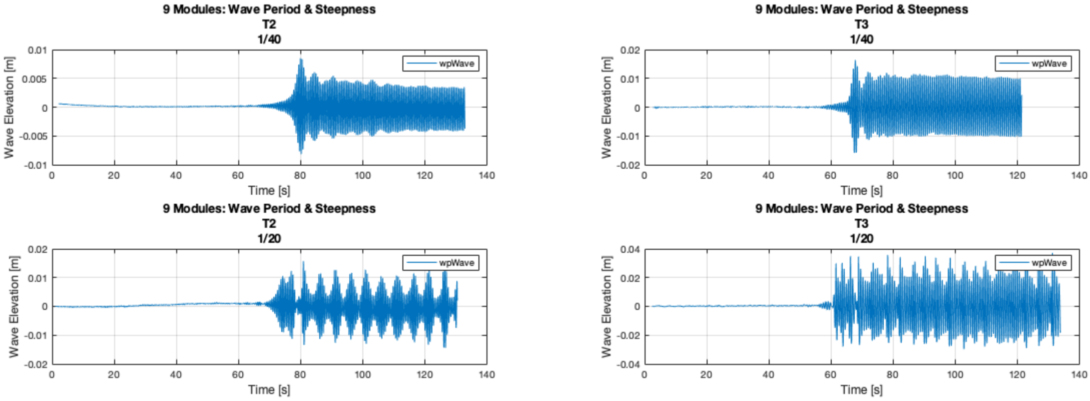

Figur F.1: Measurements of the generated wave at wave-probe *wave* (positioned at the wave-entry of the model) in the 9 modules model tests with $T = 2$s (left) and $T = 3$s (right), with steepness $H/\lambda = 1/40$ (top) and $H/\lambda = 1/20$ (bottom).

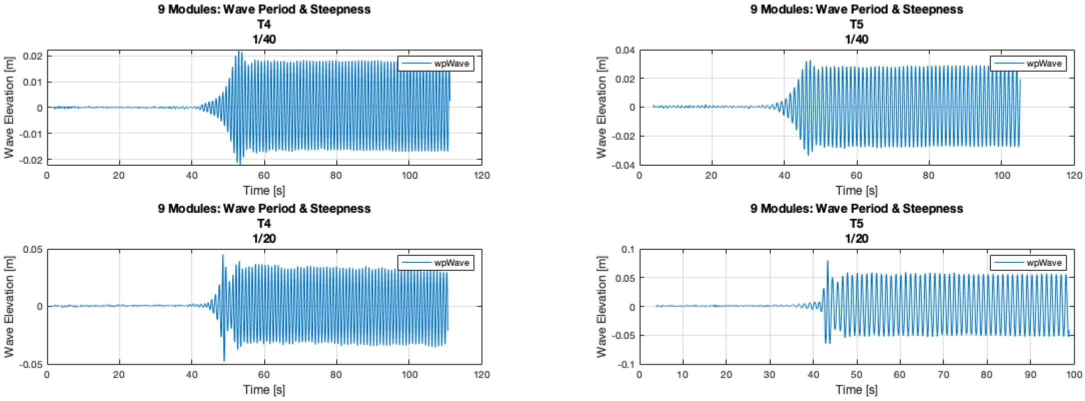

Figur F.2: Measurements of the generated wave at wave-probe *wave* (positioned at the wave-entry of the model) in the 9 modules model tests with $T = 4$s (left) and $T = 5$s (right), with steepness $H/\lambda = 1/40$ (top) and $H/\lambda = 1/20$ (bottom).

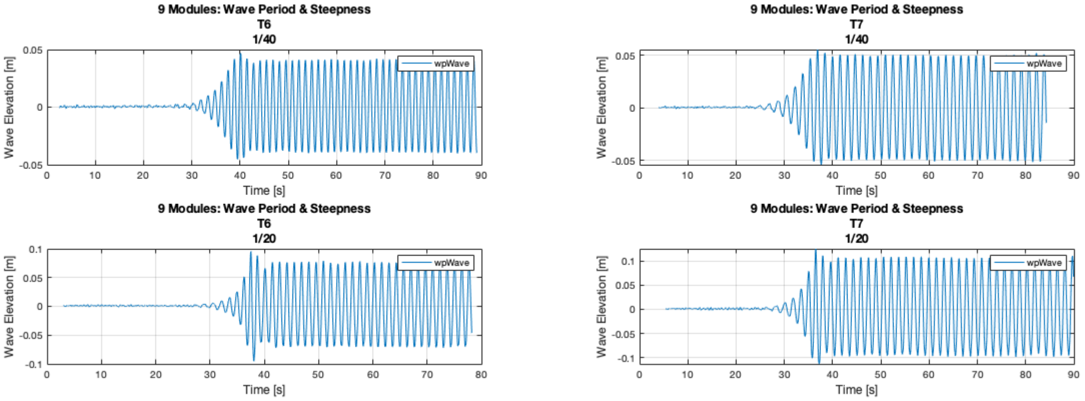

Figur F.3: Measurements of the generated wave at wave-probe *wave* (positioned at the wave-entry of the model) in the 9 modules model tests with $T = 6$s (left) and $T = 7$s (right), with steepness $H/\lambda = 1/40$ (top) and $H/\lambda = 1/20$ (bottom).

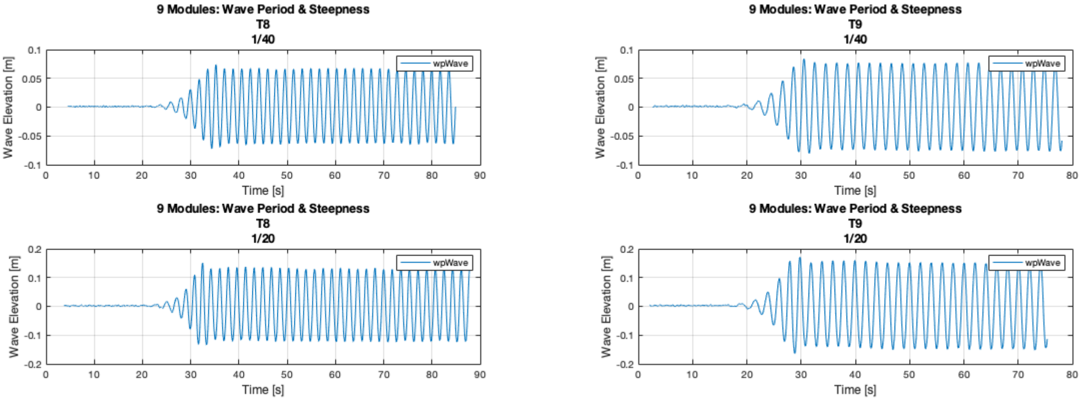

Figur F.4: Measurements of the generated wave at wave-probe *wave* (positioned at the wave-entry of the model) in the 9 modules model tests with $T = 8$s (left) and $T = 9$s (right), with steepness $H/\lambda = 1/40$ (top) and $H/\lambda = 1/20$ (bottom).

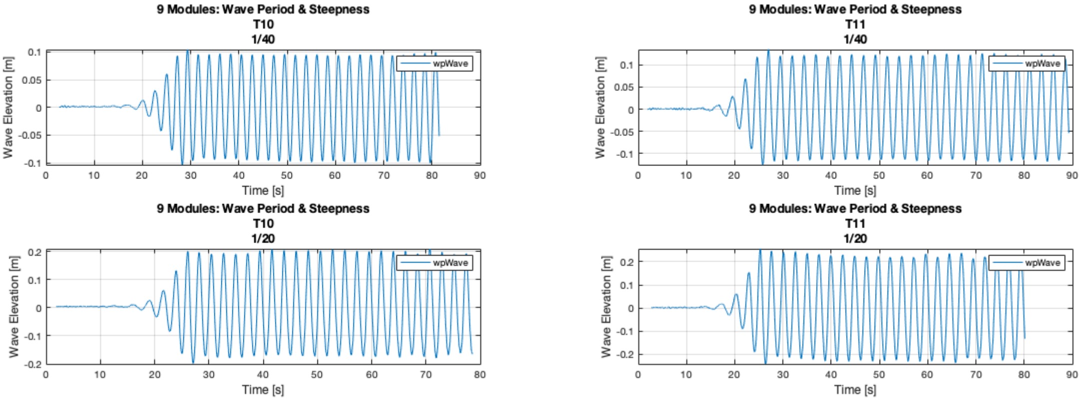

Figur F.5: Measurements of the generated wave at wave-probe *wave* (positioned at the wave-entry of the model) in the 9 modules model tests with $T = 10$s (left) and $T = 11$s (right), with steepness $H/\lambda = 1/40$ (top) and $H/\lambda = 1/20$ (bottom).

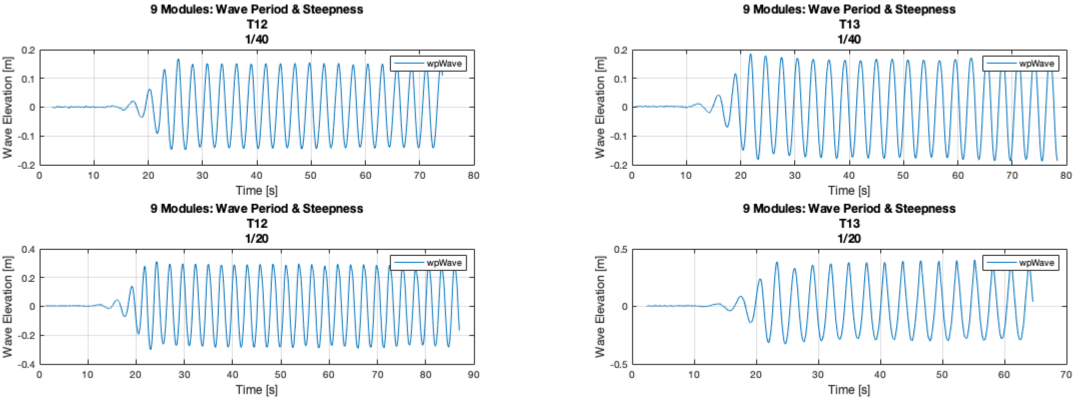

Figur F.6: Measurements of the generated wave at wave-probe *wave* (positioned at the wave-entry of the model) in the 9 modules model tests with $T = 12$s (left) and $T = 13$s (right), with steepness $H/\lambda = 1/40$ (top) and $H/\lambda = 1/20$ (bottom).

Appendix G

Examples of 1st Order Band-pass Filter - Regular Waves

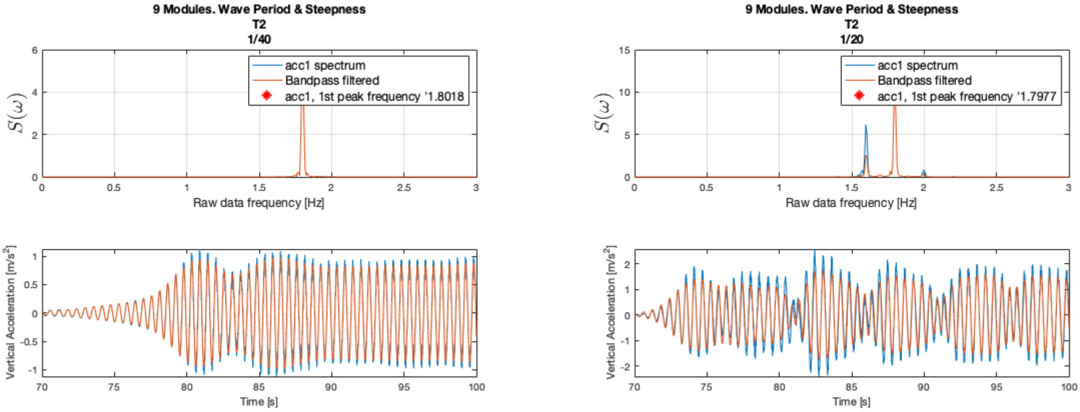

Figur G.1: 9 modules model test in $T = 2$s with steepness $H/\lambda = 1/40$ (left) and $H/\lambda = 1/20$ (right), showing unfiltered (blue) and filtered (red) acceleration measurements and corresponding spectrum at *acc1* positioned at the first end of the first module.

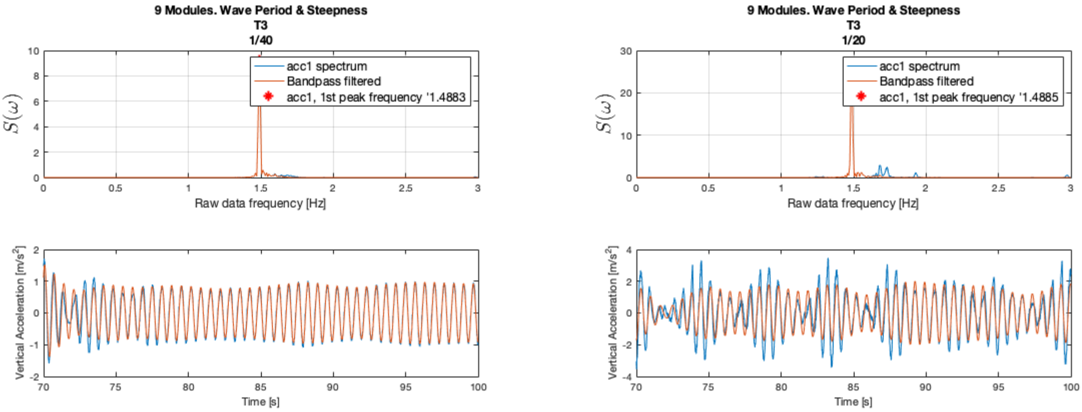

Figur G.2: 9 modules model test in $T = 3$s with steepness $H/\lambda = 1/40$ (left) and $H/\lambda = 1/20$ (right), showing unfiltered (blue) and filtered (red) acceleration measurements and corresponding spectrum at *acc1* positioned at the first end of the first module.

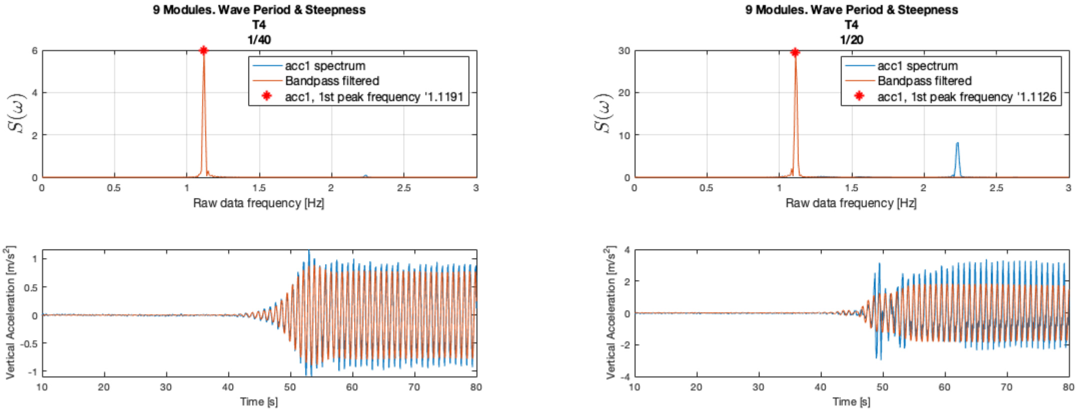

Figur G.3: 9 modules model test in $T = 4$s with steepness $H/\lambda = 1/40$ (left) and $H/\lambda = 1/20$ (right), showing unfiltered (blue) and filtered (red) acceleration measurements and corresponding spectrum at *acc1* positioned at the first end of the first module.

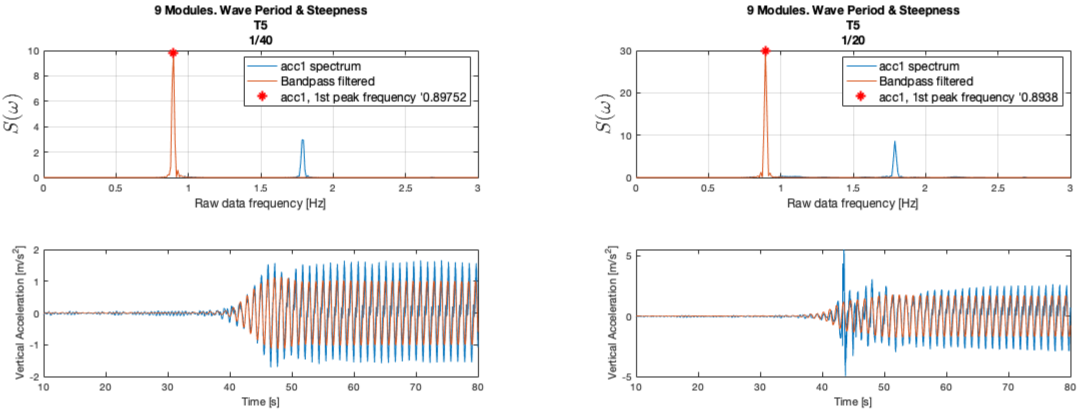

Figur G.4: 9 modules model test in $T = 5$s with steepness $H/\lambda = 1/40$ (left) and $H/\lambda = 1/20$ (right), showing unfiltered (blue) and filtered (red) acceleration measurements and corresponding spectrum at *acc1* positioned at the first end of the first module.

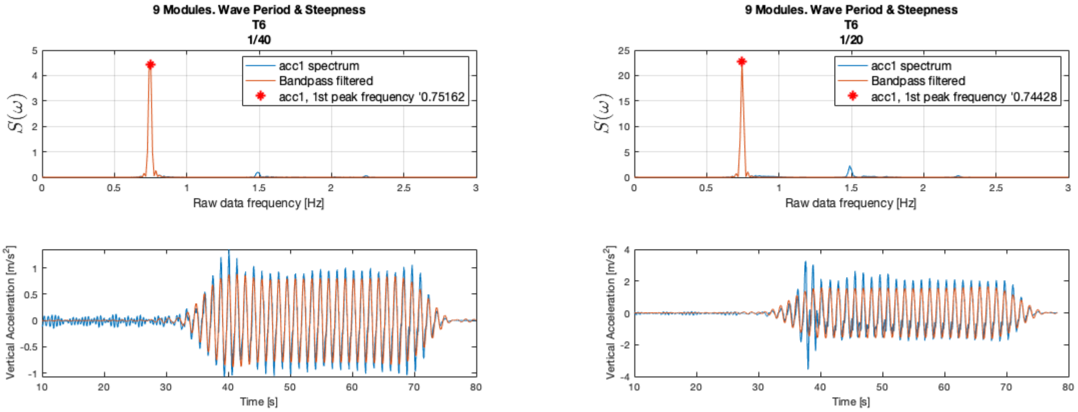

Figur G.5: 9 modules model test in $T = 6$s with steepness $H/\lambda = 1/40$ (left) and $H/\lambda = 1/20$ (right), showing unfiltered (blue) and filtered (red) acceleration measurements and corresponding spectrum at *acc1* positioned at the first end of the first module.

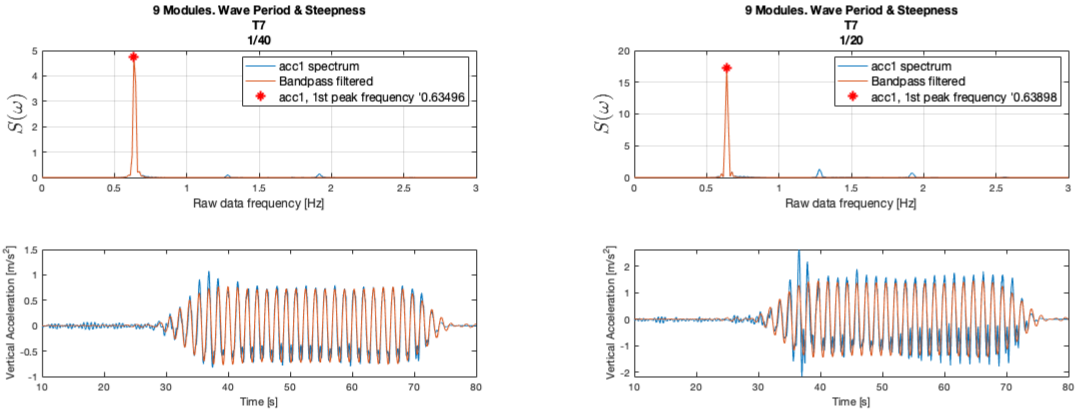

Figur G.6: 9 modules model test in $T = 7$s with steepness $H/\lambda = 1/40$ (left) and $H/\lambda = 1/20$ (right), showing unfiltered (blue) and filtered (red) acceleration measurements and corresponding spectrum at *acc1* positioned at the first end of the first module.

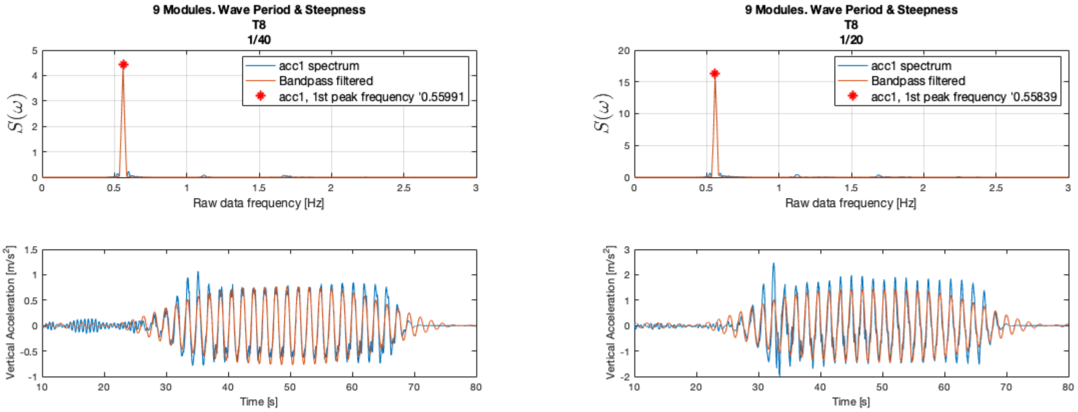

Figur G.7: 9 modules model test in $T = 8$s with steepness $H/\lambda = 1/40$ (left) and $H/\lambda = 1/20$ (right), showing unfiltered (blue) and filtered (red) acceleration measurements and corresponding spectrum at *acc1* positioned at the first end of the first module.

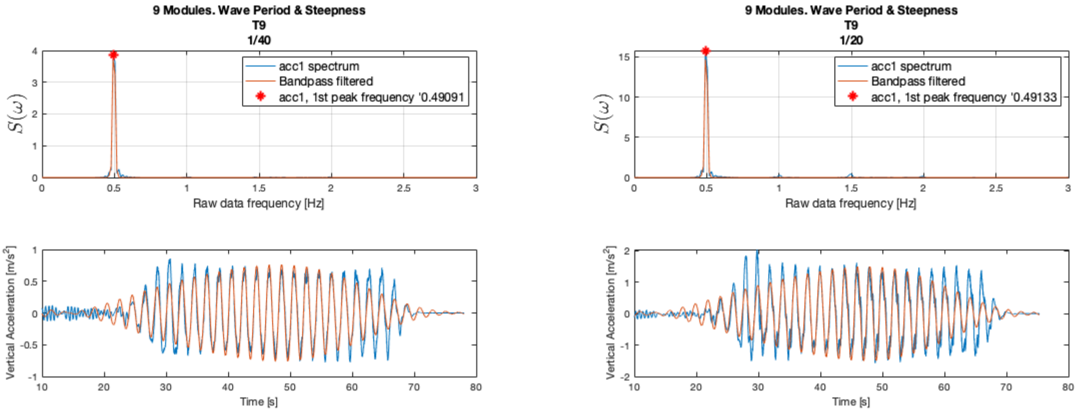

Figur G.8: 9 modules model test in $T = 9$s with steepness $H/\lambda = 1/40$ (left) and $H/\lambda = 1/20$ (right), showing unfiltered (blue) and filtered (red) acceleration measurements and corresponding spectrum at *acc1* positioned at the first end of the first module.

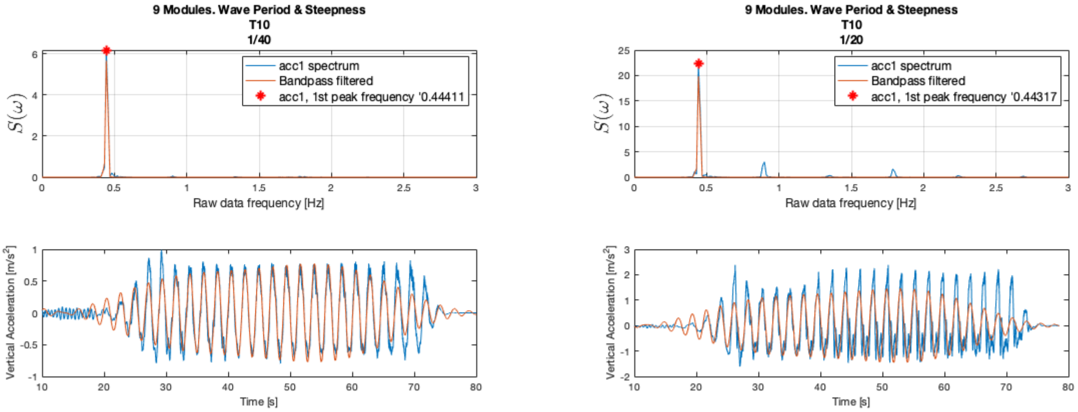

Figur G.9: 9 modules model test in $T = 10$s with steepness $H/\lambda = 1/40$ (left) and $H/\lambda = 1/20$ (right), showing unfiltered (blue) and filtered (red) acceleration measurements and corresponding spectrum at *acc1* positioned at the first end of the first module.

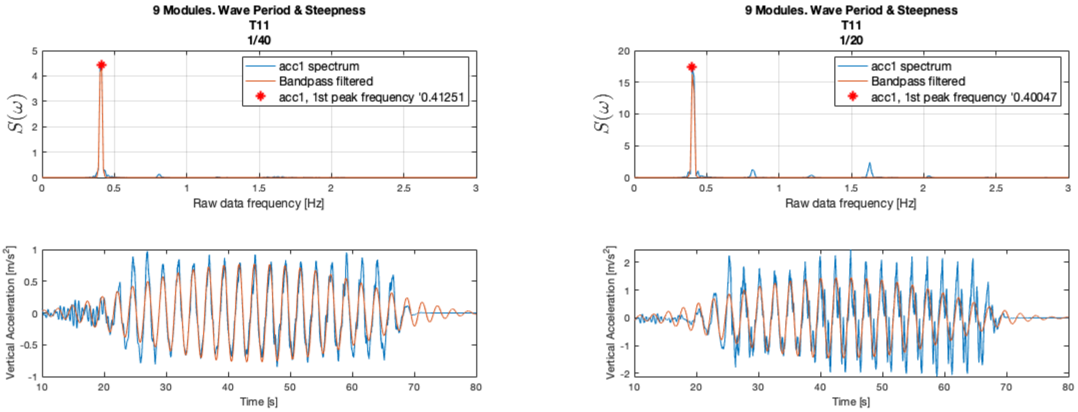

Figur G.10: 9 modules model test in $T = 11$s with steepness $H/\lambda = 1/40$ (left) and $H/\lambda = 1/20$ (right), showing unfiltered (blue) and filtered (red) acceleration measurements and corresponding spectrum at *acc1* positioned at the first end of the first module.

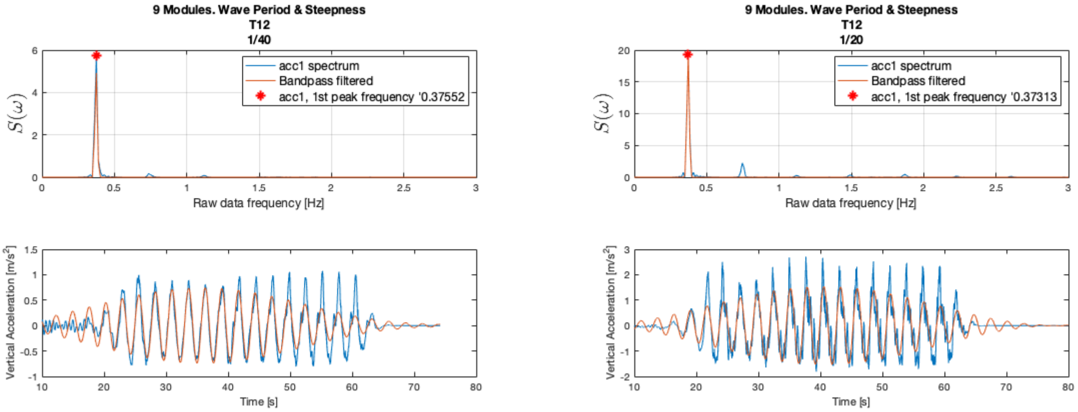

Figur G.11: 9 modules model test in $T = 12$s with steepness $H/\lambda = 1/40$ (left) and $H/\lambda = 1/20$ (right), showing unfiltered (blue) and filtered (red) acceleration measurements and corresponding spectrum at *acc1* positioned at the first end of the first module.

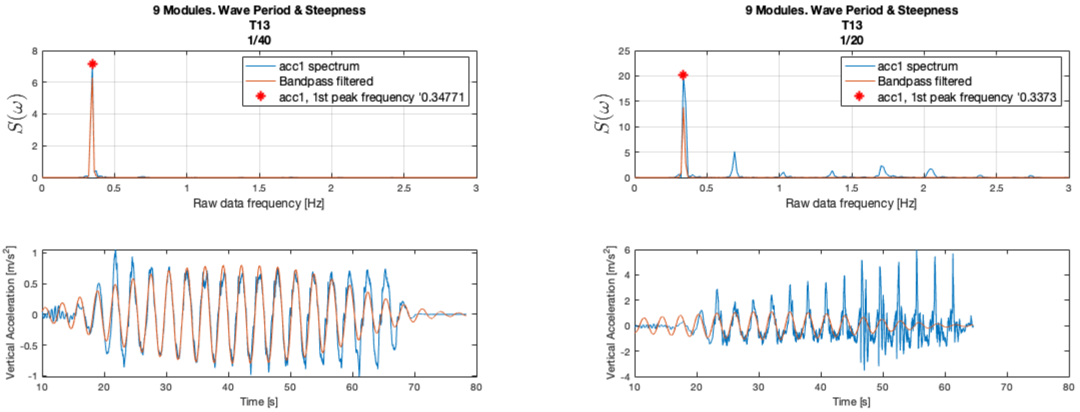

Figur G.12: 9 modules model test in $T = 13$s with steepness $H/\lambda = 1/40$ (left) and $H/\lambda = 1/20$ (right), showing unfiltered (blue) and filtered (red) acceleration measurements and corresponding spectrum at *acc1* positioned at the first end of the first module.

Appendix H

Wave-maker Instability - Regular Waves

This appendix shows the generated waves within the period ranges that contain instability for some wave-steepnesses in the model tests for each of the 3 cases. The figures illustrates this phenomena using the raw time-series for the wave-probe *wave* with its corresponding spectrum. The latter obtained by FFT.

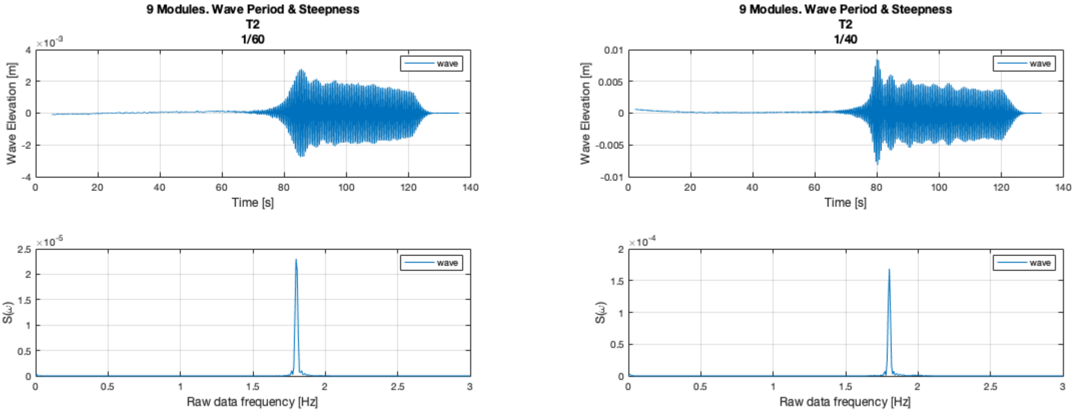

Figur H.1: Wave elevation measurements in $T = 2$s and steepness $H/\lambda = 1/60$ (left) and $H/\lambda = 1/40$ (right), taken at wave-probe *wave* positioned at the wave-entry of the model.

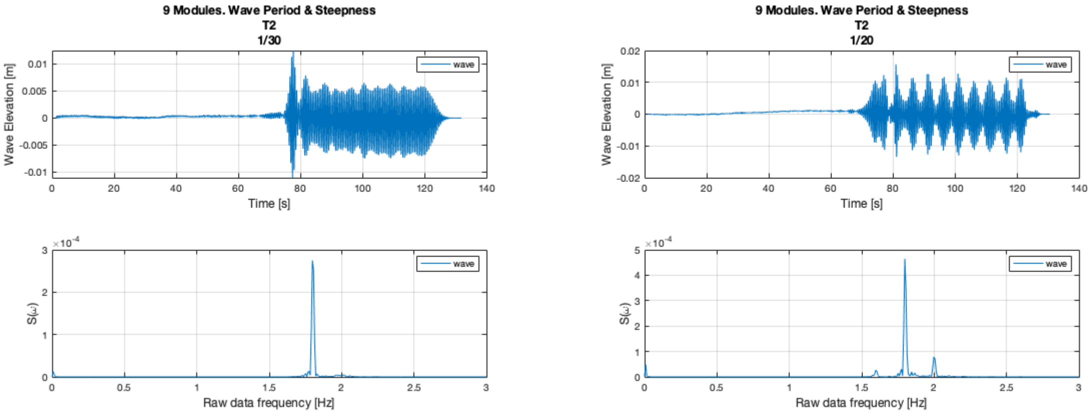

Figur H.2: Wave elevation measurements in $T = 2$s and steepness $H/\lambda = 1/30$ (left) and $H/\lambda = 1/20$ (right), taken at wave-probe *wave* positioned at the wave-entry of the model.

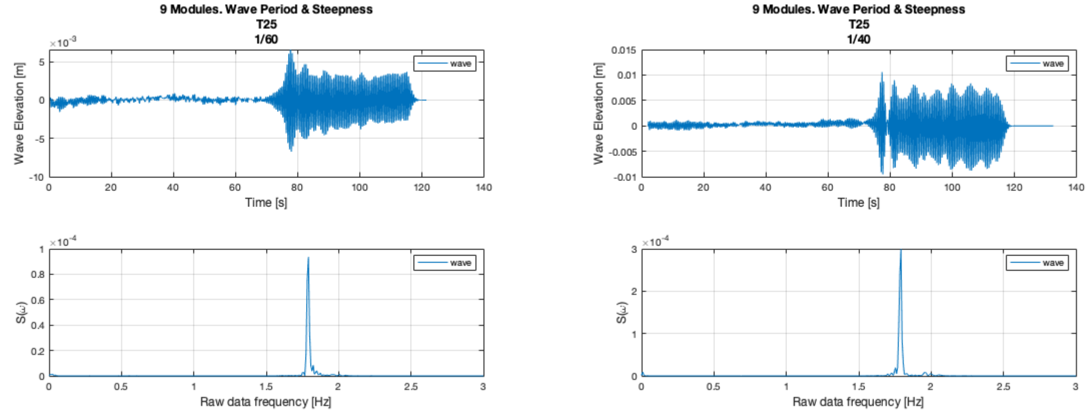

Figur H.3: Wave elevation measurements in $T = 2.5$s and steepness $H/\lambda = 1/60$ (left) and $H/\lambda = 1/40$ (right), taken at wave-probe *wave* positioned at the wave-entry of the model.

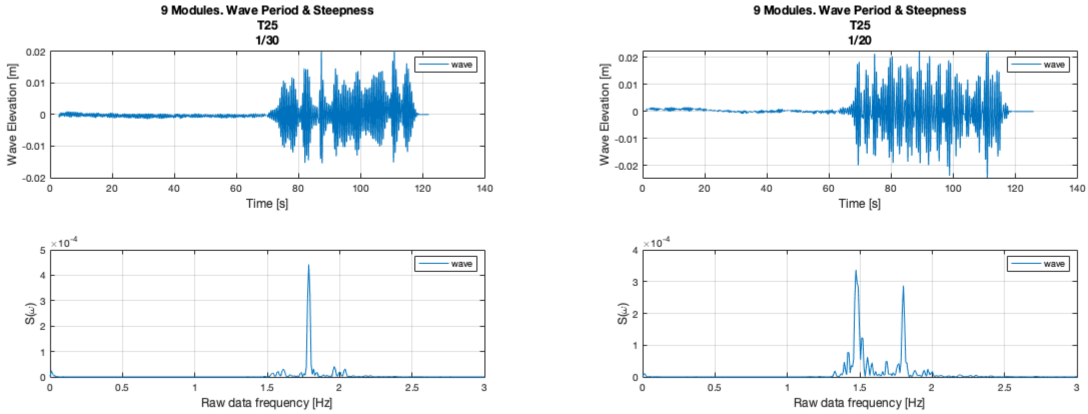

Figur H.4: Wave elevation measurements in $T = 2.5$s and steepness $H/\lambda = 1/30$ (left) and $H/\lambda = 1/20$ (right), taken at wave-probe *wave* positioned at the wave-entry of the model.

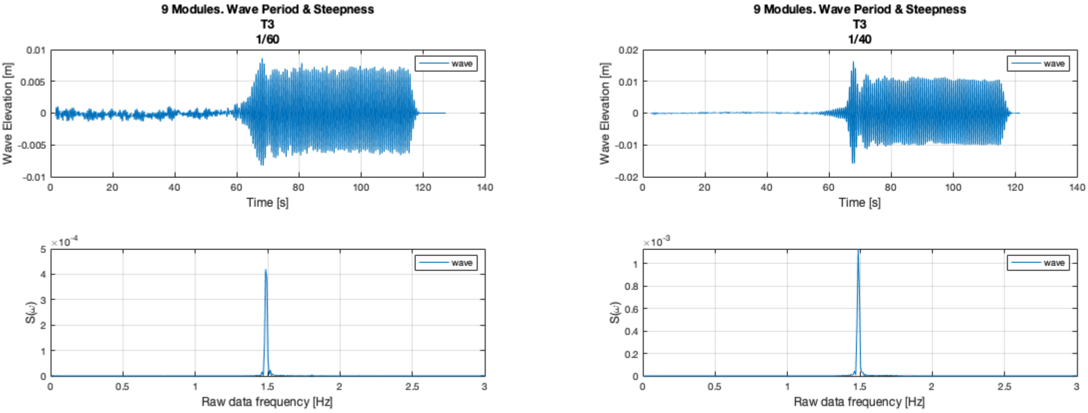

Figur H.5: Wave elevation measurements in $T = 3$s and steepness $H/\lambda = 1/60$ (left) and $H/\lambda = 1/40$ (right), taken at wave-probe *wave* positioned at the wave-entry of the model.

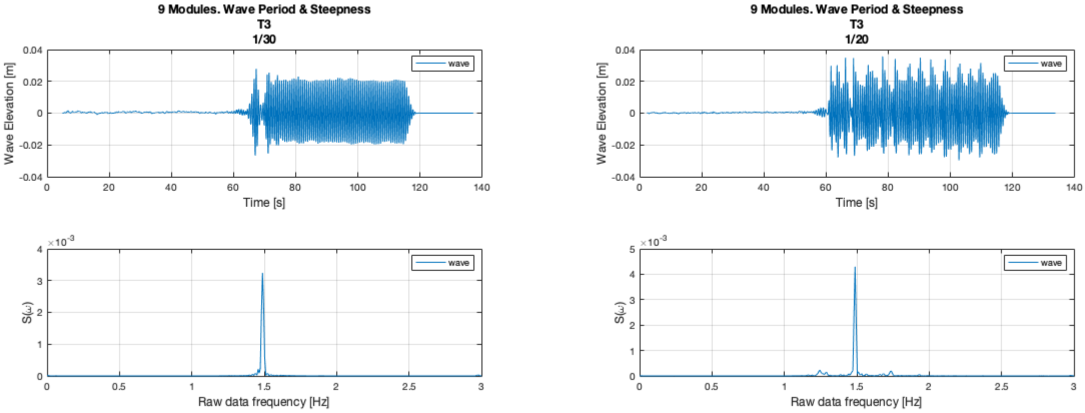

Figur H.6: Wave elevation measurements in $T = 3$s and steepness $H/\lambda = 1/30$ (left) and $H/\lambda = 1/20$ (right), taken at wave-probe *wave* positioned at the wave-entry of the model.

Appendix I

Model Test Results - Regular Waves

I.1 Vertical Response Amplitude Operators

I.1.1 Case 1

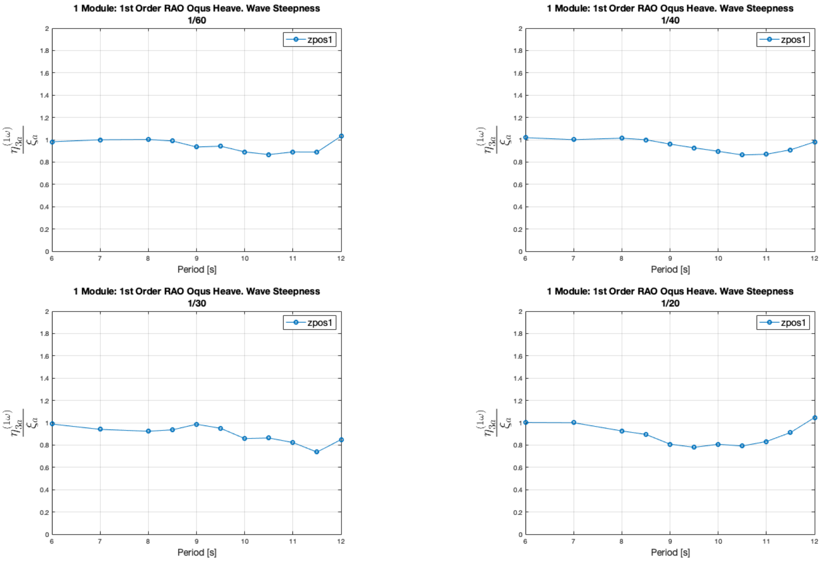

Figur I.1: 1 Module, 1st order vertical RAO in heave, computed with motion capture measurements. Shown by theoretical wave-period input in full scale.

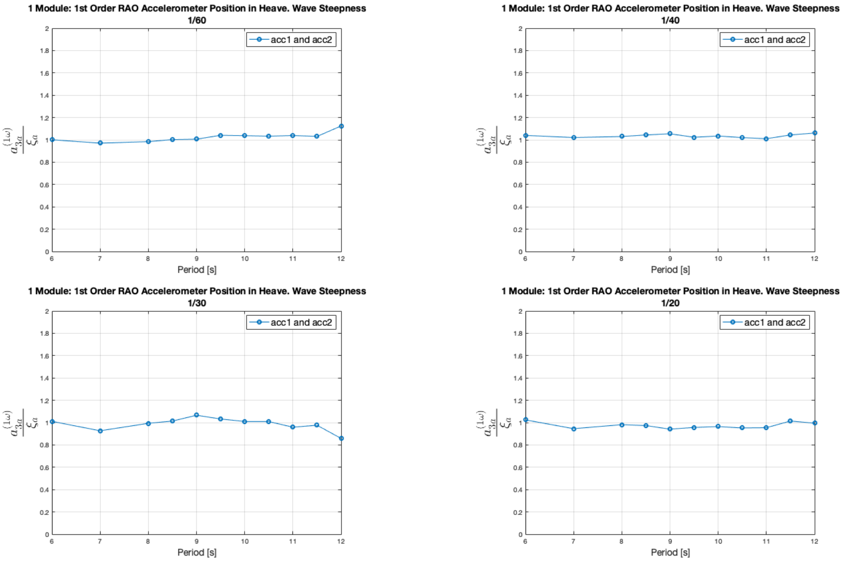

Figur I.2: 1 Module, 1st order vertical RAO in heave, computed by acceleration measurements. Shown by theoretical wave-period input in full scale.

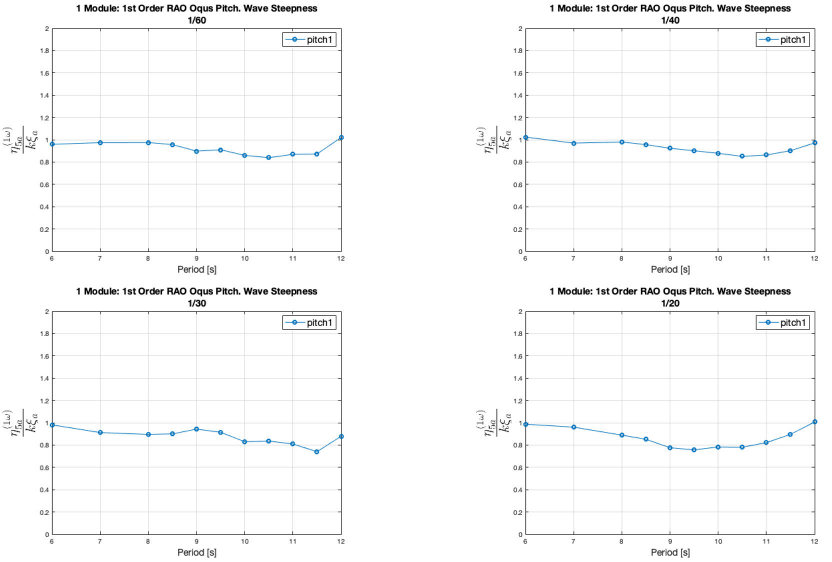

Figur I.3: 1 Module, 1st order vertical RAO in pitch, computed by motion capture measurements. Shown by theoretical wave-period input in full scale.

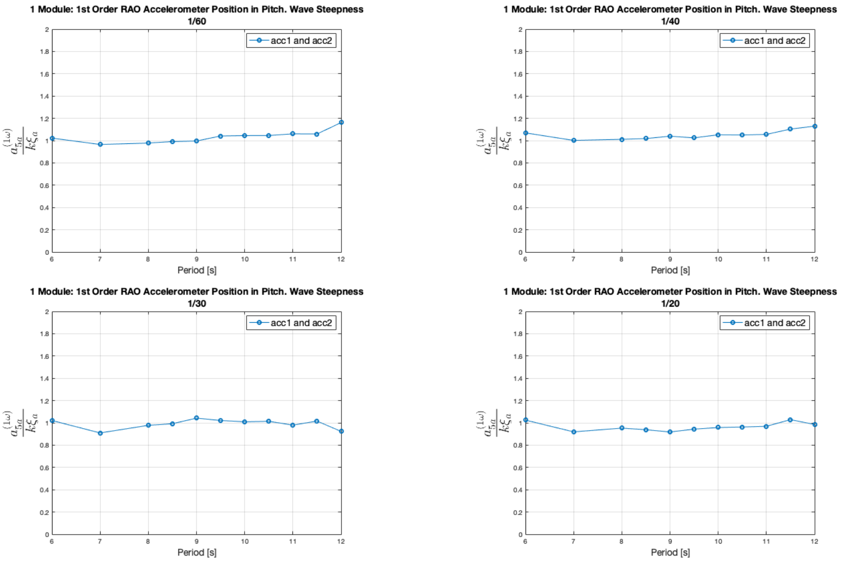

Figur I.4: 1 Module, 1st order vertical RAO in pitch, computed by acceleration measurements. Shown by theoretical wave-period input in full scale.

I.1.2 Case 2

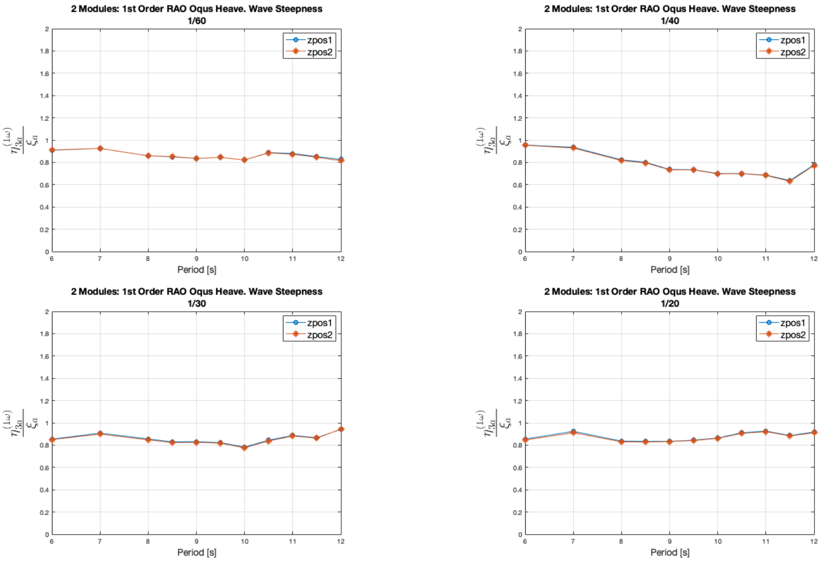

Figur I.5: 2 Modules, 1st order vertical RAO in heave, computed with motion capture measurements. Shown by theoretical wave-period input in full scale.

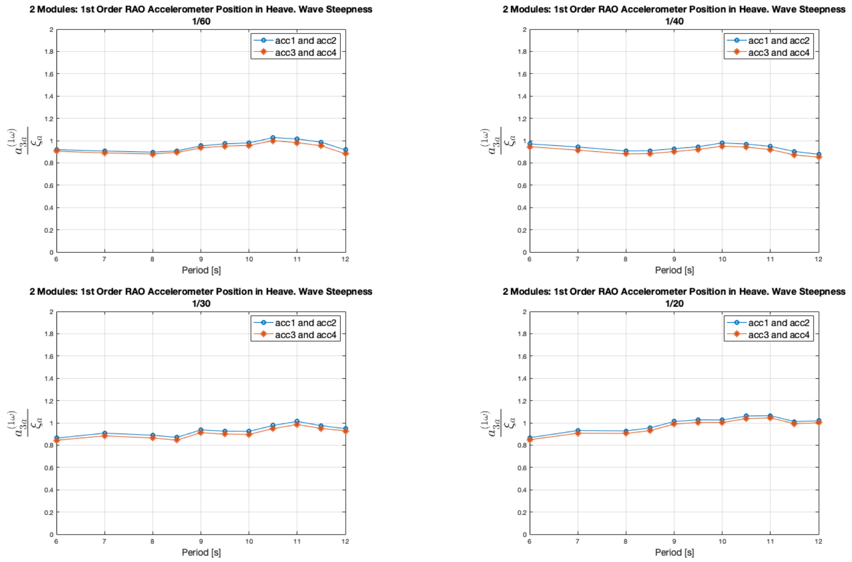

Figur I.6: 2 Modules, 1st order vertical RAO in heave, computed by acceleration measurements. Shown by theoretical wave-period input in full scale.

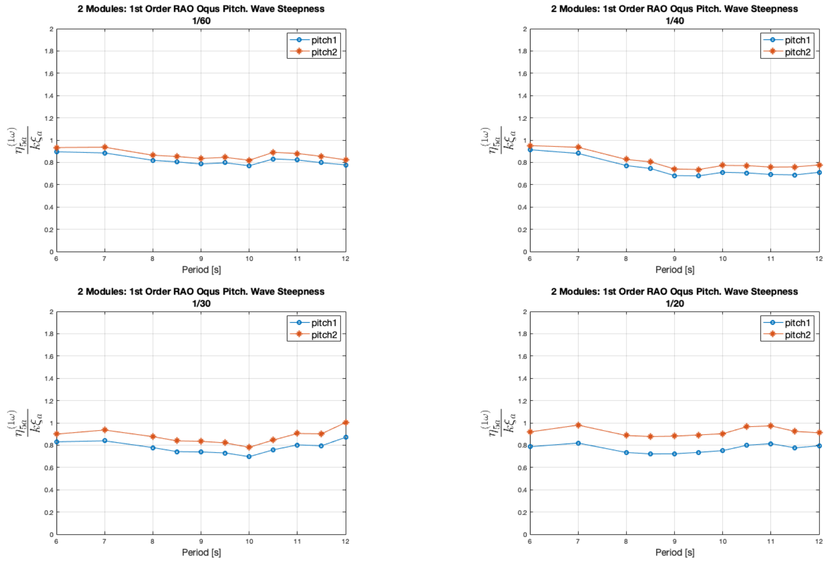

Figur I.7: 2 Modules, 1st order vertical RAO in pitch, computed by motion capture measurements. Shown by theoretical wave-period input in full scale.

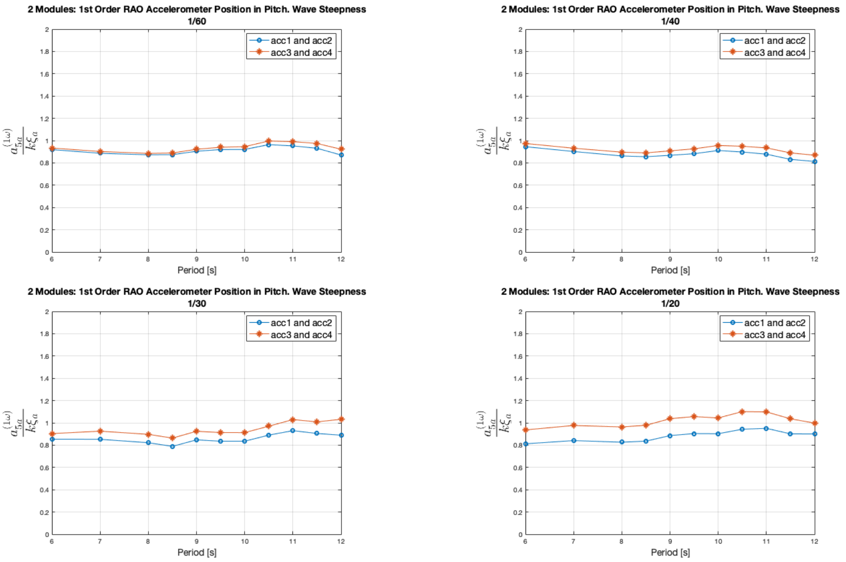

Figur I.8: 2 Modules, 1st order vertical RAO in pitch, computed by acceleration measurements. Shown by theoretical wave-period input in full scale.

I.1.3 Case 3

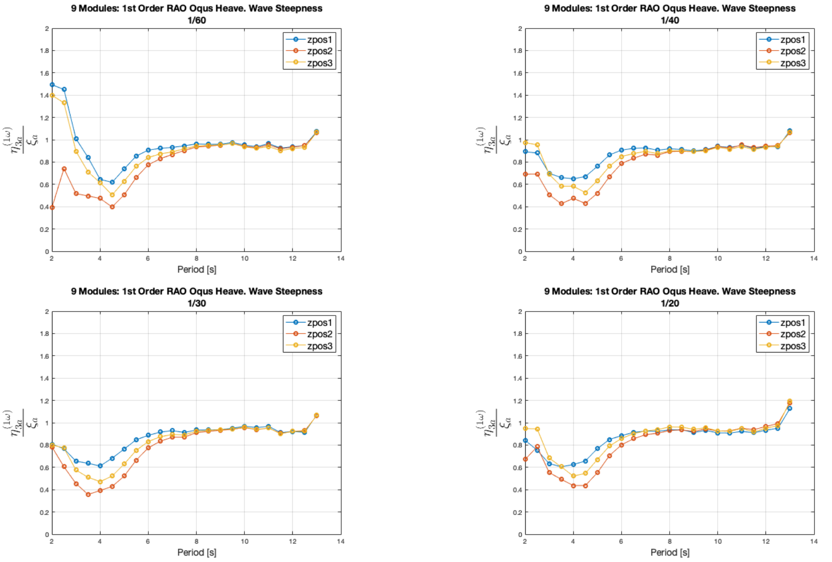

Figur I.9: 9 Modules, 1st order vertical RAO in heave, computed with motion capture measurements. Shown by theoretical wave-period input in full scale.

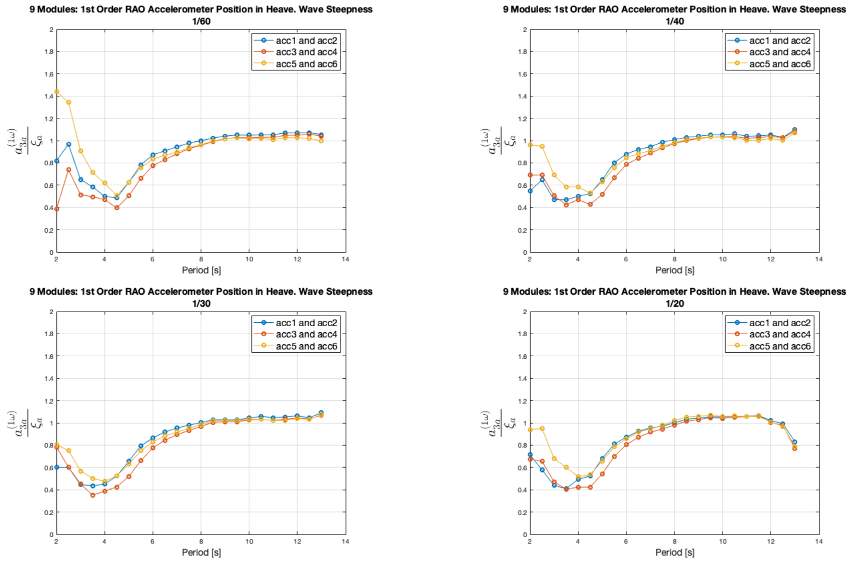

Figur I.10: 9 Modules, 1st order vertical RAO in heave, computed by acceleration measurements. Shown by theoretical wave-period input in full scale.

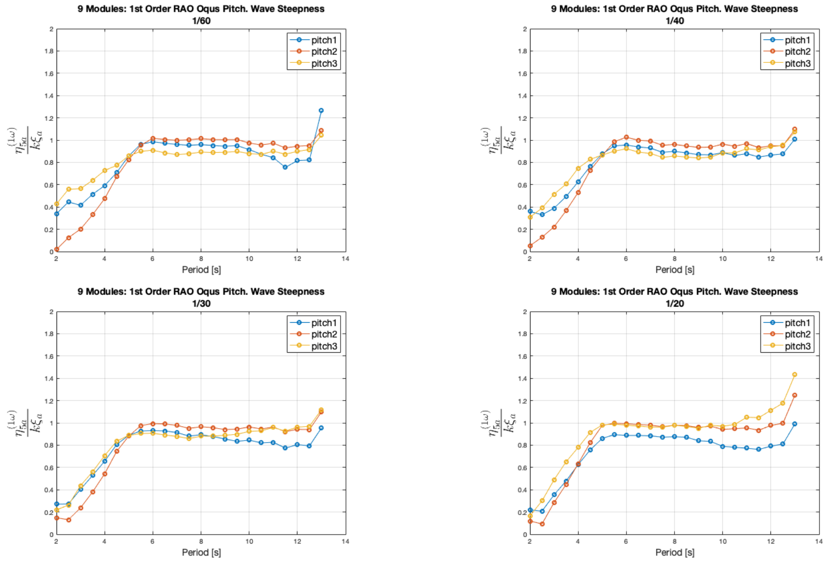

Figur I.11: 9 Modules, 1st order vertical RAO in pitch, computed by motion capture measurements. Shown by theoretical wave-period input in full scale.

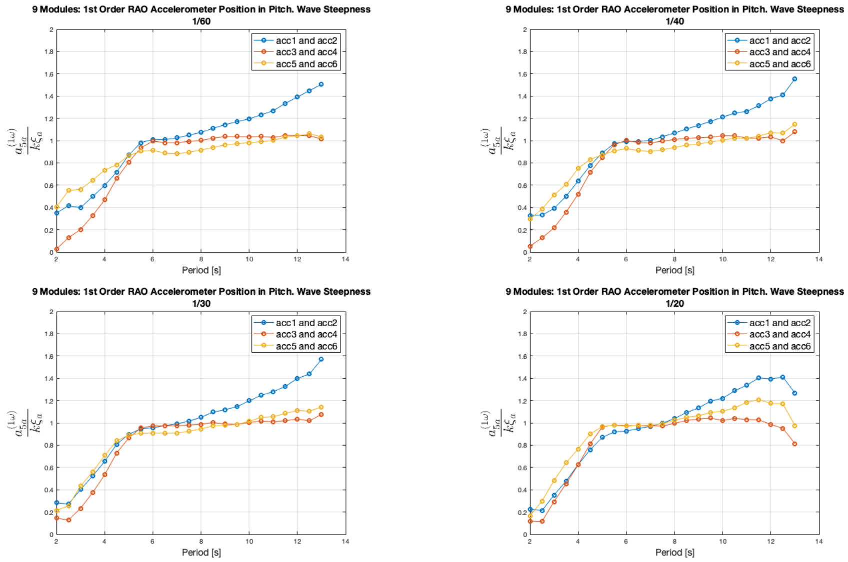

Figur I.12: 9 Modules, 1st order vertical RAO in pitch, computed by acceleration measurments. Shown by theoretical wave-period input in full scale.

I.2 Case 3 Theoretical Model Comparison

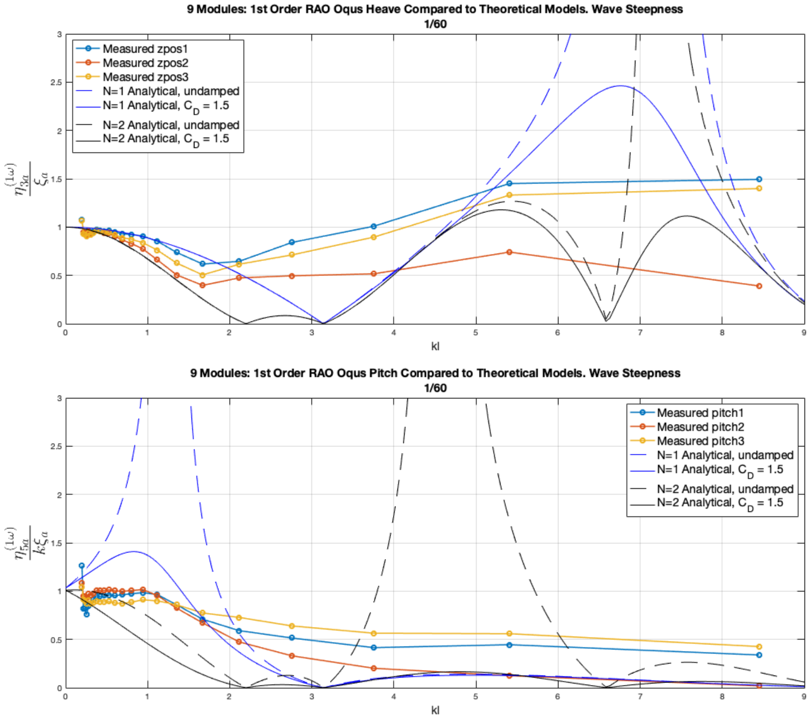

Figur I.13: 9 Modules, 1st order vertical RAO in heave (top) and pitch (bottom) from motion capture measurements in $H/\lambda = 1/60$, compared to the theoretical model heave and pitch RAO with $N = 1$ and $N = 2$ bodies. Both shown as undamped and viscous damped with drag coefficient $C_D = 1.5$. Made non-dimensional by the wave amplitude ζ_a and wave-number k plotted against the non-dimensional wave-number kl.

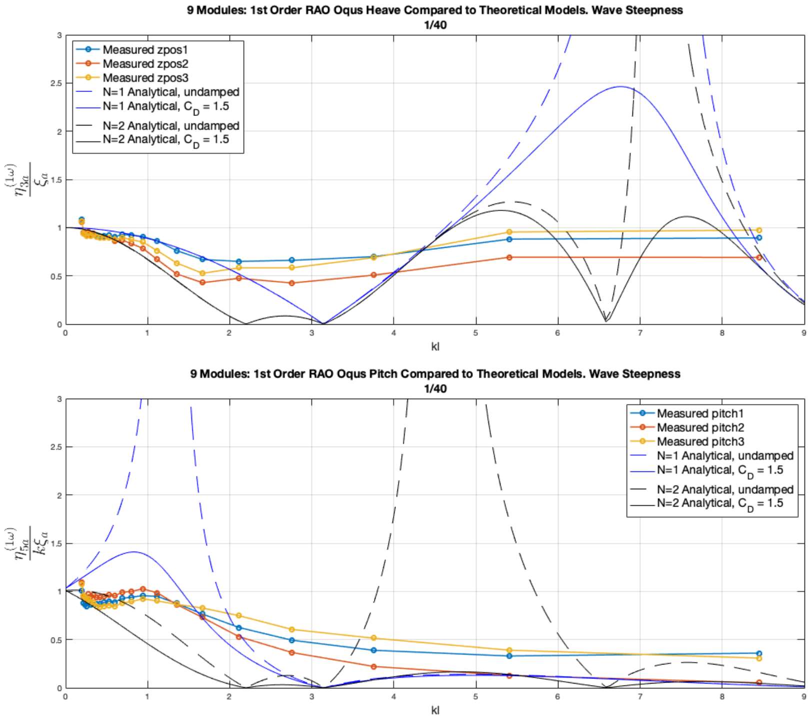

Figur I.14: 9 Modules, 1st order vertical RAO in heave (top) and pitch (bottom) from motion capture measurements in $H/\lambda = 1/40$, compared to the theoretical model heave and pitch RAO with $N = 1$ and $N = 2$ bodies. Both shown as undamped and viscous damped with drag coefficient $C_D = 1.5$. Made non-dimensional by the wave amplitude ζ_a and wave-number k plotted against the non-dimensional wave-number kl.

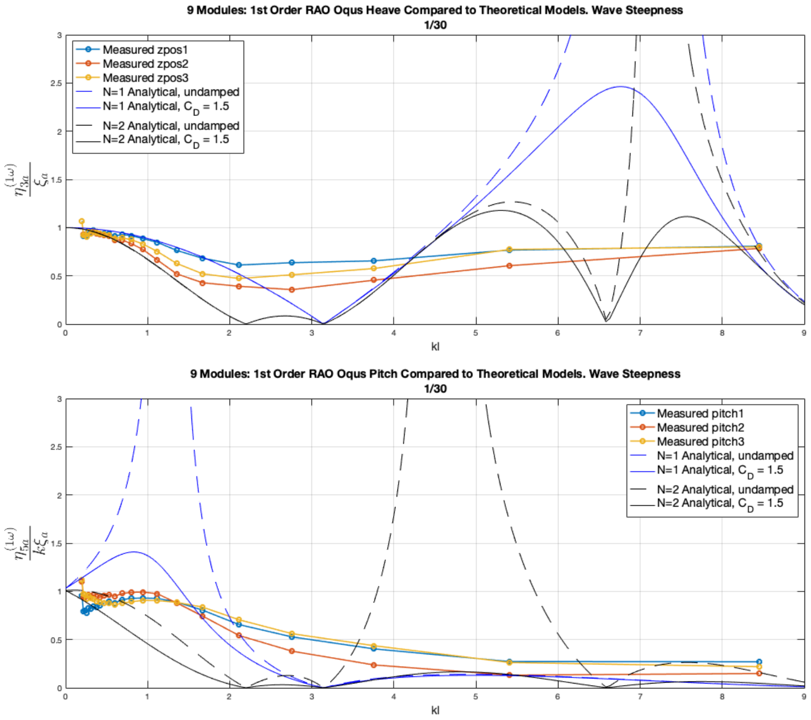

Figur I.15: 9 Modules, 1st order vertical RAO in heave (top) and pitch (bottom) from motion capture measurements in $H/\lambda = 1/30$, compared to the theoretical model heave and pitch RAO with $N = 1$ and $N = 2$ bodies. Both shown as undamped and viscous damped with drag coefficient $C_D = 1.5$. Made non-dimensional by the wave amplitude ζ_a and wave-number k plotted against the non-dimensional wave-number kl.

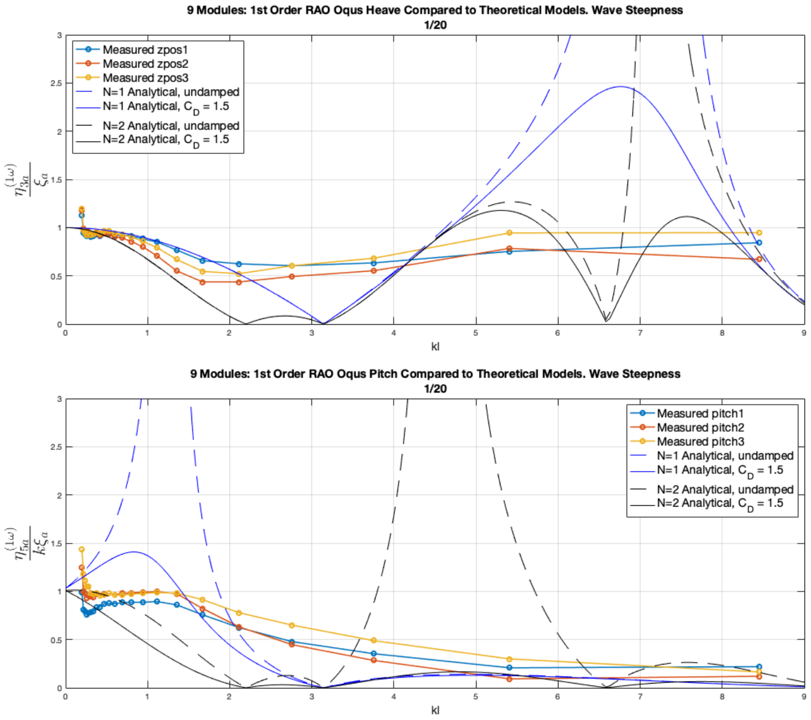

Figur I.16: 9 Modules, 1st order vertical RAO in heave (top) and pitch (bottom) from motion capture measurements in $H/\lambda = 1/20$, compared to the theoretical model heave and pitch RAO with $N = 1$ and $N = 2$ bodies. Both shown as undamped and viscous damped with drag coefficient $C_D = 1.5$. Made non-dimensional by the wave amplitude ζ_a and wave-number k plotted against the non-dimensional wave-number kl.

Appendix J

Input Spectrum - Irregular Waves

The following plots shows the measured spectrum for all wave-probes with the corresponding input JONSWAP spectrum for all irregular wave-series.

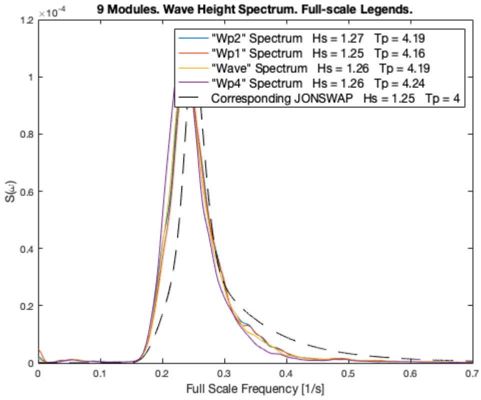

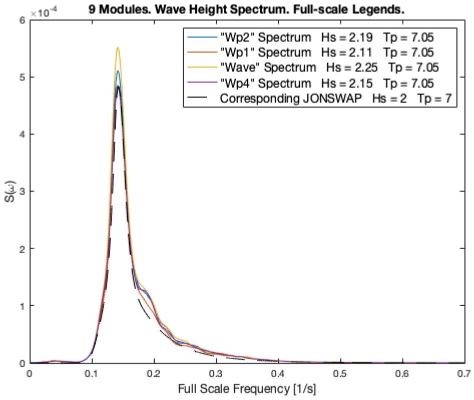

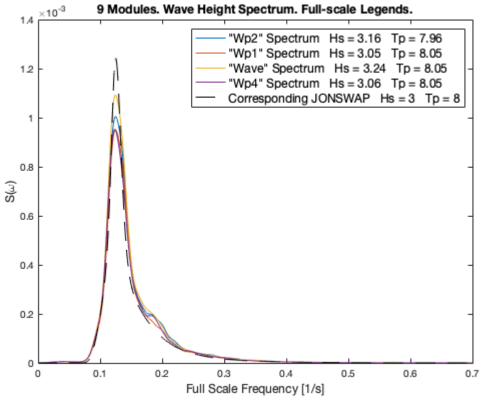
9 Modules. Wave Height Spectrum. Full-scale Legends.
×10^-3
"Wp2" Spectrum Hs = 3.16 Tp = 7.96
"Wp1" Spectrum Hs = 3.05 Tp = 8.05
"Wave" Spectrum Hs = 3.24 Tp = 8.05
"Wp4" Spectrum Hs = 3.06 Tp = 8.05
Corresponding JONSWAP Hs = 3 Tp = 8
S(ω)
Full Scale Frequency [1/s]
0
0.2
0.4
0.6
0.8
1
1.2
1.4
0.1
0.3
0.5
0.7

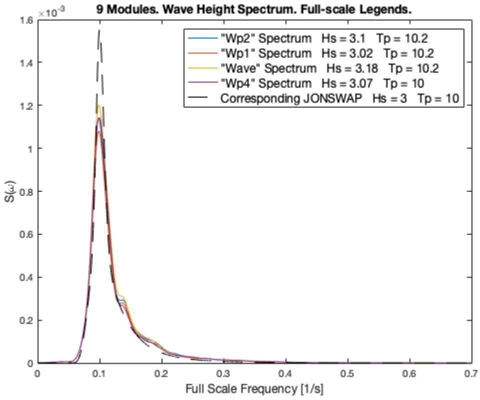
9 Modules. Wave Height Spectrum. Full-scale Legends.
×10^-3
"Wp2" Spectrum Hs = 3.1 Tp = 10.2
"Wp1" Spectrum Hs = 3.02 Tp = 10.2
"Wave" Spectrum Hs = 3.18 Tp = 10.2
"Wp4" Spectrum Hs = 3.07 Tp = 10
Corresponding JONSWAP Hs = 3 Tp = 10
S(ω)
Full Scale Frequency [1/s]
0
0.2
0.4
0.6
0.8
1
1.2
1.4
1.6
0.1
0.3
0.5
0.7

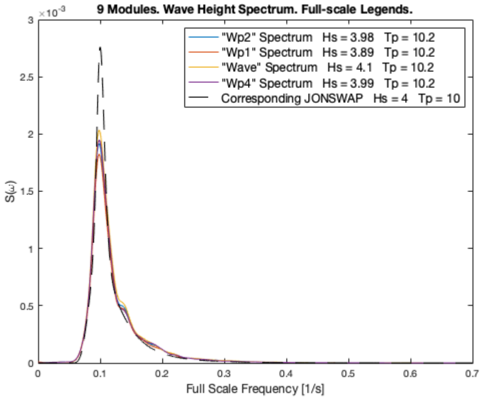
9 Modules. Wave Height Spectrum. Full-scale Legends.
×10^-3
"Wp2" Spectrum Hs = 3.98 Tp = 10.2
"Wp1" Spectrum Hs = 3.89 Tp = 10.2
"Wave" Spectrum Hs = 4.1 Tp = 10.2
"Wp4" Spectrum Hs = 3.99 Tp = 10.2
Corresponding JONSWAP Hs = 4 Tp = 10
S(ω)
Full Scale Frequency [1/s]
0
0.5
1
1.5
2
2.5
3
0.1
0.3
0.5
0.7

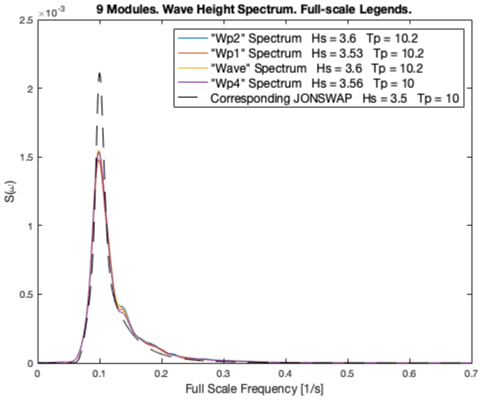
9 Modules. Wave Height Spectrum. Full-scale Legends.
×10^-3
"Wp2" Spectrum Hs = 3.6 Tp = 10.2
"Wp1" Spectrum Hs = 3.53 Tp = 10.2
"Wave" Spectrum Hs = 3.6 Tp = 10.2
"Wp4" Spectrum Hs = 3.56 Tp = 10
Corresponding JONSWAP Hs = 3.5 Tp = 10
S(ω)
Full Scale Frequency [1/s]
0
0.5
1
1.5
2
2.5
0.1
0.3
0.5
0.7

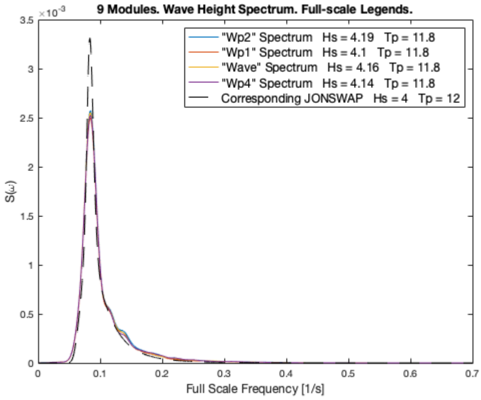
9 Modules. Wave Height Spectrum. Full-scale Legends.
×10^-3
"Wp2" Spectrum Hs = 4.19 Tp = 11.8
"Wp1" Spectrum Hs = 4.1 Tp = 11.8
"Wave" Spectrum Hs = 4.16 Tp = 11.8
"Wp4" Spectrum Hs = 4.14 Tp = 11.8
Corresponding JONSWAP Hs = 4 Tp = 12
S(ω)
Full Scale Frequency [1/s]
0
0.5
1
1.5
2
2.5
3
3.5
0.1
0.3
0.5
0.7

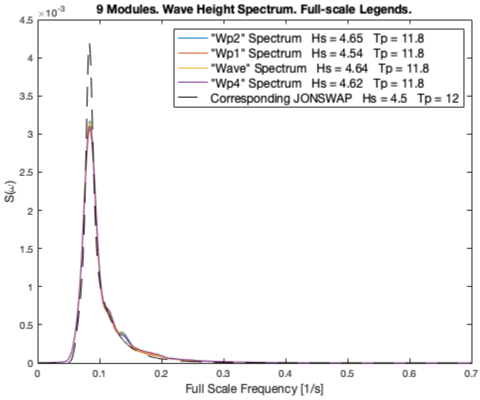
9 Modules. Wave Height Spectrum. Full-scale Legends.
×10^-3
"Wp2" Spectrum Hs = 4.65 Tp = 11.8
"Wp1" Spectrum Hs = 4.54 Tp = 11.8
"Wave" Spectrum Hs = 4.64 Tp = 11.8
"Wp4" Spectrum Hs = 4.62 Tp = 11.8
Corresponding JONSWAP Hs = 4.5 Tp = 12
S(ω)
Full Scale Frequency [1/s]
0
0.5
1
1.5
2
2.5
3
3.5
4
4.5
0.1
0.3
0.5
0.7

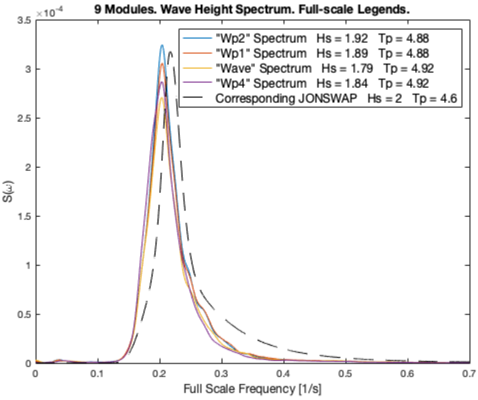
9 Modules. Wave Height Spectrum. Full-scale Legends.
×10^-4
"Wp2" Spectrum Hs = 1.92 Tp = 4.88
"Wp1" Spectrum Hs = 1.89 Tp = 4.88
"Wave" Spectrum Hs = 1.79 Tp = 4.92
"Wp4" Spectrum Hs = 1.84 Tp = 4.92
Corresponding JONSWAP Hs = 2 Tp = 4.6
S(ω)
Full Scale Frequency [1/s]
0
0.1
0.2
0.3
0.4
0.5
0.6
0.7
0.5
1
1.5
2
2.5
3
3.5

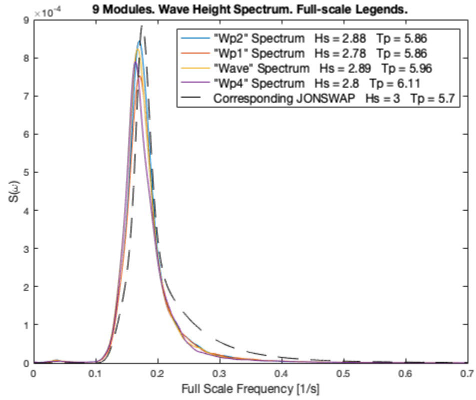
9 Modules. Wave Height Spectrum. Full-scale Legends.
×10^-4
"Wp2" Spectrum Hs = 2.88 Tp = 5.86
"Wp1" Spectrum Hs = 2.78 Tp = 5.86
"Wave" Spectrum Hs = 2.89 Tp = 5.96
"Wp4" Spectrum Hs = 2.8 Tp = 6.11
Corresponding JONSWAP Hs = 3 Tp = 5.7
S(ω)
Full Scale Frequency [1/s]
0
0.1
0.2
0.3
0.4
0.5
0.6
0.7
1
2
3
4
5
6
7
8
9

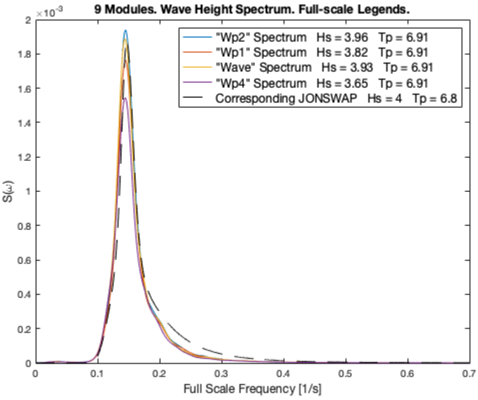
9 Modules. Wave Height Spectrum. Full-scale Legends.
×10^-3
"Wp2" Spectrum Hs = 3.96 Tp = 6.91
"Wp1" Spectrum Hs = 3.82 Tp = 6.91
"Wave" Spectrum Hs = 3.93 Tp = 6.91
"Wp4" Spectrum Hs = 3.65 Tp = 6.91
Corresponding JONSWAP Hs = 4 Tp = 6.8
S(ω)
Full Scale Frequency [1/s]
0
0.1
0.2
0.3
0.4
0.5
0.6
0.7
0.2
0.4
0.6
0.8
1
1.2
1.4
1.6
1.8
2

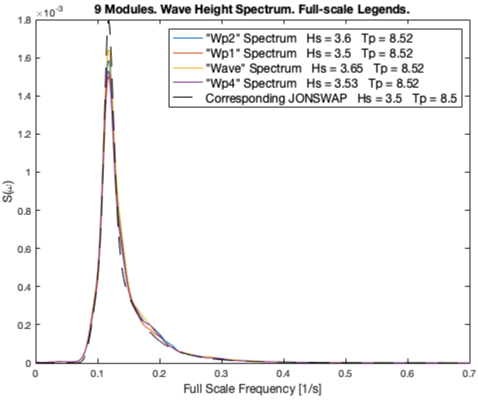
9 Modules. Wave Height Spectrum. Full-scale Legends.
×10^-3
"Wp2" Spectrum Hs = 3.6 Tp = 8.52
"Wp1" Spectrum Hs = 3.5 Tp = 8.52
"Wave" Spectrum Hs = 3.65 Tp = 8.52
"Wp4" Spectrum Hs = 3.53 Tp = 8.52
Corresponding JONSWAP Hs = 3.5 Tp = 8.5
S(ω)
Full Scale Frequency [1/s]
0
0.1
0.2
0.3
0.4
0.5
0.6
0.7
0.2
0.4
0.6
0.8
1
1.2
1.4
1.6
1.8

J.1 Input & Measured Significant Wave Height & Peak Period Deviation

The following plots shows the deviation in H_s and T_p for all irregular wave-series at each wave-probe.

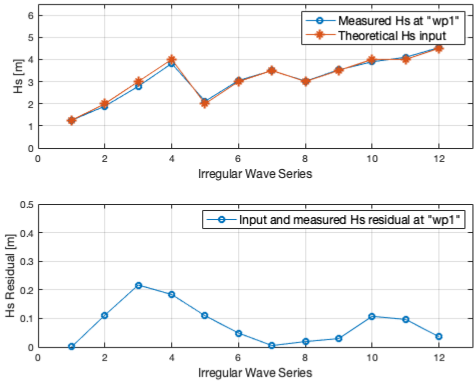

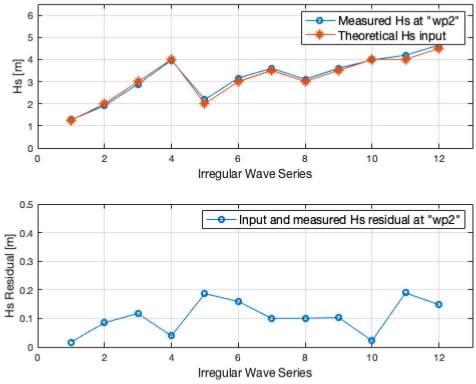

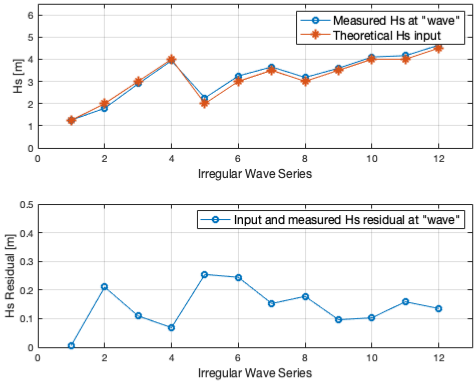

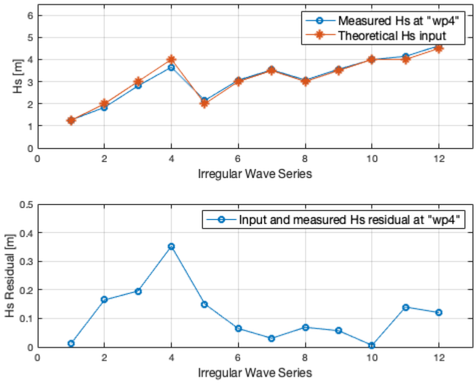

Appendix K

Model Test Results - Irregular Waves

Here, all plots for the measured response spectrum and response amplitude operators are shown. These measurements are cut accordingly by the wave-input spectra, and is shown for every irregular wave-series

K.1 Motion Capture Heave Response Spectrum

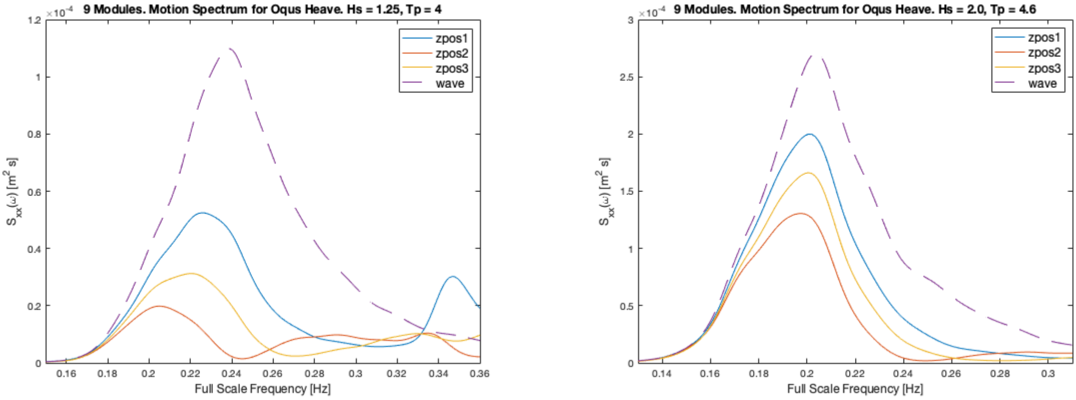

Figur K.1: Motion Spectrum for the motion capture heave measurements, shown in model scale spectral density and plotted against the full-scale frequency, for an irregular wave field with $H_s = 1.25$m and $T_p = 4$s (left), and $H_s = 2$m and $T_p = 4.6$s (right).

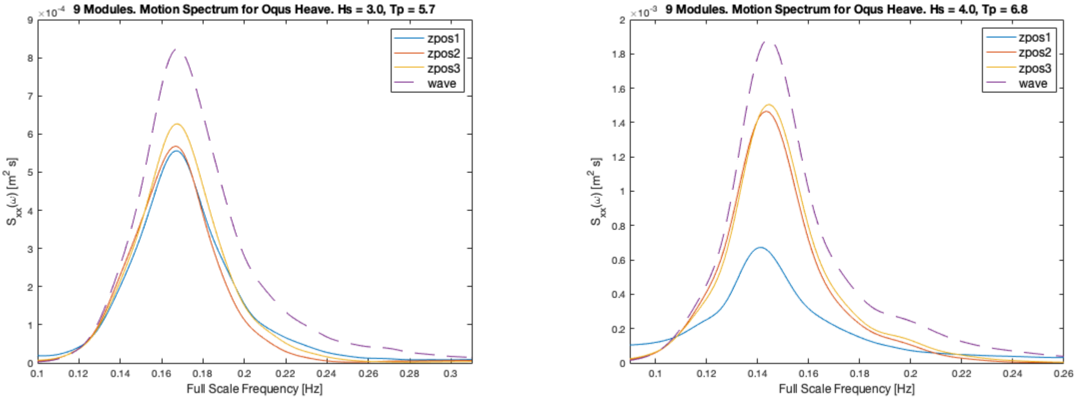

Figur K.2: Motion Spectrum for the motion capture heave measurements, shown in model scale spectral density and plotted against the full-scale frequency, for an irregular wave field with significant wave height $H_s = 3$m and peak period $T_p = 5.7$s (left), and $H_s = 4$m and peak period $T_p = 6.8$s (right).

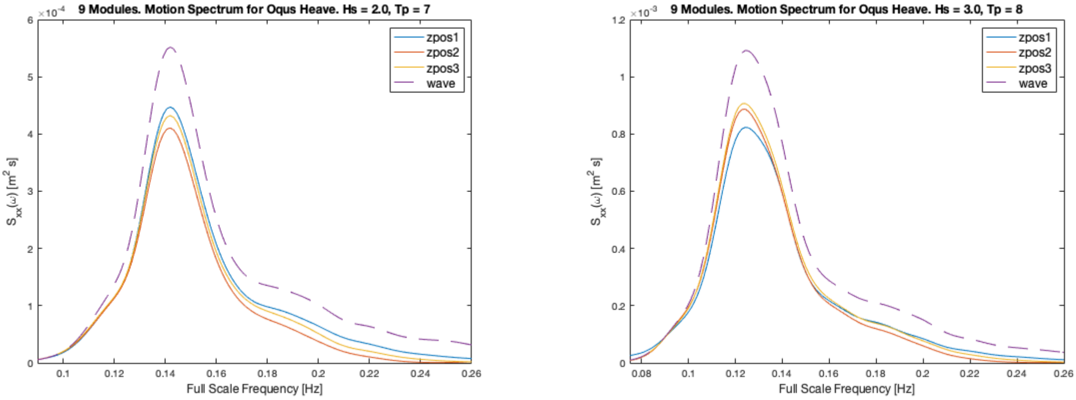

Figur K.3: Motion Spectrum for the motion capture heave measurements, shown in model scale spectral density and plotted against the full-scale frequency, for an irregular wave field with significant wave height $H_s = 2$m and peak period $T_p = 7$s (left), and $H_s = 3$m and peak period $T_p = 8$s (right).

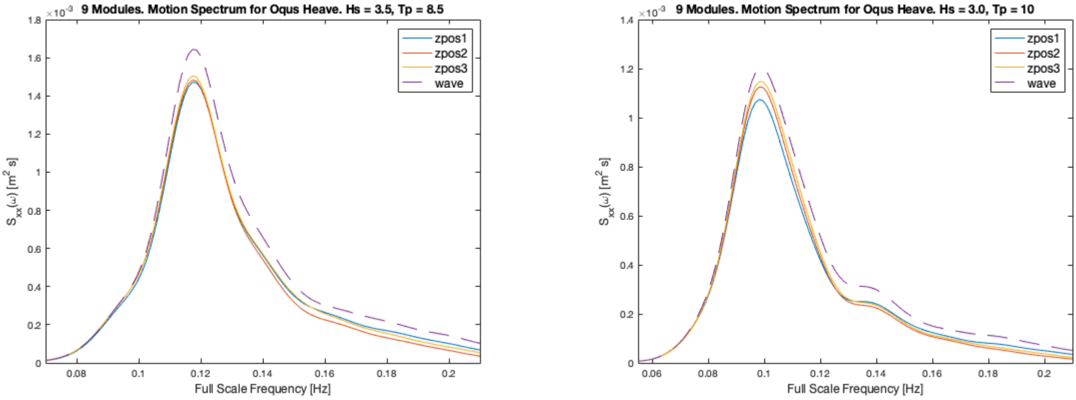

Figur K.4: Motion Spectrum for the motion capture heave measurements, shown in model scale spectral density and plotted against the full-scale frequency, for an irregular wave field with significant wave height $H_s = 3.5$m and peak period $T_p = 8.5$s (left), and $H_s = 3$m and peak period $T_p = 10$s (right).

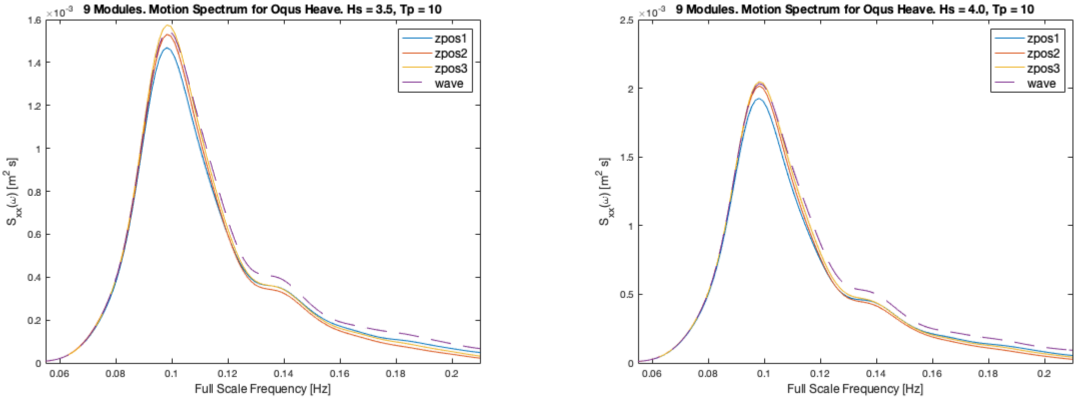

Figur K.5: Motion Spectrum for the motion capture heave measurements, shown in model scale spectral density and plotted against the full-scale frequency, for an irregular wave field with significant wave height $H_s = 3.5$m and peak period $T_p = 10$s (left), and $H_s = 4$m and peak period $T_p = 10$s (right).

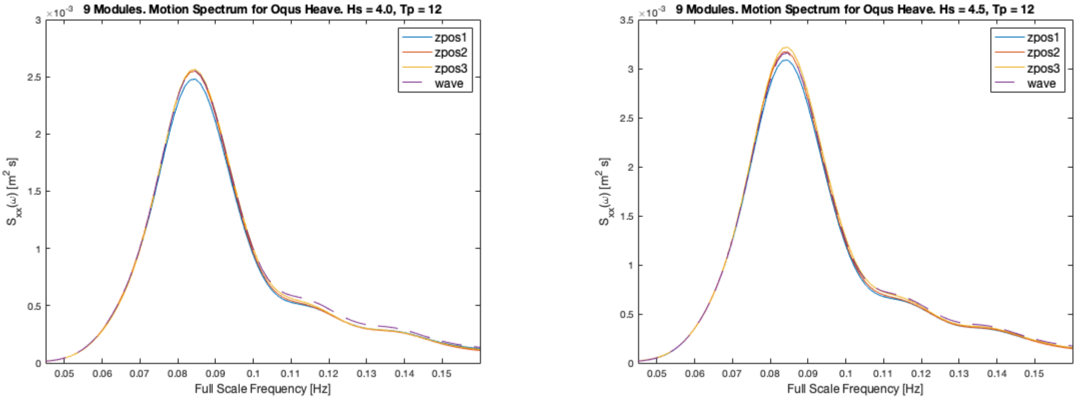

Figur K.6: Motion Spectrum for the motion capture heave measurements, shown in model scale spectral density and plotted against the full-scale frequency, for an irregular wave field with significant wave height $H_s = 4$m and peak period $T_p = 12$s (left), and $H_s = 4.5$m and peak period $T_p = 12$s (right).

K.2 Accelerometer Positions Heave Response Spectrum

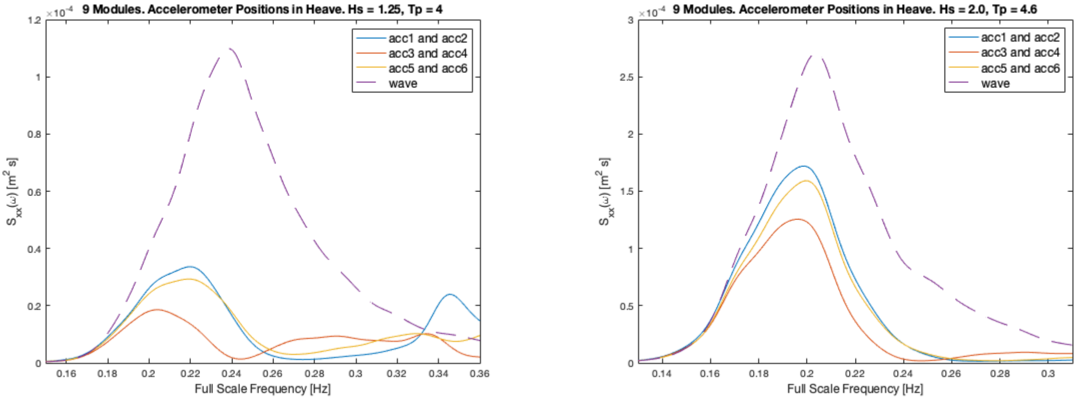

Figur K.7: Motion Spectrum for the combined accelerometer positions in heave, shown in model scale spectral density and plotted against the full-scale frequency, for an irregular wave field with significant wave height $H_s = 1.25$m and peak period $T_p = 4$s (left), and $H_s = 2$m and peak period $T_p = 4.6$s (right).

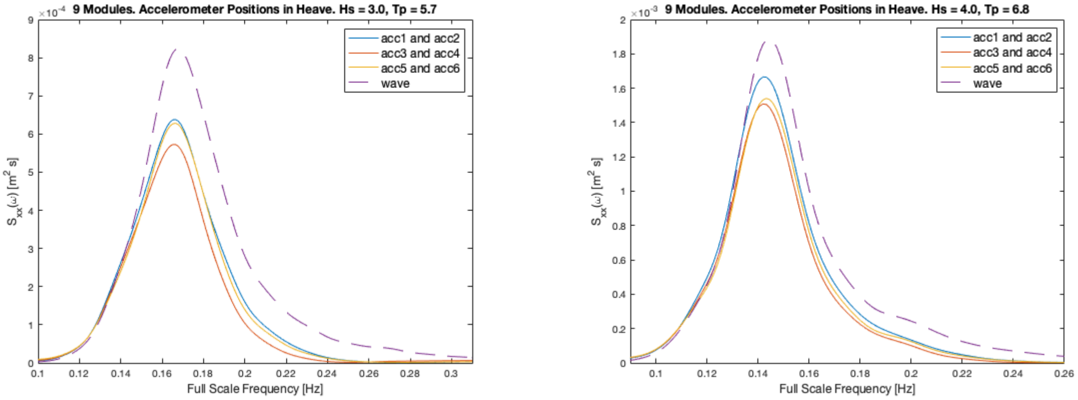

Figur K.8: Motion Spectrum for the combined accelerometer positions in heave, shown in model scale spectral density and plotted against the full-scale frequency, for an irregular wave field with significant wave height $H_s = 3\text{m}$ and peak period $T_p = 5.7\text{s}$ (left), and $H_s = 4\text{m}$ and peak period $T_p = 6.8\text{s}$ (right).

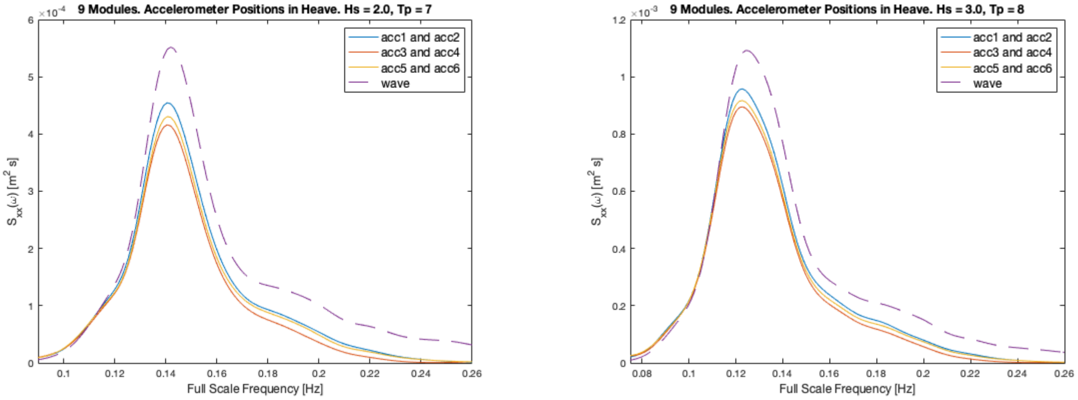

Figur K.9: Motion Spectrum for the combined accelerometer positions in heave, shown in model scale spectral density and plotted against the full-scale frequency, for an irregular wave field with significant wave height $H_s = 2\text{m}$ and peak period $T_p = 7\text{s}$ (left), and $H_s = 3\text{m}$ and peak period $T_p = 8\text{s}$ (right).

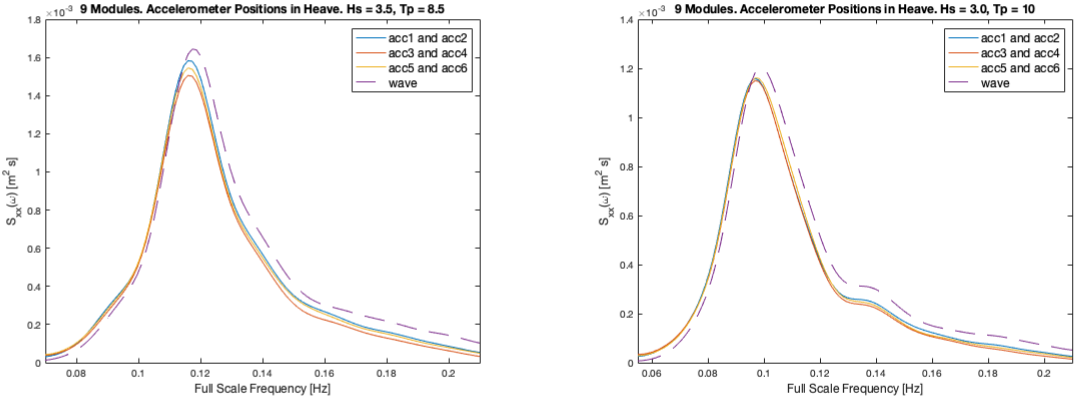

Figur K.10: Motion Spectrum for the combined accelerometer positions in heave, shown in model scale spectral density and plotted against the full-scale frequency, for an irregular wave field with significant wave height $H_s = 3.5$m and peak period $T_p = 8.5$s (left), and $H_s = 3$m and peak period $T_p = 10$s (right).

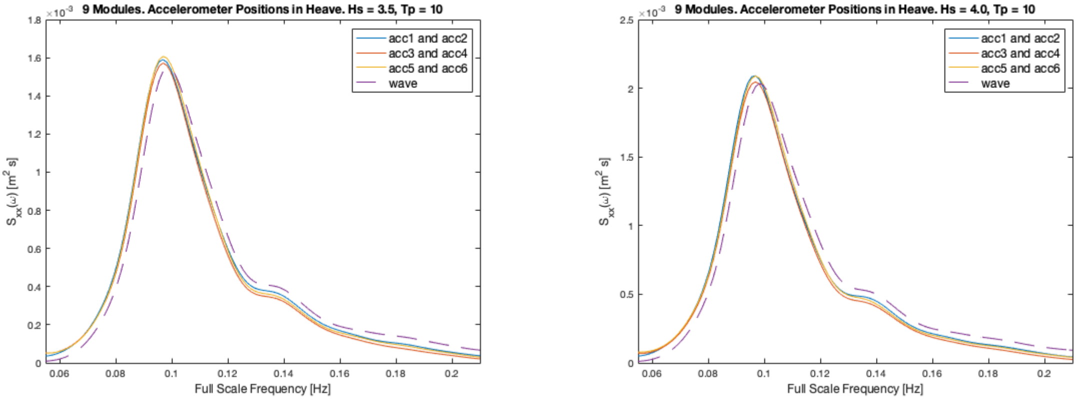

Figur K.11: Motion Spectrum for the combined accelerometer positions in heave, shown in model scale spectral density and plotted against the full-scale frequency, for an irregular wave field with significant wave height $H_s = 3.5$m and peak period $T_p = 10$s (left), and $H_s = 4$m and peak period $T_p = 10$s (right).

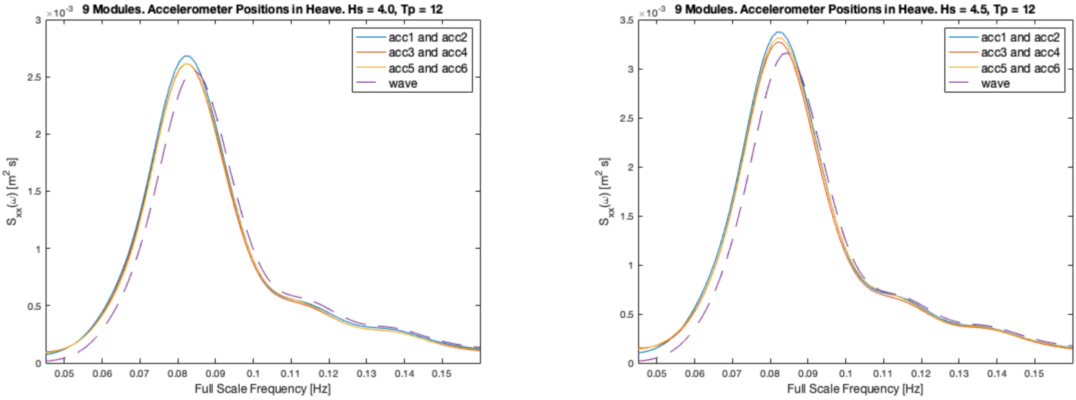

Figur K.12: Motion Spectrum for the combined accelerometer positions in heave, shown in model scale spectral density and plotted against the full-scale frequency, for an irregular wave field with significant wave height $H_s = 4$m and peak period $T_p = 12$s (left), and $H_s = 4.5$m and peak period $T_p = 12$s (right).

K.3 Motion Capture Pitch Response Spectrum

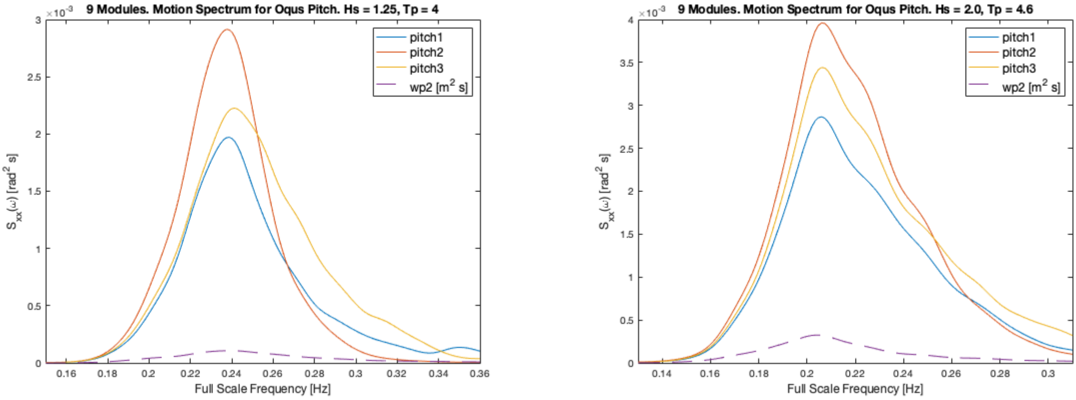

Figur K.13: Motion Spectrum for the motion capture pitch measurements, shown in model scale spectral density and plotted against the full-scale frequency, for an irregular wave field with significant wave height $H_s = 1.25$m and peak period $T_p = 4$s (left), and $H_s = 2$m and peak period $T_p = 4.6$s (right).

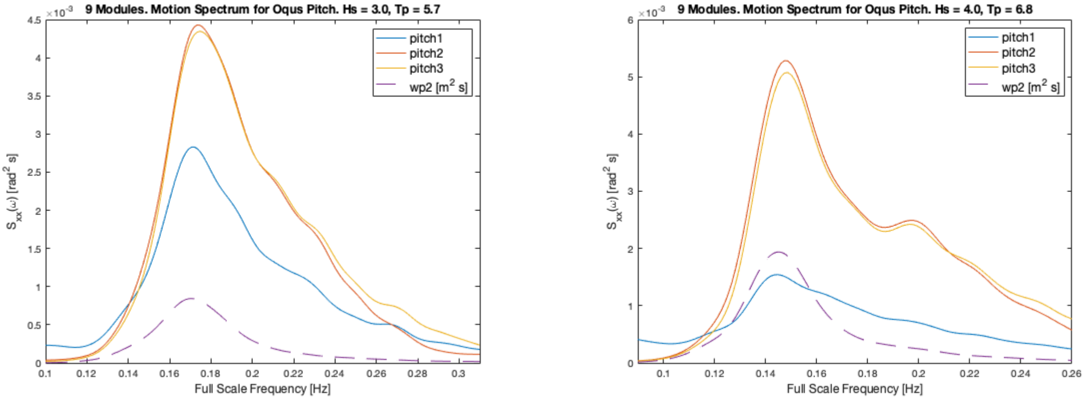

Figur K.14: Motion Spectrum for the motion capture pitch measurements, shown in model scale spectral density and plotted against the full-scale frequency, for an irregular wave field with significant wave height $H_s = 3$m and peak period $T_p = 5.7$s (left), and $H_s = 4$m and peak period $T_p = 6.8$s (right).

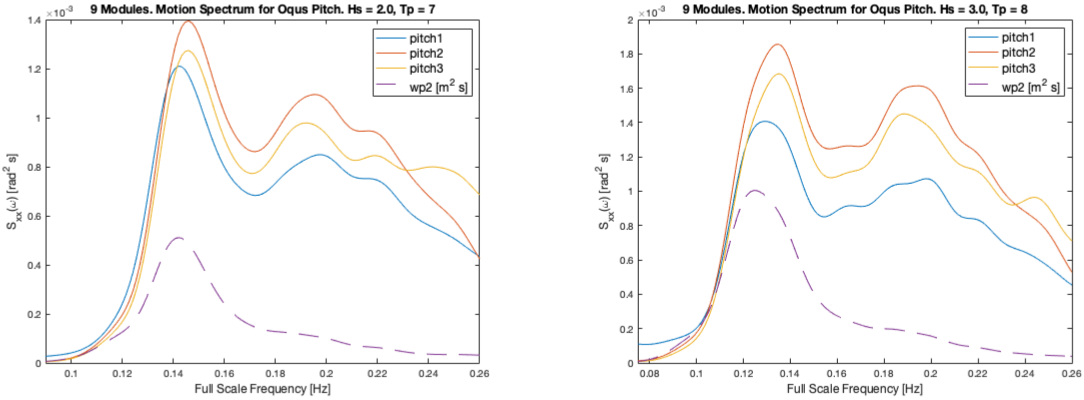

Figur K.15: Motion Spectrum for the motion capture pitch measurements, shown in model scale spectral density and plotted against the full-scale frequency, for an irregular wave field with significant wave height $H_s = 2$m and peak period $T_p = 7$s (left), and $H_s = 3$m and peak period $T_p = 8$s (right).

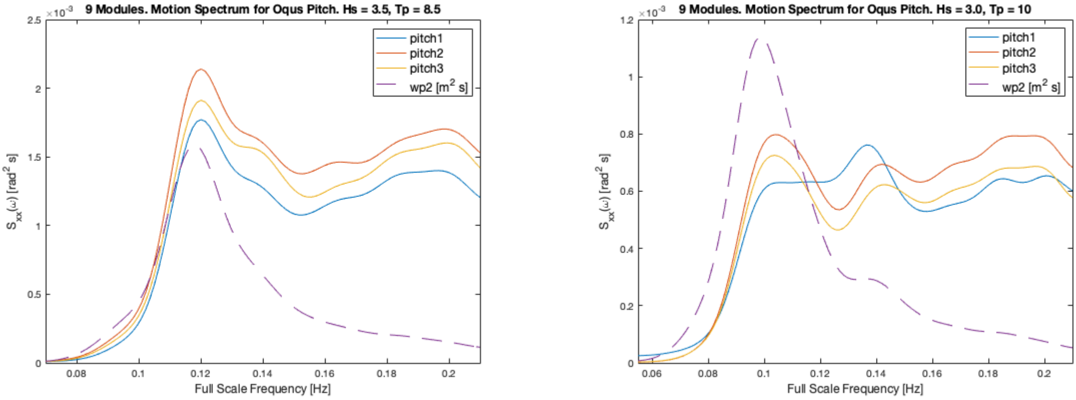

Figur K.16: Motion Spectrum for the motion capture pitch measurements, shown in model scale spectral density and plotted against the full-scale frequency, for an irregular wave field with significant wave height $H_s = 3.5$m and peak period $T_p = 8.5$s (left), and $H_s = 3$m and peak period $T_p = 10$s (right).

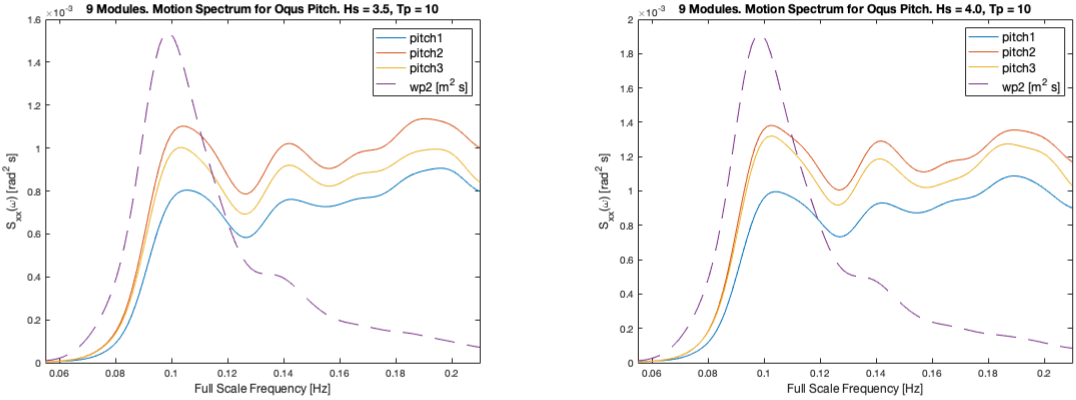

Figur K.17: Motion Spectrum for the motion capture pitch measurements, shown in model scale spectral density and plotted against the full-scale frequency, for an irregular wave field with significant wave height $H_s = 3.5$m and peak period $T_p = 10$s (left), and $H_s = 4$m and peak period $T_p = 10$s (right).

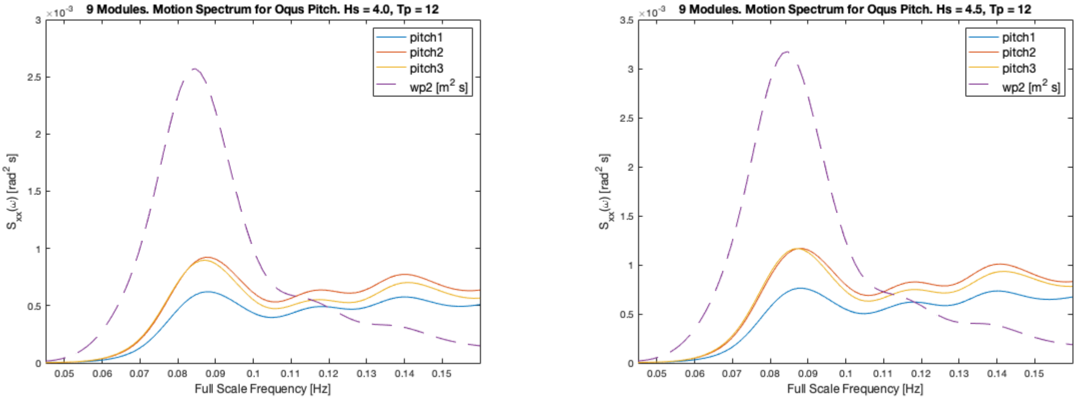

Figur K.18: Motion Spectrum for the motion capture pitch measurements, shown in model scale spectral density and plotted against the full-scale frequency, for an irregular wave field with significant wave height $H_s = 4$m and peak period $T_p = 12$s (left), and $H_s = 4.5$m and peak period $T_p = 12$s (right).

K.4 Accelerometer Positions Pitch Response Spectrum

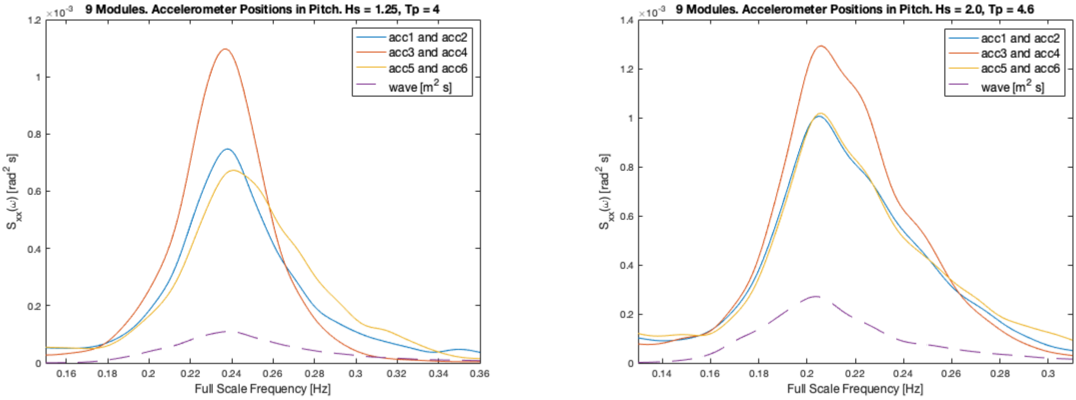

Figur K.19: Motion Spectrum for the combined accelerometer positions in heave, shown in model scale spectral density and plotted against the full-scale frequency, for an irregular wave field with significant wave height $H_s = 1.25$m and peak period $T_p = 4$s (left), and $H_s = 2$m and peak period $T_p = 4.6$s (right).

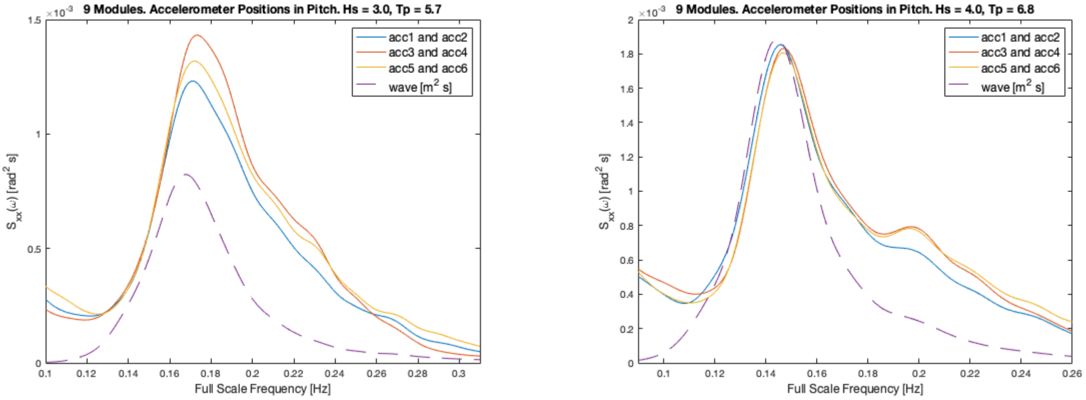

Figur K.20: Motion Spectrum for the combined accelerometer positions in heave, shown in model scale spectral density and plotted against the full-scale frequency, for an irregular wave field with significant wave height $H_s = 3$m and peak period $T_p = 5.7$s (left), and $H_s = 4$m and peak period $T_p = 6.8$s (right).

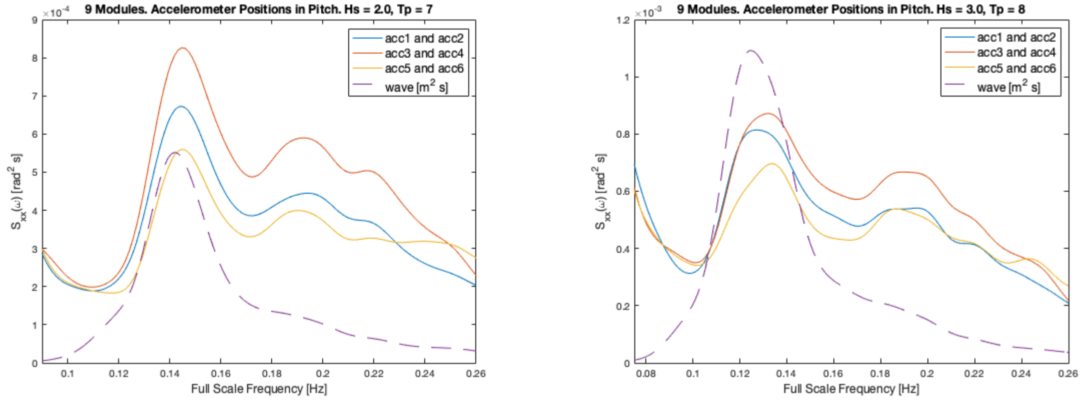

Figur K.21: Motion Spectrum for the combined accelerometer positions in heave, shown in model scale spectral density and plotted against the full-scale frequency, for an irregular wave field with significant wave height $H_s = 2$m and peak period $T_p = 7$s (left), and $H_s = 3$m and peak period $T_p = 8$s (right).

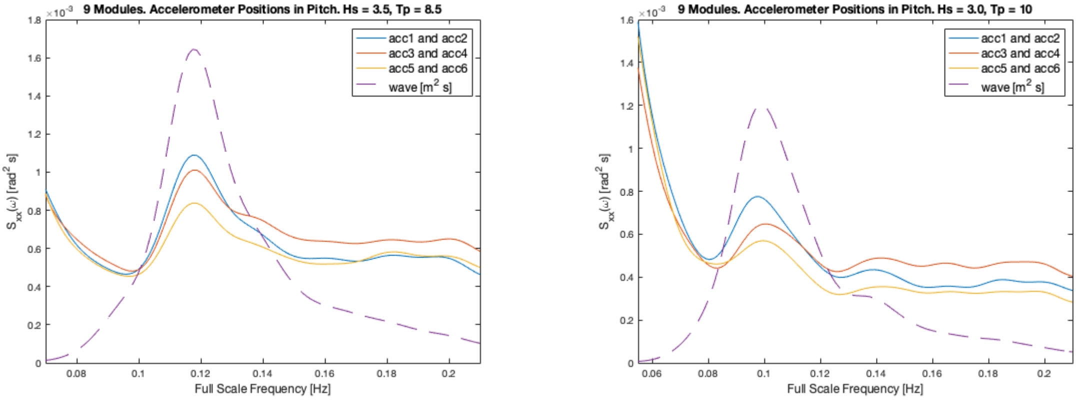

Figur K.22: Motion Spectrum for the combined accelerometer positions in heave, shown in model scale spectral density and plotted against the full-scale frequency, for an irregular wave field with significant wave height $H_s = 3.5$m and peak period $T_p = 8.5$s (left), and $H_s = 3$m and peak period $T_p = 10$s (right).

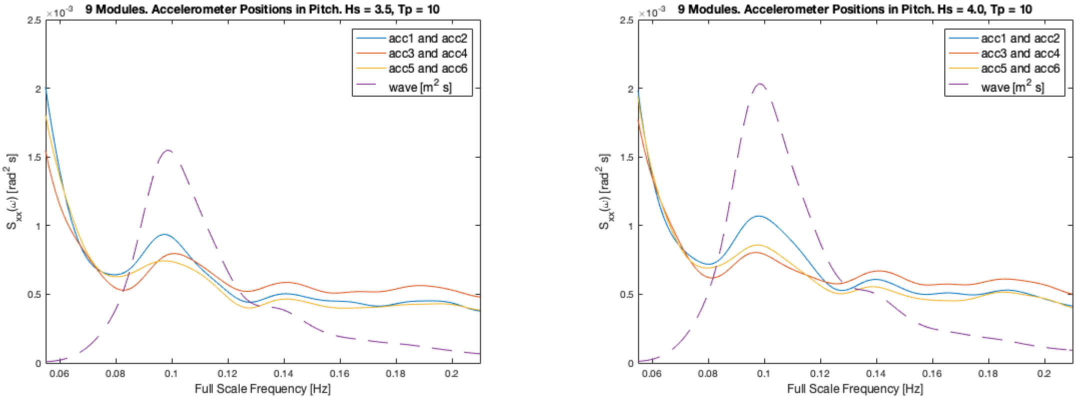

Figur K.23: Motion Spectrum for the combined accelerometer positions in heave, shown in model scale spectral density and plotted against the full-scale frequency, for an irregular wave field with significant wave height $H_s = 3.5$m and peak period $T_p = 10$s (left), and $H_s = 4$m and peak period $T_p = 10$s (right).

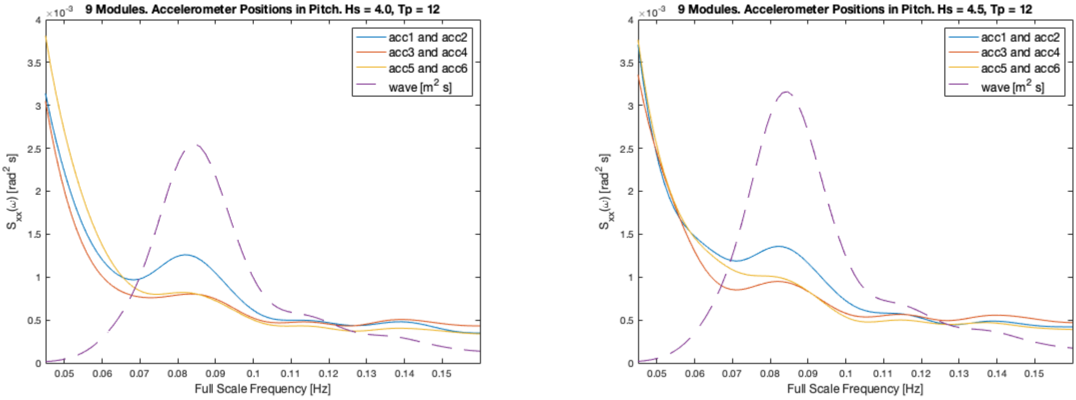

Figur K.24: Motion Spectrum for the combined accelerometer positions in heave, shown in model scale spectral density and plotted against the full-scale frequency, for an irregular wave field with significant wave height $H_s = 4$m and peak period $T_p = 12$s (left), and $H_s = 4.5$m and peak period $T_p = 12$s (right).

K.5 Irregular Heave RAO

K.5.1 Motion Capture Results

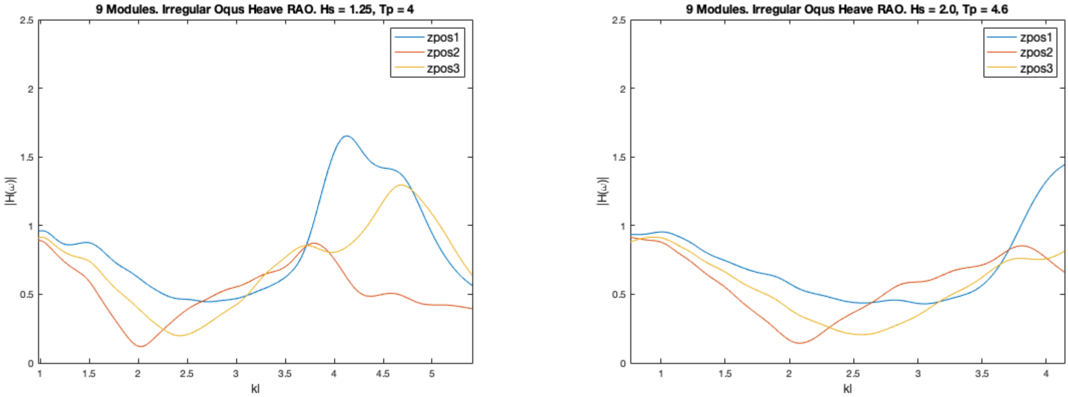

Figur K.25: Heave RAO for the motion capture measurements for each instrumented module, in irregular waves with $H_s = 1.25$m and $T_p = 4$s (left), and $H_s = 2$m and $T_p = 4.6$s (right). Represented as the transfer function $|H(\omega)|$ plotted against the dimensionless wave-number kl.

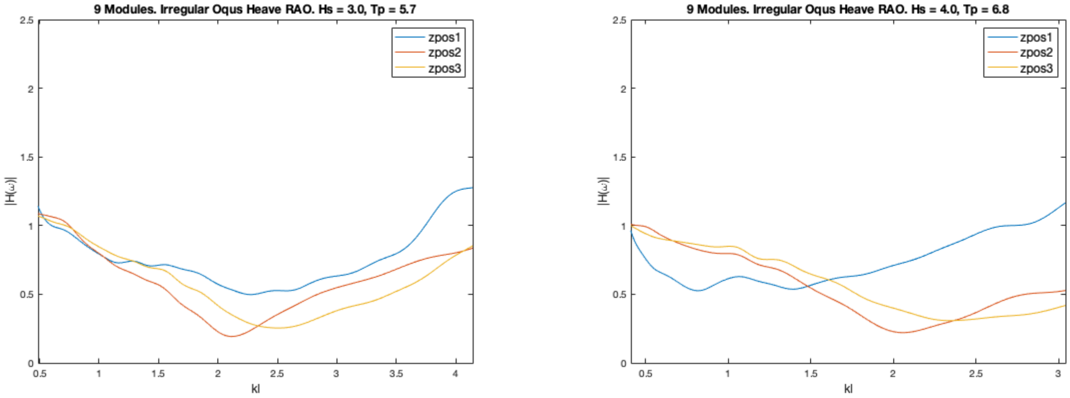

Figur K.26: Heave RAO for the motion capture measurements for each instrumented module, in irregular waves with $H_s = 3$m and $T_p = 5.7$s (left), and $H_s = 4$m and $T_p = 6.8$s (right). Represented as the transfer function $|H(\omega)|$ plotted against the dimensionless wave-number kl.

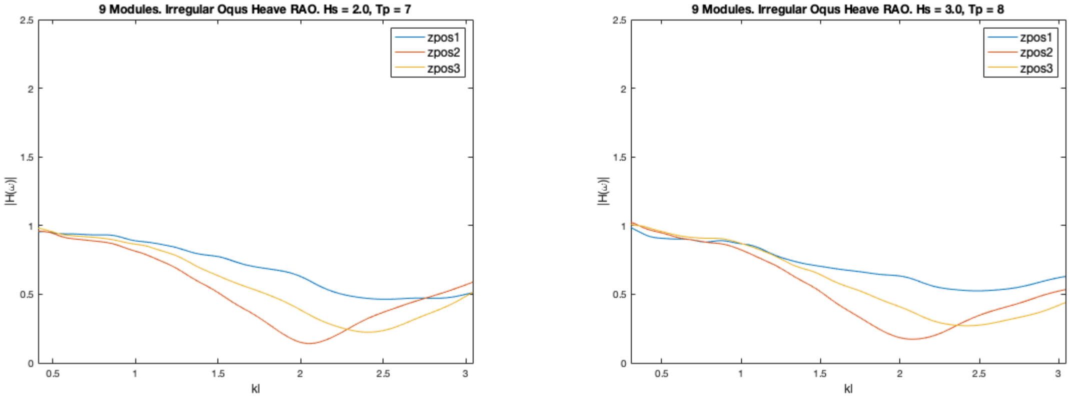

Figur K.27: Heave RAO for the motion capture measurements for each instrumented module, in irregular waves with $H_s = 2$m and $T_p = 7$s (left), and $H_s = 3$m and $T_p = 8$s (right). Represented as the transfer function $|H(\omega)|$ plotted against the dimensionless wave-number kl.

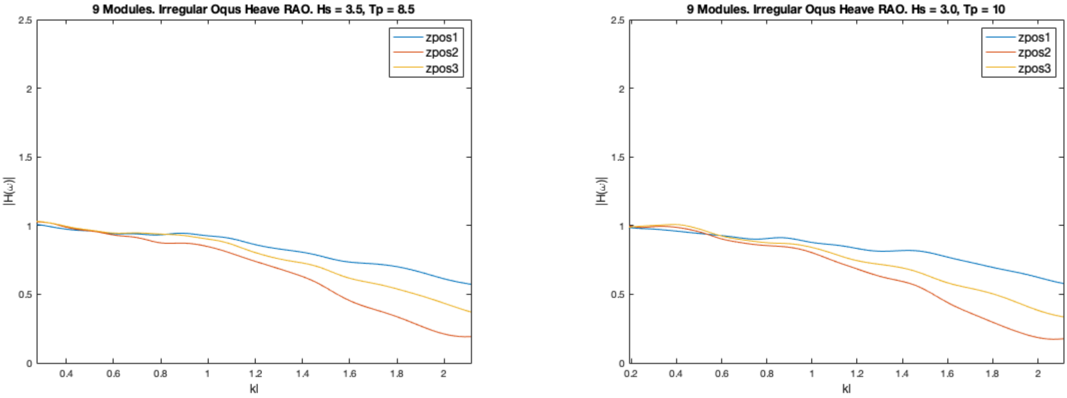

Figur K.28: Heave RAO for the motion capture measurements for each instrumented module, in irregular waves with $H_s = 3.5$m and $T_p = 8.5$s (left), and $H_s = 3$m and $T_p = 10$s (right). Represented as the transfer function $|H(\omega)|$ plotted against the dimensionless wave-number kl.

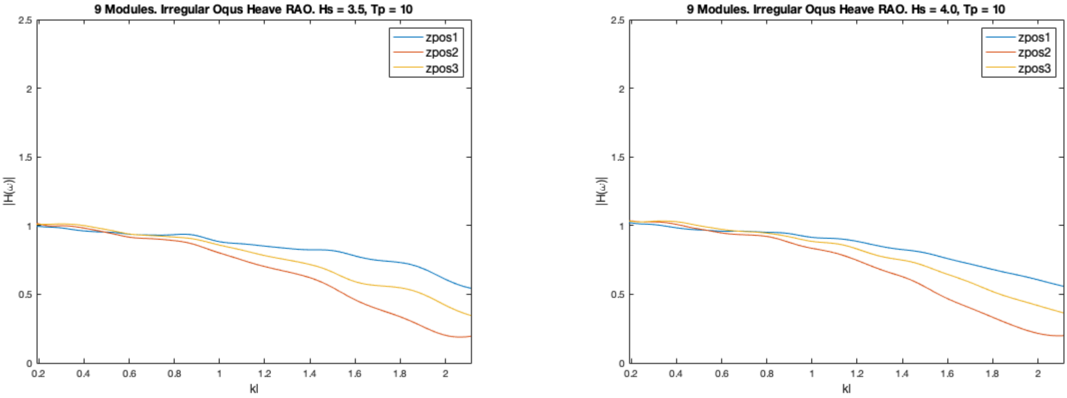

Figur K.29: Heave RAO for the motion capture measurements for each instrumented module, in irregular waves with $H_s = 3.5$m and $T_p = 10$s (left), and $H_s = 4$m and $T_p = 10$s (right). Represented as the transfer function $|H(\omega)|$ plotted against the dimensionless wave-number kl.

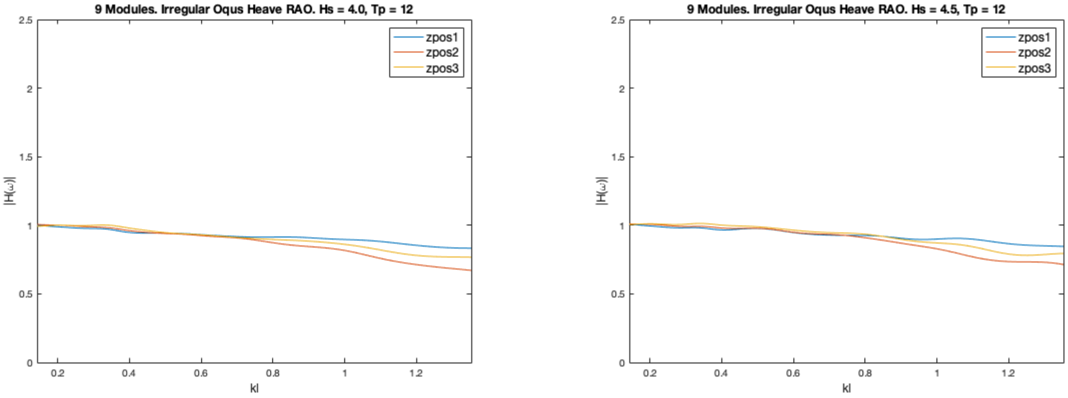

Figur K.30: Heave RAO for the motion capture measurements for each instrumented module, in irregular waves with $H_s = 4\text{m}$ and $T_p = 12\text{s}$ (left), and $H_s = 4.5\text{m}$ and $T_p = 12\text{s}$ (right). Represented as the transfer function $|H(\omega)|$ plotted against the dimensionless wave-number kl.

K.5.2 Accelerometer Positions Results

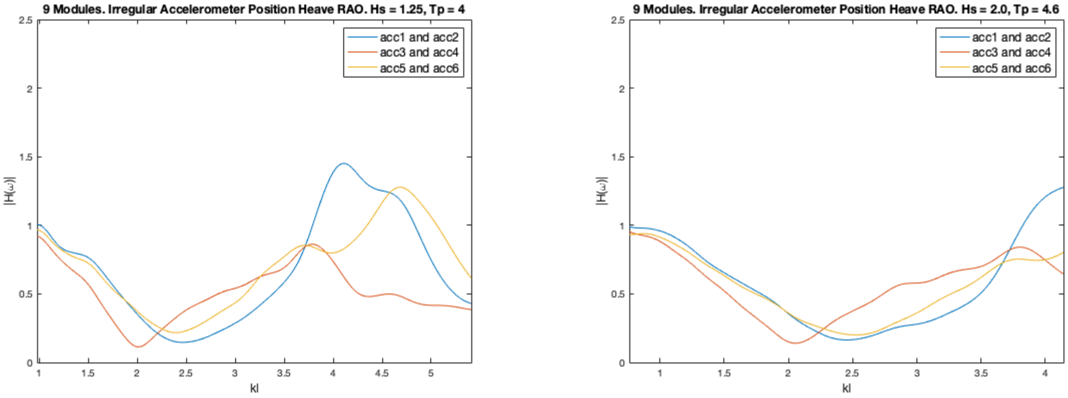

Figur K.31: Heave RAO for the combined accelerometer positions for each instrumented module, in irregular waves with $H_s = 1.25\text{m}$ and $T_p = 4\text{s}$ (left), and $H_s = 2\text{m}$ and $T_p = 4.6\text{s}$ (right). Represented as the transfer function $|H(\omega)|$ plotted against the dimensionless wave-number kl.

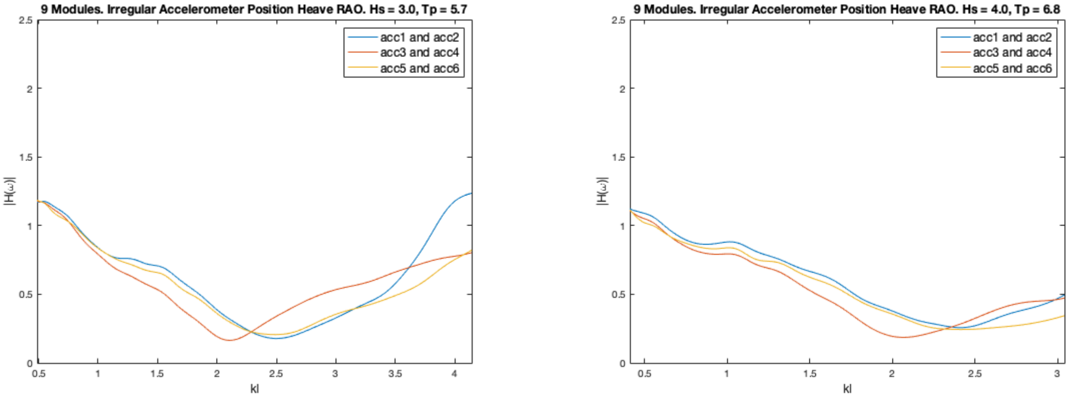

Figur K.32: Heave RAO for the combined accelerometer positions for each instrumented module, in irregular waves with $H_s = 3$m and $T_p = 5.7$s (left), and $H_s = 4$m and $T_p = 6.8$s (right). Represented as the transfer function $|H(\omega)|$ plotted against the dimensionless wave-number kl.

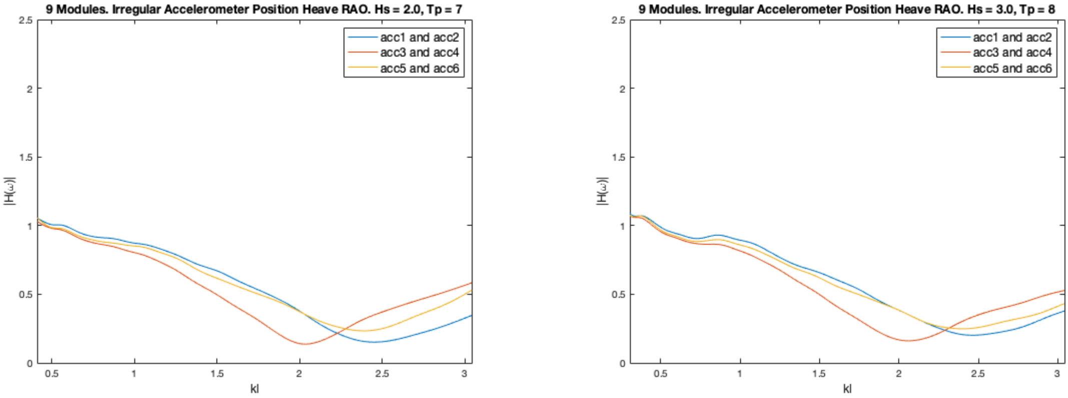

Figur K.33: Heave RAO for the combined accelerometer positions for each instrumented module, in irregular waves with $H_s = 2$m and $T_p = 7$s (left), and $H_s = 3$m and $T_p = 8$s (right). Represented as the transfer function $|H(\omega)|$ plotted against the dimensionless wave-number kl.

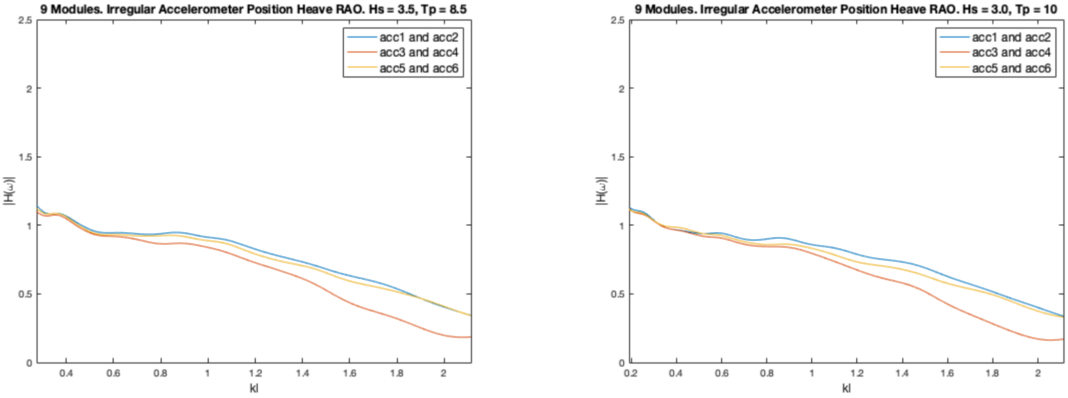

Figur K.34: Heave RAO for the combined accelerometer positions for each instrumented module, in irregular waves with $H_s = 3.5$m and $T_p = 8.5$s (left), and $H_s = 3$m and $T_p = 10$s (right). Represented as the transfer function $|H(\omega)|$ plotted against the dimensionless wave-number kl.

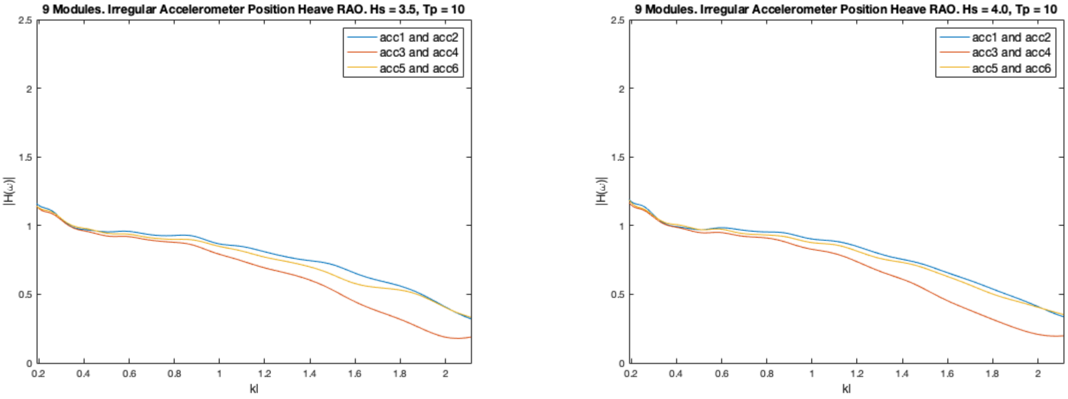

Figur K.35: Heave RAO for the combined accelerometer positions for each instrumented module, in irregular waves with $H_s = 3.5$m and $T_p = 10$s (left), and $H_s = 4$m and $T_p = 10$s (right). Represented as the transfer function $|H(\omega)|$ plotted against the dimensionless wave-number kl.

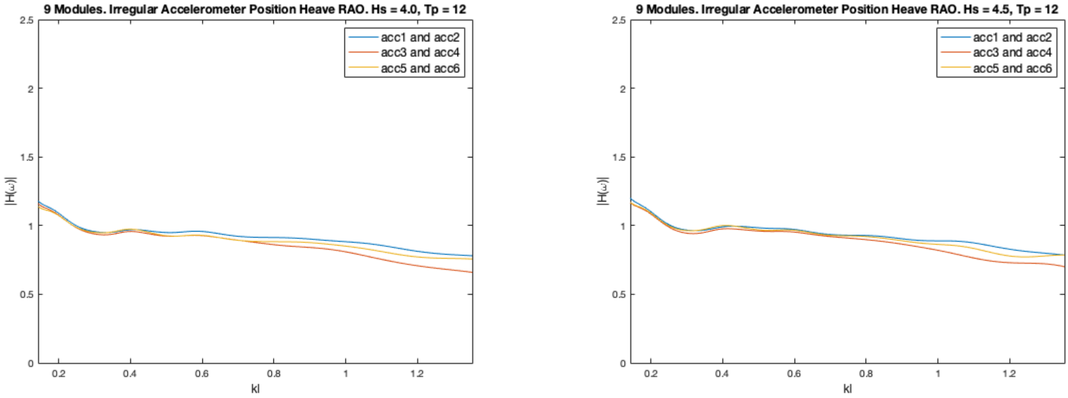

Figur K.36: Heave RAO for the combined accelerometer positions for each instrumented module, in irregular waves with $H_s = 4$m and $T_p = 12$s (left), and $H_s = 4.5$m and $T_p = 12$s (right). Represented as the transfer function $|H(\omega)|$ plotted against the dimensionless wave-number kl.

K.6 Irregular Pitch RAO

K.6.1 Motion Capture Results

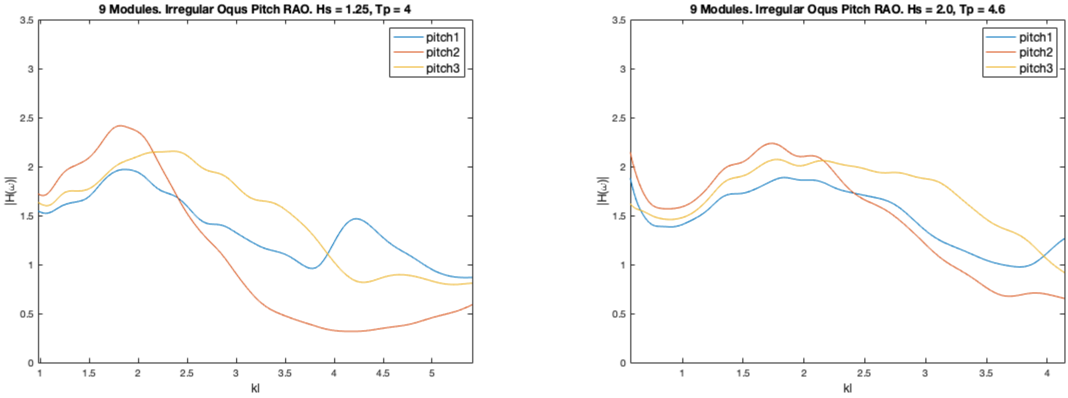

Figur K.37: Pitch RAO for the motion capture measurements for each instrumented module, in irregular waves with $H_s = 1.25$m and $T_p = 4$s (left), and $H_s = 2$m and $T_p = 4.6$s (right). Represented as the transfer function $|H(\omega)|$ plotted against the dimensionless wave-number kl.

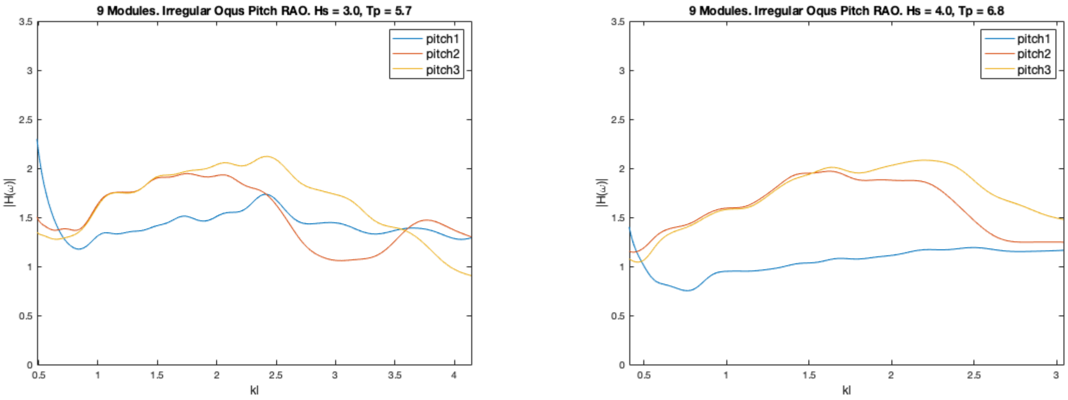

Figur K.38: Pitch RAO for the motion capture measurements for each instrumented module, in irregular waves with $H_s = 3$m and $T_p = 5.7$s (left), and $H_s = 4$m and $T_p = 6.8$s (right). Represented as the transfer function $|H(\omega)|$ plotted against the dimensionless wave-number kl.

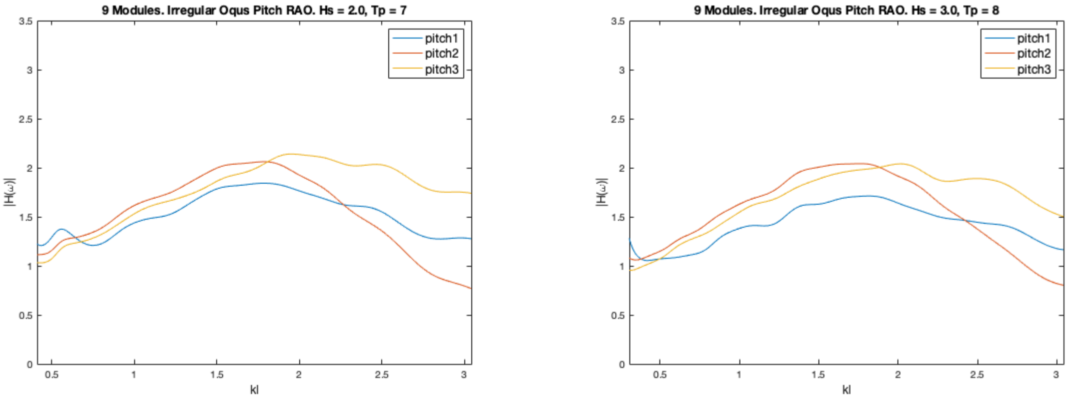

Figur K.39: Pitch RAO for the motion capture measurements for each instrumented module, in irregular waves with $H_s = 2$m and $T_p = 7$s (left), and $H_s = 3$m and $T_p = 8$s (right). Represented as the transfer function $|H(\omega)|$ plotted against the dimensionless wave-number kl.

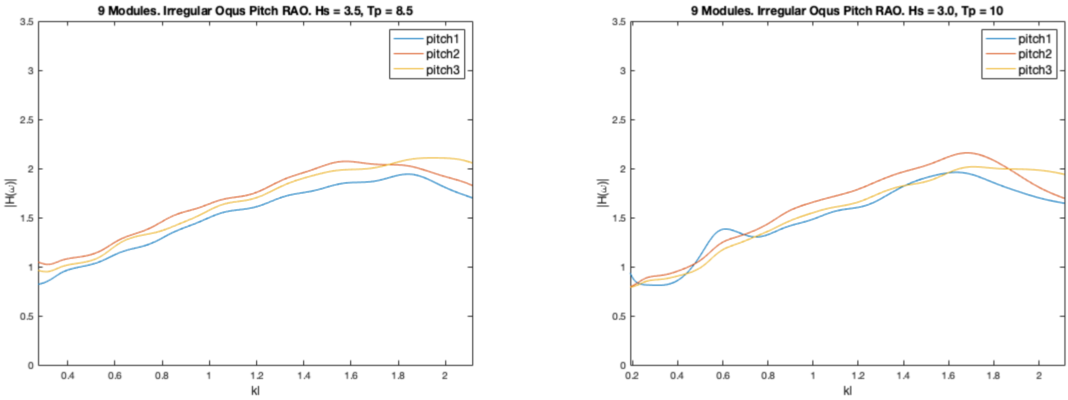

Figur K.40: Pitch RAO for the motion capture measurements for each instrumented module, in irregular waves with $H_s = 3.5$m and $T_p = 8.5$s (left), and $H_s = 3$m and $T_p = 10$s (right). Represented as the transfer function $|H(\omega)|$ plotted against the dimensionless wave-number kl.

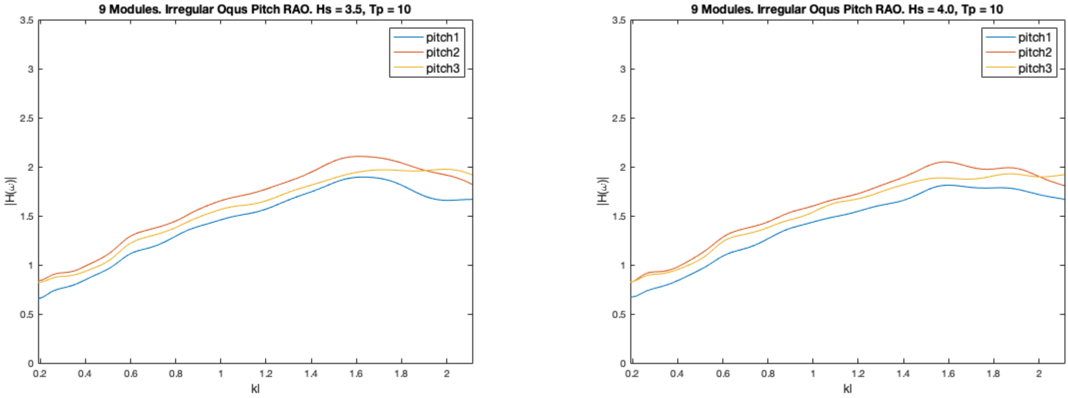

Figur K.41: Pitch RAO for the motion capture measurements for each instrumented module, in irregular waves with $H_s = 3.5$m and $T_p = 10$s (left), and $H_s = 4$m and $T_p = 10$s (right). Represented as the transfer function $|H(\omega)|$ plotted against the dimensionless wave-number kl.

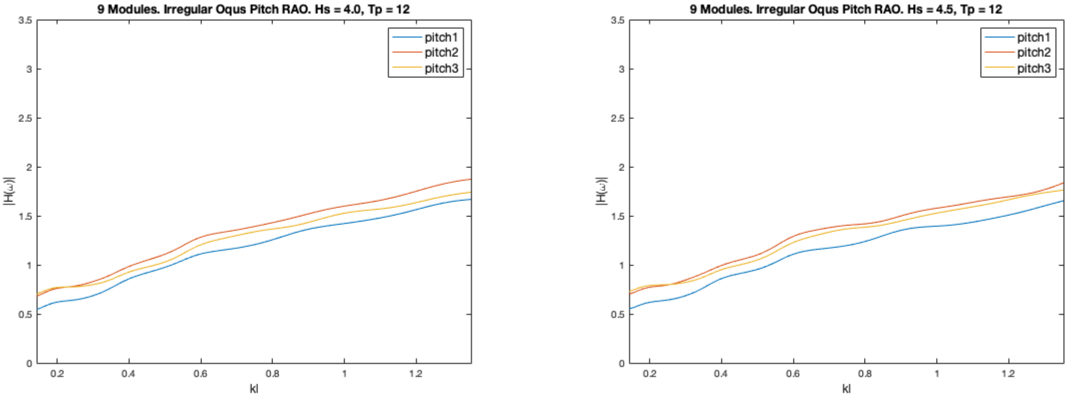

Figur K.42: Pitch RAO for the motion capture measurements for each instrumented module, in irregular waves with $H_s = 4$m and $T_p = 12$s (left), and $H_s = 4.5$m and $T_p = 12$s (right). Represented as the transfer function $|H(\omega)|$ plotted against the dimensionless wave-number kl.

Magnus Onsrud

An Experimental Study on the Wave-Induced Vertical Response of an Articulated Multi-Module Floating Solar Island

NTNU
Norwegian University of
Science and Technology